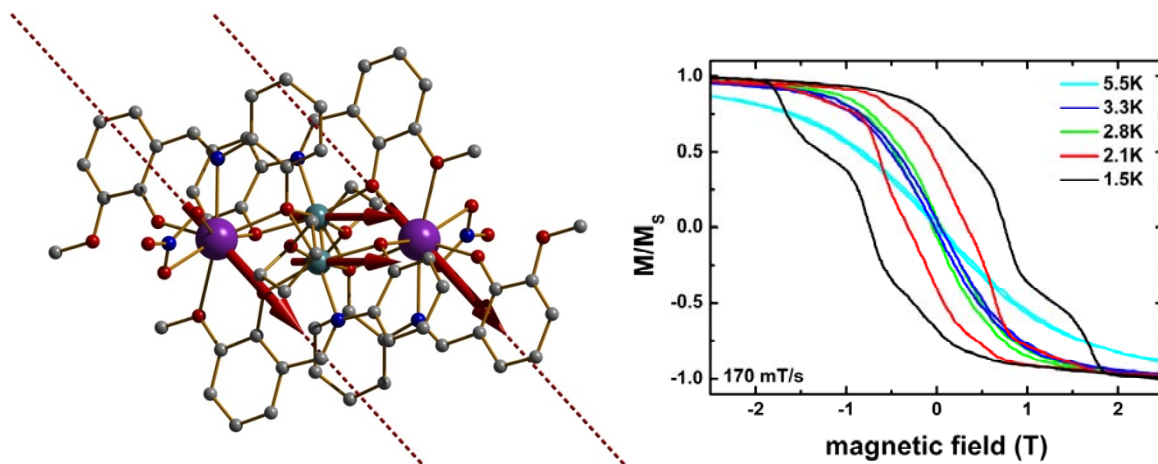


Syntheses, Structures and Properties of f and d-f Complexes using O-vanillin-derived Schiff base Ligands



DISSERTATION

von

M. S.-Chem. Kartik Chandra Mondal

aus Khukurdaha, W. B, India.

Syntheses, Structures and Properties of f and d-f Complexes using O-vanillin-derived Schiff base

Ligands

Zur Erlangung des akademischen Grades eines

DOKTORS DER NATURWISSENSCHAFTEN

(Dr. rer. nat.)

Fakultät für Chemie und Biowissenschaften

Karlsruher Institut für Technologie (KIT) – Universitätsbereich

vorgelegte

DISSERTATION

von

M. S.-Chem. Kartik Chandra Mondal

aus Khukurdaha, W. B, India.

Dekan: Prof. Dr. S. Bräse

Referent: Prof. Dr. A. K. Powell

Korreferent: Prof. Dr. P. W. Roesky

Tag der mündlichen Prüfung: 15.04.2011

To

My English teacher Bipad Baran Gangula (late)

And

My Science teacher IES. Eng. Swapan Kumar Mondal

Contents

Chapter 1		1
1.1	Introduction to Molecular Magnetism	1
1.1.1	Magnetic Susceptibility	2
1.1.2	Classification of Magnetic Behaviour	3
1.1.3	Single Molecule Magnets (SMMs)	7
1.2	Fluorescence Property	14
1.3	Synthetic Strategies towards Coordination Clusters	15
1.3.1	3d Coordination Chemistry	15
1.3.2	4f Coordination Chemistry	15
1.3.3	3d-4f and 4d-4f Coordination Chemistry	16
1.3.4	Ligand Selection and Synthetic Strategy	16
1.4	Thesis Overview	20
Chapter 2	Research Objectives	21
Chapter 3	Ni-Ln Coordination Clusters with (E)-2-(2-hydroxy-3-methoxybenzylideneamino)-phenol (H₂L1)	22
3.1	Introduction	22
3.2	Synthetic strategy	23
3.2.1	Crystal structures of [Dy ₂ Ni ₂ (L1) ₄ (NO ₃) ₂ (DMF) ₂] (1) and [Ln ₂ Ni ₂ (L1) ₄ (NO ₃) ₂ (H ₂ O) ₂]·3MeOH (2-7); [Ln = Dy(2), Y(3), Gd(4), Tb(5), Ho(6), Er(7)]	25
3.2.2	Static magnetic properties of compounds 1-7	27
3.2.3	Dynamic magnetic properties of 1-7	30
3.3.1	Crystal structures of [Ln ₂ Ni ₂ (CO ₃)(L1) ₄ (MeOH) ₆] ₂ [Ln ₂ Ni ₂ (CO ₃)(L1) ₄ (MeOH) _{6-x} (H ₂ O) _x]·yMeOH; [Ln = Dy(8), x = 1, y = 14; Ln = Sm(9), Eu(10), x = 2, y = 15; Ln = Gd(11), x = 2, y = 17 and Tb(12), x = 1, y = 14]	35
3.3.2	Static magnetic properties of 8-12	37
3.3.3	Dynamic magnetic properties of 8-12	40
3.4.1	Crystal structures of ring like [Ln ₄ Ni ₈ (CO ₃) ₄ (L1) ₈ (NO ₃) ₂ (H ₂ O) ₈ (MeOH) ₄](NO ₃) ₂ ·5MeOH·4H ₂ O;	

	[Ln = Dy(13), Y(14), Gd(15), Tb(16), Ho(17) and Er(18)]	43
3.4.2	Static magnetic properties of 13-18	45
3.4.3	Dynamic magnetic properties of 13-18	48
3.5.1	Crystal structure of half-ring like	
	[Dy ₂ Ni ₄ (OH) ₂ (L1) ₄ (MeOH) ₄ (NO ₃) ₄].4MeOH (19)	51
3.5.2	Static magnetic properties of the Dy ₂ Ni ₄ half-ring (19)	53
3.5.3	Dynamic magnetic properties of the Dy ₂ Ni ₄ half-ring (19)	54
3.6.1	Crystal structure of complex	
	[Dy ₄ Ni ₈ (OH) ₄ (L1) ₈ (MeOH) ₄ (H ₂ O) ₄ (C ₂ O ₄) ₂](NO ₃) ₄ ·4H ₂ O·8MeOH (20)	56
3.6.2	Static magnetic properties of 20	57
3.6.3	Dynamic magnetic properties of 20	58
3.7	Discussion	59
3.8	Conclusion	63
Chapter 4	Other 3d-Ln and 4d-Ln Coordination Clusters with	
	(E)-2-(2-hydroxy-3-methoxy-benzylideneamino)phenol (H₂L1)	64
4.1	Introduction	64
4.2	Synthetic strategy	65
4.2.1	Crystal structure of complexes	
	[Ln ₂ Zn ₃ (OH)(L1) ₅ (MeOH) _{2.5} (H ₂ O) _{1.5}].Cl·3MeOH·2.5H ₂ O;	
	[Ln = Dy(21), Eu(22), Gd(23), Tb(24) and Ho(25)]	66
4.2.2	Static magnetic properties of 21-25	68
4.2.3	Dynamic magnetic properties of 21-25	71
4.2.4	Fluorescence properties of 21-25	72
4.3.1	Crystal structure of complex	
	[Dy ₇ Zn ₄ (OH) ₄ (L1) ₈ (Cl) ₆ (H ₂ O) ₄].Cl ₃ ·35H ₂ O (26)	73
4.3.2	Static magnetic properties of 26	75
4.3.3	Dynamic magnetic properties of 26	76
4.3.4	Fluorescence properties of 26	77
4.4.1	Crystal structures of [Ln ₆ Cd ₆ (CO ₃) ₂ (OH) ₄ (μ-Cl) ₂ (Cl) ₂ (L1) ₈ (OH ₂) ₁₂]	
	Cl ₂ ·10THF; [Ln = Dy(27), Tb(28), Ho(29) and Er(30)]	78
4.4.2	Static magnetic properties of 27-30	79

4.4.3	Dynamic magnetic properties of 27-30	82
4.4.4	Fluorescence properties of 27-30	84
4.5.1	Crystal structures of $[\text{Ln}_3\text{Cu}_2(\mu_3\text{-OH})_2(\text{L1})_5(\text{NO}_3)(\text{MeOH})_2(\text{H}_2\text{O})]\cdot 3\text{MeOH}\cdot x\text{H}_2\text{O}$; [Ln = Dy(31), Gd(32), Tb(33), and Ho(34), x = 0 for 31, 32, 33 and x = 1 for 34]	86
4.5.2	Static magnetic properties of 31-34	87
4.5.3	Dynamic magnetic properties of 31-34	90
4.6.1	Crystal structures of $[\text{Ln}_2\text{Co}_2(\text{L1})_4(\text{NO}_3)_2(\text{THF})_2]\cdot 4\text{THF}$; [Ln = Dy(35), Y(36), Gd(37), Tb(38), Ho(39) and Er(40)]	91
4.6.2	Static magnetic properties of 35-40	92
4.6.3	Dynamic magnetic properties of 35-40	95
4.7	Conclusion	100
Chapter 5	Tetranuclear 4f Coordination Clusters with (E)-2-(2-hydroxy-3-methoxybenzylidene-amino)phenol (H₂L1) and (E)-N'-(2-hydroxy-3-methoxybenzylidene)-(2-hydroxy)-benzohydrazide (H₃L3)	103
5.1	Introduction	103
5.2	Synthetic strategy	104
5.2.1	Crystal Structures of $[\text{Ln}_4(\text{OH})_2(\text{L1})_4(\text{HL1})_2]\cdot 2\text{THF}$; [Ln = Dy(41), Gd(42), Tb(43), Ho(44) and Er(45)]	105
5.2.2	Static magnetic properties of 41-45	107
5.2.3	Dynamic properties of 41-45	111
5.3.1	Crystal structures of $(\text{Et}_3\text{NH})_6[\text{Ln}_4(\text{HL3})_2(\text{NO}_3)_{10}(\text{H}_2\text{O})_4](\text{NO}_3)_4$; [Ln = Er(46), Gd(47), Tb(48), Dy(49) and Ho(50)]	115
5.3.2	Static magnetic properties of 46-50	117
5.3.3	Dynamic properties 46-50	120
5.4	Conclusion	123
Chapter 6	Cu-Ln Coordination Clusters with (E)-N'-(2-hydroxy-3-methoxybenzylidene)benzo-hydrazide (H₂L2) and bis-(E)-N,N'-(2-hydroxy-3-methoxy)-benzylhydrazone (H₂L4)	124
6.1	Introduction	124
6.2	Synthetic strategy	125

6.2.1	Crystal structure of complex [DyCu(L2)(OMe)(NO ₃) ₂ (H ₂ O)(MeOH)]·2MeOH (51)	127
6.2.2	Static magnetic properties of 51	129
6.3.1	Crystal structures of the complexes [DyCu ₂ (L2) ₂ (OMe) ₂ (NO ₃)(H ₂ O) ₂]·H ₂ O·1.5MeOH (52) and [DyCu ₂ (L2) ₂ (N ₃) ₃ (MeOH)(H ₂ O)]·3MeOH·1.5H ₂ O (53)	130
6.3.2	Static magnetic properties of 52-53	133
6.3.3	Dynamic magnetic properties of 52 and 53	135
6.4.1	Crystal Structure of [LnCu ₃ (L2) ₃ (OMe) ₃]·xMeOH·yH ₂ O; [Ln = Dy(54), x = 1.5, y = 0.215; Tb(55) and Gd(56) x = 1, y = 0; Ho(57) and Er(58) x = 1.5, y = 0.215]	138
6.4.2	Static magnetic properties of 54 -58	141
6.4.3	Dynamic magnetic properties of 54-58	144
6.5.1	Crystal structure of [Dy ₂ Cu ₆ (OMe) _{2.76} (N ₃) _{1.24} (L2) ₆ (H ₂ O)(MeOH)(L4)]·10MeOH·2H ₂ O (59)	151
6.5.2	Static magnetic properties of 59	153
6.5.3	Dynamic magnetic properties of 59	154
6.6.1	Crystal structures of [Ln ₉ Cu ₂ (L2) ₄ (HL2) ₄ (OH) ₈ (CO ₃) ₃ (NO ₃) ₃ (H ₂ O) ₄ (EtOH)] (NO ₃) ₂ ·9EtOH·6H ₂ O; [Ln = Dy(60) and Er(61)]	156
6.6.2	Static magnetic properties of 60 and 61	158
6.6.3	Dynamic magnetic properties of 60 and 61	160
6.7.1	Crystal structure of [Dy ₂ Cu(OH)(L2) ₂ (HL2) ₂ (H ₂ O)]Cl·5EtOH·2.5H ₂ O (62)	161
6.7.2	Static magnetic properties of 62	162
6.7.3	Dynamic magnetic properties of 62	163
6.8	Conclusion	164
Chapter 7	Conclusion and Outlook	167
Chapter 8	Experimental Section	171
Chapter 9	Crystallographic Data	191
Chapter 10	Bibliography	202

Chapter 11	Appendix	208
Appendix A:	List of compounds	208
Appendix B:	List of organic ligands	210
Appendix C:	List of abbreviations	210

Chapter 1

1.1 Introduction to Molecular Magnetism

Historically, the intriguing phenomenon of magnetism was first noticed (900 B.C.) when the naturally occurring magnet lodestone, found in Magnesia (Greece) was observed to attract iron. The phenomenon was observed by the Greeks and used by the Chinese to create the floating compass.¹ In 1269 Petrus Peregrinus de Maricourt identified that magnets have poles which he called “North” and “South”, which are maintained on breaking a magnet. He observed that opposite poles attract each other while the similar magnetic poles repelled. At the beginning of the 20th century, the French physicist, Pierre-Ernest Weiss, developed the theory of ferromagnetism based on the assumption that the interaction between magnetic centers could be described empirically considering an internal molecular field. Later, the Danish physicist Niels Bohr pointed out the spinning nature of an electron in the course of his work on atomic structure.²

Over the centuries, mankind has made use of magnetism in mechanical applications such as electromotors or electric generators, or in communication technologies such as telephones and television. More recently, magnetism had found widespread applications in the area of data storage and processing, from magnetic tape to floppy disks and computer hard drives.

The most usable types of magnets are either ferro- or ferrimagnets, each of which has a characteristic Curie temperature, below which it shows its magnetic properties. Such magnets can be pure metals, alloys, metal oxides or molecular magnets. The spins on the magnetic centres are interacting with their neighbours in the three dimensional lattice of a conventional magnet and their spontaneous magnetization relies on the alignment of the very large number of spin centres in the bulk material. The bulk magnetic structure is divided into many magnetic domains, within each of which the spins are aligned, but with the different domains having different alignment directions such that their overall magnetic moments cancel out. However, the application of a small external magnetic field can orient the magnetic moments of all domains in the direction of the applied field. The data storage capacity of such conventional magnets is therefore limited by the size of the domains. Thus there is now a quest for new materials which could show magnetic behaviour, allowing a very much higher data storage density.

Historically in 1980, T. Lis³ reported the mixed-valence coordination cluster $[\text{Mn}_{12}\text{O}_{12}(\text{OAc})_{16}(\text{H}_2\text{O})_4].2\text{AcOH}.4\text{H}_2\text{O}$ (usually abbreviated as $\text{Mn}_{12}\text{-Ac}$) while trying to oxidize Mn^{II} ions by using permanganate (MnO_4^-) in acetic acid. A decade later, dynamic magnetic susceptibility measurements on this complex led to the observation of slow relaxation of its magnetization,^{4,5} while hysteresis measurements revealed^{6a} steps at low temperature (below 2 K). This discovery represented a major breakthrough in nanomagnetism, providing evidence of the coexistence of classical and quantum effects in the dynamics of the magnetization.⁶ Since the oxo-bridged polynuclear core is surrounded by diamagnetic organic ligands, the magnetic properties of the compound are molecular-based rather than a bulk property,^{4,7} and $\text{Mn}_{12}\text{-Ac}$ can be considered as a Single Molecular Magnet (SMM).⁸ SMMs have also been observed to show quantum tunneling^{6,8a} of magnetization and quantum phase^{8b} interference, which are the key properties needed for materials to function as quantum bits (qubits).⁹

Besides their size, SMMs have a number of other advantages over the traditional magnets. The SMMs are soluble in organic solvents because of the peripheral organic ligands which also prevent the magnetic cores from interacting with each other. SMMs have uniform size and structure, and they are mostly air-stable for long term storage. Over the past two decades of research in SMMs, fine details of the properties of these tiny magnets have become better understood and the synthesis of diverse compounds has been developed, but the blocking temperatures (T_b : the temperature below which a molecule acts as a magnet) of SMMs still remains very low (often below 4 K).¹⁰ Thus there is now a continuous quest for new SMMs, in order to understand better both the structural aspects that favour SMM behaviour, and also the synthetic methodologies needed to achieve this, with the long-term goal of developing such systems with more useful (*i.e.* higher) blocking temperatures.

1.1.1 Magnetic Susceptibility

In magnetism the magnetic susceptibility is the degree of magnetization induced in a material in response to a given applied magnetic field. Magnetic measurements can give information about the electronic structure of a substance with unpaired electrons. Complexes of paramagnetic metal ions may have exchange interactions between the metal centres. This section provides a brief overview of how magnetic measurements can be applied to this area of inorganic

chemistry. More detailed accounts are given in standard texts by Mababas and Machin,^{11a} O'Connor,^{11b} Carlin,^{11c} and Kahn.^{11d}

Rotational motion of an electric charge generates a magnetic field in a material. Magnetism is therefore a characteristic property of all materials that contain electrically charged particles, and for most purposes can be considered to be entirely of electronic origin. In an atom, the magnetic field is associated with the motion of the electrons which gives rise to the coupled spin and orbital magnetic moments. The first of these results from precession of unpaired electrons about their own axes, while the second is due to the motion of electrons around the nucleus. The magnetization, M is defined as the magnetic moment per unit volume. The magnetic susceptibility, χ is the degree to which a material can be magnetized in an external magnetic field. The magnetic susceptibility per unit volume is then:¹¹

$$\chi = M/H \text{ (cgs)} \quad \text{or} \quad \chi = \mu_0 M/H \text{ (SI)} \quad \text{Eq. 1.1}$$

where H is the macroscopic magnetic field intensity in Oersted, Gauss or Tesla. It is sometimes convenient to refer to M/H as susceptibility without specifying the system units. The molar susceptibility is designated as χ_M , and the magnetic moment per gram is sometimes written as σ . In general χ is the algebraic sum of two contributions:^{11c}

$$\chi = \chi^D + \chi^P \quad \text{Eq. 1.2}$$

where χ^D and χ^P represent the diamagnetic and paramagnetic susceptibilities, respectively. The former is negative and the latter is positive.

1.1.2 Classification of Magnetic Behavior

The origin of magnetism lies in the orbital and spin motion of electrons as well the interaction of these electrons with one another. In some materials there is no collective interaction between the atomic magnetic moments, whereas in some there can be a very strong interaction between the moments on neighbouring atoms. The magnetic behavior of materials can be classified into the following six major groups, based on the responses of materials to magnetic fields:

Diamagnetism The interaction of the magnetic field with the motion of the electrons in their orbitals leads to diamagnetism. In this case, magnetic susceptibility is usually independent of the temperature and the strength of the applied field. This is the only magnetic response, when a substance is composed of atoms which have no net magnetic moments because all the occupied orbitals are containing a pair of electrons. When exposed to a magnetic field, a negative

magnetization is produced, and the susceptibility is thus also negative, and the substance is repelled by the field. This is a fundamental property of all matter, even substances that also contain some unpaired electrons, but is usually very weak.

Paramagnetism: Any atom, ion or molecule that has one or more unpaired electrons is paramagnetic and possesses a net magnetic moment. Such substances are attracted to a magnetic field due to a partial alignment of the atomic magnetic moments in the direction of the field, resulting in a net positive magnetization and positive susceptibility. The individual magnetic moments, however, do not interact magnetically and do not retain any magnetization in the absence of an externally applied magnetic field because thermal motion causes the spins to become randomly oriented.

Ferromagnetism: Substances which have magnetic interactions between neighboring paramagnetic centers such that the individual moments are aligned parallel to each other, leading to an increase in the magnetic moment, are designated as ferromagnets. A ferromagnetic substance usually divides into domains to minimize its total free energy; a spontaneous magnetization arises in each domain even in the absence of a magnetic field. The saturation of magnetization corresponds to the complete alignments of all magnetic domains. Its magnetic susceptibility is positive and very large.^{12a} However, above its Curie temperature (T_C) the interactions are no longer strong enough to maintain the individual moments in alignment, and the substance then behaves as a simple paramagnet.

Antiferromagnetism: When the magnetic interactions between paramagnetic centers lead to an antiparallel alignment of the moments, the substance is known as an antiferromagnet. Because of the complete compensation of the magnetic moments, the substance does not show any spontaneous magnetisation.^{12a} Analogously to ferromagnetism, above its Néel temperature (T_N) an antiferromagnet behaves as a paramagnet.

Ferrimagnetism: Substances where the magnetic moments are aligned antiparallel but there is an incomplete compensation of the spins are termed ferrimagnets. This usually results either from unequal numbers of spins being oriented in the two directions, or when the two types of spin centers have different numbers of unpaired electrons. Ferrimagnets exhibit spontaneous magnetization as in the case of ferromagnets.^{12b}

Canted Antiferromagnetism: When, below T_N the equilibrium distribution of moments is not collinear; the system is “canted” with incomplete compensation of the spins, giving rise to a

spontaneous magnetization. The resulting hysteresis loops below the critical temperature confer a memory effect on the material. This phenomenon is known as canted antiferromagnetism or weak ferromagnetism.¹³⁻¹⁵

Determination of Magnetic behavior: It was shown by Pierre Curie that for most paramagnetic substances with isolated magnetic sites; the magnetic susceptibility varies inversely with temperature. The magnetization of paramagnets follows Curie's law to a good approximation:

$$M = C.H / T \quad \text{where } C = Ng^2\mu_B^2 / 4k_B \quad \text{Eq. 1.3}$$

where M is the resulting magnetization, H is the applied field and C is the Curie constant. Since the magnetic susceptibility is $\chi = M/H$, in this case:

$$\chi = C / T \quad \text{Eq. 1.4}$$

When the paramagnetic ions or atoms interact this law is no longer valid, and the magnetic exchange between spin carriers then needs to be included in the model. As a result, in ferromagnets and antiferromagnets the Curie-Weiss law¹⁶ is applicable:

$$M = \frac{H}{T - \theta} \quad \text{with } C = \frac{Ng^2\mu_B^2}{4k_B} \quad \text{and } \theta = \frac{2zJ}{2k_B} \quad \text{Eq. 1.5}$$

where θ is the Weiss constant and the magnetic susceptibility is now given by:

$$\chi = \frac{C}{T - \theta} \quad \text{Eq. 1.6}$$

There are three ways to plot the temperature dependence of the magnetic susceptibility, and these are shown in Fig. 1.1. These plots give information about the kind of magnetic interactions present in a compound. A Curie-Weiss plot, of $1/\chi$ against T, usually gives a straight line, although it may start to curve at lower temperatures. The Curie constant C can be obtained from the gradient, and the Weiss constant θ from the extrapolated intercept on the T axis. A paramagnet should have this intercept at the origin, while for ferromagnets and antiferromagnets the intercept is positive or negative, respectively. For all three classes of substance, at higher temperatures χ shows a steady increase as the temperature decreases. For an antiferromagnet, χ starts to decrease again as the temperature goes below T_N , while for a ferromagnet (or a ferrimagnet) χ starts to increase very sharply as the temperature passes below T_C . Plots of χT against T are the most often used. For a paramagnet, χT is independent of temperature, and the plot shows a horizontal straight line. For antiferromagnets, the plot shows a decrease of χT with decreasing temperature, extrapolating to zero if the ground state has $S = 0$. For a ferromagnet, χT

increases as the temperature is lowered, while for a ferrimagnet, χT first decreases to a minimum and then increases sharply as the temperature is further decreased.

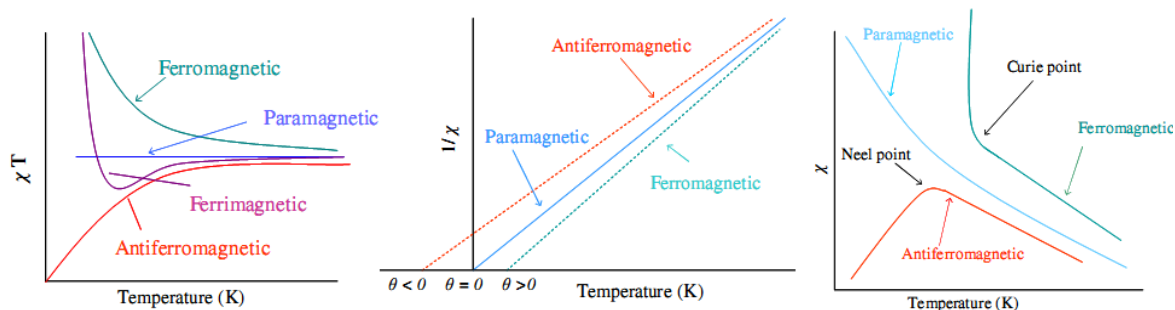


Fig. 1.1 Plots of χT (left), $1/\chi$ (middle) and χ (right) as a function of temperature for paramagnetic, ferromagnetic, antiferromagnetic and ferrimagnetic materials.

Magnetic interactions between paramagnetic centres that are either isotropic or weakly anisotropic are generally characterised by the Heisenberg-Dirac-Van Vleck (HDVV) or “Spin-only” Hamiltonian:

$$\mathbf{H} = -2J(\mathbf{S}_1 \cdot \mathbf{S}_2) \quad \text{Eq. 1.7}$$

Where \mathbf{S}_1 and \mathbf{S}_2 are the spins on the two metal centers, and J is the exchange integral characterizing the coupling between them, which is usually given in units of cm^{-1} or K, where $1 \text{ cm}^{-1} \equiv 1.44 \text{ K}$. For antiferromagnetic and ferromagnetic coupling, J is negative and positive respectively.

It should be noted that these types of magnetic behavior only hold for isotropic or weakly anisotropic paramagnetic metal ions. Most of the 3d metal ions in fact closely obey the Curie law, with the exception of Co^{II} . Because of spin orbit coupling, the Co^{II} ion inherently possesses a large orbital momentum contribution towards its total magnetic moment. First order spin-orbit coupling splits the $^4\text{T}_{1g}$ ground state into a set of three levels ($J = 5/2$, $J = 3/2$ and $J = 1/2$). As the temperature is lowered, thermal depopulation of the upper levels occurs and the χT product, even of an isolated Co^{II} ion, now shows a decrease as the temperature is reduced to low values. Such a plot resembles that of an antiferromagnetic material, and when a compound contains highly anisotropic ions it can be difficult to establish if this behavior results from dominant antiferromagnetic coupling, the anisotropy of the ion, or a combination of these. Rare-earth ions (4f) can also have large unquenched orbital angular momentum associated with

the internal nature of the valence f orbitals. The Eu^{II} and Gd^{III} (f^7) ions are isotropic and all the orbital angular momentum is quenched. However, all the other paramagnetic rare-earth ions have orbitally degenerate ground states, which are split by spin-orbit coupling and crystal-field effects. As for Co^{II} , χT then decreases with decreasing temperature due to thermal depopulation of the Stark sublevels.

1.1.3 Single Molecule Magnets (SMMs)

SMMs are molecular complexes which act as nanomagnets below their blocking temperature (T_B). SMM behavior was first observed in $\text{Mn}_{12}\text{-Ac}$ but has subsequently been found in mononuclear coordination complexes as well as polynuclear coordination clusters. To act as a SMM, a coordination complex should have negative uni-axial magnetic anisotropy (D) and non zero spin ground state (S). The uni-axial anisotropy removes the degeneracy of the ground spin state splitting into $M_S = -S$ to $+S$. These two parameters combine to give rise a significant energy barrier towards the reversal of spin reorientation with the result that the relaxation of magnetization becomes slower. The energy barrier is given by $U_{\text{eff}} = |D| S^2$ or $|D| (S^2 - 1/4)$ for integral or half integral spin respectively. In this context we can take the well established double well potential formalism (Fig. 1.2) for $\text{Mn}_{12}\text{-Ac}$. The molecule can then have energy states starting from $M_S = -S$ to $M_S = +S$. For zero applied magnetic field, the probability of finding the molecule in either potential well is equal ($M_S = \pm S$). One of the potential wells can be preferentially more populated by applying magnetic field in a certain desired direction ($M_S = +S$ or $-S$). On switching off the magnetic field the molecules will try to head for the equilibrium population distribution through the thermally activated energy levels, e.g. equal distribution in both potential wells. However, there is also the alternative to tunnel through the potential energy

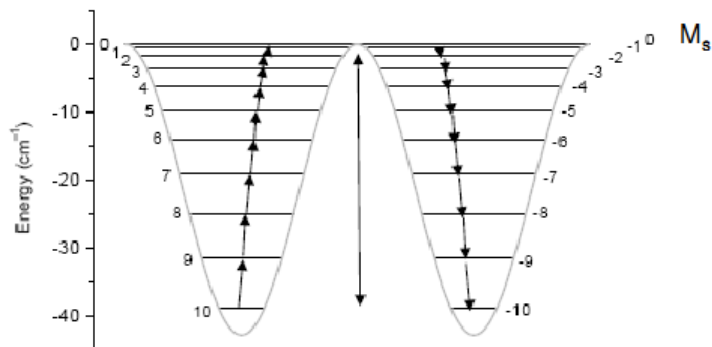


Fig. 1.2 Plots of energies of the microstates in $S = 10$ system.^{8a}

which equates to quantum tunneling of magnetization (QTM). If the energy barrier is high enough, a SMM can be characterized by in-phase (χ'), out-of-phase (χ'') signals and hysteresis loops. During ac susceptibility measurement, it produces two components; one is susceptibility (χ) and other one is phase shift (ϕ) producing a real component of susceptibility ($\chi' = \chi \cos\phi$) and an imaginary component ($\chi'' = \chi \sin\phi$). Thus, when real part of susceptibility increases time imaginary component decreases (Fig. 1.3). The maximum of χ'' vs T plot at a particular frequency is called blocking temperature (T_b) and below this temperature a molecule can act as a SMM. The SMM can thus be quantified by its effective energy barrier (U_{eff}) and relaxation time (τ_0). These two parameters are generally estimated from an Arrhenius plot (τ vs $1/T$), for which data of χ'' vs T or frequency are utilized. The linear fitting on the Arrhenius plot produces U_{eff} and τ_0 from the slope and intersection respectively. The higher the slope, the higher the energy barrier and the better is the SMM. The blocking temperature depends on the values of the U_{eff} and τ_0 and can be estimated from Arrhenius equation by replacing $\tau = \tau_0$ and $T = T_B$.

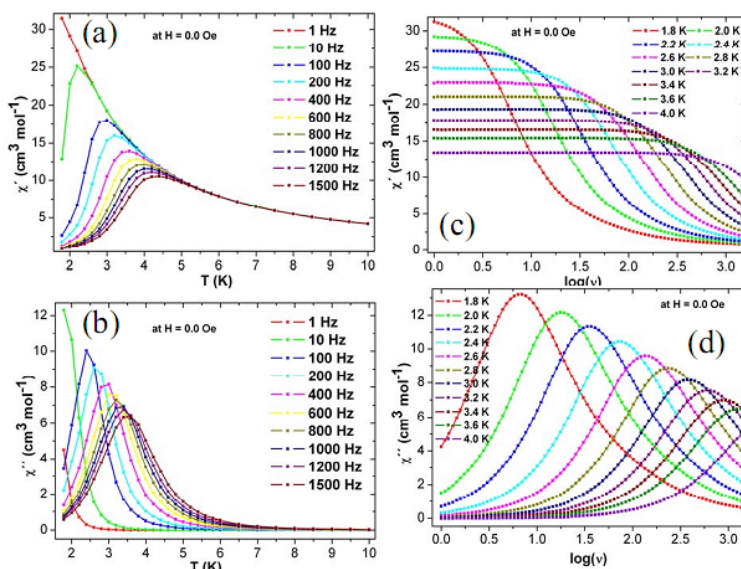


Fig. 1.3 An example of ac susceptibility measurements as a function of temperature at different frequencies, and as a function of frequency at different temperatures (a, c) in-phase and (b, d) out-of-phase signals.

If just a single relaxation process is involved, then a plot of χ'' versus temperature will display a maximum at the temperature where the ac frequency of the magnetic field matches the spin reorientation rate, $1/\tau$. Furthermore, since $1/\tau$ increases with temperature, this peak should

shift to higher temperatures when the frequency is increased. The relaxation time for the magnetization in a Single Molecule Magnet can be expected to follow an Arrhenius relationship:⁷

$$\tau = \tau_0 \cdot e^{\left(\frac{U_{eff}}{K_B T}\right)} \quad \text{Eq. 1.8}$$

If the energy barrier is low enough, then the frequency of spin reorientation is faster than the applied frequency and in that case the peak the maxima in χ'' vs T plots may not be observe or even no out-of-phase signal may not be detected.

There can be additional influences on the SMM behavior, such as quantum effects or inter-complex magnetic interactions. Furthermore, at low enough temperature, quantum relaxation of the magnetization can be experimentally observed since it becomes faster than the thermally activated relaxation induced by U_{eff} . A key factor is the transverse magnetic anisotropy, which influences the quantum tunneling of the magnetization (QTM). When two M_S microstates on either side of the energy barrier have similar energies, then there is an increased probability of quantum tunneling of the magnetization (QTM). In a molecule exhibiting purely axial anisotropy, the wave functions associated with the energy levels constituting each $\pm M_S$ pair are orthogonal to one another, thereby eliminating quantum tunneling as a possible relaxation pathway. However, the introduction of transverse magnetic anisotropy E allows mixing of the $\pm M_S$ levels, in turn allowing the system to tunnel from the $+M_S$ level through the thermal barrier to the $-M_S$ level.^{8a,17} Transverse anisotropy in what should be axial single molecule magnets was found to originate from the multi-spin nature of the system and from the breakdown of the strong exchange approximation.¹⁸ Overall SMM complexes can be described as unique systems for studying fundamental phenomena such as quantum spin tunneling and quantum interference. There is the propsept that these may find applications in the future applications in molecular electronics.¹⁹

3d based SMMs:

Many SMMs based on 3d metal ions have been reported.^{7,19} These SMMs can be homometallic (Ni^{II} ,²⁰ Co^{II} ,²¹ Fe^{II} ,²² Fe^{III} ,²³ $Mn^{II/III}$,²⁴ $Mn^{II/III/IV}$,²⁵ V^{III} ²⁶ etc.) or heterometallic.²⁷ mixed metal ions. The most studied SMMs are those belonging to the Mn_{12} -Ac family,³⁻⁶ although Fe^{III}_4 and Mn^{III}_6 families have also been studied extensively. Mn_{12} -Ac has a blocking

temperature (T_B) of 2.1 K, while the current best SMM $[\text{Mn}_6\text{O}_2(\text{Etsao})_6(\text{O}_2\text{CPh}(\text{Me})_2)_2(\text{EtOH})_6]$ {Et-saoH₂ = 2-hydroxyphenylpropanone oxime} has an $S = 12$ ground state, an energy barrier to magnetization reversal of 86 K and a blocking temperature T_B of 4.5 K.²⁸

The characteristics of the 3d metal ions can be summarized as follows. Cu^{II} (d^9) shows the well-known Jahn-Teller distortion due to its otherwise orbitally degenerate ground state, but is only very weakly anisotropic and there is no SMM based on purely Cu^{II} ions. The Ni^{II} (d^8) ion has second order orbital angular momentum, and zero-field splitting (ZFS)^{11d} can result in significant single-ion anisotropy.²⁹ The Fe^{II} (d^6) ion also has significant single ion magnetic anisotropy. Recently, the mononuclear SMM $[(\text{tpaMes})\text{Fe}^{\text{II}}]^-$ was reported,^{22b} the first 3d mononuclear SMM. By contrast, Fe^{III} (d^5) is generally isotropic, but weak anisotropy in Fe^{III} ions can result from an asymmetric ligand field,^{23a} resulting in Zero Field Splitting, and some Fe^{III} -based SMMs are therefore known.^{23c} However, no SMM containing only Mn^{II} ions (also d^5) has yet been reported, probably because of smaller value of the ZFS parameter for Mn^{II} ions.³⁰ Mn^{III} (d^4) ions are rich in single ion magnetic anisotropy, undergoing a Jahn-Teller distortion (usually elongation along the z axis) within the ligand field. Because of this intrinsic uniaxial single-ion anisotropy, the majority of SMMs so far reported are based on Mn^{III} ions.^{5,31-33} Unlike the other 3d ions, Co^{II} has first order orbital angular momentum, and are frequently found have effective spin $S_{\text{eff}} = 1/2$ at low temperature. For polynuclear Co^{II} systems, the anisotropy can therefore easily be of the same order of magnitude or even larger than the exchange coupling, and most polynuclear Co^{II} systems are best described as being in the weak exchange limit. A further consequence of using Co^{II} is that the equation relating the height of the energy barrier to S^2 and D is no longer valid, as S is not a good quantum number for polynuclear Co^{II} clusters.²¹

4f based SMMs:

The ac magnetic susceptibility measurements by Ishikawa et al. on a series of phthalocyanine double-decker complexes, $\text{N}(\text{C}_4\text{H}_9)_4^+[\text{Pc}_2\text{Ln}]^-$ ($\text{Ln}^{\text{III}} = \text{Tb}, \text{Dy}, \text{Ho}, \text{Er}, \text{Tm}, \text{or Yb}$; $\text{H}_2\text{Pc} = \text{phthalocyanine}$), showed slow relaxation of magnetization in the Tb^{III} and Dy^{III} complexes^{34-35a-b}, similar to that previously observed for 3d metal containing SMMs, but with blocking temperatures of 50 K and 25 K, respectively. However, this class of compounds functions as magnets at the molecular level by a mechanism different from that of the transition-metal-cluster SMMs, with a formalism that does not use the double-well-potential picture. In the

Tb complex, the lowest sub-states are assigned to $J_z = 6$, which are the maximum and minimum values in the $J = 6$ ground state. The energy separation from the rest of the sub-states is more than 400 cm^{-1} . If the relaxation occurs through a path consisting of stepwise transitions from J_z to $J_z \pm 1$ states, the “rate-determining step” is the first transition from $J_z = 6$ to $J_z = 5$ (or from -6 to -5) because of the large energy gap. In the Dy complex, the lowest sub-states are characterized as $J_z = +13/2$ and $-13/2$, which are the second largest in the $J = 15/2$ ground state. The sublevels are distributed more evenly than in the Tb case. This implies a possibility that there is no step requiring extremely high energy in the relaxation path. This can be regarded as a situation similar to that of the transition-metal-cluster SMMs but resulting in a much higher thermal barrier between the $+J_z$ and $-J_z$ sub-states. The change in single-ion anisotropy from easy-axial to easy-planar-type occurs between the Ho^{III} and Er^{III} complexes.

There are three major processes to be considered for the transition between the lowest two sub-states: (1) *the direct process*; (2) *the Raman process*; and (3) *the Orbach process*.^{35b} In Tb^{III} complexes, the two-phonon Orbach process is dominant in the temperature range 25-40 K, and either the direct or Raman process becomes the fastest path below 25 K. In Dy^{III} complexes, the Orbach process is the main path in the range 3-12 K.^{35b}

The magnetic properties of rare-earth ions are well-known and dominated by the unpaired electrons in their 4f orbitals, which give rise to strong unquenched orbital angular momentum and by spin-orbit coupling (λ). Because the 4f orbitals are generally shielded by the more extensive 5p and 6s orbitals, the intramolecular magnetic coupling within polynuclear coordination clusters is weaker than for 3d ions. To date, 4f metal clusters with nuclearities ranging from Ln_2 to Ln_{60} have been reported.³⁶ The Dy^{III} analogues of some of these series show interesting magnetic properties.³⁶⁻⁴⁰ A Dy^{III}_2 complex showed ferromagnetic coupling at low temperature, with slow relaxation of magnetization characteristic of SMMs with high energy barriers.³⁷ The trinuclear $[\text{Dy}_3(\mu_3\text{-OH})_2(\text{L})_3\text{Cl}(\text{H}_2\text{O})_5]^{3+}$ ^{38a} (HL = isovanillin) has an equilateral triangular topology with $(\mu_3\text{-OH})$ bridges above and below the Dy^{III}_3 plane. Single crystal magnetic studies^{38b} combined with a theoretical analysis^{38c} show the complete compensation of the magnetic moments in the nonmagnetic ground state, originating from the noncollinearity of the single-ion easy axes of magnetization of the Dy^{III} ions that lie in the plane of the triangle at 120° from each other. The slow relaxation dynamics observed in the ac susceptibility between 2

and 20 K with stepped hysteresis could be associated with level crossing to a magnetic excited state.

Opening up the triangular^{38a} Dy^{III}₃ unit into a linear^{38d} Dy^{III}₃ by modifying the ligand led to a different situation. The linear Dy^{III}₃ no longer has a nonmagnetic ground state; it is ferromagnetically coupled and ac susceptibility measurements show slow relaxation of magnetization with two relaxation pathways. The fitting to Arrhenius plot produced two energy barriers (28.7 and 69.3 K). An *ab initio* calculation revealed the presence of Ising-type anisotropy in all three Dy^{III} ions with almost parallel alignment of the magnetic moments.^{38d}

A tetranuclear hydroxy-bridged Dy^{III}₄ cubane^{36a} showed weak SMM behavior, while Dy^{III}₄ systems with defect-dicubane^{36b-d} topologies showed much clearer slow magnetic relaxation. The dynamic magnetic behavior was found to change when peripheral ligands were changed.^{36b-c} One such complex exhibits slow relaxation of magnetization with two ac peaks (9 and 30 K) and corresponding energy barriers are found to be 9.7 and 170 K respectively. The main contribution to the energy barrier in these Dy^{III}₄ arises mainly from the individual uniaxial single-ion anisotropies, and the two maxima of the out-of-phase (χ'') ac signals can then be naturally associated with two relaxation barriers corresponding to two types of dysprosium ions.^{36c} In addition, a linear Dy^{III}₄^{39a} and a pyramidal Dy^{III}₅^{39b} clusters were also found to be SMMs with energy barriers around 30 K and 20 K respectively.

When two of the Dy^{III}₃ triangles discussed earlier are linked into a Dy^{III}₆ cluster,⁴⁰⁻⁴¹ the magnetic structure becomes more complex, with the temperature regime for slow relaxation of magnetization increasing from 8 K to 25 K.⁴¹ This occurs in spite of the fact that the linkage involves an antiferromagnetic interaction. The observation of two relaxation regimes is apparently associated to a change in the nature of the overall molecular anisotropy from an easy plane to easy axis type⁴² on increasing the temperature; this was explained by symmetry-lowering induced by linking the triangles.

The geometry of the ligand field is a significant factor in determining whether the single-ion anisotropy of a Ln^{III} ion is uniaxial or easy-plane in nature, but the effect differs according to the electronic nature of the ion. For example, the Dy^{III} ion with an f⁹ configuration has a ⁶H_{15/2} ground state which splits into sub-levels $|J, J_z\rangle = |15/2, J_z\rangle$ with $-15/2 \leq J_z \leq +15/2$. The anisotropy will be uniaxial if the sub-levels with $J_z = \pm 15/2$ are lowest in energy. These sub-levels have an oblate profile, and will therefore be stabilised if the ligand field is prolate in form,

i.e. the hard negatively charge coordinating atoms have an axial distribution about the ion. The same is true for Tb^{III} and to a lesser extent Ho^{III}. However, for Er^{III}, the sub-levels with the highest J_z are prolate in profile, and uniaxial anisotropy will now be favoured by a ligand field in which the hard atoms form an equatorial plane about the Er^{III} ion.

From the above discussion it can be stated that the magnetic aspects of 3d and 4f metal ions are completely different. A brief overview has been presented on both 3d and 4f- based SMMs, and without such knowledge it will be ambiguous to rationalize the behavior of hybrid heterometallic 3d-4f magnetic systems.

d-f SMMs

In pure Ln^{III} clusters, the magnetic interactions between f electrons on different metal centres are expected to be very small. However, the magnetic coupling between f electrons with electrons in the d orbitals of transition metal ions should be stronger than f-f coupling, thus producing measurable effects at higher temperatures, and the problem of orbital degeneracy may be limited.

The first 3d-4f magnetic system (Cu^{II}-Ln^{III}) was reported in 1975 but only magnetically characterized in 1985.⁴³ A large number of papers have been published on Cu^{II}-Gd^{III} (3d⁹-4f) systems in order to understand the nature of the magnetic coupling.⁴³ The Cu^{II} and Gd^{III} ions are both isotropic (or nearly so) and usually ferromagnetic coupling was observed between them. Replacing isotropic Gd^{III} ions by anisotropic Ln^{III} (Dy^{III}, Tb^{III} etc.) in a Cu^{II}-Ln^{III} (3d⁹-4f) series is a possible route to systems showing SMM behavior, and some Cu^{II}-Dy^{III} and Cu^{II}-Tb^{III} systems were found to be SMMs.⁴⁴ Ni^{II} ions have second order orbital angular momentum, and several Ni^{II}-Ln^{III} (Ni₂Ln,^{45b,d} Ni₆Ln,^{45c} NiLn₂,^{45e} Ni₂Ln₂,^{45k} La₂₀Ni₃₀,^{45h} Ln₂₀Ni₂₁,^{45h} Ni₈Ln₈,^{45l} Ni₂Ln,^{45b,d} NiDy₂,^{46a} Ni₂Dy,^{46b} Ni₃Dy,^{46e} Ni₂Dy₂,^{46f} etc.) compounds have also been reported. The Ni^{II}-Gd^{III} (3d⁸-4f⁷) systems were again always found to be ferromagnetically coupled,⁴⁵ and again some Ni^{II}-Dy^{III} and Ni^{II}-Tb^{III} compounds exhibit slow relaxation characteristic of SMM.^{45e,i,l, 46}

Co^{II} ions have first order orbital angular momentum and thus can lead to large Ising type magnetic anisotropy depending upon geometry and ligand field. Thus a combination of Co^{II} and Gd^{III} (3d⁷-4f) can lead to SMM behavior; in a reversal of the usual situation for 3d-4f systems, here it is the 3d ion which is providing the anisotropy.⁴⁷⁻⁴⁸

There are few Fe^{III}-Ln^{III} (3d⁵-4f) systems which are also found to be SMM in some cases.⁴⁹ Generally, interactions in Fe^{III}-Ln^{III} systems are either antiferromagnetic or very weak.^{49a-b} Till now there is no Mn^{II}-Ln^{III} (3d⁵-4f) SMM reported.

Since the Mn^{III} ion possesses uniaxial anisotropy, and homometallic Mn-containing complexes are often found to be SMMs, it is not surprising that combining both of the anisotropic Mn^{III} and Dy^{III} ions (3d⁴-4f) in the same systems can result in SMMs,⁵⁰ often showing both QTM and hysteresis loops.^{50a-b} The mixed valence Mn^{III/IV}-Ln^{III}^{50c} and Mn^{II/III}-Ln^{III}^{50d} systems were also found to have slow relaxation of magnetization.

Zn^{II}-Ln^{III} (3d¹⁰-4f)^{51a} and Cd^{II}-Ln^{III} (4d¹⁰-4f) complexes can be magnetically regarded as Ln^{III} complexes since the d¹⁰ Zn^{II} and Cd^{II} ions are diamagnetic in nature. However, such systems could display interesting photophysical properties resulting from Zn^{II} or Cd^{II}.^{51a}

1.2 Fluorescence Property

Lanthanide ions possess extremely interesting optical properties^{51b-c-52} and have found applications in economical luminescent lamps, light emitting diodes, television and computer displays, optical fibres, optical amplifiers and lasers. In addition, responsive luminescent stains for biomedical analysis, medical diagnosis, and cell imaging rely heavily on lanthanide ions. The recent effort has been devoted to near infrared (NIR) luminescent Ln^{III} (Nd, Yb or Er) complexes with long-lived and characteristic line-like emission bands, because of their pivotal applications in fluoro-immunoassays, organic light-emitting diodes (OLED) and optical telecommunication. However, due to the forbidden parity for f-f transitions, the absorption coefficients of these lanthanide ions are normally very low. Although many cyclic or acyclic aromatic ligands with fully allowed $\pi-\pi^*$ transitions in the UV region have been designed for overcoming the low light absorbance of Ln^{III} ions, it is more difficult to find ligand-centered chromophores suitable for wavelengths longer than the UV. A good source of strongly-absorbing chromophores spanning the visible region is the d-block metal complexes^{51b} which can display absorption bands at almost any desired wavelength, and the desired excited states (¹LC, ³LC, ³MLCT or ³LMCT), have been demonstrated to transfer energy indirectly to Ln^{III} ions efficiently. There is currently growing interest in the synthesis and magnetic behavior of d-f heterometallic complexes with compartmental Salen-type Schiff-base ligands,^{51a} although there have been relatively few studies on the photo-physical properties of these compounds. Attention has also been given to the

characterization of Zn/Cd-Schiff-base complexes with intense and tunable absorption maxima in the visible region, as antennae or sensitizers (donors) for luminescence of Ln^{III} ions complexes (acceptors).^{51a,52a-b} Thus the combination of Zn^{II} or Cd^{II} with Ln^{III} ions in a complex could result in compounds showing a photo-magnetic effect.

1.3 Synthetic Strategies towards Coordination Clusters

1.3.1 3d Coordination Chemistry

A prerequisite for a magnetically-interesting coordination cluster is that the metal centres are linked by bridging ligands that can mediate magnetic interactions between them. An important strategy towards 3d polynuclear complexes has been to allow transition metal salts to react under hydrolytic or solvolytic conditions with organic ligands. Small polynuclear oxo- or hydroxo-bridges units form but are trapped by the chelating ligands, forming the coordination cluster. The organic ligands both prevent the magnetic core from growing further, and also prevent magnetic interactions with other molecules. Initially carboxylates were used for construction of Mn-based SMMs.⁴⁻⁶ Later, cyanide,²⁷ polyalcohol,⁷ aminol, iminocarboxylate and different Schiff-bases have all been used to prepare homometallic or heterometallic 3d-based SMMs. It was often found useful to use a mixture of ligand and smaller co-ligands (such as carboxylate or azide) that can provide additional bridging between the metal centres. In Mn-based coordination clusters, hydroxide, oxide, azide or alkoxide bridges mediate better magnetic interaction. Other 3d-based systems often contain fewer oxide bridges but more hydroxide bridges. The advantage of this type of chemistry is that it can be carried out under ambient conditions, or sometimes with relatively mild heating. The ligand systems can also be easily modified to favour different structural motifs.

1.3.2 4f Coordination Chemistry

Since 4f metal ions are oxophilic in nature, many carboxylate based 4f compounds have been prepared.^{38d} Oxygen-containing ligands such as o-vanillin have been utilized for the synthesis of magnetically interesting triangular Dy^{III}₃^{38a-c} and bis-triangular Dy^{III}₆⁴⁰⁻⁴¹ complexes. With Schiff-bases of o-vanillin, linear Dy^{III}₂,³⁷ Dy^{III}₃^{38d} and Dy^{III}₁₀^{36d} complexes were also reported. The phenolic O-atom acts as a bridge between the metal centers in the above

mentioned compounds. For Ln containing complexes it is found that monoatomic bridges (hydroxide, oxide or alkoxide) are better for mediating magnetic interaction. Thus chelating amino-alcohol ligands^{36b-d} are finding increasing use in this respect.

1.3.3 3d-4f and 4d-4f Coordination Chemistry

For the construction of 3d-4f bimetallic complexes, Schiff-base ligands of salicyl aldehyde or o-vanillin have been widely employed (Cu-Ln,⁴³⁻⁴⁴ Ni-Ln,⁴⁵⁻⁴⁶ and Co-Ln⁴⁷) because of strong affinity of these ligands towards both 3d and 4f metal ions. For the synthesis of Ni^{II}-Ln^{III} complexes, initially the Schiff-base ligand {2,2'-[1-Methyl-1,2-propanediyl-bis(nitrilomethylidene)]-di(6-methoxyphenolato)}^{45a} was utilized. Later on Schiff-bases of tripodal tri-^{45b} or tetraamines^{45d} and either salicylaldehyde^{45c,i} or o-vanillin were used to synthesize trinuclear Ni₂Ln complexes. Amino acids, iminodiacetic acid and the oximes of dipyritylketone and 2-pyridinealdehyde were used for the synthesis of Ni₆Ln,^{45c} NiLn₂,^{45e} Ni₂Ln₂,^{45k} La₂₀Ni₃₀,^{45h} Ln₂₀Ni₂₁^{45h} and Ni₈Ln₈.^{45l} Bis(2-pyridylcarbonyl)amine, a thiophosphorous-containing tripodal hydrazone, the oxime of 2-pyridinealdehyde and the Schiff-base of o-vanillin and 1,3-diaminopropane ligands have been employed for the synthesis of NiDy₂,^{46a} Ni₂Dy,^{46b} Ni₃Dy,^{46c} and Ni₂Dy₂^{46d} compounds, respectively. Recently N-alkyldiethanolamine ligands have been found to be very efficient for the preparation of 3d-4f (Fe-Ln⁴⁹ and Mn-Ln^{50e}) based SMMs. The magnetic centers may be connected through oxide, hydroxide, alkoxy, azide or carboxylate bridges depending upon the ligand and magnetic coupler used for the synthesis of the compounds. Thus, those ligands are desired which will not only bind to different metal centers but also mediate magnetic coupling.

There are very few reports in the literature of the preparation of Cd^{II}-Ln^{III} compound.^{52a-b} An imidazoledicaboxylate^{52a} or a mixture of carboxylate and 1,10-phenanthroline (phen) ligands^{52b} have been used to synthesize Cd^{II}-Ln^{III} compounds.

1.3.4 Ligand Selection and Synthetic Strategy

The main objective of this research is to construct heterometallic d-f coordination clusters and to study their magnetic and/or optical properties. In contrast to M^{III}-Ln^{III} systems, N-alkyldiethanol ligands (Fig. 1.4) have mostly not been efficient in synthesizing heterometallic M^{II}-Ln^{III} compounds containing lanthanide and divalent d ions, such as Cu^{II}, Ni^{II}, Co^{II}, Zn^{II} and

Cd^{II} . In this work the diprotic Schiff-base ligands (E)-2-(2-hydroxy-3-methoxybenzylideneamino)-phenol ($\text{H}_2\text{L1}$), (E)-N'-(2-hydroxy-3-methoxybenzylidene)-benzohydrazide ($\text{H}_2\text{L2}$), (E)-N'-(2-hydroxy-3-methoxybenzylidene)-(2-hydroxy)benzohydrazide ($\text{H}_3\text{L3}$) and bis-(E)-N,N'-(2-hydroxy-3-methoxy)-benzylhydrazone ($\text{H}_2\text{L4}$) were selected.

These ligands have previously been used in the synthesis of a small number of relatively simple homometallic complexes. With $\text{H}_2\text{L1}$, mononuclear metal complexes were reported.^{52c} Mononuclear Mn complexes^{52d} and a Cu^{II}_4 ^{52e} cubane were reported with $\text{H}_2\text{L2}$. Some mononuclear metal complexes with $\text{H}_3\text{L3}$ were reported^{52f} without their crystal structures while the *cis*-conformation of $\text{H}_2\text{L4}$ is trapped in Dy_4 complex.^{36c} The ligands $\text{H}_2\text{L1}$, $\text{H}_2\text{L2}$ and $\text{H}_3\text{L3}$ have two pockets, I (ONO) and II (OO), the first of which is expected to have a good affinity for divalent 3d ions, while the second pocket can coordinate oxophilic lanthanide ions. $\text{H}_2\text{L2}$ and $\text{H}_3\text{L3}$ are related to the enol form of $\text{H}_2\text{L1}$ (Fig. 1.4, top) and in the presence of metal ion ligands can transform into different tautomers. It was therefore considered that these ligands were highly suitable for the synthesis of complexes containing both divalent 3d ions and lanthanides.

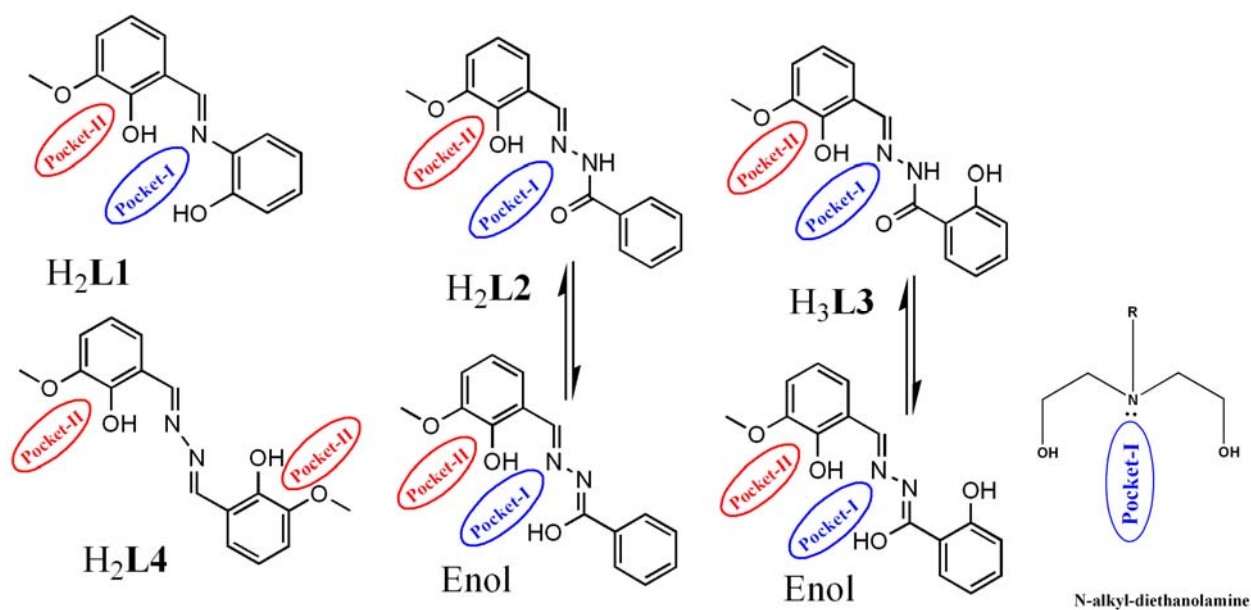


Fig. 1.4. All four ligands ($\text{H}_2\text{L1}$, $\text{H}_2\text{L2}$, $\text{H}_3\text{L3}$ and $\text{H}_2\text{L4}$) are shown. For comparison N-alkyldiethanolamine with pocket-I(ONO) (right).

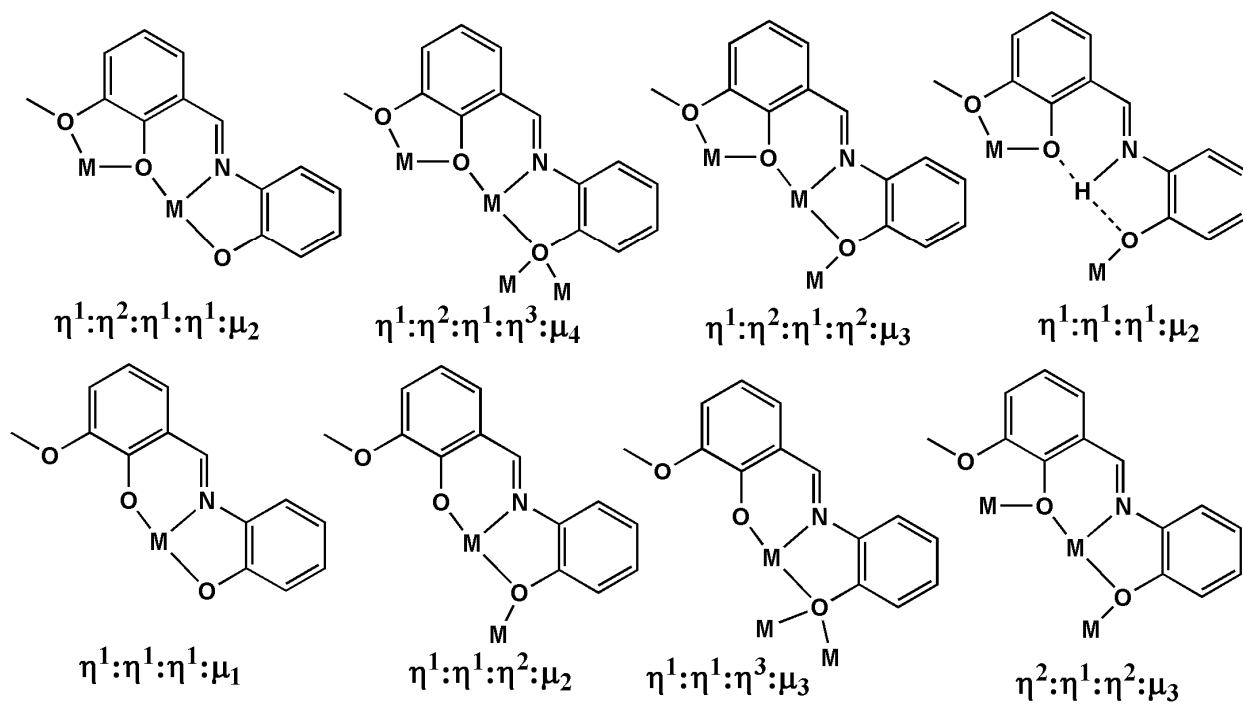


Fig. 1.5. Observed bridging modes of $(L1)^{2-}$.

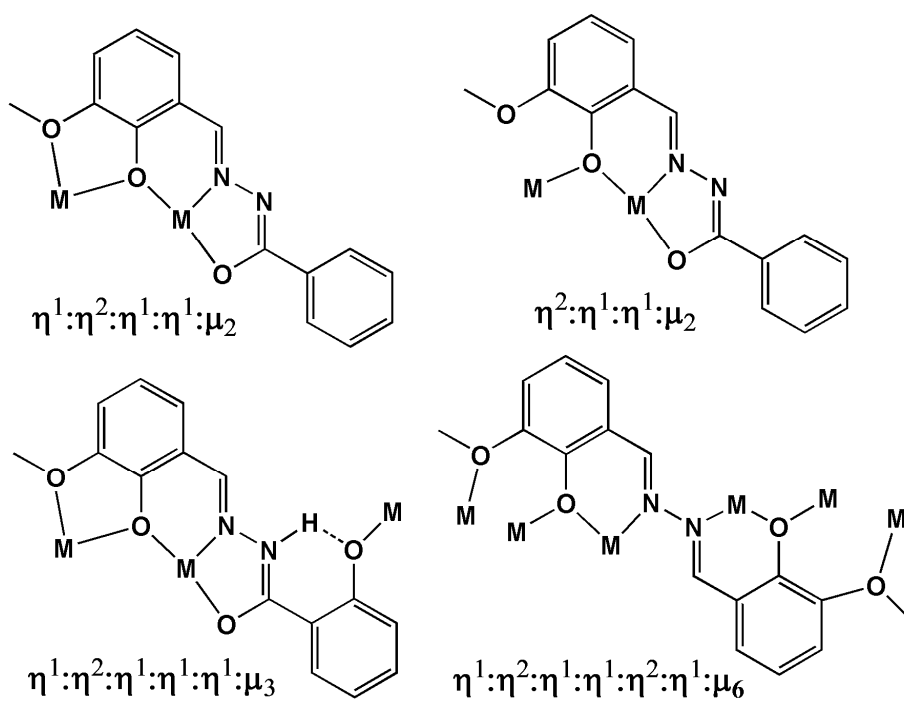


Fig. 1.6. Known bridging modes of $(L2)^{2-}$ (left), $(HL3)^{2-}$ (middle) and $(L4)^{2-}$ (right).

As a general synthetic strategy to prepared polynuclear clusters of d-f metal ions, the appropriate mixture of divalent d and trivalent f metal ions was reacted with the ligand (H_2L1 or H_2L2) in the presence of base (Et_3N), mostly in methanol solution at room temperature. In addition, 3d or 4f metal ions were also reacted separately with either H_2L1 or H_2L2 to make homometallic 3d or 4f compounds. In some cases, clusters linked into higher nuclearity systems, using either the modified ligands H_3L3 or H_2L4 or small bridging ligands such as oxalate. The bridging modes of all four Schiff base ligands (H_2L1 , H_2L2 , H_3L3 and H_2L4 ,) are given above (Fig. 1.4-1.6). In some of our systems CO_2 fixation has been observed and it is converted into carbonate (CO_3^{2-}). Some of the selected bridging modes are given below (Fig. 1.7).

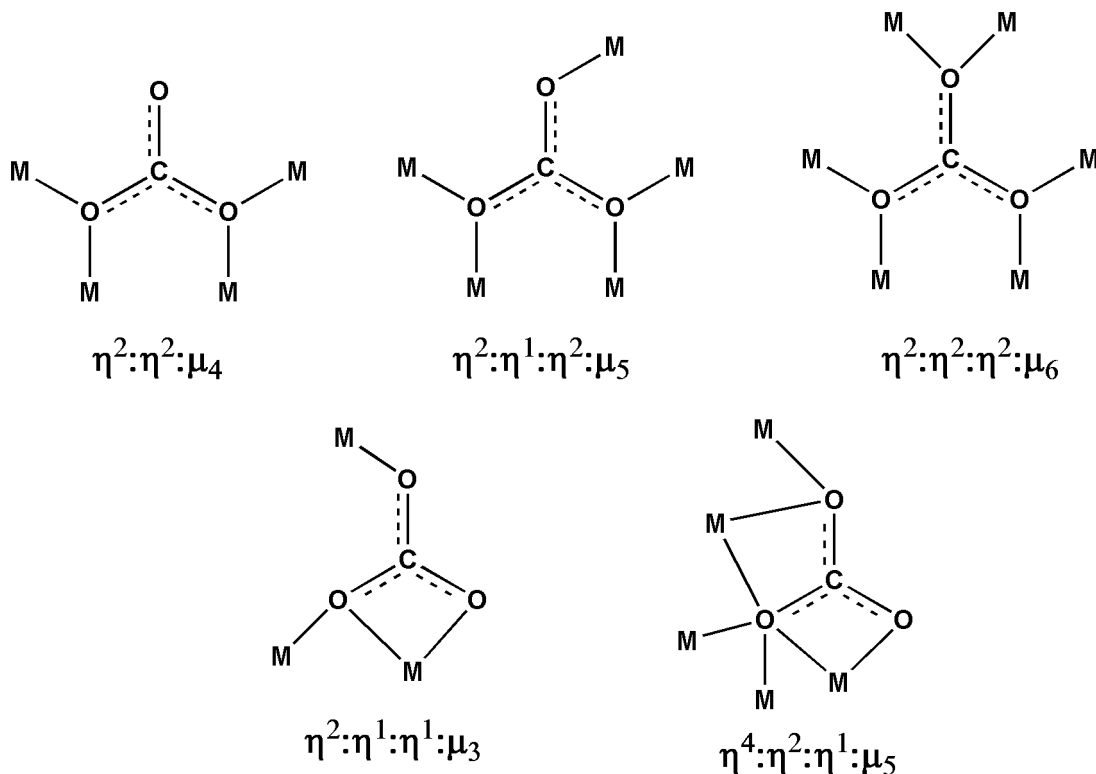


Fig. 1.7. Selected bridging modes of carbonate (CO_3^{2-}).

1.4 Thesis Overview

This thesis describes the synthesis of homo- and heterometallic complexes which have been crystallographically characterized and their magnetic and/or optical properties investigated. The research results are divided into four chapters (3, 4, 5 and 6). Chapter 3 describes the synthetic strategy, crystal structure descriptions and magnetic properties of Ni^{II}-4f based coordination clusters. Chapter 4 describes the synthetic strategy, crystal structures and magnetic and/or optical investigations of other 3d-4f and 4d-4f based coordination clusters along with fluorescence properties of Zn^{II}-4f and Cd^{II}-4f compounds. Chapter 5 describes the synthetic strategy, crystal structures and magnetic properties of tetranuclear 4f coordination clusters. Chapter 6 describes the synthetic strategy, crystal structures and magnetic properties of Cu^{II}-4f coordination clusters. This chapter shows how some of those clusters could be linked or grown into bigger clusters either by adjusting the synthetic technique or by modifying the organic ligand, and the resulting effect on their magnetic properties. Chapter 7 summarizes the experimental results and the findings of this research project, concluding with an outlook. Chapter 8 gives the experimental details and describes the characterization techniques. Chapter 9 provides crystallographic data. Chapter 10 contains bibliography which supports the whole research work.

Chapter 11 contains lists of coordination compounds, organic compounds and abbreviations. Finally, the author acknowledges those people who have supported him while he carried out this Ph.D. research and concluded it in the form of this thesis. Curriculum vitae, list of publications, and details of conferences attended and poster presentations are also provided.

Chapter 2: Research Objectives

It has been observed that the synthesis of coordination clusters showing SMM behavior is mostly serendipitous.⁷ Although some progress has been made in optimizing the magnetic properties of existing SMMs, it is still not easy to control the key parameters in an existing cluster. It is difficult to control the arrangement of the metal ions with respect to each other, the magnetic coupling between them and the relative orientations of the single-ion anisotropy axes. These three factors all have profound effects on the height of the energy barrier to spin reorientation, the splitting of the magnetic states and the possibilities of Quantum Tunneling of the Magnetization. In this thesis, a set of related ligands is used in a systematic study to target new SMMs with improved properties.

The key requirement for SMM behavior is a combination of sufficient spin and uniaxial anisotropy within the molecule. Some metal ions, such as Fe^{III}, Mn^{II}, Cr^{III} and Gd^{III}, can contribute high spin but minimal anisotropy, whereas others, such as Mn^{III}, Co^{II} and most of the trivalent lanthanide ions, can contribute high single ion anisotropy. Some of these ions can contribute both spin and anisotropy. Previous work has shown that it can be advantageous to introduce both spin and anisotropy into a coordination cluster using a combination of 3d and 4f metal ions in a heterometallic complex.

To this end, Schiff-base ligands were designed incorporating two different pockets, each with different sets of donor groups, in order to utilize the HSAB principle. Thus, one pocket has an O₂N donor set, while the other contains only O-donors suitable for oxophilic lanthanide ions. A first objective was to investigate the coordination chemistry of these ligands with either a single 3d ion or a single 4f ion. Drawing on these results, it was then possible to utilize the ligands to design the syntheses of heterometallic 3d-4f complexes.

By concentrating on just a small set of related ligands, it was possible to use a highly systematic approach, involving the variation of one reaction parameter at a time, towards the synthesis of optimized SMMs. These studies were supported by full structural determinations using single-crystal X-ray diffraction, detailed magnetic susceptibility measurements and in appropriate cases (those containing d¹⁰ ions) optical studies.

Chapter 3

Ni-Ln Coordination Clusters with (E)-2-(2-hydroxy-3-methoxybenzylideneamino)-phenol (H₂L1)

3.1 Introduction

The combination of a large ground state spin (S) along with (negative) magnetic anisotropy (D), is a necessary condition for SMM behavior, creating an energy barrier to spin reversal in an uniaxial (Ising type) system. Initially, S was thought to be the more essential parameter for producing better SMMs, since the barrier height is given by the relation $U_{\text{eff}} = |D|S^2$ for integer or $|D|(S^2 - 1/4)$ for half-integer ground spin states. However, subsequently it has been realized that enhancement of D is likely to be the deciding factor in increasing the barrier height, since the parameter S is also implicated in equations describing spin-orbit coupling in such a way that the contribution of this parameter is actually only proportional to S and not its square.⁶⁰ Thus, as a result of these considerations much work has focused on the synthesis of coordination magnetic compounds with both large S and D . The SMM behavior also depends on certain pivotal parameters, such as the symmetry of the compound, the relative position of the particular spin centers, the geometry of each ion, the magnitude of magnetic coupling, the orientation of single-ion anisotropic axis, the ligand field etc. None of these parameters are easy to control.

SMM behavior in purely Ni^{II} based compounds, is not as well studied as that of Mn^{III} compounds,²⁰ even though Ni^{II} ions have a favorable zero field splitting parameter D . Although the single-ion anisotropy (D) can be bigger in Ni^{II} ions ($S = 1$) as compared to Mn^{III} ions ($S = 2$), the spin is lower for Ni^{II} ions. The overall molecular D value is a tensor sum of the individual single-ion terms. Consequently, more attentions have been given to Mn-Ln⁵⁰ compounds in comparison with Ni-Ln⁴⁵⁻⁴⁶ compounds until recently. To date, among Dy^{III}-Ni^{II} compounds (Ni₂Ln,^{45b,d} Ni₆Ln,^{45c} NiLn₂,^{45e} Ni₂Ln₂,^{45k} La₂₀Ni₃₀,^{45h} Ln₂₀Ni₂₁,^{45h} Ni₈Ln₈,^{45l} Ni₂Ln,^{45b,d} NiDy₂,^{46a} Ni₂Dy,^{46b} Ni₃Dy,^{46e} Ni₂Dy₂^{46f} etc.) some (NiDy₂,^{45e} NiDy^{45e} and Ni₈Ln₈^{45l}) show slow relaxation but without an observable maximum peak in χ' or χ'' vs T plots, while NiDy₂,^{46a} Ni₂Dy,^{46b} Ni₃Dy,^{46e} and Ni₂Dy₂^{46f} are found to be SMMs (with a maximum in χ' or χ'' vs T plots). The Dy^{III}₂Ni^{II}₂^{46f} compound has been found to have $\Delta \approx 17$ K, the highest among all Ln-Ni based SMMs.

N-alkyldiethanolamine ligands have been recognized as useful in the preparation of compounds containing trivalent 3d ions and tri- or higher valent rare-earth 4f based compounds, mostly in the presence of carboxylate as a co-ligand.^{49,50e} However, the preparation of compounds based on divalent 3d and trivalent 4f ions does not seem to be so straight forward. For this, reason the design and synthesis of new ligands which can accommodate both 3d and 4f metal ions is required.

The ligand (E)-2-(2-hydroxy-3-methoxybenzylideneamino)-phenol (H₂L1) is a diprotic Schiff base, similar to N-alkyl-diethanolamine (Fig. 1.4), but it is more rigid and has one extra methoxy (OMe) arm. This ligand (H₂L1) has been designed to have the two pockets, I (ONO) and II (OO) (Fig. 1.4). The presence of an extra methoxy (OMe) arm helps by providing further binding to the Ln^{III} ions and thus a co-ligand may not be required.

3.2 Synthetic strategy

It is now well-known that factors such as the ratio, metal salt, temperature, solvent, reaction time and so on can all affect the nature of the final product. A range of reaction conditions have been investigated, leading to different products as shown in Table 3.1.

Table 3.1. Synthetic strategies of preparing Dy^{III}-Ni^{II} compounds (**1**, **2**, **8**, **13**, **19** and **20**).

Ratio ^a	Solvent	Volume (mL)	Temperature	Atmosphere	Time of stir (min.)/Crystallization (day)	Compound
A:B:C:E = 1:1:2:5	DMF	10	150°C	air	15/14	Dy ₂ Ni ₂ (1)
A:B:C:E = 1:1:2:5	MeOH	20	rt	air	5-10/0.5	Dy ₂ Ni ₂ (2)
A:B:C:E = 1:2:2:5.4	MeOH	20	rt	N ₂	1-2/7	Dy ₂ Ni ₂ (2)
A:B:C:E = 1:2:2:5.4	MeOH	20	rt	air	1-2/7	Dy ₂ Ni ₂ (8)
A:B:C:E = 1:1:1:3	MeOH	20	rt	air	5/21	Dy ₄ Ni ₈ (13)
A:B:C:E = 1:2:2:5.4	MeOH	20	rt	air	5/7	Dy ₄ Ni ₈ (13)
A:B:C:E = 1:1:2:5.4	MeOH	20	rt	N ₂	5/2	Dy ₂ Ni ₄ (19)
A:B:C:D:E = 2:2:1.22:1.1:4.8	MeOH	15	rt	air	5/14	Dy ₄ Ni ₈ (20)

(a) A = Dy(NO₃)₃·6H₂O, B = Ni(NO₃)₂·6H₂O, C = H₂L1, D = H₂C₂O₄·2H₂O and E = Et₃N.

The reaction of $\text{Dy}(\text{NO}_3)_3 \cdot 6\text{H}_2\text{O}$, $\text{Ni}(\text{NO}_3)_2 \cdot 6\text{H}_2\text{O}$ and $\text{H}_2\text{L1}$ in the presence of base (Et_3N), in the molar ratio 1:1:2:5 in DMF, produced red-green color, block-shaped crystals of $[\text{Dy}_2\text{Ni}_2(\text{L1})_4(\text{NO}_3)_2(\text{DMF})_2]$ (**1**) after two weeks. When the same reaction was performed using MeOH in the same molar ratio of 1:1:2:5, light green, plate-shaped crystals of $[\text{Ln}_2\text{Ni}_2(\text{L1})_4(\text{NO}_3)_2(\text{MeOH})_2] \cdot 3\text{MeOH}$ [where Ln = Dy(**2**), Y(**3**), Gd(**4**), Tb(**5**), Ho(**6**), Er(**7**)] were obtained within three hours provided the solution is stirred for 5-10 min and then left for crystallization. Thus no effect on nuclearity of the compound was observed on changing the reaction medium from DMF to MeOH. The crystal structures of **1-7** reveal that they all have similar defect-dicubane structural topology.

If the reaction solution, which produces **2** is stirred for just 1-2 min before crystallization, red block-like crystals were obtained after one week, the crystal structure of which reveals a non-planar, distorted, U-shaped compound $[\text{Dy}_2\text{Ni}_2(\text{CO}_3)(\text{L1})_4(\text{MeOH})_6]_2[\text{Dy}_2\text{Ni}_2(\text{CO}_3)(\text{L1})_4(\text{MeOH})_5(\text{H}_2\text{O})] \cdot 14\text{MeOH}$ (**8**). If the same reaction is performed in inert atmosphere it results in **2**. The general formula of this series is $[\text{Ln}_2\text{Ni}_2(\text{CO}_3)(\text{L1})_4(\text{MeOH})_6]_2[\text{Ln}_2\text{Ni}_2(\text{CO}_3)(\text{L1})_4(\text{MeOH})_{6-x}(\text{H}_2\text{O})_x] \cdot y\text{MeOH}$ [Ln = Dy(**8**), x = 1, y = 14; Ln = Sm(**9**), Eu(**10**), x = 2, y = 15; Ln = Gd(**11**), x = 2, y = 17 and Tb(**12**), x = 1, y = 14].

The crystal structure of **8** shows that there is one carbonate (CO_3^{2-}) and there are two terminal ligands each of which are coordinated to each Dy^{III} ion. If the reaction which produces **8**, is carried out in inert atmosphere, formation **2** is obtained. Thus the carbonate ligands results from atmospheric CO_2 and it seems that the further growth of the nuclearity is prevented by coordination of the ligand $(\text{L1})^{2-}$ to each Dy^{III} center. Hence the reaction parameters were adjusted and the amounts of ligand base were decreased. When the reaction condition reaches a ratio of $\text{Dy}(\text{NO}_3)_3 \cdot 6\text{H}_2\text{O}:\text{Ni}(\text{NO}_3)_2 \cdot 6\text{H}_2\text{O}:\text{H}_2\text{L1}:\text{Et}_3\text{N}$ equal to 1:1:1:3, octahedral shape, red-brown crystals of $[\text{Ln}_4\text{Ni}_8(\text{CO}_3)_4(\text{L1})_8(\text{NO}_3)_2(\text{H}_2\text{O})_8(\text{MeOH})_4] (\text{NO}_3)_2 \cdot 5\text{MeOH} \cdot 4\text{H}_2\text{O}$ [Ln = Dy(**13**), Y(**14**), Gd(**15**), Tb(**16**), Ho(**17**) and Er(**18**)] are obtained. The yield is improved, if the above ratio is changed to 1:2:2:5.4. The crystal structure shows that there are four CO_3^{2-} which unambiguously come from atmospheric CO_2 . To prove this, a similar reaction was performed in same ratio (1:2:2:5.4) in MeOH under N_2 atmosphere, which resulted in green crystals of $[\text{Dy}_2\text{Ni}_4(\text{OH})_2(\text{L1})_4(\text{MeOH})_4(\text{NO}_3)_4] \cdot 4\text{MeOH}$ (**19**) without any carbonate (CO_3^{2-}) in the structure. Instead there are four NO_3^- anions, two of which are coordinated to each Dy^{III} ion. Having in mind the next step was to replace these nitrates by oxalates ($\text{C}_2\text{O}_4^{2-}$) to link these units. Thus, in-

situ reaction of $\text{Dy}(\text{NO}_3)_3 \cdot 6\text{H}_2\text{O}:\text{Ni}(\text{NO}_3)_2 \cdot 6\text{H}_2\text{O}:\text{H}_2\text{L}:\text{H}_2\text{C}_2\text{O}_4 \cdot 2\text{H}_2\text{O}:\text{Et}_3\text{N}$ in the ratio 2:2:1.22:1.1:4.8 in MeOH led to the formation of $[\text{Dy}_4\text{Ni}_8(\text{OH})_4(\text{L}1)_8(\text{MeOH})_4(\text{H}_2\text{O})_4(\text{C}_2\text{O}_4)_2](\text{NO}_3)_4 \cdot 4\text{H}_2\text{O} \cdot 8\text{MeOH}$ (**20**). The overall synthetic strategies of preparing $\text{Dy}^{\text{III}}\text{-Ni}^{\text{II}}$ compounds (**1**, **2**, **8**, **13**, **19** and **20**) are given in Table 3.1.

In this chapter the syntheses, crystal structures and magnetic properties of compounds **1-20** will be discussed.

3.2.1 Crystal structures of $[\text{Dy}_2\text{Ni}_2(\text{L}1)_4(\text{NO}_3)_2(\text{DMF})_2]$ (**1**) and $[\text{Ln}_2\text{Ni}_2(\text{L}1)_4(\text{NO}_3)_2(\text{MeOH})_2 \cdot 3\text{MeOH}$ (**2-7**); [Ln = Dy(**2**), Y(**3**), Gd(**4**), Tb(**5**), Ho(**6**), Er(**7**)]:

The complex **1** crystallizes in the monoclinic space group $P2_1/n$ with inversion symmetry. The asymmetric crystallographic unit contains one Ni^{II} ion, one Dy^{III} ion, two dianionic ligands $(\text{L}1)^{2-}$, one nitrate (NO_3^-) and one coordinated DMF molecule (Fig. 3.1, left).

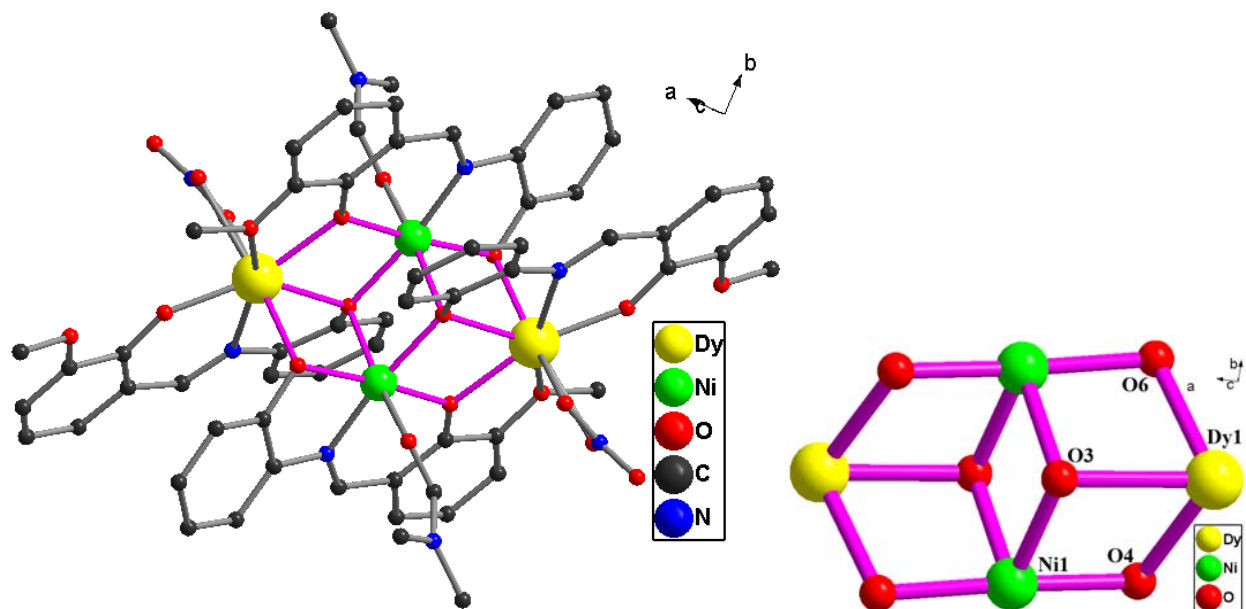


Fig. 3.1. Molecular structure (left) and core (right) of coordination cluster in compound **1**.

The Ni^{II} ion has a distorted octahedral geometry with an O_5N donor set, while the Dy^{III} ion has a distorted square antiprismatic geometry with an O_7N donor set. The Ni^{II} ion is ligated in pocket-I and is coordinated by ONO atoms on three equatorial positions while the fourth equatorial and the axial positions are occupied by two μ_3 -phenoxide O-atoms of the amino phenol part of Schiff base ligands and one O-atom of the solvent (DMF) molecule. Each Dy^{III}

ion is ligated by both pocket-I (ONO) and II (OO) from opposite directions, filling up the five coordination sites. The sixth coordination site is occupied by μ -O-atom (phenoxide) of the aminophenol part of the Schiff base ligand and seventh and eighth sites are taken by two O-atoms of a chelating nitrate.

The complex **1** has a heterometallic defect-dicubane or butterfly core (Dy_2Ni_2) with two Ni^{II} ions in the *body* positions and each Dy^{III} ion in the *wing* positions (Fig. 3.1, right). Two dianionic ligands (L1)²⁻ coordinate and bridge among the metal centers, one from above and one from below the plane of co-planar Dy_2Ni_2 unit, displaying $\eta^1:\eta^1:\eta^3:\mu_3$ (Fig. 1.5) bridging mode. Two more ligands also bind and bridge side-wise to the Dy_2Ni_2 core to display $\eta^1:\eta^2:\eta^1:\eta^2:\mu_3$ bridging mode (Fig. 1.5). Two μ_3 -phenoxide O-atoms of the aminophenol part of the Schiff base ligands bridge Ni-Ni-Dy ions in a triangular fashion, one from above and another from below the plane ($\text{O3-Ni1Dy1Ni1}' = 1.052 \text{ \AA}$) of the Dy_2Ni_2 unit and other four bridging positions are single-atomically bridged by alternating μ -O-atoms of phenoxide of the aminol and aldehyde part of the Schiff base ligands (L1)²⁻. The Ni-O/N and Dy-O/N bond distances vary from 2.009(3) to 2.167(4) \AA and 2.148(3) to 2.503(4) \AA respectively. Selected distances and angles are given in Table 3.2. There is π - π stacking ($\text{C-C} \approx 3.5 \text{ \AA}$) interactions between the aromatic rings within the complex **1**. The closest inter complex Dy1-Dy1 distance is 7.678 \AA along the a-axis.

The structures of **2-4** and **6-7** are isomorphous to that of Tb_2Ni_2 (**5**) which was structurally characterized, confirmed by the unit cell constants. The Tb_2Ni_2 (**5**) and Dy_2Ni_2 (**1**) are structurally similar; two coordinated DMF on two Ni^{II} ions in **1** are replaced by two MeOH molecules in **5**. There are hydrogen-bonding interactions between the molecules in **5**.

Table 3.2. Selected bond lengths (\AA) and bond angles ($^\circ$) within the coordination cluster in **1**.

Dy1—O1	2.148 (3)	Dy1—O7	2.441 (5)	Dy1—N3	2.873 (5)
Dy1—O4	2.285 (3)	Dy1—N1	2.460 (5)	Dy1—O5	2.503 (4)
Dy1—O6 ⁱ	2.310 (4)	Dy1—O8	2.479 (4)	Dy1—O3	2.372 (3)
Ni1—O3 ⁱ	2.167 (4)	Ni1—O3	2.079 (4)	Ni1—O6	2.041 (3)
Ni1—O4	2.009 (3)	Ni1—O10	2.050 (4)	Ni1—N2	2.012 (5)
Dy1—Ni1 ⁱ	3.3913 (7)	Dy1—Ni1	3.4533 (7)	Ni1—O3—Ni1 ⁱ	98.70 (16)
Ni1 ⁱ —Dy1—Ni1	56.15 (2)	Dy1 ⁱ —Ni1—Dy1	123.85 (2)	Ni1—O4—Dy1	106.92 (15)
Ni1—O3—Dy1	101.57 (14)	Ni1 ⁱ —O3—Dy1	96.59 (13)	Ni1—O6—Dy1 ⁱ	102.23 (14)

Symmetry code: (i) $-x+1, -y+1, -z+1$.

3.2.2 Static magnetic properties of compounds 1-7.

The temperature dependence of magnetic susceptibilities of complexes **1-7**, were measured on powdered samples in the temperature range 1.8-300 K under applied dc magnetic field of 1 and/or 10 kOe. Selected dc magnetic data (Fig. 3.2-3.6) are given in Table 3.3. The χT values of **1-7** at room temperature are in good agreement with the theoretically expected χT values. The χT product of $\text{Y}^{\text{III}}_2\text{Ni}^{\text{II}}_2$ (**3**) slowly increases with decreasing temperature to reach a maximum of $3.13 \text{ cm}^3 \text{ K mol}^{-1}$ at 7 K followed by a sharp fall to $1.88 \text{ cm}^3 \text{ K mol}^{-1}$ at 1.80 K. The fall below 7 K is due to ZFS of Ni^{II} ions (Fig. 3.4) and/or weak intermolecular antiferromagnetic interactions. The shape of χT vs T plot of **3** indicates weak ferromagnetic coupling between two Ni^{II} centers in the defect-dicubane unit of $\text{Y}^{\text{III}}_2\text{Ni}^{\text{II}}_2$ (**3**). The general trend of the χT product vs T plots (Fig. 3.2 and 3.4) is similar for all the complexes except **3** and **4**, i.e, from room temperature χT product decreases with decreasing temperature because of depopulation of Stark sub-levels, while the sharp increase at low temperature is due to ferromagnetic coupling between $\text{Ni}^{\text{II}}\text{-Ni}^{\text{II}}$ and $\text{Ni}^{\text{II}}\text{-Ln}^{\text{III}}$ centers (implied from the maximum value at 1.8 K). The χT values of **1-7** at 1.80 K are given in Table 3.3.

Table 3.3. The dc magnetic data of compounds **1-7**.

Compound	Ground state of Ln^{III} ion	χT expected for non-interacting ions per complex ($\text{cm}^3\text{Kmol}^{-1}$)	χT measured at 300 K per complex ($\text{cm}^3\text{Kmol}^{-1}$)	χT measured at 1.8 K per complex ($\text{cm}^3\text{Kmol}^{-1}$)	Magnetization at 2 K and 7 T (μ_B)
$\text{Dy}^{\text{III}}_2\text{Ni}^{\text{II}}_2$ (1)	${}^6\text{H}_{15/2}$	30.34	30.61	58.97	14.26
$\text{Dy}^{\text{III}}_2\text{Ni}^{\text{II}}_2$ (2)	${}^6\text{H}_{15/2}$	30.34	31.11	60.28	14.70
$\text{Y}^{\text{III}}_2\text{Ni}^{\text{II}}_2$ (3)	-	2.0	2.47	1.88	3.83
$\text{Gd}^{\text{III}}_2\text{Ni}^{\text{II}}_2$ (4)	${}^8\text{S}_{7/2}$	17.76	18.53	39.05	18.62
$\text{Tb}^{\text{III}}_2\text{Ni}^{\text{II}}_2$ (5)	${}^7\text{H}_6$	25.64	26.64	41.79	13.79
$\text{Ho}^{\text{III}}_2\text{Ni}^{\text{II}}_2$ (6)	${}^5\text{I}_8$	30.14	31.19	42.73	14.51
$\text{Er}^{\text{III}}_2\text{Ni}^{\text{II}}_2$ (7)	${}^4\text{I}_{15/2}$	24.96	25.97	24.86	13.82

The field dependence of magnetization of **1** and **2** rapidly increases below 1 T and at higher fields, increases almost linearly and reaches the maximum value of 14.26 (**1**) and 14.70 μ_B (**2**) at 7 T without a true saturation at 2 K (Fig. 3.3). The magnetization at 2 K of $\text{Y}^{\text{III}}_2\text{Ni}^{\text{II}}_2$ (**3**) slowly increases and reaches 3.83 μ_B at 7 T which is lower than 4 μ_B for two ferromagnetically

coupled Ni^{II} ions with $S = 1$ and $g = 2.0$. Both χT vs T and M vs H plots of **3** suggest that two Ni^{II} ions are weakly ferromagnetically coupled in **3**. The magnetization of Gd^{III}₂Ni^{II}₂ (**4**) at 2 K reaches expected value of saturation of magnetization given in Table 3.3.

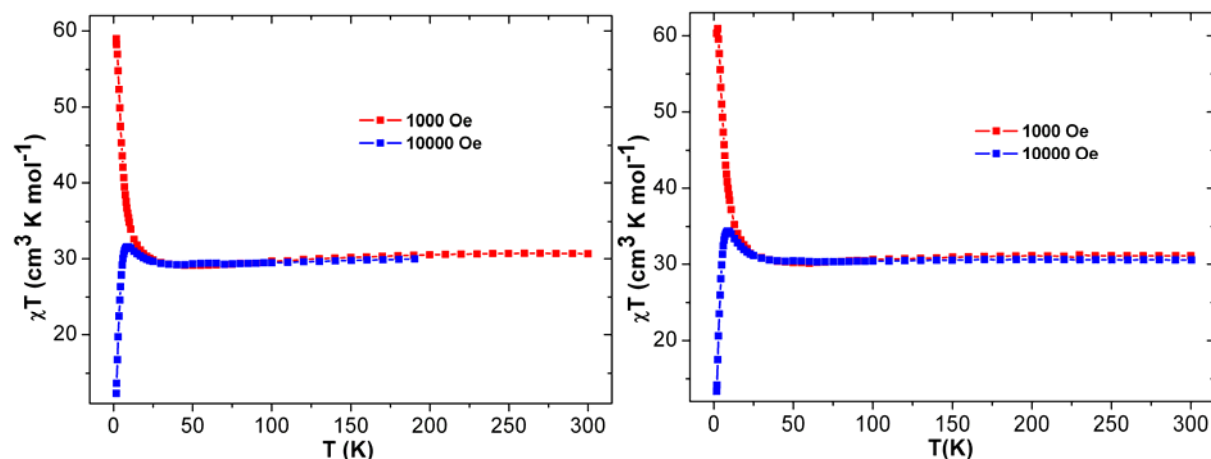


Fig. 3.2. Plots of χT vs T of **1** (left) and **2** (right) under indicated applied dc magnetic fields.

The magnetization of **5**, **6** and **7** also rapidly increases below 1 T and at higher field increases (Fig. 3.5-3.6) almost linearly to reach the maximum values given in Table 3.3. The plots (Fig. 3.3-3.6) of reduced magnetization of **1-7** (M vs H/T plots) at different temperatures do not superpose on to a single master curve, indicating the presence of low lying energy states and/or anisotropy in the systems.⁴³

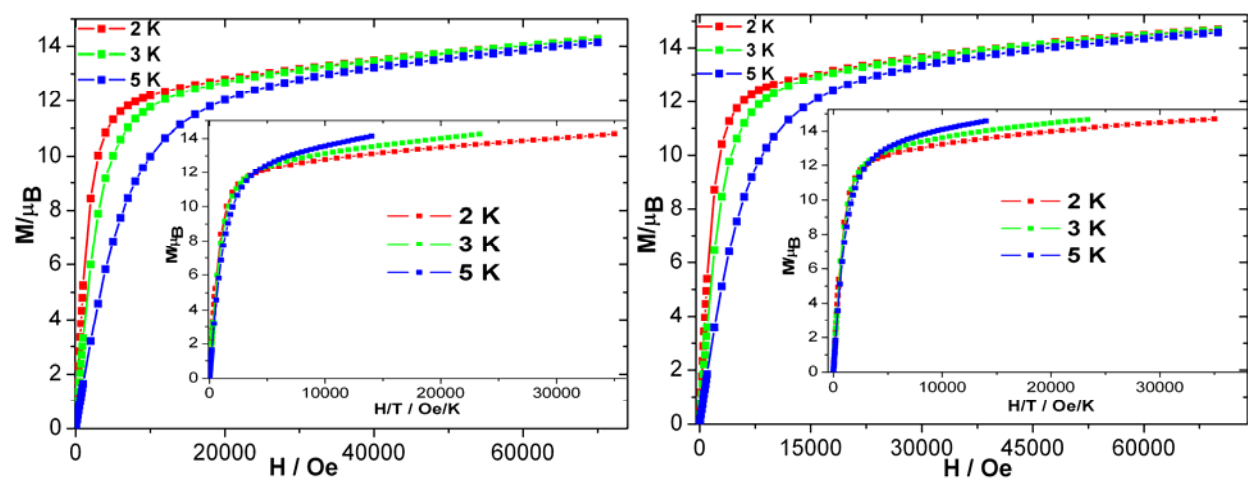


Fig. 3.3. Plots of M vs H and M vs H/T (inset) of **1** (left) and **2** (right).

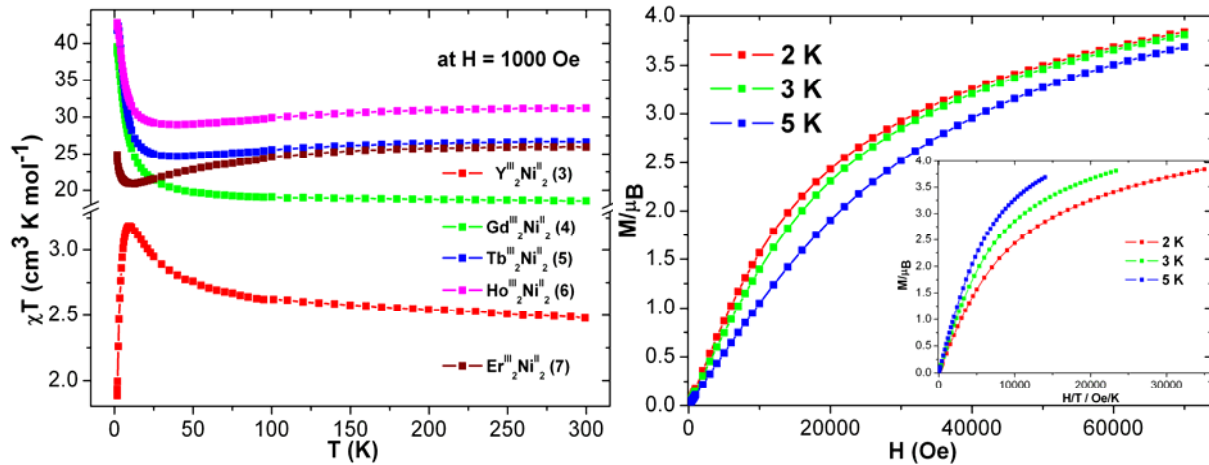


Fig. 3.4. Plots of χT vs T of 3-7 (left). Plots of M vs H and M vs H/T (inset) of 3 (right).

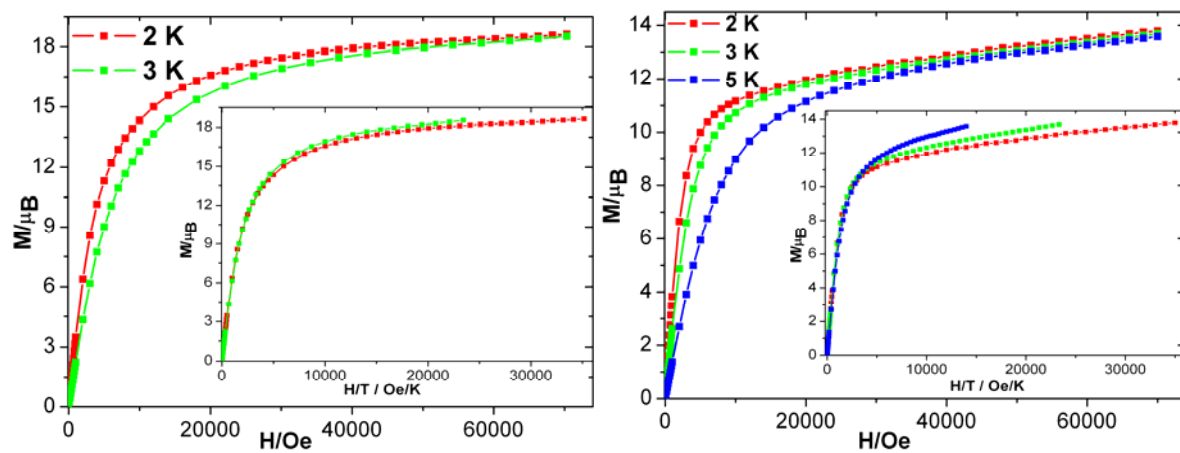


Fig. 3.5. Plots of M vs H and M vs H/T (inset) of 4 (left) and 5 (right).

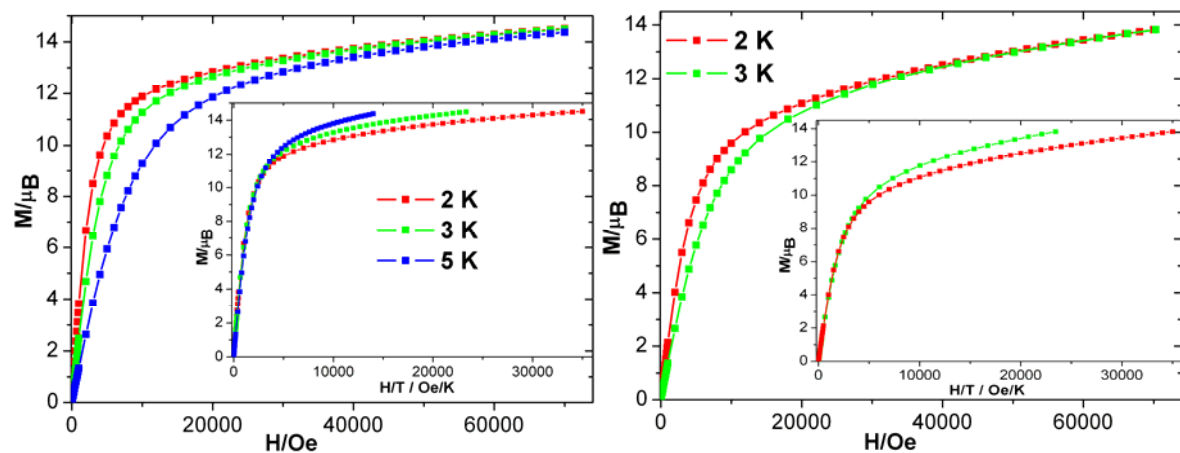


Fig. 3.6. Plots of M vs H and M vs H/T (inset) of 6 (left) and 7 (right).

3.2.3 Dynamic magnetic properties of 1-7

The temperature dependent ac susceptibility measurements on the compounds (**1-7**) show the presence of strong in-phase (χ') and out-of-phase (χ'') signals (Fig. 3.7) for both $\text{Dy}^{\text{III}}_2\text{Ni}^{\text{II}}_2$ (**1** and **2**) complexes and weak signal (without a maximum in χ' and χ'' vs T) (Fig. 3.8) for $\text{Tb}^{\text{III}}_2\text{Ni}^{\text{II}}_2$ (**5**) below 10 K.

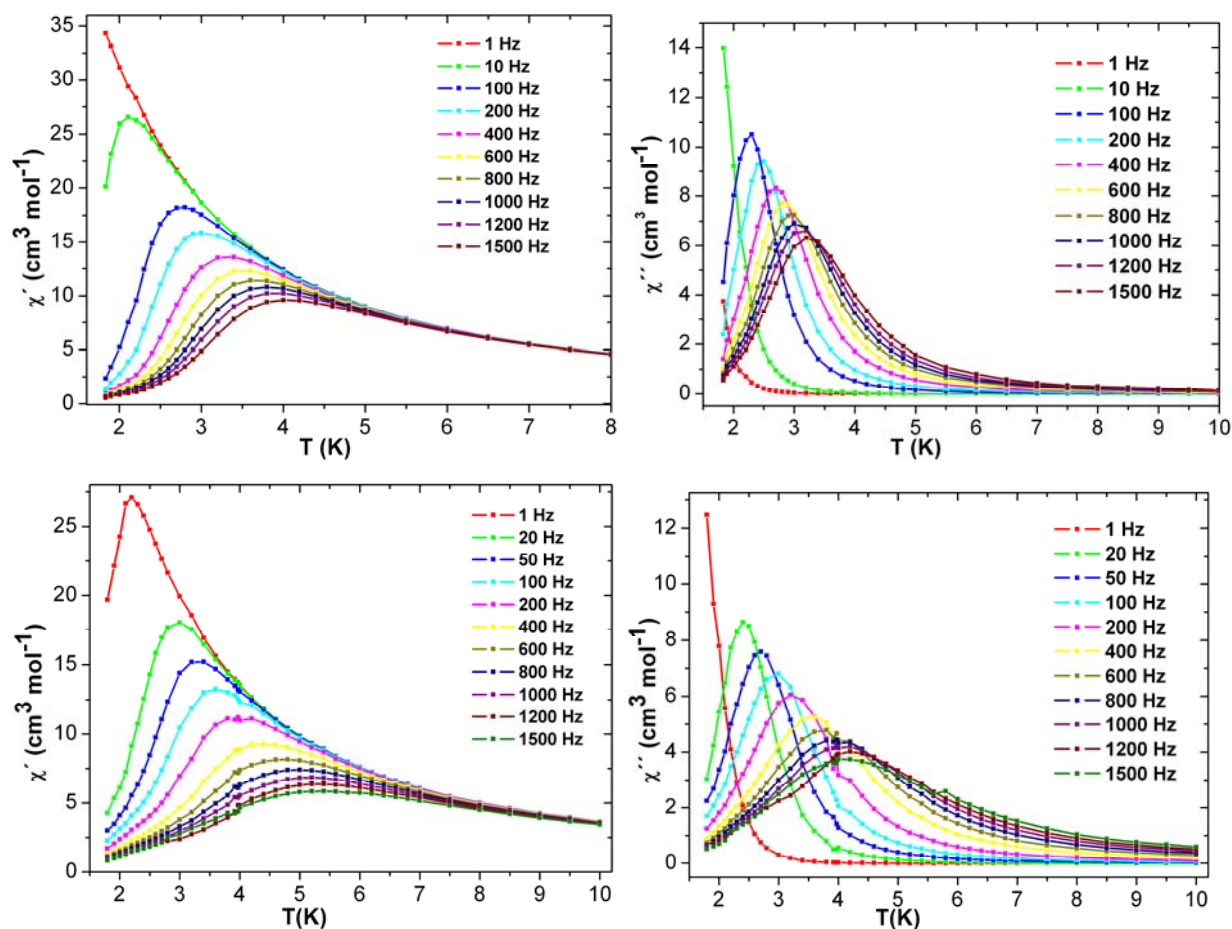


Fig. 3.7. Plots of in-phase (χ') vs T (left) and out-of-phase (χ'') vs T (right) of **1** (top) and **2** (bottom).

The blocking temperatures (maximum of χ'' vs T plot) (T_b) of **1** and **2** are 3.2 and 4.2 K at 1500 Hz respectively (Fig. 3.7). The 3D packing structure of **1** shows no H-bonding interactions between molecules while, that of **2** reveals H-bonding interactions between the molecules through the coordinated H_2O on the Ni^{II} ions. In addition, slight changes in bond lengths and bond angles on replacing DMF (**1**) by water (**2**) molecule may result in the different

blocking temperatures for **1** and **2**. The slow relaxation of magnetization is similar in both the complexes (**1** and **2**). Both the temperature (Fig. 3.7) and frequency dependent (Fig. 3.9) ac (χ' and χ'') signals are similar but complex **2** has a higher blocking temperature than that of **1**. The frequency dependent ac measurements (Fig. 3.10) at 1.8 K under different applied magnetic fields infer the existence of QTM effects. Because of QTM, the SMMs can undergo faster magnetic relaxation from one magnetic state to the other one by tunneling through the relaxation energy barrier. The ac (χ' and χ'') susceptibilities of **2** were recorded under 4 kOe applied dc magnetic field (Fig. 3.11) to switch off the slow relaxation of magnetization through QTM pathways and the blocking temperature of **2** was found to increase from 4.2 to 5.5 K (Fig. 3.11, right).

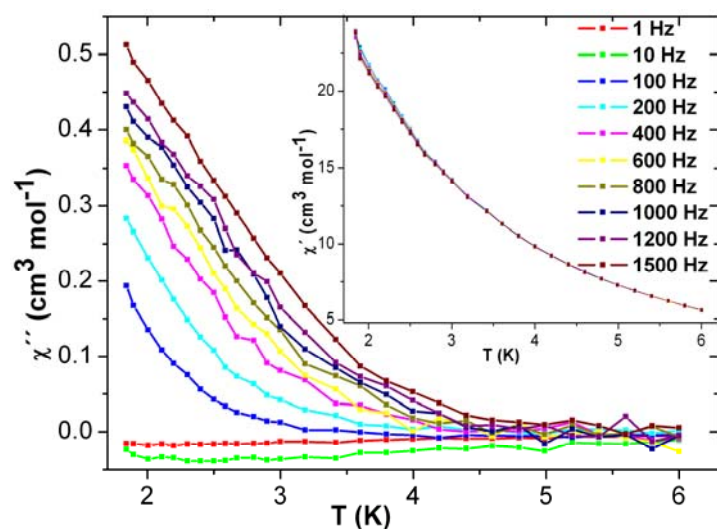
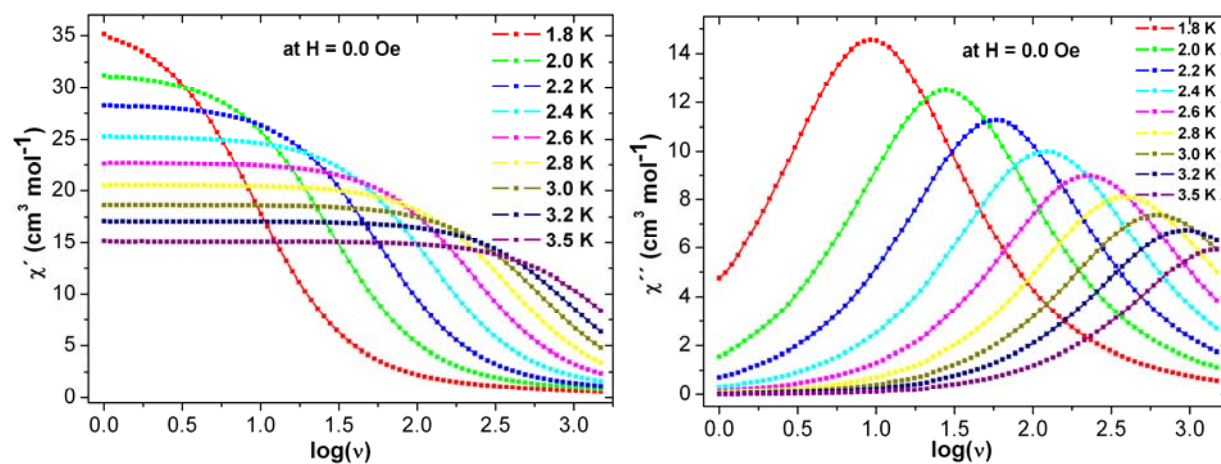


Fig. 3.8. Plots of χ'' vs T and χ' vs T (inset) of **5**.



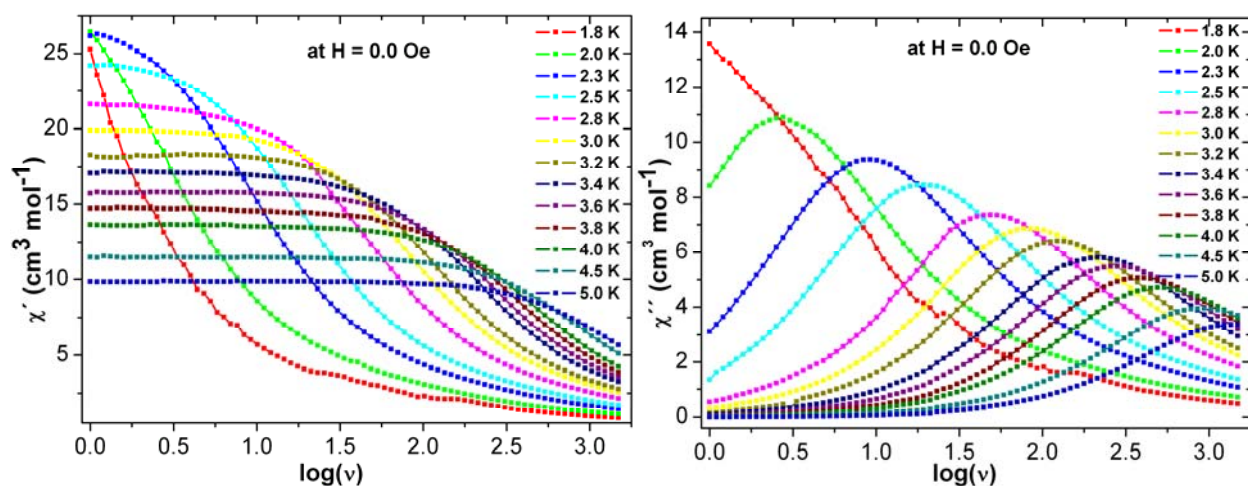


Fig. 3.9. Plots of χ' vs $\log(\nu)$ (left) and χ'' vs $\log(\nu)$ (right) of **1** (top) and **2** (bottom).

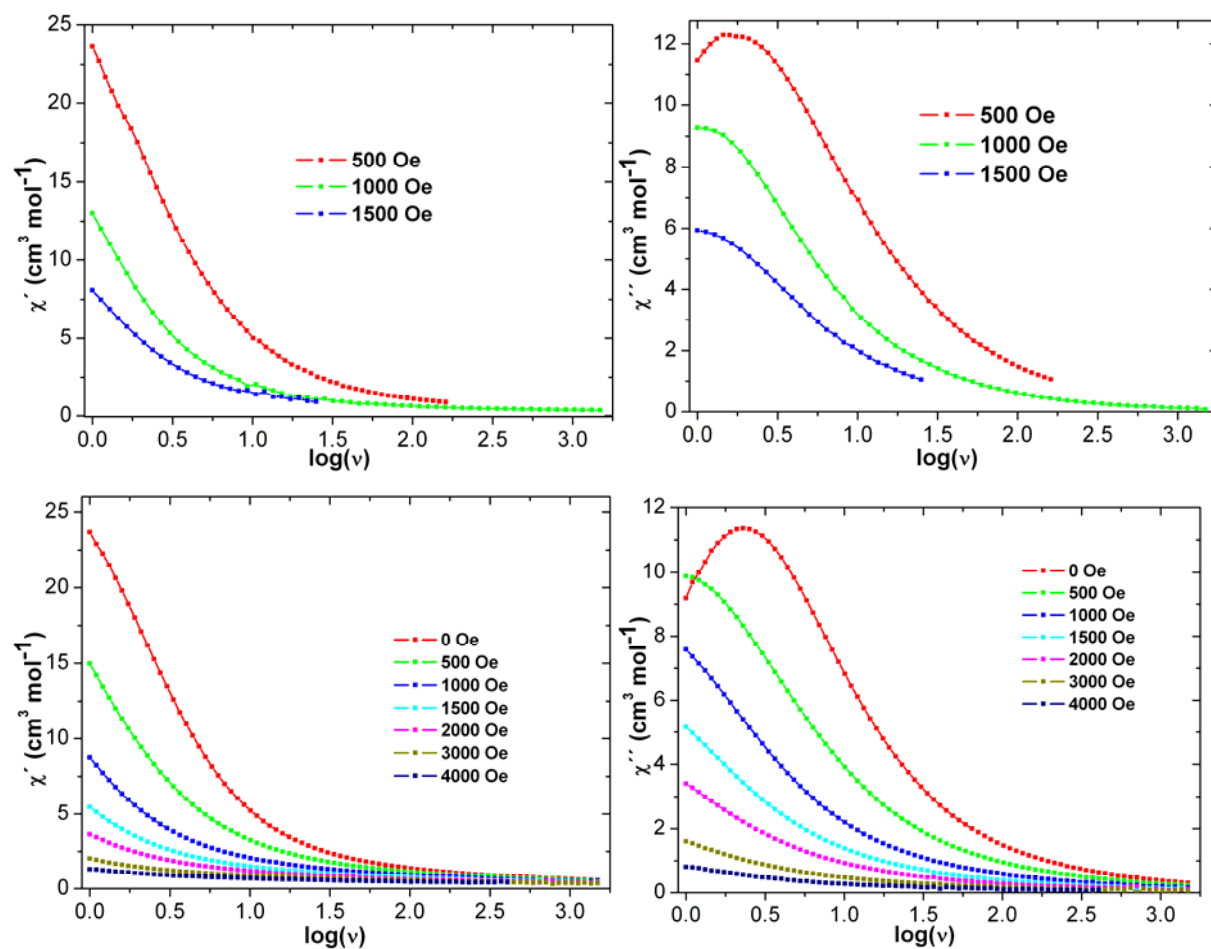


Fig. 3.10. Plots of χ' vs $\log(\nu)$ (left) and χ'' vs $\log(\nu)$ (right) of **1** (top) and **2** (bottom) at 1.8 K at indicated applied magnetic fields.

The linear fitting (τ vs $1/T$) on Arrhenius plots of **1** (Fig. 3.12) and **2** (Fig. 3.13) extracted energy barriers (Δ) of 18.5 (**1**) and 21.3 K (**2**) under zero applied magnetic field with relaxation time $\tau_0 = 5.4 \times 10^{-7}$ (**1**) and 1.5×10^{-6} s (**2**). The energy barrier of **2** was found to increase to 28.5 K (Fig. 3.13, right) with $\tau_0 = 2.8 \times 10^{-6}$ s (**2**) under applied dc magnetic field of 4 kOe.

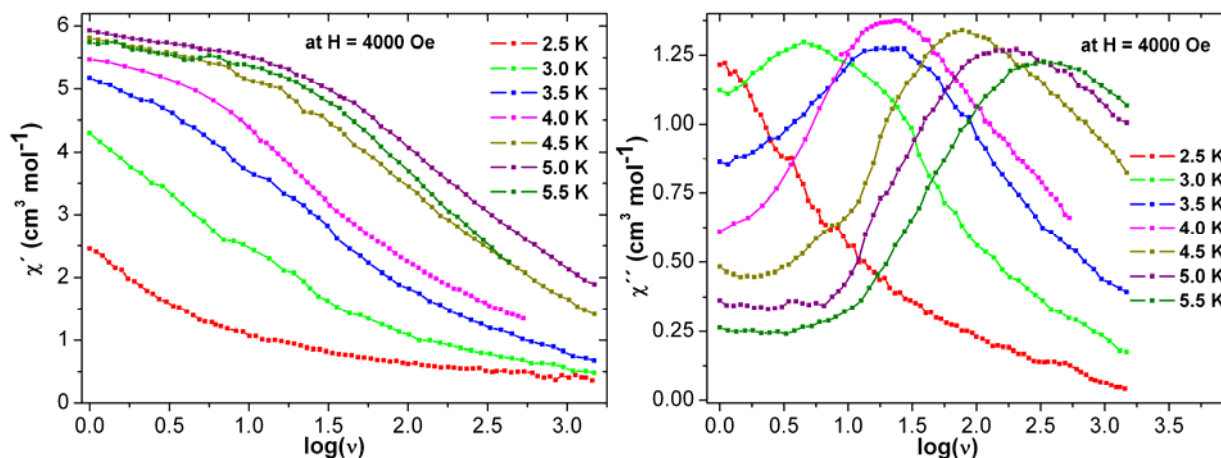


Fig. 3.11. Plots of χ' (left) and χ'' vs $\log(\nu)$ (right) of **2** under 4 kOe applied dc magnetic field.

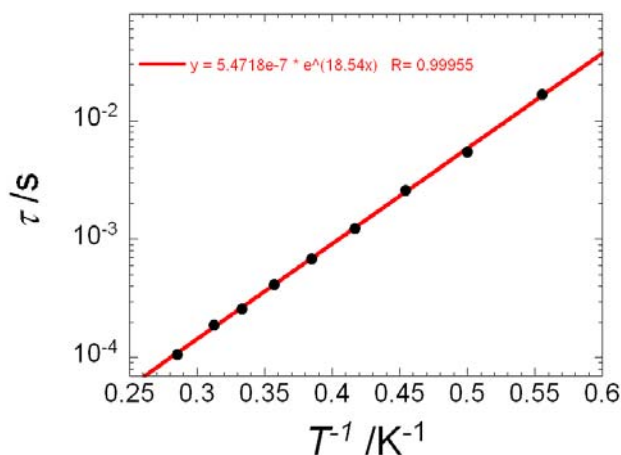


Fig. 3.12. Arrhenius Plot of **1** under zero applied dc field.

The Cole-Cole plots (χ'' vs χ' at different temperatures) of **1** and **2** are found to be semicircular (Fig. 3.14) which is frequently noticed in SMMs or SCMs. All the ac measurements on **1** and **2** indicate SMM behavior in both complexes. To confirm the SMM behavior, micro SQUID measurements were performed on a single crystal of **1**. The presence of temperature

(Fig. 3.15, left) and sweep rate dependent (Fig. 3.15, right) step-like hysteresis loops below 1.2 K confirms SMM behavior in **1**.

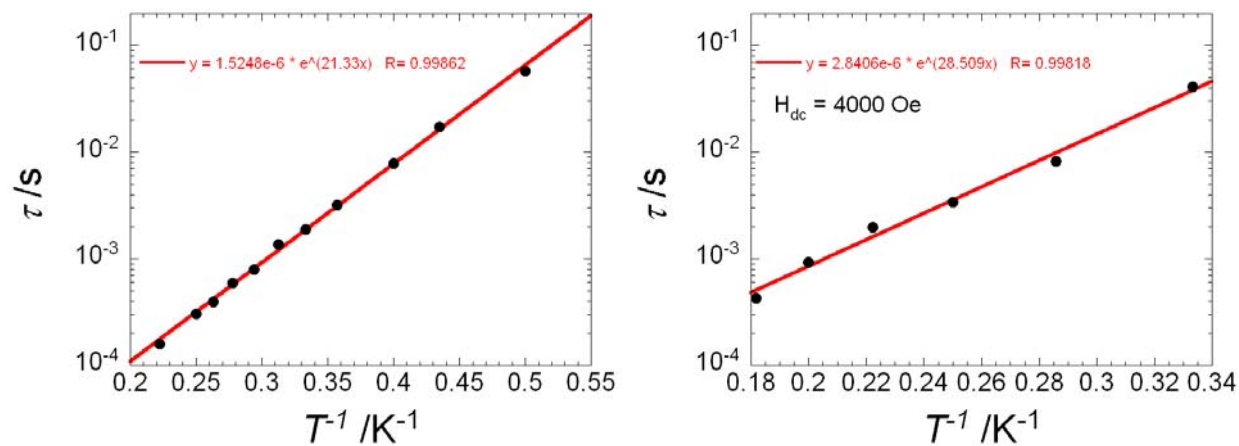


Fig. 3.13. Arrhenius Plots of **2** under applied fields of 0.0 (left) and 4 kOe (right).

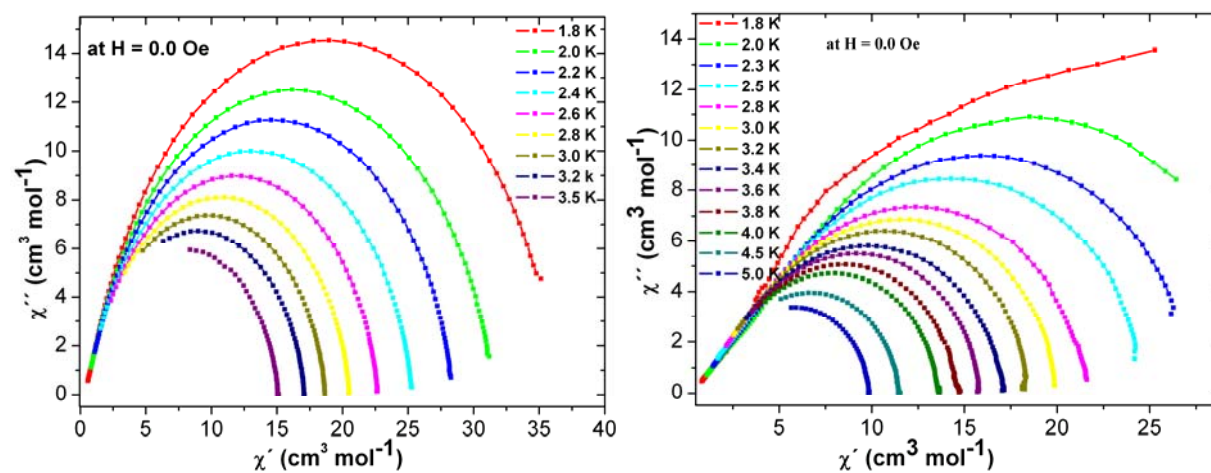


Fig. 3.14. Cole-Cole plots (χ'' vs χ') of **1** (left) and **2** (right) under zero applied dc field.

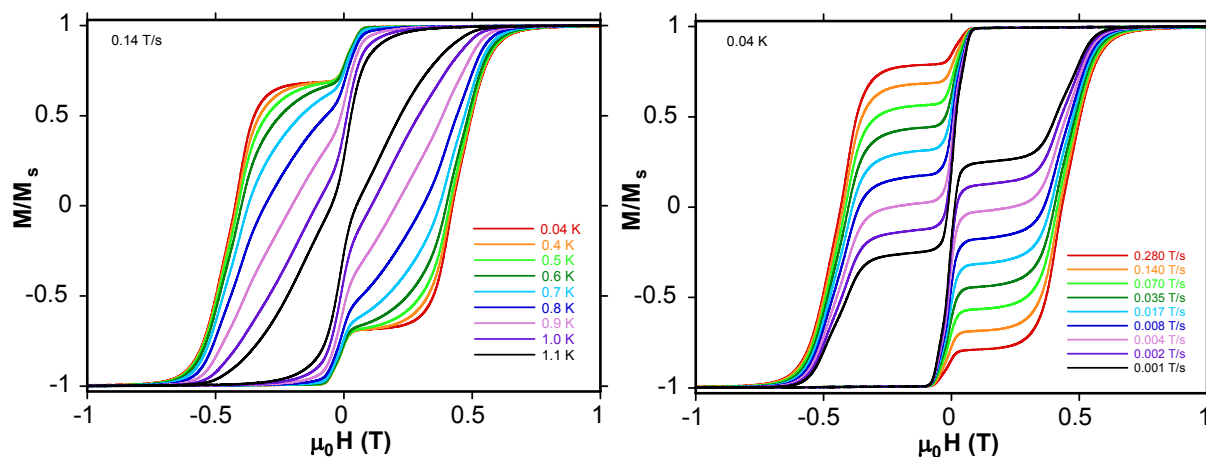


Fig. 3.15. Temperature (left) and sweep rate dependent (right) hysteresis loops of **1**.

3.3.1 Crystal structures of $[\text{Ln}_2\text{Ni}_2(\text{CO}_3)(\text{L1})_4(\text{MeOH})_6]_2[\text{Ln}_2\text{Ni}_2(\text{CO}_3)(\text{L1})_4(\text{MeOH})_{6-x}(\text{H}_2\text{O})_x] \cdot y\text{MeOH}$; [Ln = Dy(8**), $x = 1$, $y = 14$; Ln = Sm(**9**), Eu(**10**), $x = 2$, $y = 15$; Ln = Gd(**11**), $x = 2$, $y = 17$ and Tb(**12**), $x = 1$, $y = 14$].**

The compounds **8-12** are isostructural and differ from each other with respect to either coordinated or free solvent molecules. The structure of **8** is described here, and crystallizes in monoclinic space group ($C2/c$). The asymmetric unit contains two different entities of Dy_2Ni_2 units; one is (Dy_2Ni_2) and other one is $(\text{Dy}_2\text{Ni}_2)_{0.5}$. This indicates that within **8** there are two kinds of Dy_2Ni_2 molecules. One molecule contains six coordinated methanols $[\text{Dy}_2\text{Ni}_2(\text{L1})_4(\text{MeOH})_6]$ and in on a general site, while the other one contains five coordinated methanols and one water $[\text{Dy}_2\text{Ni}_2(\text{L1})_4(\text{MeOH})_5(\text{H}_2\text{O})]$, and is on a 2-fold axis with disorder the ligands. Both molecules are structurally similar but differ with one H_2O molecule in the place of one MeOH molecule for the second one.

All the Ni^{II} ions adopt a distorted octahedral geometry with an O_5N donor set, while all Dy^{III} ions adopted a distorted square antiprismatic geometry with an O_7N donor set. The complete molecule can be considered as a four-membered heterometallic (Dy_2Ni_2) , non planar, distorted U-shaped molecule with Dy-Ni-Ni-Dy torsion angle $80.74(2)^\circ$. There are two Ni^{II} ions at the bottom and two Dy^{III} ions at the top of the arms of the U. The further growth of this molecule has been terminated by two more dianionic ligands $(\text{L1})^{2-}$, each of which coordinated to each terminal Dy^{III} ion. There are two kinds of bridging modes displayed by $(\text{L1})^{2-}$. One binds

and bridges ($\eta^1:\eta^2:\eta^1:\eta^2:\mu_3$) between the metal ions while other one only chelates to Dy^{III} ion without bridging ($\eta^1:\eta^1:\eta^1:\mu_1$) (Fig. 1.5).

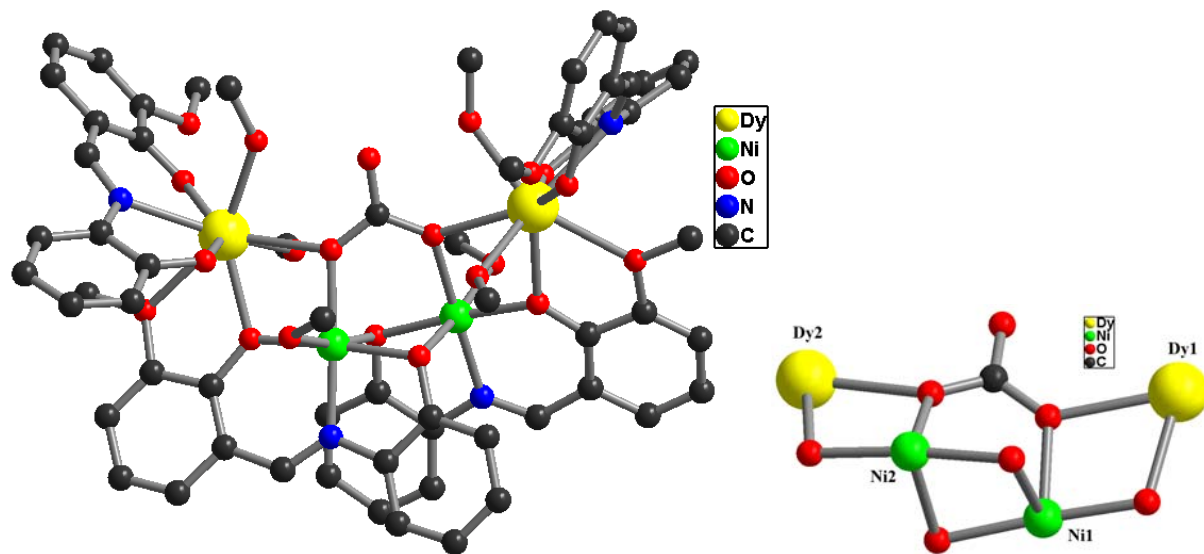
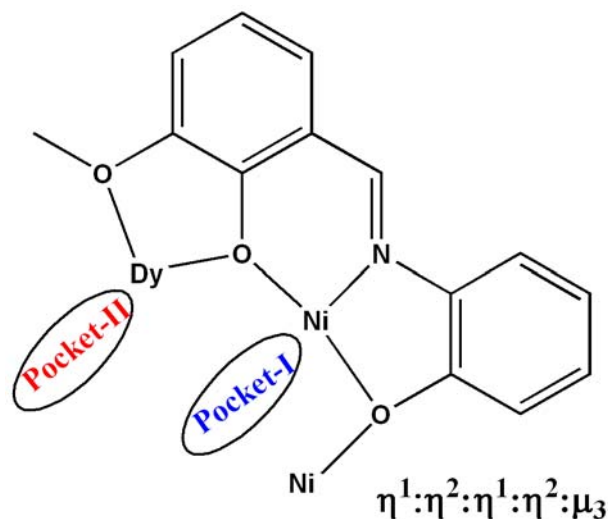


Fig. 3.16. Molecular structure (left) and core (right) of coordination cluster in compound **8**.

The equatorial positions of each Ni^{II} ion, are ligated by pocket-I (ONO) (scheme 3.1) and one O-atom of CO₃²⁻ while the axial positions are occupied by one MeOH and one μ -O-atom of iminophenol part of the ligand. Thus the Ni^{II}₂ unit is bridged by two μ -O-atom of imino-phenol part (Ni1-O-Ni2 \approx 90°). The OO (pocket-II) (scheme 3.1) coordination sites direct away from each other, occupied by the Dy^{III} ion. The Ni^{II}₂ unit is doubly bridged to each Dy^{III} ion by one phenolic μ -O-atom and μ -O-atom of CO₃²⁻ ion to the each side of Ni^{II}₂ unit. The coordination environment of each Dy^{III} are completed by one terminal ligand ($\eta^1:\eta^1:\eta^1:\mu_1$) and solvent (MeOH/H₂O) oxygen atoms.

The tetradentate carbonate (CO₃²⁻) displays a $\eta^2:\eta^2:\mu_4$ bridging mode (Fig. 1.7) and also participates in hydrogen-bonding with coordinated MeOH/H₂O on each Dy^{III} ions through the non coordinated oxygen. The other MeOH molecules are not only coordinated to Ni^{II}/Dy^{III} ion but also are H-bonded to the phenolic oxygen of the ligand. The Ni1-Ni2, Ni2-Dy1 and Ni2-Dy1 distances are 2.944, 3.506 and 3.491 Å respectively. Selected distances and angles are given in Table 3.4.



Scheme 3.1. Ni^{II} in pocket-I (ONO) and Dy^{III} ion in pocket-II (OO).

Table 3.4. Selected bond lengths (Å) and bond angles (°) within the coordination cluster in **8**.

Dy1—O6	2.235 (3)	Dy1—O25	2.406 (3)	Dy1—O24	2.338 (3)
Dy1—O8	2.275 (3)	Dy1—O1	2.477 (3)	Dy1—O12	2.368 (3)
Dy1—O13	2.521 (3)	Dy1—N1	2.503 (4)		
Dy2—O29	2.312 (3)	Dy2—O9	2.207 (3)	Dy2—O11	2.286 (3)
Dy2—O15	2.340 (3)	Dy2—O28	2.416 (3)	Dy2—O2	2.483 (3)
Dy2—N2	2.517 (4)	Dy2—O16	2.532 (3)		
Ni1—O14	2.040 (3)	Ni1—O12	1.990 (3)	Ni1—O26	2.108 (3)
Ni1—O1	2.069 (3)	Ni1—N3	2.000 (3)	Ni1—O17	2.132 (3)
Ni2—N4	2.009 (3)	Ni2—O2	2.061 (3)	Ni2—O15	1.995 (3)
Ni2—O17	2.036 (3)	Ni2—O27	2.096 (3)	Ni2—O14	2.158 (3)
Ni3—O23 ⁱ	2.125 (3)	Ni3—Ni3 ⁱ	2.9593 (10)		
Ni1—Ni1 ⁱ	2.945(5)	Ni1—O1—Dy1	100.48 (10)	Ni2—O2—Dy2	99.97 (10)
Ni1—Dy1	3.505(4)	Ni1—Dy2	3.491(3)	Ni3—Dy3	3.512(4)
Ni2—O17—Ni1	89.88 (11)	Ni1—O12—Dy1	106.76 (11)	Ni1—O14—Ni2	89.05 (10)
Ni3—O21—Dy3	107.46 (12)	Ni3—O23—Ni3 ⁱ	90.48 (10)	Ni2—O15—Dy2	107.03 (11)

Symmetry code: (i) $-x+1, y, -z+1/2$.

3.3.2 Static magnetic properties of 8-12

The dc magnetic data of **8-12** are summarized in Table 3.5. The room temperature χT values (under applied dc magnetic field of 1 kOe) of all the complexes are in good agreement with the theoretical values (Fig. 3.17). The Sm^{III} ion has very low value of susceptibility, while, Eu^{III} has a diamagnetic ground state. For Sm^{III}₂Ni^{II}₂ (**9**) and Eu^{III}₂Ni^{II}₂ (**10**) the experimental χT

values are higher because of population of low lying higher magnetic excited states. For **9**, χT slowly decreases on decreasing temperature from room temperature value to $2.725 \text{ cm}^3 \text{ K mol}^{-1}$ at 90 K and then slowly increases to $3.03 \text{ cm}^3 \text{ K mol}^{-1}$ at 19 K followed by a gradual fall to $1.79 \text{ cm}^3 \text{ K mol}^{-1}$ at 1.8 K. The upturn is due to ferromagnetic coupling between Ni-Ni and/or Ni-Sm centers and the fall at low temperature is due to ZFS of Ni^{II}/Sm^{III} ions. For **10** the gradual decrease of χT on decreasing temperature is due to thermal depopulation of magnetic excited states of Eu^{III} ions and reaches a plateau before it falls at low temperature. The plateau ($3.80 \text{ cm}^3 \text{ K mol}^{-1}$) of χT vs T in the temperature range 50-7 K is because of additional ferromagnetic interaction between Ni^{II} and populated electrons on excited magnetic states of Eu^{III} ions in **10**. The Gd^{III} ions are ferromagnetically coupled to Ni^{II} ions in **11** through oxygen bridges and thus χT product increases throughout the temperature ranges to reach $35.52 \text{ cm}^3 \text{ K mol}^{-1}$ at 1.8 K (Fig. 3.17). The χT products of **8** and **12** slowly decrease down to 30 K (due to depopulation of Stark sub-levels) and then increase (possibly due to ferromagnetic coupling between Ni^{II}-Dy^{III}/Tb^{III} centers) till 4 K followed by a sharp fall till 1.8 K (due to ZFS of Ni^{II} and Dy^{III}/Tb^{III} ions).

Table 3.5. The dc magnetic data of compounds **8-12**.

Compound	Ground state of Ln ^{III} ion	χT expected for non-interacting ions per complex ($\text{cm}^3 \text{ K mol}^{-1}$)	χT measured at 300 K per complex ($\text{cm}^3 \text{ K mol}^{-1}$)	χT measured at 1.8 K per complex ($\text{cm}^3 \text{ K mol}^{-1}$)	Magnetization at 2 K and 7 T (μ_B)
Dy ^{III} ₂ Ni ^{II} ₂ (8)	⁶ H _{15/2}	30.34	30.38	28.94	14.47
Sm ^{III} ₂ Ni ^{II} ₂ (9)	⁶ H _{5/2}	2.18	2.79	1.79	3.34
Eu ^{III} ₂ Ni ^{II} ₂ (10)	⁷ F ₀	2.0	5.21	2.27	3.95
Gd ^{III} ₂ Ni ^{II} ₂ (11)	⁸ S _{7/2}	17.76	18.44	35.52	18.28
Tb ^{III} ₂ Ni ^{II} ₂ (12)	⁷ H ₆	25.64	26.00	30.39	13.74

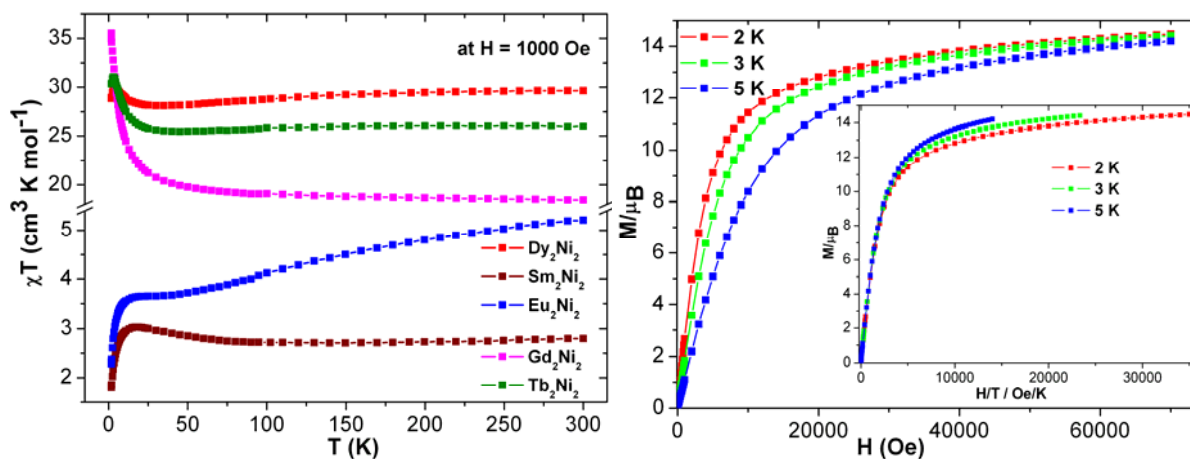


Fig. 3.17. Plots of χT vs T of **8-12** (left) under applied dc magnetic field of 1 kOe. Plots of M vs H and M vs H/T (inset) of **8** (right).

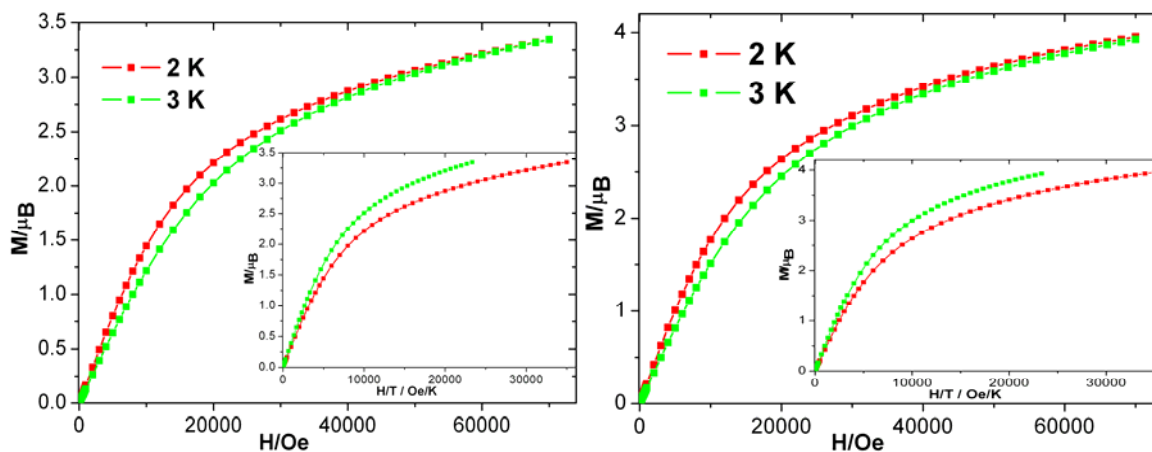


Fig. 3.18. Plots of M vs H and M vs H/T (inset) of **9** (left) and **10** (right).

The magnetization (M) increases rapidly on increasing the dc magnetic field (H) for complex $\text{Dy}^{\text{III}}_2\text{Ni}^{\text{II}}_2$ (**8**), $\text{Gd}^{\text{III}}_2\text{Ni}^{\text{II}}_2$ (**11**) and $\text{Tb}^{\text{III}}_2\text{Ni}^{\text{II}}_2$ (**12**) rapidly below 1 T, above which it linearly increases till 7 T to reach maximum values of 14.47 (**8**) (Fig. 3.17, right), 18.28 (**11**) (Fig. 3.19, left) and 13.74 μ_B (**12**) (Fig. 3.19, right) at 2 K. The corresponding M (Fig. 3.18) of $\text{Sm}^{\text{III}}_2\text{Ni}^{\text{II}}_2$ (**9**) and $\text{Eu}^{\text{III}}_2\text{Ni}^{\text{II}}_2$ (**10**) increase less rapidly and reach the values at 7 T given in Table 3.5. The M vs H/T plots (Fig. 3.16-19, inset) for all the complexes (**8-12**) do not superpose on a single master curve at different temperatures, indicating the presence of low lying energy states and/or anisotropy in the systems.⁴³

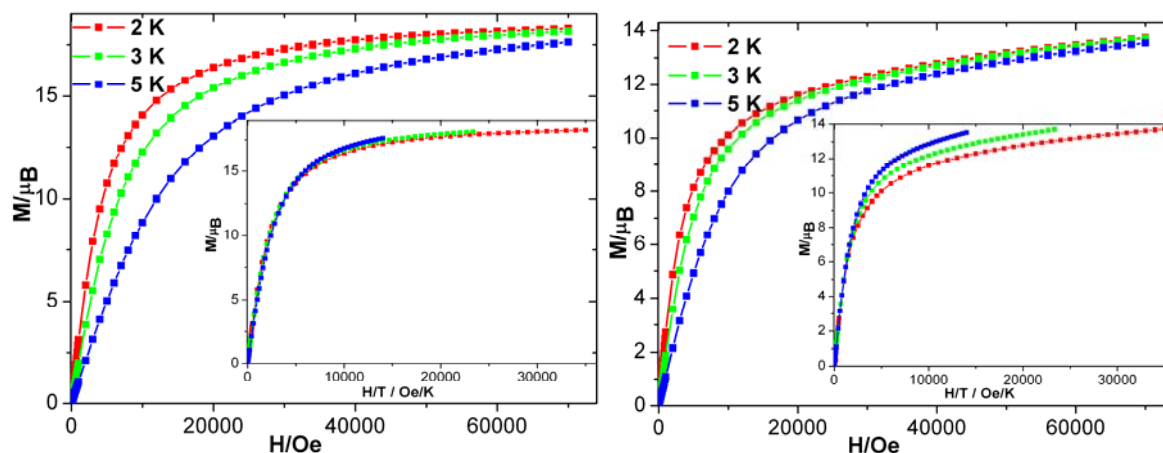


Fig. 3.19. Plots of M vs H and M vs H/T (inset) of **11** (left) and **12** (right).

3.3.3 Dynamic magnetic properties of 8-12

The temperature dependent ac susceptibility measurements on all complexes (**8-12**) reveal the presence of weak in-phase (χ') and out-of-phase (χ'') signals (Fig. 3.20, left) below 15 K for $\text{Dy}^{\text{III}}_2\text{Ni}^{\text{II}}_2$ (**8**) and below 4 K for $\text{Tb}^{\text{III}}_2\text{Ni}^{\text{II}}_2$ (**12**). There is no maximum in χ' and χ'' vs T plots for either of the complexes.

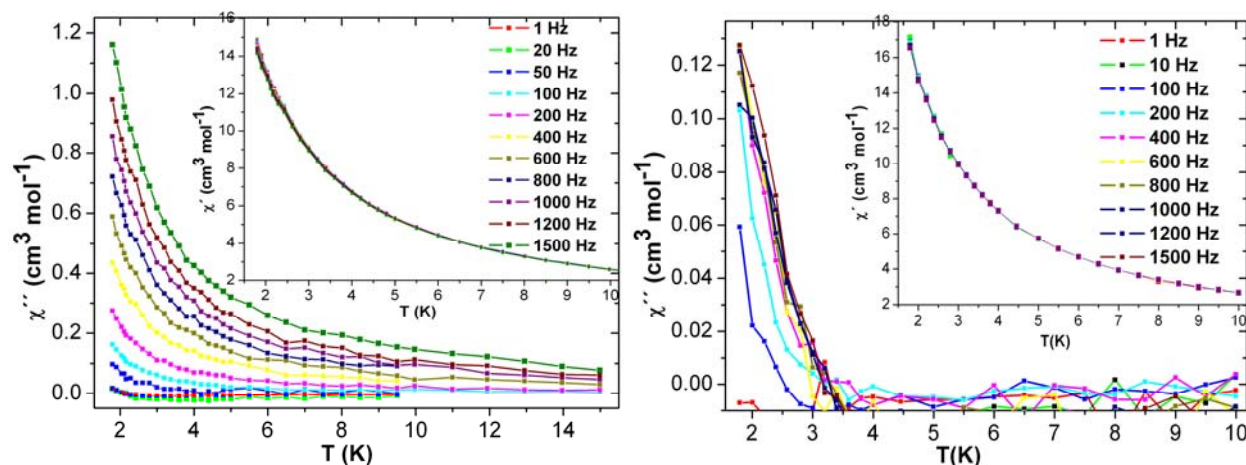


Fig. 3.20. Plots of χ'' vs T and χ' vs T (inset) of **8** (left) and **12** (right).

This kind of slow relaxation of magnetization indicates that both **8** and **12** might be SMMs with a blocking temperature below 1.8 K and/or they may possess quantum tunneling of magnetization (QTM). The slow relaxation of magnetization could be faster through QTM pathways leading to a lower blocking temperature (T_b).

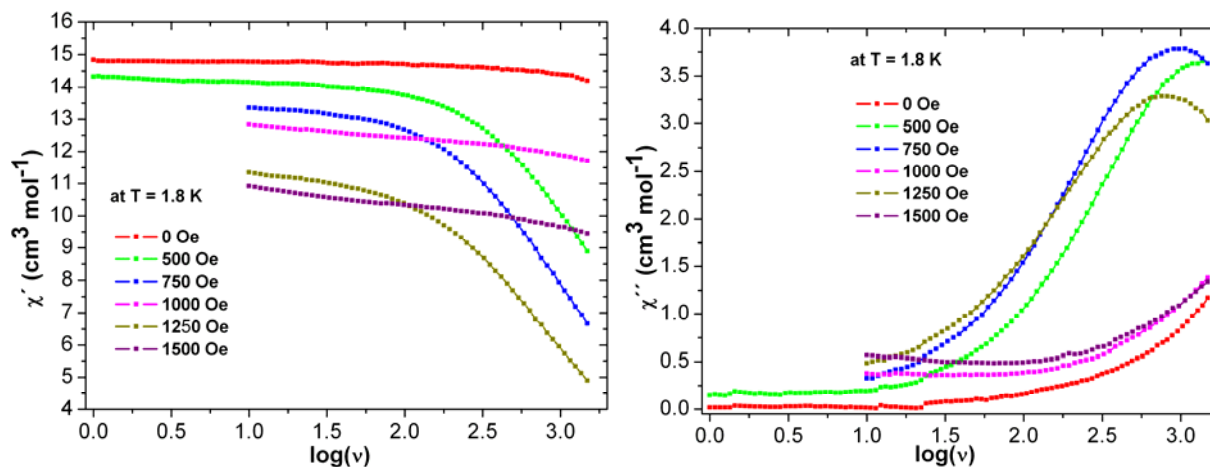


Fig. 3.21. In-phase (χ') and out-of phase (χ'') vs frequency plots for **8** at 1.8 K under different applied dc magnetic fields.

The χ' and χ'' vs frequency measurements (Fig. 3.21) were performed at 1.8 K under applied dc magnetic fields from 0-1.5 kOe. The maximum of χ'' (Fig. 3.21, right) shifts to lower and higher frequencies from 0-750 Oe and 1000-1250 Oe respectively suggesting a small dc magnetic field of 1 kOe could be sufficient to suppress the faster relaxation of magnetization through QMT pathways. Thus, χ' and χ'' vs frequency (Fig. 3.22) measurements were performed under applied dc magnetic field of 1 kOe in the temperature range of 1.9 to 2.3 K. The maximum in χ'' vs frequency (Fig. 3.22, right) shifts from lower to higher frequency with the increase of temperature.

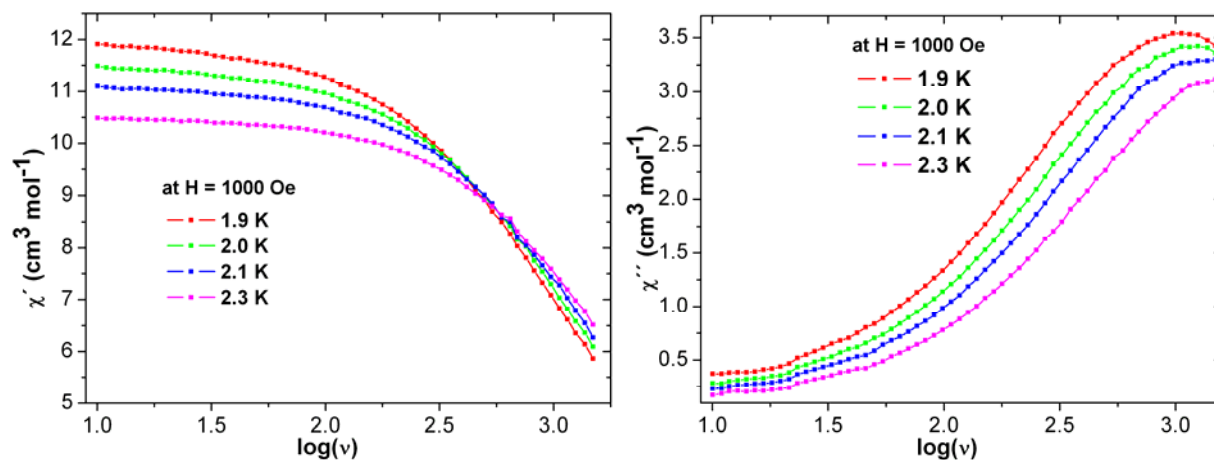


Fig. 3.22. In-phase (χ') and out-of phase (χ'') vs frequency plots for **8** under 1 kOe applied field.

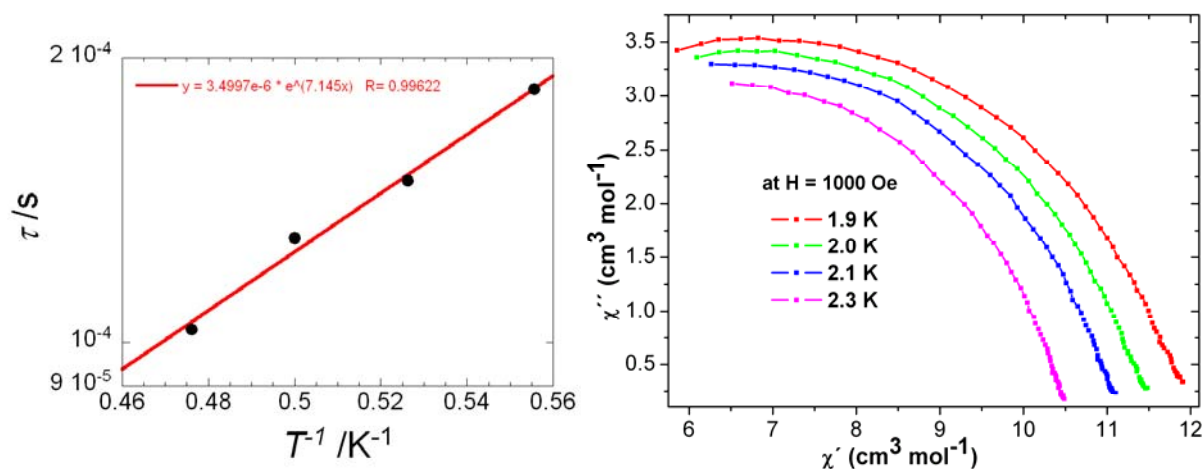


Fig. 3.23. Arrhenius plot (left) and Cole-Cole plots (χ'' vs χ') of **8** (right).

The data of Fig. 3.22 were used for the Arrhenius plot to evaluate the effective energy barrier of slow relaxation (Fig. 3.23, left) and for Cole-Cole plots (Fig. 3.22, right). The Cole-Cole plots look semi-circular, indicating single relaxation pathway. The linear fitting on Arrhenius plots (τ vs $1/T$) of **8** (Fig. 3.12) gave energy barrier of 7.1 K (**8**) under 1 kOe applied dc magnetic field with relaxation time $\tau_0 = 4.5 \times 10^{-7}$ s (**8**) (Fig. 3.23, left). Micro SQUID measurements were performed on single crystal of **8**. Sweep rate dependent (Fig. 3.24, right), hysteresis loops at 0.04 K showed extremely small coercivities.

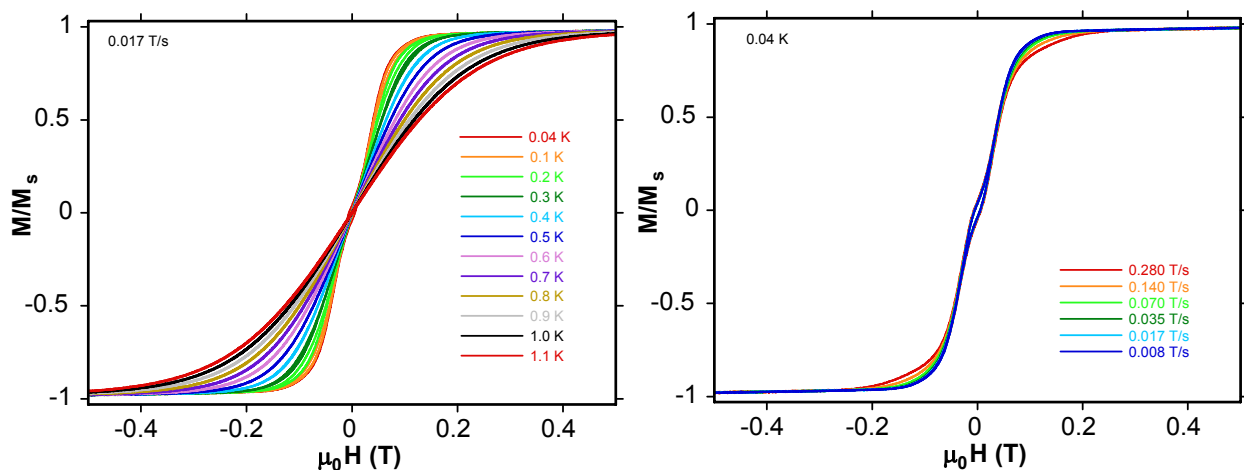


Fig. 3.24. Temperature (left) and sweep rate dependent (right) hysteresis loop of **8**.

3.4.1 Crystal structures of ring like

$[\text{Ln}_4\text{Ni}_8(\text{CO}_3)_4(\text{L1})_8(\text{NO}_3)_2(\text{H}_2\text{O})_8(\text{MeOH})_4](\text{NO}_3)_2 \cdot 5\text{MeOH} \cdot 4\text{H}_2\text{O}$; $[\text{Ln} = \text{Dy}(13), \text{Y}(14), \text{Gd}(15), \text{Tb}(16), \text{Ho}(17) \text{ and } \text{Er}(18)]$:

Complexes **13-18** are isomorphous (confirmed by the unit cell constants); hence only structure of **13** is described below. The complex **13** crystallizes in the tetragonal space group $P-42_1/c$ with a four-fold symmetry. The asymmetric crystallographic unit contains two Ni^{II} ions, one Dy^{III} ion, two dianionic ligands $(\text{L1})^{2-}$, one carbonate (CO_3^{2-}) , one coordinated MeOH , two coordinated H_2O and one nitrate (NO_3^-) . All the Ni^{II} ions adopted a distorted octahedral geometries with an O_5N donor set, while all Dy^{III} ions adopted an O_9 coordination environment which can be best described as capped square anti-prism with O7 capping the square of O1 , O2 , O11A and O8 . The chelating nitrate ligands are disordered over two of the four Dy^{III} ions in the ring; these Dy^{III} ions have a nitrate and a water ligand, each of the other two Dy instead has three water ligands.

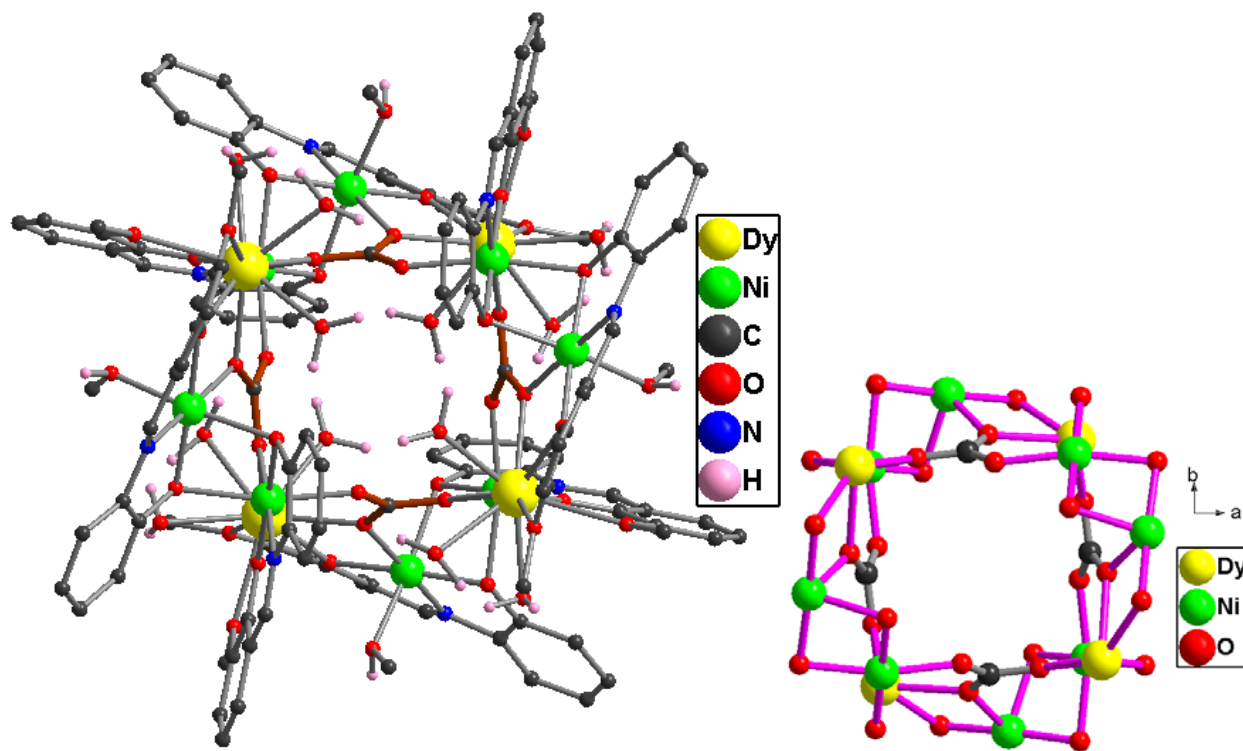


Fig.3.25. Molecular structure (left) and core (right) of the coordination cluster in compound **13**.

The total molecule can be considered as a 12-membered heterometallic non-planar wheel with alternating Ni^{II}₂ units and Dy^{III} ions. Both **8** and **13** had a similar Ni^{II}₂ unit with similar bridging mode of the ligands. The equatorial positions of each Ni^{II} ion, are ligated by pocket-I (ONO) (Fig. 1.5 and Scheme 3.1) and one O-atom of CO₃²⁻ while the axial positions are occupied by one MeOH and one μ -O-atom of the iminophenol part of the ligand. Thus all Ni^{II}₂ units are bridged by two iminophenol μ -O-atoms (Ni1-O6-Ni2 = 89.1(2) and Ni1-O-Ni2' = 87.12(17)°). The OO (pocket II) (Fig. 1.5 and Scheme 3.1) coordination sites direct away from each other ligating the Dy^{III} ions. The Ni^{II}₂ unit and Dy^{III} ion are doubly bridged by one phenolic μ -O-atom and one μ -O-atom of CO₃²⁻ ion. Each Dy^{III} ion is coordinated by four O-atoms of the ligand and other five O-atoms coming from water and partially from nitrate anions. All four CO₃²⁻ ions come from atmospheric CO₂. All four CO₃²⁻ are μ_5 and display $\eta^2:\eta^1:\eta^2:\mu_5$ bridging mode (Fig. 1.7). In the crystal structure, all four CO₃²⁻ are crystallographically equivalent and bridge between both Ni^{II} and Dy^{III} ions from the interior part of the Ni₈Dy₄ molecule and make H-bonds with coordinated H₂O on each Dy^{III} ion. This water molecule is not only coordinated to Dy^{III} ion but also is H-bonded (for H-bonding distance see Table 3.6) between O-atom of CO₃²⁻ ion and O-atom of imino-phenol part (O-O \approx 2.73 Å). Selected bond lengths and angles are given in the Table 3.6.

Table 3.6. Selected bond lengths (Å) and bond angles (°) within the coordination cluster in **13**.

Dy1—O4	2.320 (5)	Dy1—O1	2.456 (4)	Dy1—O5	2.547 (6)
Dy1—O2 ⁱ	2.362 (5)	Dy1—O12A	2.466 (13)	Dy1—O8	2.600 (5)
Dy1—O11B	2.367 (17)	Dy1—O12B	2.477 (13)	Dy1—O11A	2.516 (17)
Dy1—O10	2.385 (5)	O2—Dy1 ⁱⁱ	2.361 (5)		
Ni1—O1	2.059 (4)	Ni1—N1	1.989 (6)	Ni1—O14	2.089 (5)
Ni1—O6	2.033 (5)	Ni1—O4	2.009 (5)	Ni1—O9 ⁱⁱ	2.142 (5)
Ni2—O2 ⁱ	2.049 (5)	Ni2—O7	1.996 (5)	Ni2—O9	2.068 (5)
Ni2—O6 ⁱ	2.102 (5)	Ni2—N2	2.003 (6)	Ni2—O3	2.060 (5)
Ni1—Ni2	2.902 (5)	Ni1—Ni2 ⁱ	5.222 (6)	Ni2—Ni2 ⁱⁱ	5.959(6)
Ni1—Dy1	3.476(6)	Ni2—Dy1	3.397(5)	Ni2—Dy1 ⁱ	5.622(5)
Ni1—O6—Ni2 ⁱⁱ	89.1 (2)	Ni2—O9—Ni1 ⁱ	87.12 (17)	Ni2 ⁱⁱ —O2—Dy1 ⁱⁱ	100.49 (19)
Ni1—O4—Dy1	106.60 (19)	Ni2—O7—Dy1	104.7 (2)	Ni1—O1—Dy1	100.31 (16)
O10 \cdots O3 ⁱ	2.797 (7)	O14 \cdots O41	2.745 (9)	O31 \cdots O11A	2.83 (2)
O10 \cdots O9 ⁱⁱ	2.729 (8)	O31 \cdots O11B	2.91 (2)		

Symmetry codes: (i) $y, -x, -z+1$; (ii) $-y, x, -z+1$.

3.4.2 Static magnetic properties of 13-18

The dc magnetic data of **13-18** are summarized in Table 3.7. The room temperature χT values of all the complexes under applied dc magnetic field of 1 kOe are in good agreement with the theoretical values (Fig. 3.26). On decreasing temperature the χT product of **14** increases very slowly from $8.36 \text{ cm}^3 \text{ K mol}^{-1}$ at room temperature to $8.93 \text{ cm}^3 \text{ K mol}^{-1}$ at 55 K, below which slowly decreases and finally falls to $1.56 \text{ cm}^3 \text{ K mol}^{-1}$ at 1.8 K. The slight increase of χT value at higher temperature is due to weak ferromagnetic coupling and decrease at low temperatures is due to ZFS of Ni^{II} ions and/or weak intra/inter molecular antiferromagnetic coupling. Since Y^{III} is diamagnetic, $\text{Y}^{\text{III}}\text{Ni}_4^{\text{II}}_8$ (**14**) could be considered as ferromagnetically coupled four dimeric $\text{Ni}_2^{\text{II}}\text{O}_2$ units, which are weakly antiferromagnetically coupled to their nearest dimeric $\text{Ni}_2^{\text{II}}\text{O}_2$ units through *syn-anti*- CO_3 bridges.

The χT product of $\text{Gd}^{\text{III}}\text{Ni}_4^{\text{II}}_8$ (**15**) increases continuously from $40.64 \text{ cm}^3 \text{ K mol}^{-1}$ at room temperature to $44.61 \text{ cm}^3 \text{ K mol}^{-1}$ at 11 K and below that falls to $31.72 \text{ cm}^3 \text{ K mol}^{-1}$ at 1.8 K. The χT product of $\text{Tb}^{\text{III}}\text{Ni}_4^{\text{II}}_8$ (**16**) follows the same trend as **15**. The χT products of $\text{Dy}^{\text{III}}\text{Ni}_4^{\text{II}}_8$ (**13**), $\text{Ho}^{\text{III}}\text{Ni}_4^{\text{II}}_8$ (**17**) and $\text{Er}^{\text{III}}\text{Ni}_4^{\text{II}}_8$ (**18**) slowly decrease down to 25 K (due to possible antiferromagnetic coupling between Ni^{II} - Dy^{III} / Tb^{III} centers and depopulation of Stark sub-levels) followed by a sharp fall till 1.8 K (due to ZFS of Ni^{II} and Dy^{III} / Tb^{III} ions).

Table 3.7. The dc magnetic data of compounds **13-18**.

Compound	Ground state of Ln^{III} ion	χT expected for non-interacting ions per complex ($\text{cm}^3 \text{Kmol}^{-1}$)	χT measured at 300 K per complex ($\text{cm}^3 \text{Kmol}^{-1}$)	χT measured at 1.8 K per complex ($\text{cm}^3 \text{Kmol}^{-1}$)	Magnetization at 2 K and 7 T (μ_B)
$\text{Dy}^{\text{III}}\text{Ni}_4^{\text{II}}_8$ (13)	$^6\text{H}_{15/2}$	64.68	65.93	17.60	30.31
$\text{Y}^{\text{III}}\text{Ni}_4^{\text{II}}_8$ (14)	-	8.0	8.36	1.56	8.36
$\text{Gd}^{\text{III}}\text{Ni}_4^{\text{II}}_8$ (15)	$^8\text{S}_{7/2}$	39.42	40.65	31.72	37.74
$\text{Tb}^{\text{III}}\text{Ni}_4^{\text{II}}_8$ (16)	$^7\text{H}_6$	55.28	55.40	14.68	29.92
$\text{Ho}^{\text{III}}\text{Ni}_4^{\text{II}}_8$ (17)	$^5\text{I}_8$	64.28	64.07	18.87	31.51
$\text{Er}^{\text{III}}\text{Ni}_4^{\text{II}}_8$ (18)	$^4\text{I}_{15/2}$	53.92	54.55	20.24	28.48

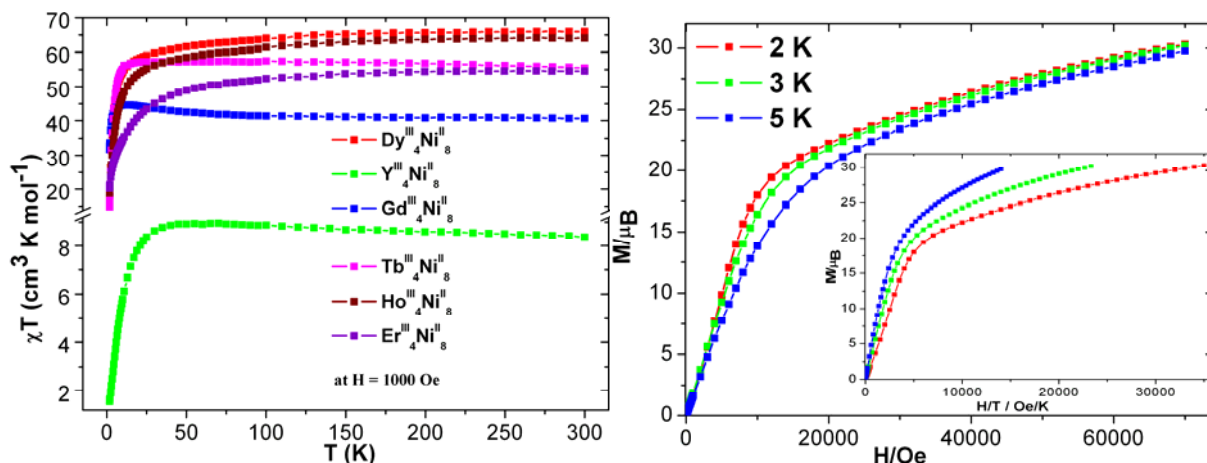


Fig.3.26. Plots of χT vs T of **13-18** (left) under applied dc magnetic field of 1 kOe. Plots of M vs H and M vs H/T (inset) of **13** (right).

The magnetization (M) of $\text{Y}^{\text{III}}_4\text{Ni}^{\text{II}}_8$ (**14**) increases with increasing field (H), almost linearly throughout the whole field range to reach a maximum value of $8.36 \mu\text{B}$ at 7 T, indicating paramagnetic like behavior (Fig. 3.27, left). The dM/dH plot at 2 K has a broad maximum at 40 kOe which could be due to either field induced spin population or intermolecular antiferromagnetic interactions. Intermolecular H-bonding was observed between the molecules in this series of complexes.

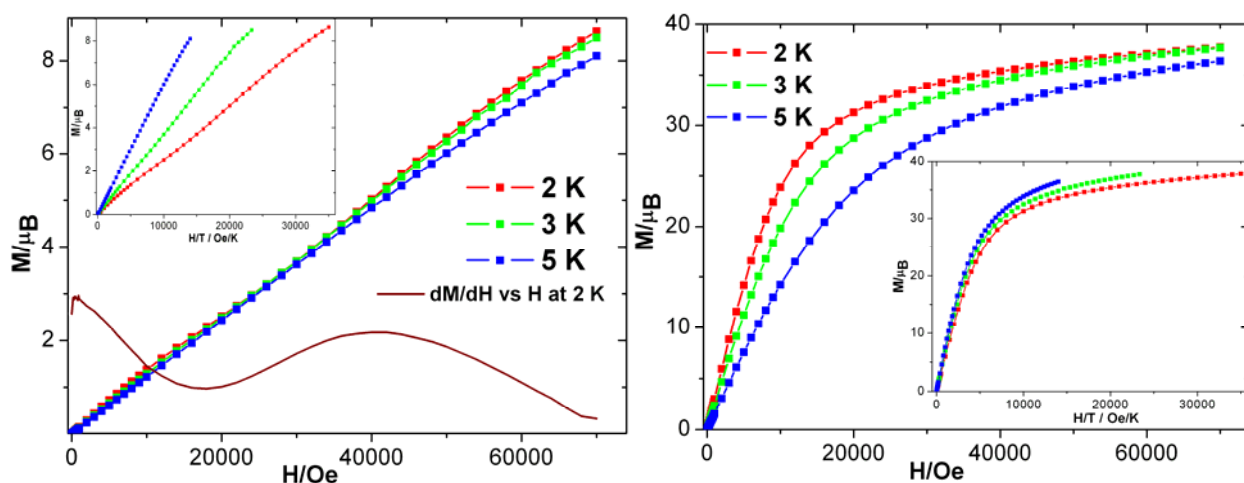


Fig. 3.27. Plots of M vs H and M vs H/T (inset) of **14** (left) and **15** (right).

The magnetization value of $\text{Gd}^{\text{III}}_4\text{Ni}^{\text{II}}_8$ (**15**) smoothly increases to $37.74 \mu_{\text{B}}$ at 7 T (Fig. 3.27, right). The 4 Gd^{III} ions are weakly ferromagnetically coupled to the corresponding Ni^{II} ions, thus contributing $28 \mu_{\text{B}}$ to the magnetization. Hence, the expected magnetization for **15** is $36.36 \mu_{\text{B}}$ which is very close to the experimental magnetization value of $37.74 \mu_{\text{B}}$.

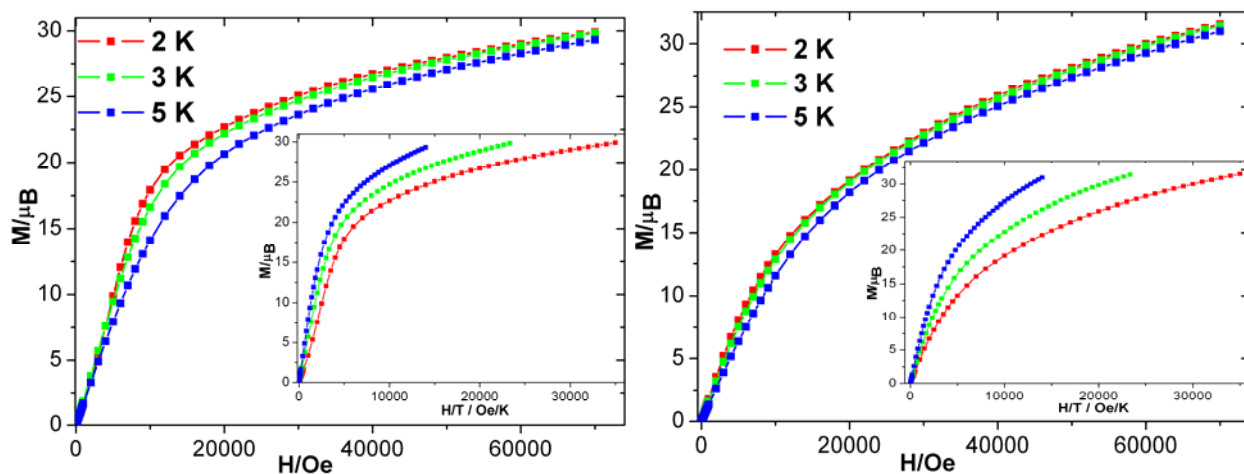


Fig. 3.28. Plots of M vs H and M vs H/T (inset) of **16** (left) and **17** (right).

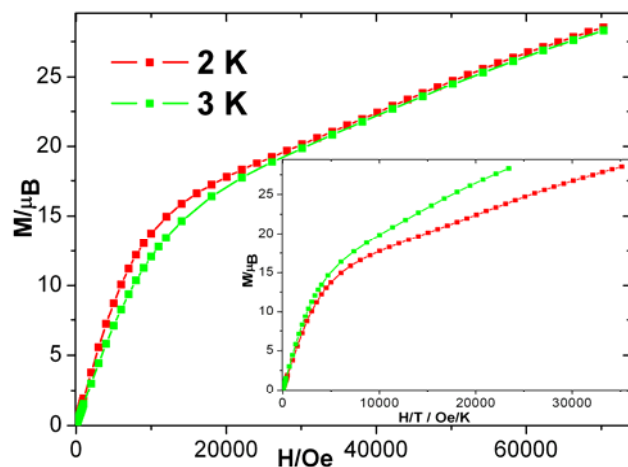


Fig. 3.29. Plots of M vs H and M vs H/T (inset) of **18**.

The magnetizations of complexes $\text{Dy}^{\text{III}}_4\text{Ni}^{\text{II}}_8$ (**13**), $\text{Tb}^{\text{III}}_4\text{Ni}^{\text{II}}_8$ (**16**) and $\text{Ho}^{\text{III}}_4\text{Ni}^{\text{II}}_8$ (**17**) increase rapidly below 1T and then linearly increase till 7 T to reach maximum values of 30.31 (**13**) (Fig. 3.26, right), 29.92 (**16**) (Fig. 3.28, left) and 31.51 (**17**) (Fig. 3.28, right) at 2 K without saturation. The M vs H/T plots at different temperatures (Fig. 3.26-28, inset) for all the

complexes (**13-18**) do not superpose on to single master curve, indicating the presence of low lying energy states and/or anisotropy in the systems.⁴³

3.4.3 Dynamic magnetic properties of 13-18

The temperature dependence of ac susceptibility measurements on the complexes (**13-18**) reveal the presence of weak in-phase (χ') and out-of-phase (χ'') signals (Fig. 3.30, left) in $\text{Dy}^{\text{III}}_4\text{Ni}^{\text{II}}_8$ (**13**) below 5 K. There are broad maxima in χ' vs T plots but the maxima are not obvious in χ'' vs T plots of **13**, indicating a blocking temperature (T_b) below 1.8 K and/or the presence of QTM. The slow relaxation of magnetization could be faster through QTM pathways, lowering the effective energy barrier. To investigate this, frequency dependence of ac susceptibilities were measured under small applied dc magnetic field.

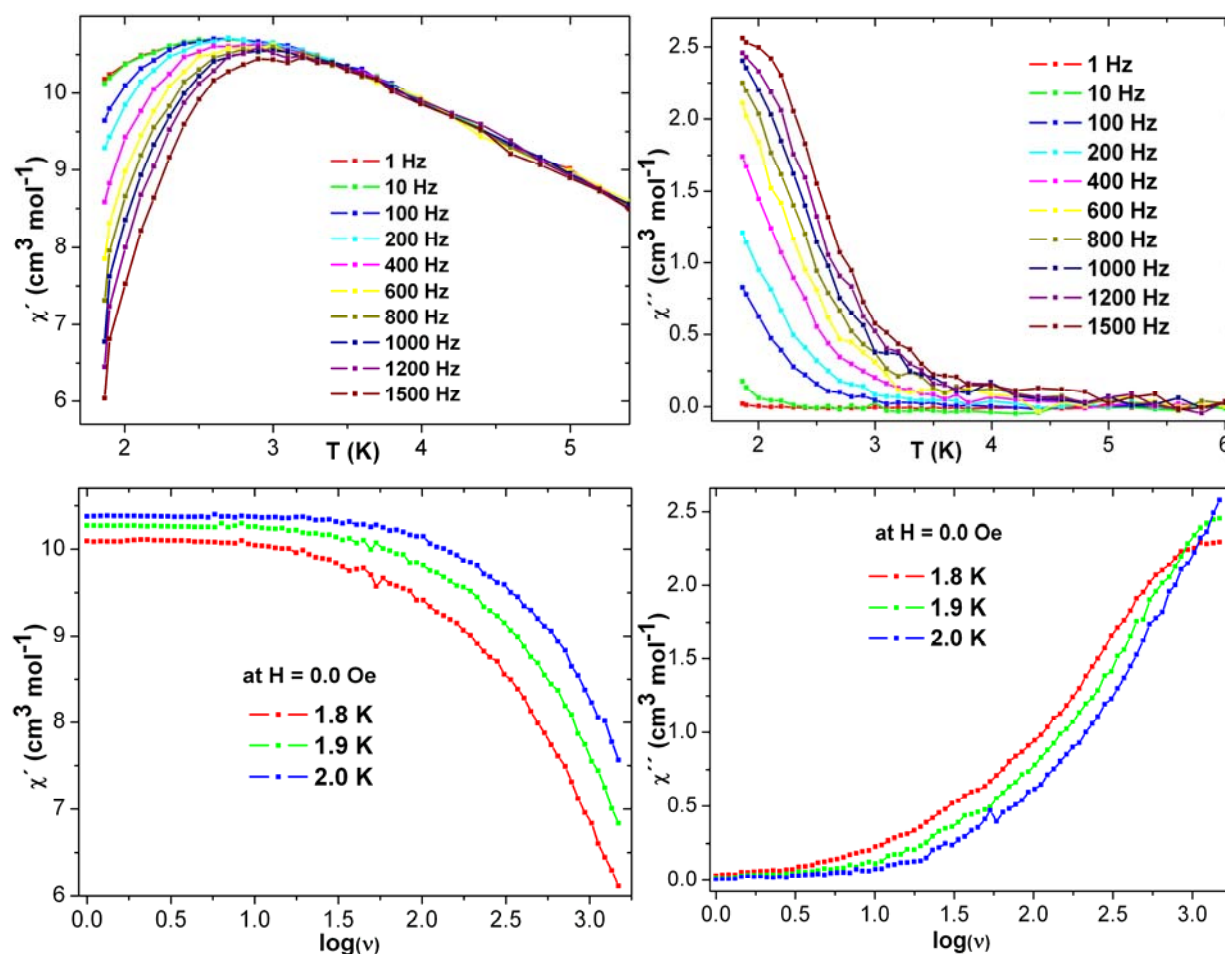


Fig. 3.30. Plots of ac susceptibility vs temperature (top) and frequency (bottom) of **13**.

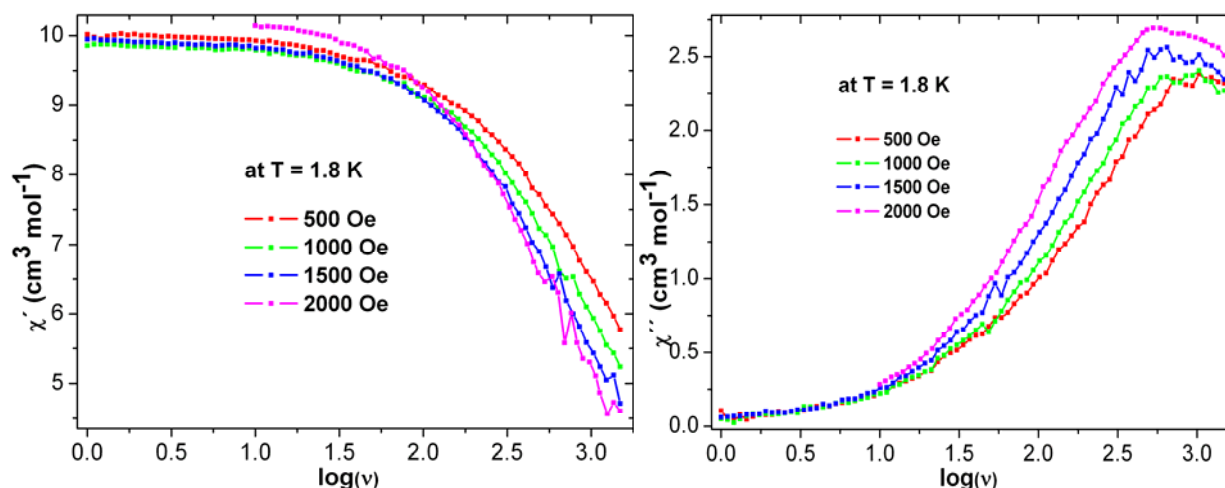


Fig. 3.31. Plots of ac susceptibility vs frequency of **13** at 1.8 K under indicated dc fields.

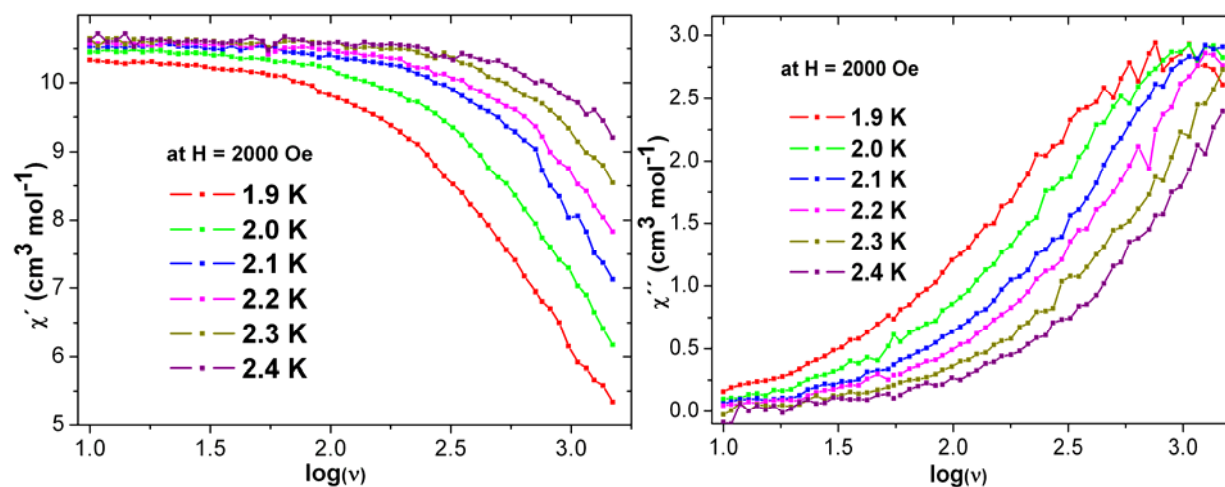


Fig. 3.32. Plots of ac susceptibility vs frequency of **13** under 2 kOe dc field at indicated temperatures.

The χ' and χ'' vs frequency (Fig. 6.31) measurements were performed at 1.8 K with dc fields of 0.5-2.0 kOe. The peak of χ'' (Fig. 3.31, right) moves from higher to lower frequency from 0.5-2.0 kOe respectively. This measurement does not envisage the presence of QTM pathways. Thus χ' and χ'' vs frequency measurements are performed under applied zero (Fig. 3.30, bottom) and 2.0 kOe (Fig. 3.32) dc magnetic field. The peak in χ'' vs frequency (Fig. 3.32, right) moves from lower to higher frequency with the increase of T. The data of Fig. 3.32 were used for Arrhenius plot to evaluate the effective energy barrier of slow relaxation (Fig. 3.33,

right) and for Cole-Cole plots (Fig. 3.33, left). The Cole-Cole plots looks semi-circular, indicating single relaxation pathway.

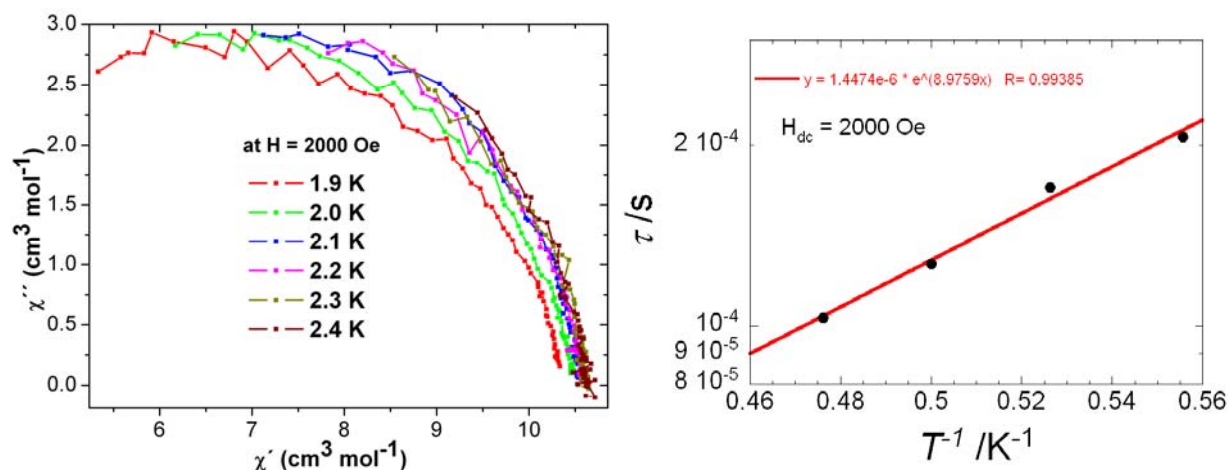


Fig. 3.33. The Cole-Cole (left) and Arrhenius (right) plots of **13**. Red line represents the fitting (right).

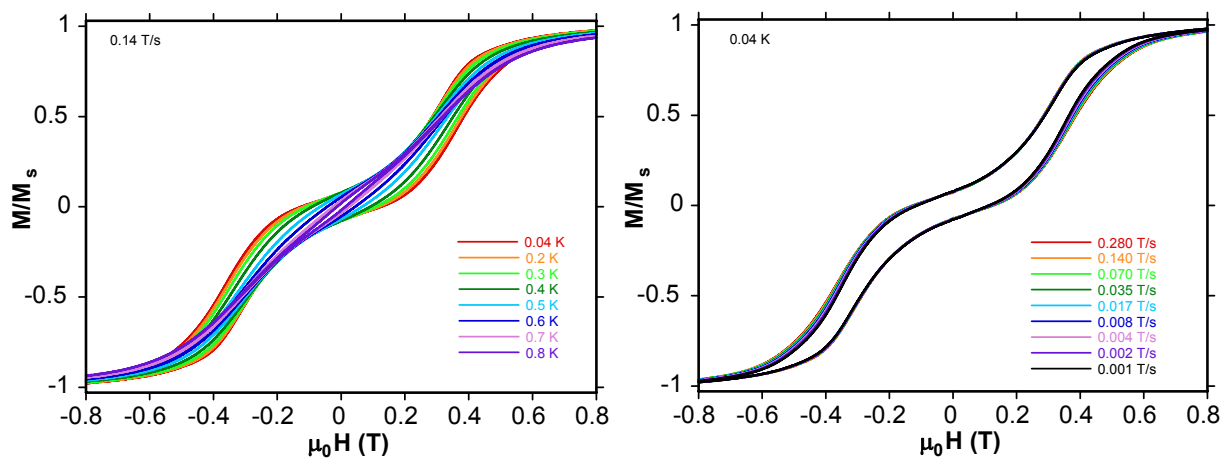


Fig. 3.34. Temperature (left) and sweep rate dependent (right) hysteresis loops of **13**.

The linear fitting to the Arrhenius plot (τ vs $1/T$) for **13** (Fig. 3.33, right) gave an energy barrier of 9.0 (**13**) under an applied dc magnetic field of 2 kOe, with relaxation time $\tau_0 = 1.4 \times 10^{-6}$ (**13**) (Fig. 3.33, right). To confirm SMM behavior, micro SQUID measurements were performed on single crystal of **13**. The presence of temperature (Fig. 3.34, left) and sweep rate dependent (Fig. 3.34, right) hysteresis loops below 0.8 K confirms SMM behavior in **13**.

3.5.1 Crystal structure of half-ring like $[\text{Dy}_2\text{Ni}_4(\text{OH})_2(\text{L}1)_4(\text{MeOH})_4(\text{NO}_3)_4]\cdot 4\text{MeOH}$ (**19**):

The hexanuclear heterometallic complex **19** crystallizes in space group $P2_1/n$. The molecular structure is shown in Fig. 3.35.

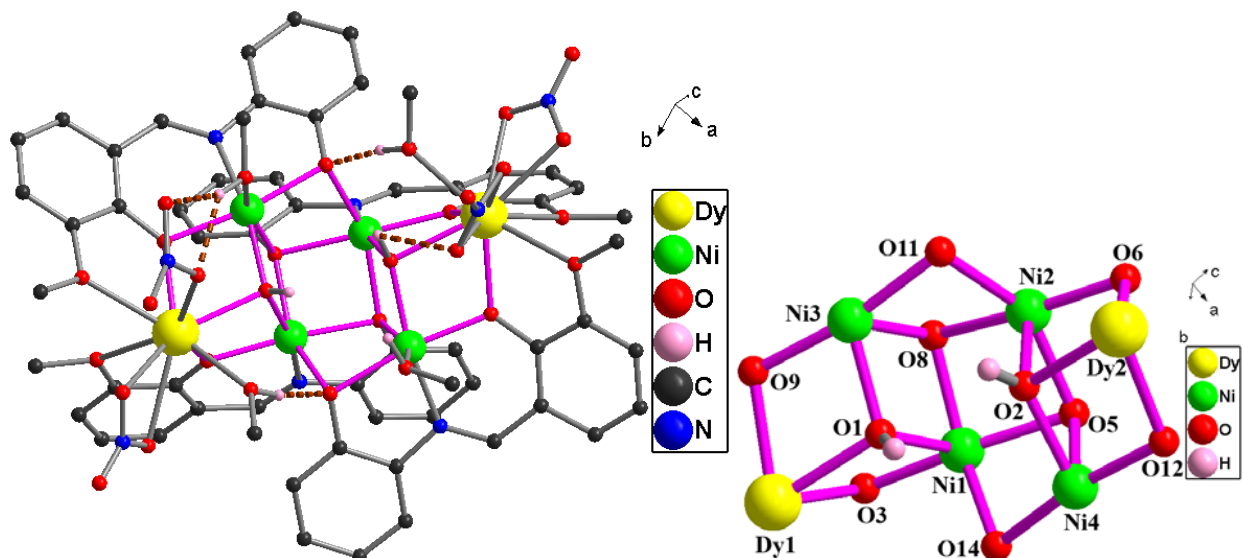


Fig. 3.35. Molecular structure (left) and core (right) of coordination cluster in compound **19**.

All the Ni^{II} ions adopt a distorted octahedral geometry with an O_5N donor set, and the Dy^{III} ions a distorted capped square antiprismatic geometry with an O_9 donor set. The complex **19** contains a butterfly shaped $\{\text{Ni}_4(\mu_3\text{-OH})_2(\text{L}1)_4(\text{MeOH})_2\}$ unit with two Dy^{III} ions at the end of the central Ni^{II}_4 butterfly unit. Each Ni^{II} ion is coordinated by one dianionic ligand ($\eta^1: \eta^2: \eta^1: \eta^3: \mu_4$; Fig. 1.5) into pocket-I (ONO) (Scheme 3.1) in such a manner that two phenoxide O-atoms of the aminophenol part of the ligand act as a μ_3 bridge ($\text{O}1\text{-Ni}1\text{Dy}1\text{Ni}3 = 0.917$ and $\text{O}2\text{-Ni}2\text{Dy}2\text{Ni}4 = 0.913$ Å) in the middle of the Ni^{II}_4 butterfly unit and the other two act as μ bridges between *wing-body* $\text{Ni}^{\text{II}}\text{-Ni}^{\text{II}}$ ions ($\text{Ni}1\text{-Ni}3$ and $\text{Ni}2\text{-Ni}4$). All four dianionic ligands use their pocket-I (Scheme 3.1) for Ni^{II} ions, directing their pocket II (Scheme 3.1) alternatively towards the opposite end of the Ni^{II}_4 butterfly unit. Thus each Dy^{III} ion is coordinated by two alternate-ligands into their pocket-II (OO) at opposite ends of the molecular unit. There are two kinds of bridging modes ($\eta^1: \eta^2: \eta^1: \eta^2: \mu_3$ and $\eta^1: \eta^2: \eta^1: \eta^3: \mu_4$ in Fig. 1.5) displayed by the dianionic ligands. There are two $\mu_3\text{-OH}^-$ groups; coming from each side of Ni^{II}_4 butterfly unit, bridging among *wing-body* $\text{Ni}^{\text{II}}\text{-Ni}^{\text{II}}$ ions ($\text{Ni}1\text{-Ni}3$ or $\text{Ni}2\text{-Ni}4$) and one Dy^{III} ion.

Thus, the overall Ni^{II}₄O₄ butterfly core connects to two Dy^{III} ions by two μ_3 -OH⁻ groups in such a manner that the two phenoxide O-atoms of o-vanillin part of the ligands act as μ -bridges between one Dy^{III} ion and one *wing/body* Ni^{II} ion of the Ni^{II}₄ butterfly core at opposite sides. There are four coordinated MeOH; two are coordinated to two *wing*-Ni^{II} ions (Ni3 and Ni4) of Ni^{II}₄ butterfly units and the rest two to two Dy^{III} ions respectively. There are two chelating nitrates on Dy2 while one chelating and one terminally coordinating nitrates are on Dy1 center. The angle between Ni1Dy1Ni3 and Ni2Dy2Ni4 is 80.85°. The four coordinated MeOH solvent molecules are making H-bonding to neighboring phenolic O-atoms/nitrates. The crystal lattice of **19** contains four MeOH solvent molecules around the cluster. Selected bond lengths and angles are given in the Table 3.8.

Table 3.8. Selected bond lengths (Å) and bond angles (°) within the coordination cluster in **19**.

Dy1—O3	2.293 (3)	Dy1—O16	2.394 (4)	Dy2—O12	2.323 (3)
Dy1—O9	2.295 (3)	Dy1—O4	2.568 (3)	Dy2—O6	2.324 (3)
Dy1—O1	2.348 (3)	Dy1—O10	2.607 (3)	Dy2—O25B	2.35 (2)
Dy1—O18B	2.354 (9)	Dy1—O15	2.701 (4)	Dy2—O24	2.364 (5)
Dy1—O27	2.375 (3)	Dy1—Ni1	3.4717 (6)	Dy2—O28	2.396 (4)
Dy1—O18A	2.391 (8)	Dy1—Ni3	3.4841 (7)	Dy2—O2	2.411 (3)
Dy2—O13	2.550 (4)	Dy2—O21	2.590 (5)	Dy2—O22	2.587 (7)
Dy2—O7	2.631 (4)			Ni3—N3	2.020 (4)
Ni1—O3	2.014 (3)	Ni2—O6	2.018 (3)	Ni3—O1	2.044 (3)
Ni1—N1	2.035 (4)	Ni2—N2	2.033 (4)	Ni3—O9	2.069 (3)
Ni1—O8	2.046 (3)	Ni2—O5	2.055 (3)	Ni3—O29	2.072 (4)
Ni1—O14	2.061 (3)	Ni2—O11	2.068 (3)	Ni3—O8	2.087 (3)
Ni1—O1	2.136 (3)	Ni2—O2	2.102 (3)	Ni3—O11	2.122 (3)
Ni1—O5	2.137 (3)	Ni2—O8	2.181 (3)	Ni4—O5	2.118 (3)
Ni4—N4	2.027 (4)	Ni4—O2	2.059 (3)	Ni4—O14	2.126 (3)
Ni4—O12	2.047 (3)	Ni4—O30	2.094 (4)	Ni1—Ni2	2.9708 (8)
Ni1—Ni3	3.292(3)	Ni1—Ni4	3.106(4)	Ni2—Ni3	3.092(3)
Ni3—O1—Ni1	103.91 (14)	Ni4—O2—Ni2	104.92 (14)	Ni2—Ni4	3.299(6)
Ni3—O1—Dy1	104.77 (13)	Ni4—O2—Dy2	104.31 (13)	Ni1—O3—Dy1	107.25 (13)
Ni1—O1—Dy1	101.37 (12)	Ni2—O2—Dy2	101.73 (13)	Ni1—O14—Ni4	95.76 (12)
Ni3—O9—Dy1	105.84 (13)	Ni1—O8—Ni2	89.24 (11)	Ni2—O11—Ni3	95.11 (12)
Ni2—O6—Dy2	107.47 (14)	Ni3—O8—Ni2	92.82 (12)	Ni1—O8—Ni3	105.57 (14)
Ni2—O5—Ni4	104.53 (13)	Ni4—O5—Ni1	93.80 (12)	Ni2—O5—Ni1	90.25 (11)

3.5.2 Static magnetic properties of the Dy₂Ni₄ half-ring (**19**)

The room temperature χT product of **19** under applied dc magnetic field of 1 kOe is 35.72 cm³ K mol⁻¹ which is close to the theoretically calculated value of 32.34 cm³ K mol⁻¹ for four non-interacting Ni^{II} ions (with $S = 1$, $g = 2.0$) and two Dy^{III} ions (with ${}^6H_{15/2}$, $g = 4/3$, $S = 5/2$). The higher value is probably due to the higher g (≈ 2.20) value of the Ni^{II} ions. The χT product gradually decreases with decreasing temperature from the room temperature value to 30.93 cm³ K mol⁻¹ at 6 K followed by slight increase to 31.30 cm³ K mol⁻¹ at 3.5 K and finally falling to 29.98 cm³ K mol⁻¹ at 1.8 K. The ferrimagnetic like shape of the χT vs T plot (Fig. 3.36, left) results from the combination of the depopulation of Stark sub-levels at higher temperatures, weak ferromagnetic interaction (between Ni^{II}-Dy^{III}) and ZFS of Ni^{II}/Dy^{III} ions at low temperature.

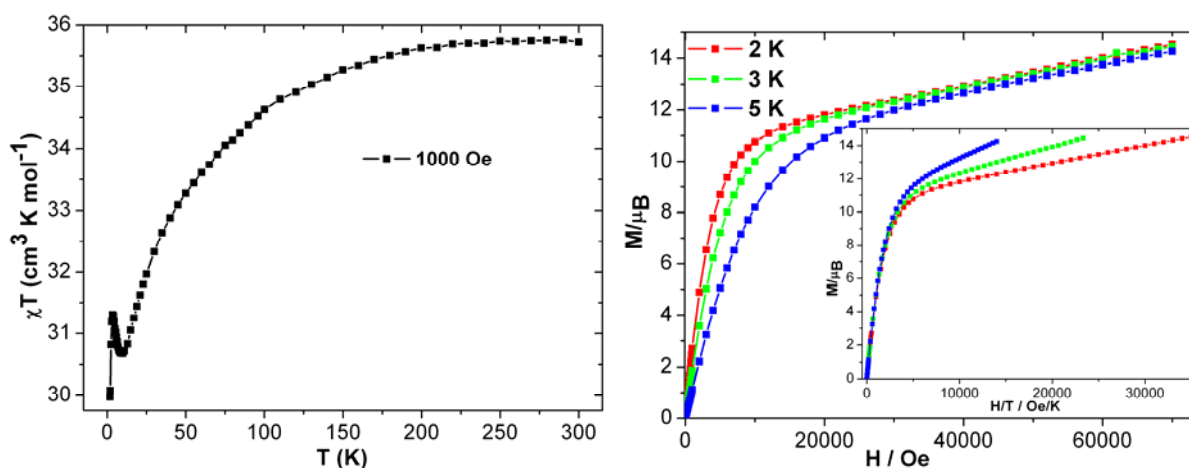


Fig.3.36. Plots of χT vs T (left), M (right) and M vs H/T (right, inset) of **19**.

The field dependent magnetization measurements show that magnetization of **19** increases rapidly below 1 T and increases linearly at higher field without reaching true saturation, indicating the presence of magnetic anisotropy in the system. The maximum magnetization value of **19** is 14.52 μ_B which is lower than the sum for four ferromagnetically coupled Ni^{II} ions ($S = 1$, $g = 2.0$) and two Dy^{III} ions. The low experimental magnetization value of **19** at 2 K is plausibly because of lack of saturation and/or antiferromagnetic coupling between Ni^{II} and Ni^{II} and/or Ni^{II} and Dy^{III}. Moreover, M vs H/T plots at different temperatures do not

superpose (Fig. 3.36, right-inset) on to a single master curve, also indicating the presence of low lying energy state and/or anisotropy in the systems.⁴³

3.5.3 Dynamic magnetic properties of the Dy₂Ni₄ half-ring (19)

The temperature dependent ac susceptibility measurements of complex (19) reveal the presence of strong in-phase (χ') and out-of-phase (χ'') signals (Fig. 3.34) in Dy^{III}₂Ni^{II}₄ (19) below 10 K. The shape of χ' and χ'' vs T plots indicates that there could be two associated relaxation processes.

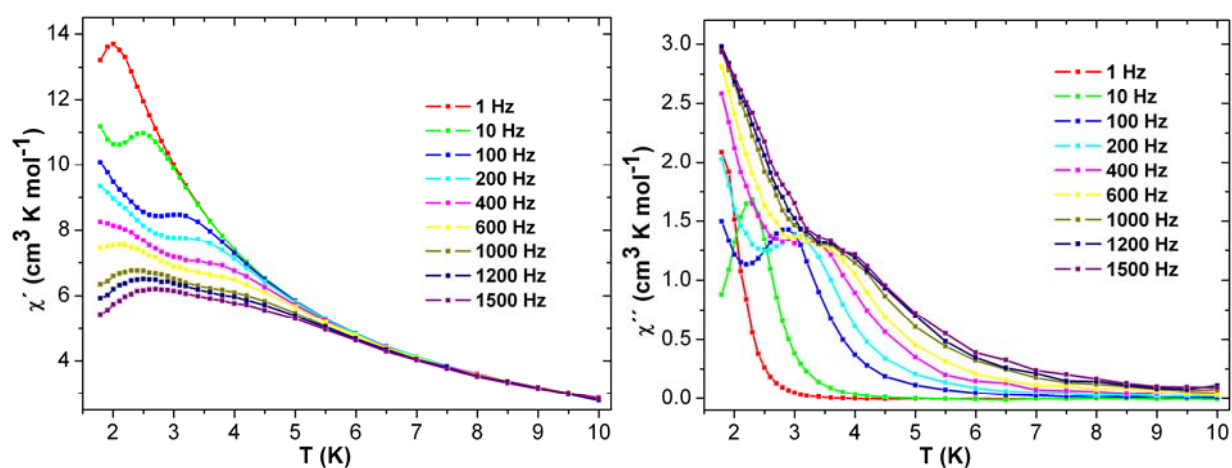


Fig. 3.37. Plots of χ' (left) and χ'' (right) vs T of 19.

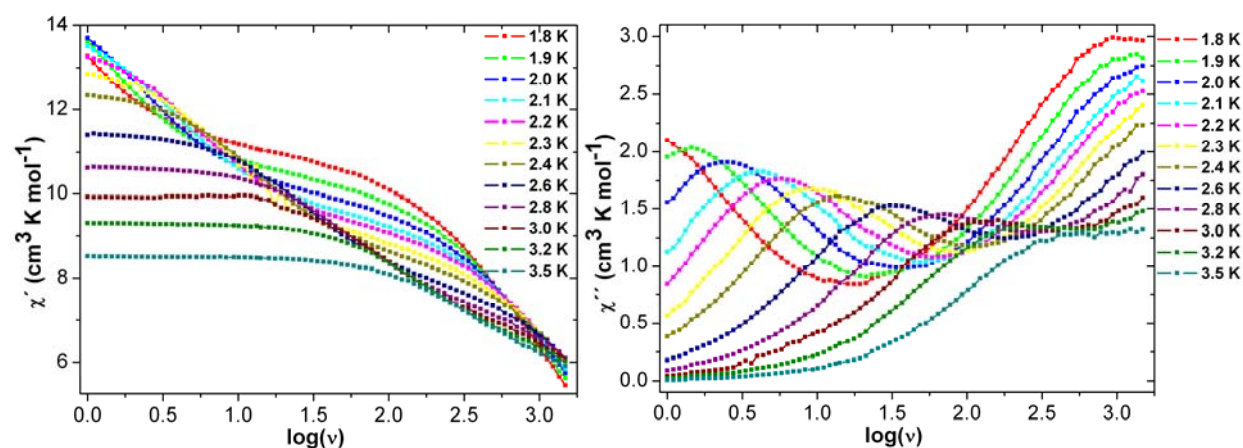


Fig. 3.38. Plots of χ' (left) and χ'' (right) vs frequency of 19 under zero dc field.

The χ' and χ'' vs frequency (Fig. 3.38) measurements were performed under zero applied dc magnetic field in the temperature range of 1.8 to 3.5 K. Both the χ' and χ'' vs frequency plots show two peaks (Fig. 3.38) moving from higher to lower frequency also indicating involvement of two clear relaxation processes. This is supported by the Cole-Cole plots which show the beginning of a second semicircle (Fig. 3.39). The linear fitting to the Arrhenius plots (τ vs $1/T$) of **19** (Fig. 3.40) gave two energy barriers; one 10.6 K (Fig. 3.40, left) and the other 23.6 K (Fig. 3.40, right) under zero applied dc magnetic field with relaxation times $\tau_0 = 4.3 \times 10^{-7}$ s and 5.6×10^{-7} s respectively.

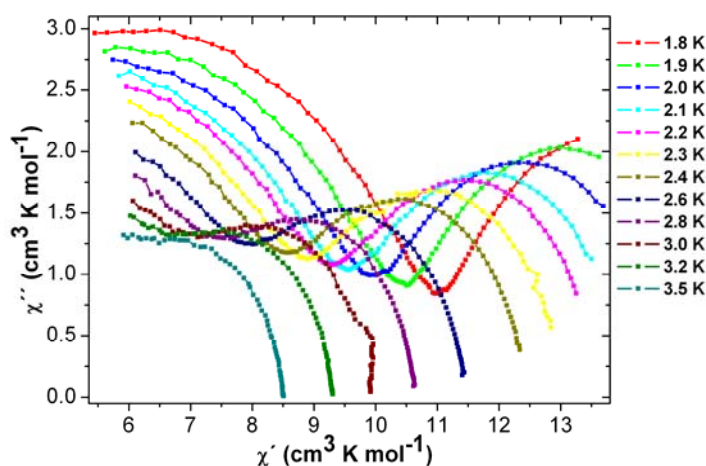


Fig. 3.39. Cole-Cole plots of **19** under zero dc field.

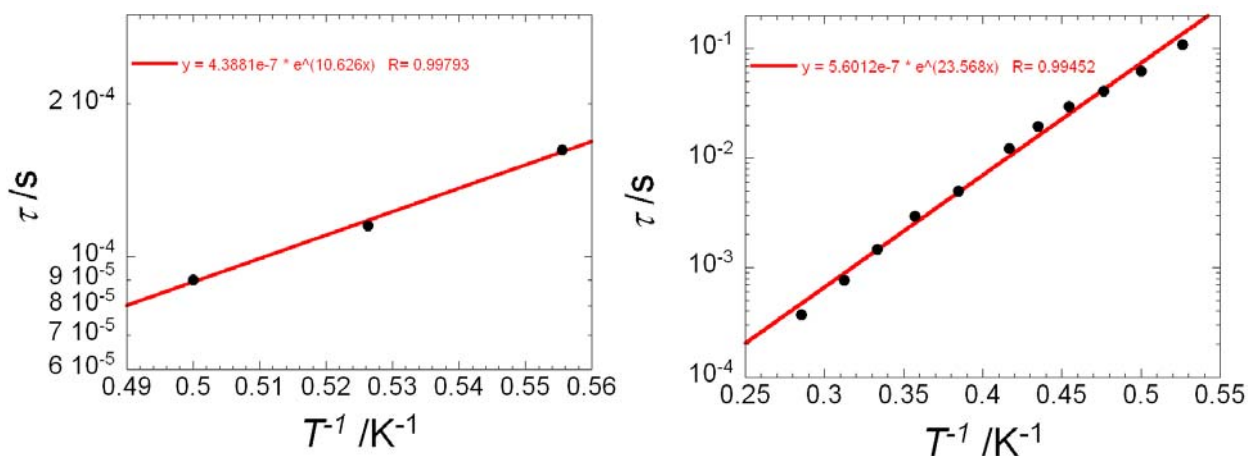


Fig. 3.40. Arrhenius plots of **19** under zero applied dc magnetic field.

3.6.1 Crystal structure of complex

$[\text{Dy}_4\text{Ni}_8(\text{OH})_4(\text{L1})_8(\text{MeOH})_4(\text{H}_2\text{O})_4(\text{C}_2\text{O}_4)_2](\text{NO}_3)_4 \cdot 4\text{H}_2\text{O} \cdot 8\text{MeOH}$ (**20**)

The dodecanuclear heterometallic complex **20** crystallizes in $C2/m$ space group with $2/m$ symmetry. The asymmetric crystallographic unit contains one Dy^{III} ion, two Ni^{II} ions, one OH^- group, two doubly deprotonated dianionic ligands (L1^{2-}), half of a dianionic oxalate ($\text{C}_2\text{O}_4^{2-}$), one fourth of a mono anionic nitrate (NO_3^-), one coordinated H_2O and one MeOH molecule.

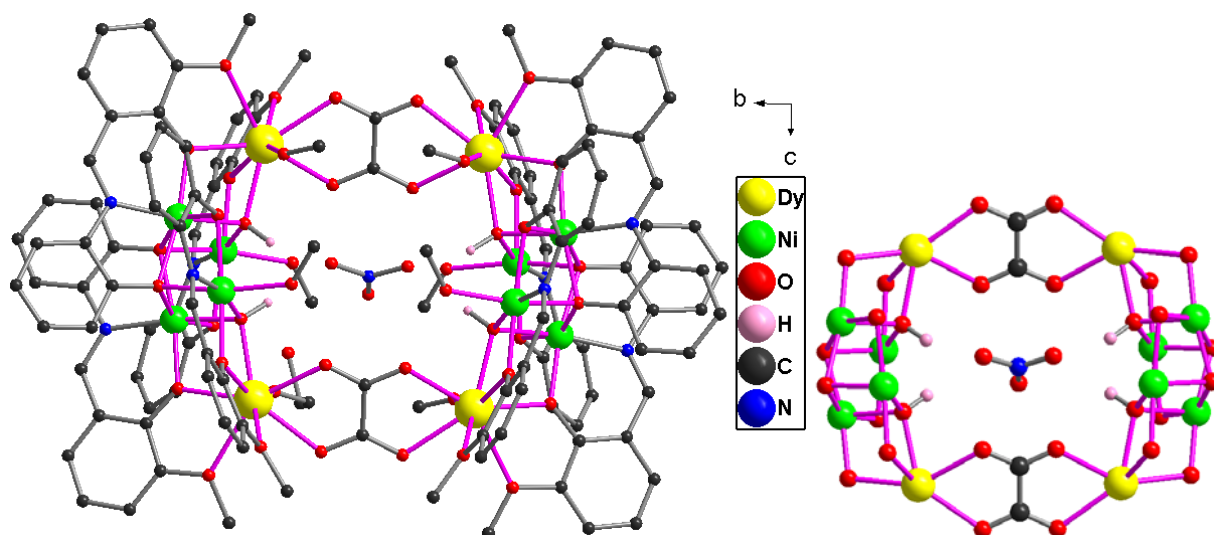


Fig. 3.41. Molecular structure (left) and core (right) of coordination cluster in compound **20**.

The complex $[\text{Dy}_4\text{Ni}_8(\text{OH})_4(\text{L1})_8(\text{MeOH})_8(\text{C}_2\text{O}_4)_2]^{4+}$ (**20**) can be divided into two units ($\{\text{Dy}_2\text{Ni}_4(\mu_3\text{-OH})_2(\text{C}_2\text{O}_4)(\text{L1})_4(\text{MeOH})_4\}^{2+}$) similar to those found in **19** (Fig. 3.41), where nitrates are replaced by oxalates. All the Ni^{II} adopt a distorted octahedral geometry with an O_5N donor set while the Dy^{III} ions adopt a square antiprismatic geometry with an O_8 donor set. These two $\{\text{Dy}_2\text{Ni}_4(\mu_3\text{-OH})_2(\text{L1})_4\}^{4+}$ units are connected into a ring like $\{\text{Dy}_4\text{Ni}_8(\mu_3\text{-OH})_4(\text{L1})_8(\text{C}_2\text{O}_4)_2(\text{MeOH})_8\}^{4+}$ unit (**20**) through two dianionic oxalate ligands. There are eight coordinated MeOH molecules of which four are coordinated to four *wing*- Ni^{II} ions of each butterfly unit and four to Dy^{III} ions. Those four $\mu_3\text{-OH}^-$ groups, four H_2O and four MeOH solvent molecules are so oriented that they all together create a hydrophilic hole within the ring like dodecanuclear complex **20** which is big enough to trap one nitrate anion (NO_3^-) stabilized by H-bonding. For the charge balance there are three more disordered nitrate anions outside the ring. Selected bond lengths and angles are given in Table 3.9. O1 lies 0.921 Å out of the

corresponding Ni1Dy1Ni2 plane and the dihedral angle between the two Ni1Dy1Ni2 planes are is 82.97°.

Table 3.9. Selected bond lengths (Å) and bond angles (°) within the coordination cluster in **20**.

Dy1—O5	2.290 (4)	Dy1—O3	2.479 (3)	Dy1—O31	2.392 (3)
Dy1—O2	2.297 (3)	Dy1—O6	2.515 (4)	Dy1—O8	2.345 (4)
Dy1—O1	2.308 (3)	Dy1—O32	2.335 (3)	Ni1—O2	2.015 (3)
Ni1—O4	2.142 (3)	Ni1—O4 ¹	2.054 (3)	Ni1—O7 ¹	2.065 (3)
Ni1—O1	2.129 (3)	Ni1—N1	2.031 (4)	Ni2—N2	2.008 (4)
Ni2—O5	2.053 (3)	Ni2—O9	2.076 (4)	Ni2—O7	2.111 (3)
Ni2—O1	2.073 (3)	Ni2—O4 ¹	2.090 (3)	O7—Ni1 ¹	2.065 (3)
Dy1—Ni1	3.4672 (6)	Ni1—Ni1 ¹	2.9841 (12)	Dy1—Ni2	3.4508 (7)
Ni1—O1—Dy1	102.72 (13)	Ni1 ¹ —O4—Ni2 ¹	105.08 (14)	Ni1 ¹ —O4—Ni1	90.64 (12)
Ni1—O2—Dy1	106.86 (13)	Ni2—O5—Dy1	105.10 (14)	Ni2 ¹ —O4—Ni1	92.40 (12)
Ni1 ¹ —O7—Ni2	94.05 (14)	Ni2—O1—Ni1	103.07 (14)	Ni2—O1—Dy1	103.81 (13)

Symmetry codes: (i) $-x+1, y, -z+1$.

3.6.2 Static magnetic properties of **20**.

The room temperature χT product of **20** is 65.30 cm³ K mol⁻¹ which is slightly larger than the theoretically calculated value of 64.68 cm³ K mol⁻¹ for eight non-interacting Ni^{II} ions (with $S = 1$, $g = 2.0$) and four Dy^{III} ions (with ${}^6H_{15/2}$, $g = 4/3$, $S = 5/2$). The χT product gradually decreases on decreasing the temperature from room temperature to 100 K (63.44 cm³ K mol⁻¹) below which it more rapidly decreases till 1.8 K (47.45 cm³ K mol⁻¹).

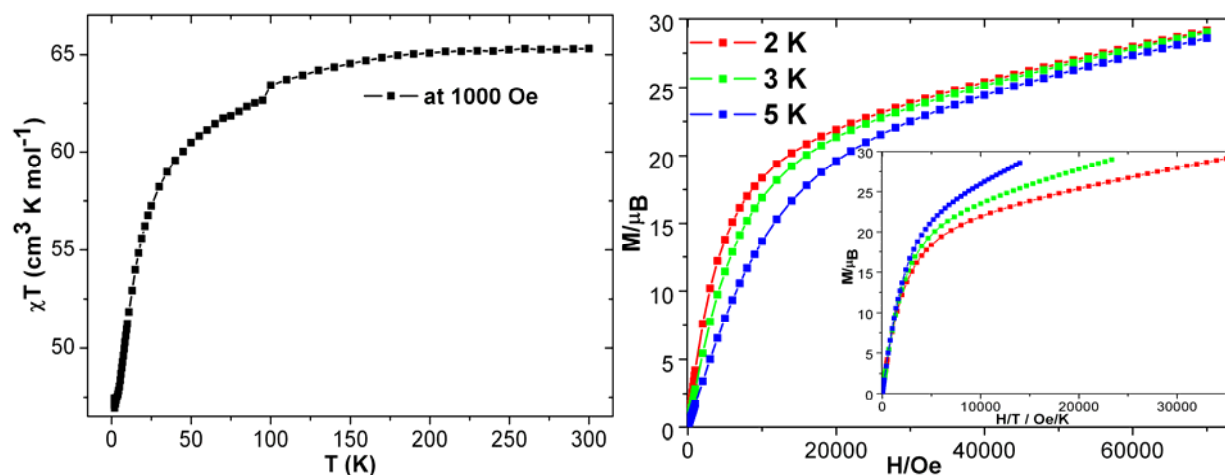


Fig.3.42. Plots of χT vs T (left), M (right) and M vs H/T (right, inset) of **20**.

The shape of the χT vs T plot (Fig. 3.42, left) results from the combination of the depopulations of Stark sub-levels at higher temperatures, weak intramolecular antiferromagnetic interactions and ZFS of $\text{Ni}^{\text{II}}/\text{Dy}^{\text{III}}$ ions at low temperature. The shape of χT vs T plot of **20** suggests antiferromagnetic interactions between the two Dy_2Ni_4 units of **20** through oxalate bridges ($\text{C}_2\text{O}_4^{2-}$) and/or $\mu_3\text{-OH}\cdots\text{NO}_3^-$ supramolecular pathways. The field dependent magnetization measurements show that M increases rapidly below 1 T and increases linearly at higher field without reaching true saturation indicating the presence of magnetic anisotropy in the system. The rate of increase of M is less than that of **19**. The maximum magnetization (M_S) value of **20** is $29.15 \mu_B$ which is all most double the M_S value of **19** but lower than the sum for all ferromagnetically coupled Ni^{II} ions ($S = 1$, $g = 2.0$) and Dy^{III} ions ($5.58 \mu_B$) ions ($16 + 22.32 = 38.32 \mu_B$) as for **19**. Moreover, M vs H/T plots at different temperatures do not superpose (Fig. 3.42, right-inset) on a single master curve, also indicating the presence of low lying energy states and/or anisotropy in the systems.⁴³

3.6.3 Dynamic magnetic properties of **20**.

The temperature dependent ac susceptibility measurements on complexes **20** reveal the presence of detectable in-phase (χ') and out-of-phase (χ'') signals (Fig. 3.43) below 6 K without a maximum in χ' and χ'' vs T plots. This kind of slow relaxation indicates that **20** may be a SMM with a blocking temperature below 1.8 K.

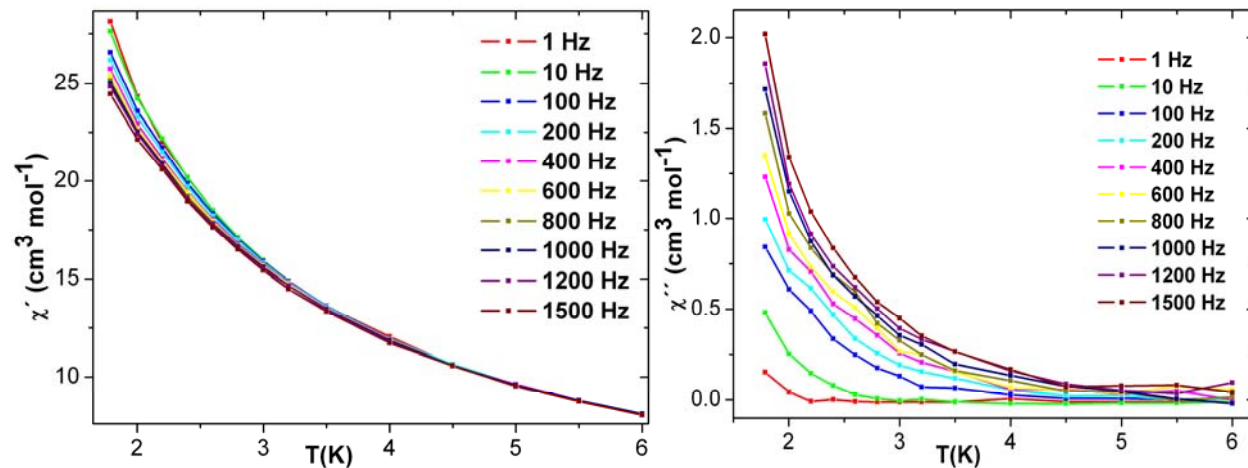


Fig. 3.43. Plots of χ' (left) and χ'' (right) vs T of **20**.

A structural comparison of **19** and **20** (based on their bond parameters; Table 3.8 and 3.9) illustrates the differences in their magnetic properties. For both the complexes **19** and **20**, there is a decrease of χT at low temperature (Fig. 3.36 and 3.42, left) but this is more pronounced in **20** than that in **19**. The relaxation dynamics of **20** have dramatically changed and the ac signals have been partially suppressed upon linking the two Dy₂Ni₄ units through oxalate (C₂O₄²⁻) bridges. The average μ_3 -HO-Ni₂Dy/RO-Ni₃ distances are 0.915/1.068 (**19**) and 0.921/1.151 Å (**20**) above/below the two Ni₂Dy-Ni₂Dy/Ni₃-Ni₃ triangular planes which change from 80.85/120.56 (**19**) to 82.97°/125.21° (**20**). The coordination geometries of both the Dy^{III} ions changed from a nine coordinated capped square antiprism in **19** to an eight coordinated distorted square antiprism in **20**. Additionally, there are some supramolecular pathways through μ_3 -OH \cdots NO₃⁻ bridges between two Ni^{II}₄ units in **20** (Fig. 3.41, right). The dipolar interactions between the two Ni^{II}₄ units through these supramolecular pathways (μ_3 -OH \cdots NO₃⁻) are likely to be weakly antiferromagnetic and/or the magnetic interaction between two Dy^{III} ions may be weakly antiferromagnetic. But a weak ferromagnetic interaction has been reported in a single oxalate bridged Dy^{III}₂ dimer.^{37c} However, magnetic interaction between two Dy^{III} ions may also depend upon their anisotropy.^{37b}

3.7 Discussion

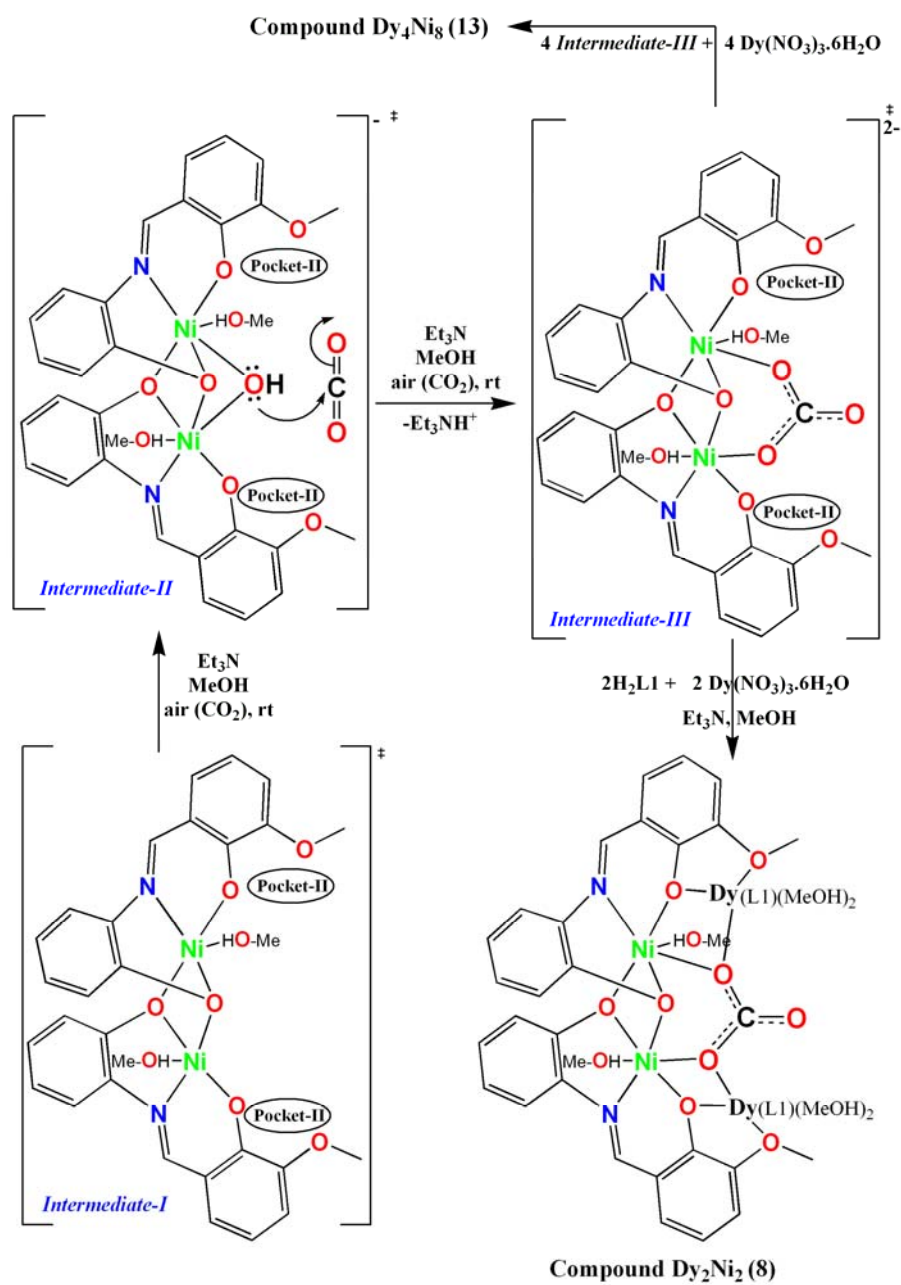
The reaction of Dy(NO₃)₃·6H₂O, Ni(NO₃)₂·6H₂O and H₂L1 in 10 mL of DMF in the presence of base (Et₃N) in the molar ratio of 1:1:2:5 with heating led to the formation of red-brown block-shaped crystals of Dy₂Ni₂ (**1**) with a defect-dicubane topology after two weeks. For charge balance it contains two nitrates (NO₃⁻) coordinated to two Dy^{III} ions. The similar reaction in the same molar ratio carried out in MeOH gave green-yellow color plate-shaped crystals of Dy₂Ni₂ (**2**) with similar topology after 12 hours, with two coordinated MeOH (**2**) instead of two DMF (**1**). If the stirring time of the reaction, which produces **2** is reduced to 1-2 min instead of 5-10 min, the color of the solution slowly turns from green to brown on standing for a week in air. The red-brown prism-shaped crystals of Dy₂Ni₂ (**8**) slowly form upon slow evaporation from air. The crystal structure reveals that there is a η^2 : η^2 : μ_4 carbonate (CO₃²⁻) rather than two nitrates (NO₃⁻) in the structure of the distorted non-planar Dy₂Ni₂ (**8**). If the reaction is carried out in inert atmosphere (N₂), it does not change its color (i.e. remains green) and exclusively produces the defect-dicubane Dy₂Ni₂ (**2**). The incorporation of carbonate (CO₃²⁻) into the structure has

changed the topology of the core with opening of the defect-dicubane Dy₂Ni₂ into a distorted non-planar U-shaped Dy₂Ni₂ core.

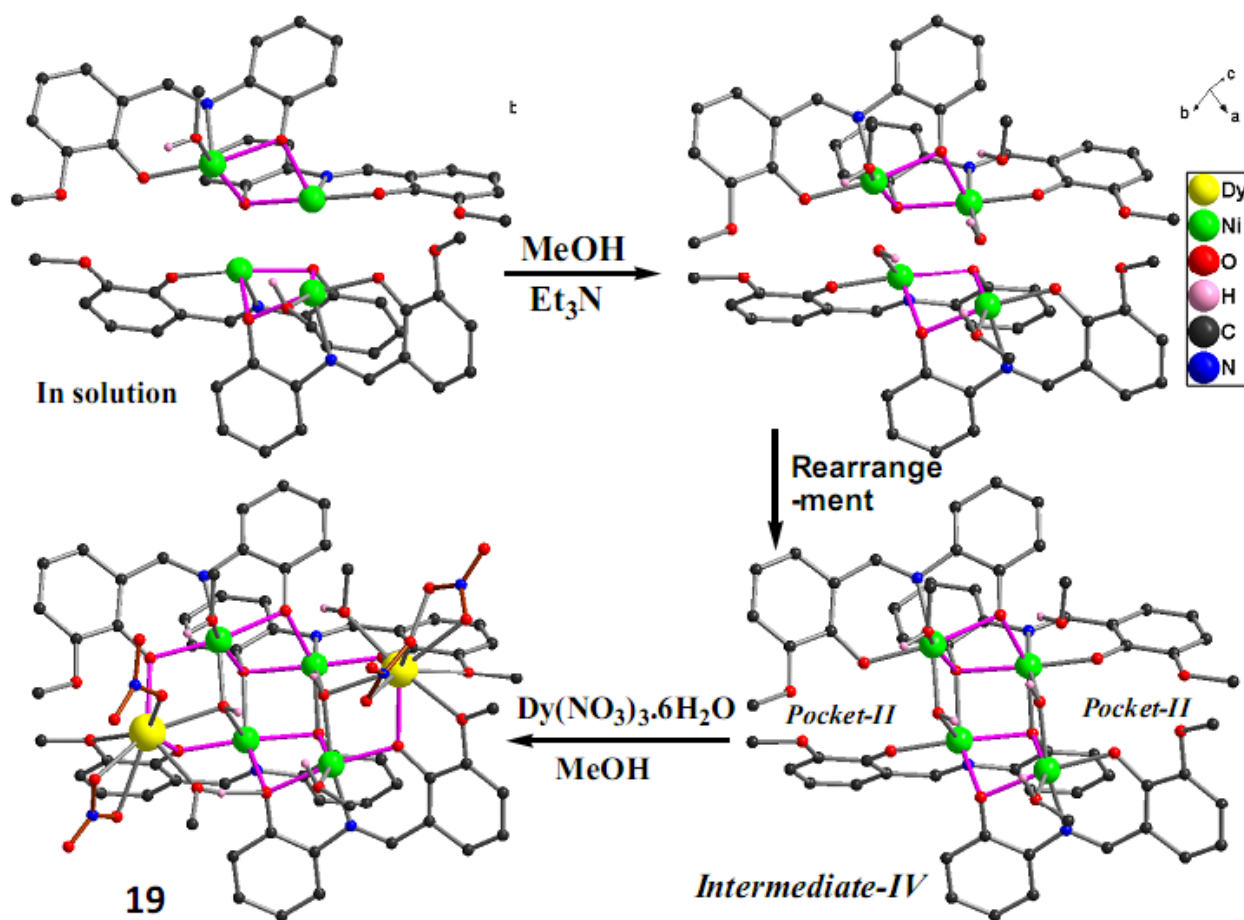
When a similar reaction is carried out with double amount of Ni^{II} ions leads to the formation of the non-planar ring like Dy₄Ni₈ (**13**) with four $\eta^2:\eta^1:\eta^2:\mu_5$ bridging carbonates (CO₃²⁻) and four non-coordinated nitrates (NO₃⁻). The same product is also obtained from the reaction in which the ratio of Dy^{III}:Ni^{II} remains 1:1, but amounts of ligand and base are slowly decreased. This observation implies that growth of nuclearity has been prevented by the terminal ligands in Dy₂Ni₂ (**8**), while the growth of nuclearity has been extended to Dy₄Ni₈ (**13**) when the number of ligands is smaller. The mechanism of formation of **8** and **13** has been illustrated in Scheme 3.2. Such CO₂ fixation also has been previously reported. The μ -OH⁻ bridged {M^{II}₂(μ -OH)} active species has been suggested.^{53a} A similar kind of intermediate species (*intermediate-II*) is plausibly involved (in our reaction conditions) in the basic solution which can react slowly with dissolve CO₂ gas to form dianionic *intermediate-III* which later on binds to two Dy^{III} ions from solution with coordination of two dianionic ligands (L¹²⁻) to produce **8**. If the amount of ligand in the solution is reduced relative to the Dy^{III} ions (*intermediate-III*:Dy^{III} = 1:1), **13** is formed.

The reaction with the same molar ratio which produces Dy₄Ni₈ (**13**), was carried out in inert atmosphere (N₂) and produces Dy₂Ni₄ (**19**) with four coordinated nitrate anions (NO₃⁻) rather than producing Dy₄Ni₈ (**13**). Since the semi-circular shaped **19** contains two NO₃⁻ ligands towards same direction, they (NO₃⁻) could be substituted by two oxalates (C₂O₄²⁻) to synthesize ring like Dy₄Ni₈ (**20**). Two common Dy₂Ni₄ units of **19** are bridged to form Dy₄Ni₈ unit in **20**.

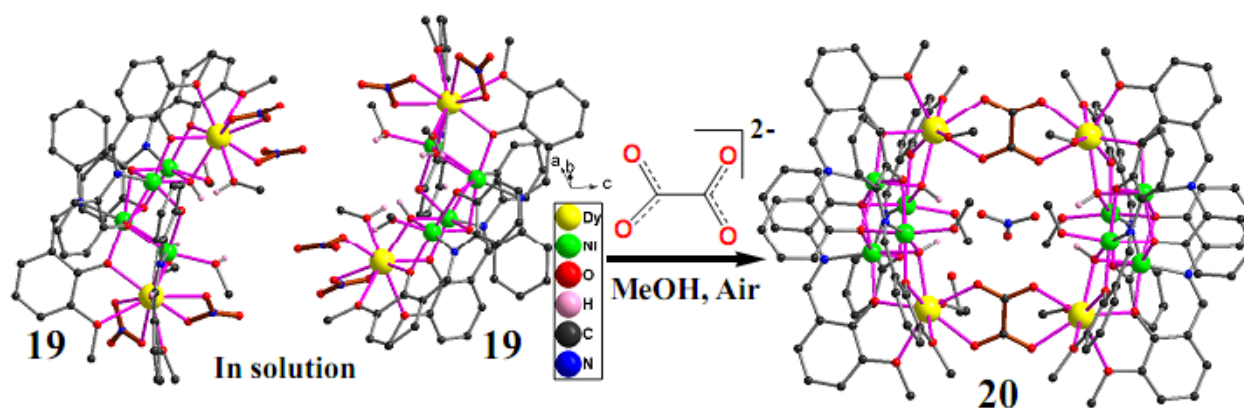
The implication of involvement of *intermediate-II* as an active species was confirmed when the reaction is carried out in inert atmosphere (N₂). Two strained *intermediate-II* can dimerize to construct (*intermediate-IV*) (Scheme 3.3) the core of Ni^{II}₄ of **19** with minor rearrangement. Indeed, OH⁻ is found to bridge in μ -fashion between two Ni^{II} and can then ligate Dy^{III} ions resulting in a μ_3 -bridging mode (DyNi₂). Additionally, in the presence of oxalate (C₂O₄²⁻), it produces **20** (Scheme 3.4) before it can react with CO₂ (Scheme 3.2).



Scheme 3.2. The proposed mechanism of formation **8** and **13**.



Scheme 3.3. The proposed mechanism of formation of **19**. The *intermediate-IV* (bottom, right) is active species for the formation of **19**.



Scheme 3.4. The proposed mechanism (substitution of 4NO₃⁻ by 2C₂O₄²⁻) of conversion of **19** into **20**.

3.8 Conclusion:

The syntheses, crystal structures and magnetic properties of six new series of different nuclearity Ni^{II}-Ln^{III} complexes (**1-20**) have been presented in this chapter. The brief synthetic strategies were given in discussion part, Table 3.1 and Scheme 3.2-3.4. The magnetic cores of the most of the complexes are unprecedented.

In all the complexes (**1-20**), ferromagnetic interactions are observed between Ni^{II} and/or Ni^{II}-Ln^{III} ions. Dynamic measurements show that the Ni^{II}-Dy^{III} compounds exhibit slow relaxation behavior, as do some of the Ni^{II}-Tb^{III} analogues. The ac properties are summarized in Table 3.10.

Table 3.10. The ac data of Dy^{III}-Ni^{II} compounds (**1**, **2**, **8**, **13**, **19** and **20**).

Compound	Dy ₂ Ni ₂ (1)	Dy ₂ Ni ₂ (2)	Dy ₂ Ni ₂ (8)	Dy ₄ Ni ₈ (13)	Dy ₂ Ni ₄ (19)	Dy ₄ Ni ₈ (20)
QTM	observed	observed	observed	observed	Not observed	Not observed
No. of processes	one	one	one	one	two	-
T _b (K)	3.2	4.2	0.04	0.8	4.0	< 1.8
Δ (K)	18.54	21.33	7.14	8.97	10.62 and 23.56	-
τ ₀ (s)	5.4×10 ⁻⁷	1.5×10 ⁻⁶	4.5×10 ⁻⁷	1.4×10 ⁻⁶	4.3×10 ⁻⁷ and 5.6×10 ⁻⁷	-

Chapter 4

Other 3d-Ln and 4d-Ln Coordination Clusters with (E)-2-(2-hydroxy-3-methoxy-benzylideneamino)phenol (H₂L1)

4.1 Introduction

Ni-Ln coordination clusters were described in the previous chapter. The Ni^{II} ion (3d⁸) frequently adopts either square planar or octahedral geometry. Ionic radius decreases with increasing atomic number, although for the transition metals the coordination geometry and electronic configuration of the ion must be taken into account. On the other hand, the M^{II} ions to the left and right of Ni^{II} show more flexibility in their coordination geometries. The M^{II} ions from Co to Zn can be conveniently considered as late 3d transition metal ions and illustrate interesting trends pertinent to their position in the periodic table. All four have relatively plastic coordination spheres with 4, 5 and 6 coordination number geometries being known, in some cases with distortions from ideality as a result of balancing ligand field and electrostatic effects. For example, considering the 6-coordinate case several factors can be taken into account, firstly, for Co^{II} both high and low spin configurations are possible and both can be subject to Jahn-Teller distortion. On the other hand, for Ni^{II}, the d⁸ configuration often leads to square planar coordination geometries as a result of ligand field effects stabilizing 16 electron complexes. For octahedral ligand fields this configuration should represent the maximum in stability for high spin complexes. However, as a result of J-T distortion in 6 coordinate Cu^{II} complexes, the maximum is actually found for this d⁹ configuration (Irving-Williams series). In addition, partly as a result of the electron configurations and partly from the significantly smaller ionic radii at this end of the first row of the d-block elements, many examples of 5 coordinate complexes are known with geometries often intermediate between trigonal bipyramidal and square-based pyramidal (the degree of distortion can be quantified via Addison and Reedijk's τ parameter).

These factors can exert tremendous influence on the nuclearity of the final product even when identical reaction conditions are used. Although Zn^{II} ions are diamagnetic, Ln^{III}-Zn^{II} compounds can be interesting because of the luminescence of this ion as was found in this work. Similarly, although, Cu^{II} ions are magnetically isotropic quantum spins they can mediate strong and often ferromagnetic coupling with Ln^{III} ions.⁴³ Here the Dy/Tb-Cu systems were found to have fascinating SMM properties. The Co^{II}-based clusters prove to be magnetically fascinating

as a result of the first order orbital angular momentum and very large Ising type single ion magnetic anisotropy.

As has already been shown in the previous chapter, most of the Ln^{III} ions, and in particular Dy and Tb have favorable magnetic anisotropy as a result of their unquenched angular orbital momentum of the Ising type. For these reasons, research within the group in Karlsruhe has aimed at looking how these contributions from d and trivalent f transition metal ions can be combined within one d-f based coordination cluster to enhance or tune the magnetic properties of SMMs. In particular, in the work presented here, it seemed a useful systematic approach to study how the combination of the late M^{II} transition metal ions with trivalent 4f ions might be used to target and understand molecules showing SMM behavior. Hence, keeping to the molecular composition found for the Ln^{II}₂Ni^{II}₂ complexes (**2**) described in chapter 3, the d metal ions Zn^{II}, Cd^{II}, Cu^{II} and Co^{II} were used in place of Ni^{II}.

4.2 Synthetic strategy

The ligand (H₂L1) has been designed to have two pockets-I(ONO) and -II(OO) (Fig. 1.4). It is well-known that the ratio, metal salt, temperature, atmosphere, solvent, the time of reaction, etc. can all affect the nature of the final product. Since the M^{II} (Zn^{II}, Cd^{II}, Cu^{II} and Co^{II}) ions can adopt different coordination, d-metal ions are varied keeping similar reaction condition. Thus, several reactions have been performed, leading to different products given in Table 4.T1. The reaction of LnCl₃·xH₂O, anhydrous ZnCl₂ salts and H₂L1 in the presence of base (Et₃N) in the molar ratio of 1:1:2:5 in MeOH produces crystals of a series of yellow fluorescent compounds [Ln₂Zn₃(OH)(L1)₅(MeOH)_{2.5}(OH₂)_{1.5}]Cl₃·3(MeOH)·2.5(H₂O); [Ln = Dy(**21**), Eu(**22**), Gd(**23**), Tb(**24**) and Ho(**25**)] from slow evaporation in air. If the reaction solution is kept in closed-vial and left undisturbed for two more weeks, it produces needle shape brown crystals of [Dy₇Zn₄(OH)₄(L1)₈(Cl)₆(H₂O)₄]Cl₃·35H₂O (**26**). When the similar reaction is carried out using CdCl₂·H₂O instead of ZnCl₂, a series of rod-shaped crystals of [Ln₆Cd₆(CO₃)₂(OH)₄(μ-Cl)₂(Cl)₂(L1)₈(H₂O)₁₂]Cl₂·10THF [Ln = Dy(**27**), Tb(**28**), Ho(**29**) and Er(**30**)] complexes are obtained.

When similar reactions are performed using Ln(NO₃)₃·xH₂O, Cu(NO₃)₂·2.5H₂O salts and H₂L1 in the presence of base (Et₃N) in the molar ratio of 1:1:2:5 in MeOH, the series [Ln₃Cu₂(μ₃-OH)₂(L1)₅(NO₃)(MeOH)₂(H₂O)]·3MeOH·xH₂O [Ln = Dy(**31**), Gd(**32**), Tb(**33**), and Ho(**34**), x = 0 for **31**, **32**, **34** and x = 1 for **33**] was obtained.

The use of $\text{Co}(\text{NO}_3)_2 \cdot 6\text{H}_2\text{O}$ instead of $\text{Cu}(\text{NO}_3)_2 \cdot 2.5\text{H}_2\text{O}$ led to the formation $[\text{Ln}_2\text{Co}_2(\text{L}1)_4(\text{NO}_3)_2(\text{THF})_2] \cdot 4\text{THF}$ [$\text{Ln} = \text{Dy}$ (**35**), Y (**36**), Gd (**37**), Tb (**38**), Ho (**39**) and Er (**40**)] from a MeOH/THF solution. The synthetic strategies of preparation of M-Dy ($\text{M} = \text{Zn}^{\text{II}}$, Cd^{II} , Cu^{II} and Co^{II}) have been summarized in Table 4.1.

Table 4.1. Synthetic strategies of preparing $\text{Dy}^{\text{III}}\text{-M}^{\text{II}}$ complexes (**21**, **26**, **27**, **31** and **36**).

Ratio ^a	A	B	Time of stir (min.)/ Crystallization(days)	Compound
A:B:C:D = 1:1:2:5	$\text{DyCl}_3 \cdot 6\text{H}_2\text{O}$	ZnCl_2	10-15/7	Dy_2Zn_3 (21)
A:B:C:D = 1:1:2:5	$\text{DyCl}_3 \cdot 6\text{H}_2\text{O}$	ZnCl_2	10-15/21	Dy_7Zn_4 (26)
A:B:C:D = 1:1:2:5	$\text{DyCl}_3 \cdot 6\text{H}_2\text{O}$	$\text{CdCl}_2 \cdot \text{H}_2\text{O}$	10/7	Dy_6Cd_6 (27)
A:B:C:D = 1:1:2:5	$\text{Dy}(\text{NO}_3)_3 \cdot 6\text{H}_2\text{O}$	$\text{Cu}(\text{NO}_3)_2 \cdot 2.5\text{H}_2\text{O}$	5/3	Dy_3Cu_2 (31)
A:B:C:D = 1:1:2:5	$\text{Dy}(\text{NO}_3)_3 \cdot 6\text{H}_2\text{O}$	$\text{Co}(\text{NO}_3)_2 \cdot 6\text{H}_2\text{O}$	1/2	Dy_2Co_2 (35)

(a) A = Dy^{III} salt, B = M^{II} salt, C = $\text{H}_2\text{L}1$, D = Et_3N and, Solvent = MeOH (20 mL) or THF (**35**).

In this chapter the syntheses, crystal structures and magnetic and/or optical properties of those novel complexes (**21-40**) are presented.

4.2.1 Crystal structure of complexes

$[\text{Ln}_2\text{Zn}_3(\text{OH})(\text{L}1)_5(\text{MeOH})_{2.5}(\text{H}_2\text{O})_{1.5}]\text{Cl} \cdot 3\text{MeOH} \cdot 2.5\text{H}_2\text{O}$; [$\text{Ln} = \text{Dy}$ (**21**), Eu (**22**), Gd (**23**), Tb (**24**) and Ho (**25**)]

The pentanuclear heterometallic compound **21** crystallizes in space group $P2_1/c$. All the complexes **21-25** are isomorphous, confirmed by the unit cell constants and X-ray powder diffraction (**21-25**). The asymmetric crystallographic unit of compound **21** consists of two Dy^{III} ions, three Zn^{II} ions, one OH^- group, one chloride (Cl^-), five doubly deprotonated ligands ($\text{L}1$)²⁻ and disordered coordinated solvent molecules (2.5 MeOH and 1.5 H_2O).

All three Zn^{II} ions ($\text{Zn}1$, $\text{Zn}2$ and $\text{Zn}3$) adopt a distorted square pyramidal geometry with an O_4N donor set. One Dy^{III} ion ($\text{Dy}1$) has adopted a nine coordinated distorted capped square anti-prism ($\text{N}9$ capping $\text{O}8\text{O}17\text{O}10\text{O}19$ square) geometry with an O_8N donor set and other the one ($\text{Dy}2$) adopts a distorted square antiprismatic geometry with an O_7N donor set. The structure can be illustrated as a combination of one tetranuclear heterometallic butterfly $\{\text{Dy}^{\text{III}}_2\text{Zn}^{\text{II}}_2(\mu_3\text{-OH})(\text{L}1)_4(\text{MeOH})_2(\text{H}_2\text{O})\}$ unit and a mono nuclear $\{\text{Zn}^{\text{II}}(\text{L}1)(\text{H}_2\text{O})_{0.5}(\text{MeOH})_{0.5}\}$ fragment. The $\{\text{Dy}^{\text{III}}_2\text{Zn}^{\text{II}}_2(\mu_3\text{-OH})(\text{L}1)_4(\text{MeOH})_2(\text{H}_2\text{O})\}$ unit can be described as one Dy^{III}_2 unit ($\text{Dy}1$ and $\text{Dy}2$)

and one Zn^{II} unit (Zn1 and Zn2) so connected into a butterfly core fragment that each type of metal ions occupy one *wing* and one *body* position of the butterfly.

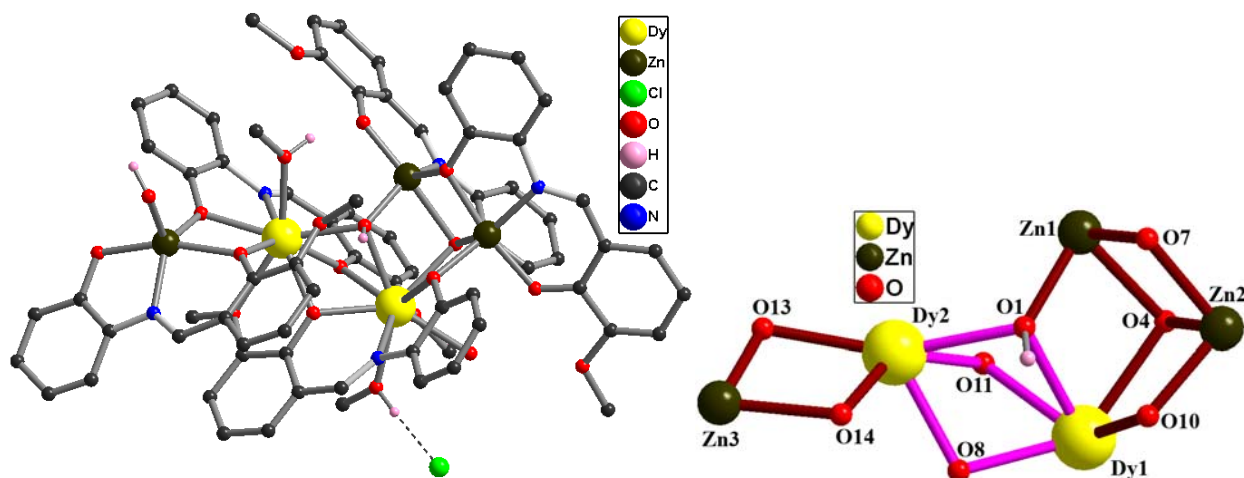


Fig. 4.1. Molecular structure (left) and core (right) of coordination cluster in compound **21**.

There are one $\mu_3\text{-OH}^-$ group to one side and one phenoxide $\mu_3\text{-O}$ -atom from iminophenol part of the ligand (L1) to the other side of the hetero-metallic *body-body* ($\text{Dy}^{\text{III}}\text{Zn}^{\text{II}}$) part of metal core. The $\mu_3\text{-OH}^-$ group bridges two Dy^{III} ions and one Zn^{II} ion 0.710 Å below the Zn1Dy1Dy2 plane. The phenoxide $\mu_3\text{-O}$ -atom of aminophenol part of iminophenol ligand bridges among two Zn^{II} ions and one Dy^{III} ion in triangular fashion from 1.166 Å above the Zn1Zn2Dy1 plane. The angle between Zn1Dy1Dy2 and Zn1Zn2Dy1 planes is 33.26°. These two distorted square pyramidal Zn^{II} ions are ligated into the pocket-I (ONO) of the ligand while each Dy^{III} ion is ligated by one pocket-I (ONO) and -II (OO). Finally the third Zn^{II} ion (Zn3) sits in pocket-I (ONO) of a ligand to form a $\{\text{Zn}^{\text{II}}(\text{L})(\text{H}_2\text{O})_{0.5}(\text{MeOH})_{0.5}\}$ fragment. The dianionic ligands (L1)²⁻ adopt $\eta^1:\eta^1:\eta^2:\mu_3$, $\eta^1:\eta^1:\eta^1:\mu_2$, $\eta^2:\eta^1:\eta^1:\mu_2$, $\eta^1:\eta^2:\eta^1:\eta^1:\mu_2$ and $\eta^1:\eta^2:\eta^1:\eta^2:\mu_3$ (Fig. 1.5) bridging modes. One MeOH and one H₂O coordinate to Dy1 and one coordinated MeOH on Dy2 making hydrogen-bonds with two O-atoms of pocket-II as does the H₂O molecule on the Dy1. The crystal lattice of **21** contains one chloride anion (Cl⁻) for charge balance which is H-bonded to two lattice MeOH solvent molecules and coordinated MeOH/H₂O on Dy1. The Dy1–O/N and Dy2–O/N distances vary from 2.291(7) to 2.651(7) Å and 2.320(7) to 2.498(9) Å respectively. The Dy1–Dy2, Dy1–Zn2, Dy2–Zn3 and Zn1–Zn2 distances are 3.6240(7), 3.4516(13), 3.4815(14) and 3.1453(19) Å respectively. The equatorial Zn–O/N distances vary from 1.978(8)

to 2.274(7) Å. The Dy1—O1—Dy2 and Dy1—O8—Dy2 and Dy1—O11—Dy2 angles are 99.1(3), 103.6(3) and 94.5(2)° respectively. Selected bond lengths and angles are provided in Table 4.2.

Table 4.2. Selected bond lengths (Å) and bond angles (°) within the coordination cluster in **21**.

Dy1—O8	2.291 (7)	Dy1—O1	2.424 (7)	Dy1—O11	2.547 (7)
Dy1—O10	2.381 (7)	Dy1—O17	2.427 (7)	Dy1—N3	2.593 (9)
Dy1—O19	2.417 (7)	Dy1—O4	2.474 (7)	Dy1—O12	2.651 (7)
Dy2—O8	2.320 (7)	Dy2—O14	2.356 (7)	Dy2—N4	2.498 (9)
Dy2—O13	2.337 (7)	Dy2—O11	2.385 (7)	Dy2—O9	2.592 (7)
Dy2—O1	2.339 (7)	Dy2—O18	2.395 (7)	Dy1—Zn2	3.4516 (13)
Dy2—Zn3	3.4815 (14)	Dy1—Dy2	3.6240 (7)	Dy2—Zn3	3.4815 (14)
Dy2—O11—Dy1	94.5 (2)	Dy2—O1—Dy1	99.1 (3)	Dy1—O8—Dy2	103.6 (3)

4.2.2 Static magnetic properties of 21-25

The temperature dependence of susceptibilities of complexes **21-25** were measured on the powder samples in the temperature range of 1.8-300 K under applied dc magnetic field of 1 kOe. The dc magnetic data (Fig. 4.2, left) of **21-25** were summarized in Table 4.3. Since Zn^{II} ions are diamagnetic, the magnetic properties of **21-25** solely originate from dimeric Ln^{III}₂ units. The experimental χT values at 300 K are in good agreement with the theoretically expected values. At room temperature, the χT product of Eu^{III}₂Zn^{II}₃ (**22**) is 2.67 cm³ K mol⁻¹ due to population of magnetic excited states. With decreasing temperature it monotonically decreases to 0.03 cm³ K mol⁻¹ at 1.8 K because of depopulation of the magnetic excited states, leaving only the diamagnetic ground state of the Eu^{III} ions occupied. The χT product of Gd^{III}₂Zn^{II}₃ (**23**) remains almost constant on decreasing the temperature from room temperature to 15 K. Below 15 K, it decreases to 13.19 cm³ K mol⁻¹ at 1.8 K, indicating the presence of weak intramolecular antiferromagnetic interactions within the Gd^{III}₂ unit. The χT product of Ho^{III}₂Zn^{II}₃ (**25**) remains almost constant from room temperature to 100 K and below which slowly decreases, possibly due to combined effect of depopulation of Stark sub-levels and weak intramolecular antiferromagnetic interactions. The similar observation has been reported in triply μ -O bridged Ln₂^{53b} complexes (Ln = Gd, Tb and Eu).

In this series of complexes (**21-25**), a different trend was observed in the χT vs T plots for Dy^{III}₂Zn^{II}₃ (**21**) and Tb^{III}₂Zn^{II}₃ (**24**). For both of them, the χT products slowly decrease (Fig.

4.2, left) on decreasing the temperature from room temperature to $25.40 \text{ cm}^3 \text{ K mol}^{-1}$ at 8 K (**21**) and $21.60 \text{ cm}^3 \text{ K mol}^{-1}$ at 17 K (**24**), and then below these temperatures χT products increase to $28.15 \text{ cm}^3 \text{ K mol}^{-1}$ (**21**) and $26.96 \text{ cm}^3 \text{ K mol}^{-1}$ (**24**) at 1.8 K.

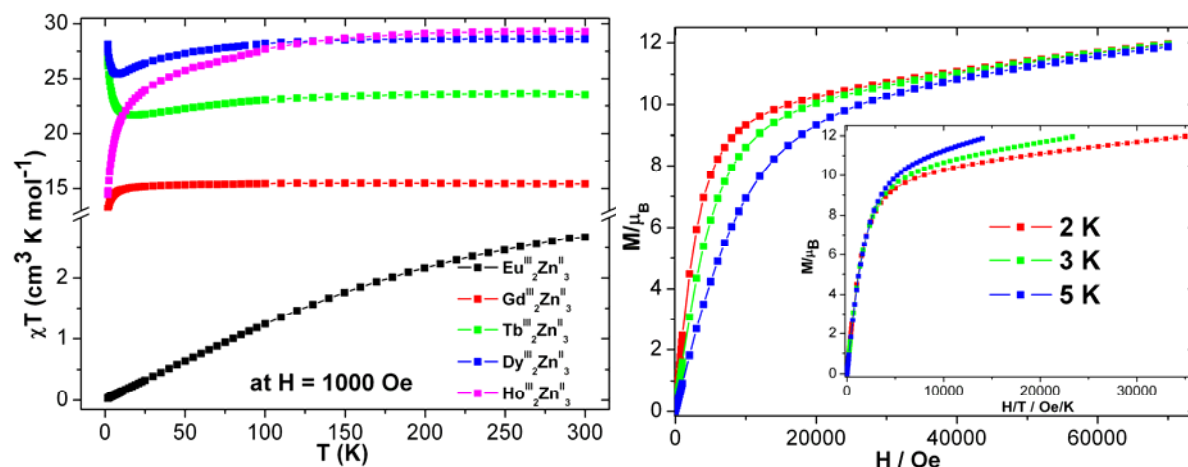


Fig. 4.2. Plots of χT vs T for **21** - **25** at 1000 Oe dc field. Plots of M vs H and H/T (inset) for **21** (right).

Table 4.3. The dc magnetic data of compounds **21-25**.

Compound	Ground state of Ln^{III} ion	χT expected for non-interacting ions per complex ($\text{cm}^3 \text{ K mol}^{-1}$)	χT measured at 300 K per complex ($\text{cm}^3 \text{ K mol}^{-1}$)	Curie constant ^a C ($\text{cm}^3 \text{ K mol}^{-1}$)	Weiss constant ^a θ (K)	Magnetization at 2 K and 7 T (μ_B)
$\text{Dy}^{\text{III}}_2 \text{Zn}^{\text{II}}_3$ (21)	${}^6\text{H}_{15/2}$	28.34	28.59	28.89	-2.46	11.97
$\text{Eu}^{\text{III}}_2 \text{Zn}^{\text{II}}_3$ (22)	${}^7\text{F}_0$	0.0	2.67	-	-	0.17
$\text{Gd}^{\text{III}}_2 \text{Zn}^{\text{II}}_3$ (23)	${}^8\text{S}_{7/2}$	15.76	15.42	15.46	-0.32	14.00
$\text{Tb}^{\text{III}}_2 \text{Zn}^{\text{II}}_3$ (24)	${}^7\text{H}_6$	23.64	23.49	23.79	-2.92	9.8
$\text{Ho}^{\text{III}}_2 \text{Zn}^{\text{II}}_3$ (25)	${}^5\text{I}_8$	28.14	29.28	30.12	-7.75	11.20

(a) Curie-Weiss fit is obtained above 15 K.

Since Dy^{III} and Tb^{III} are comparatively more anisotropic than the other rare-earth analogues, the upturn of χT at low temperature could be due to intramolecular ferromagnetic dipolar interactions between two Dy^{III} ions or two Tb^{III} ions in **21** and **24** respectively. A linear $\text{Dy}_3^{38\text{d}}$ has been reported, in which the central Dy^{III} ion is doubly connected to each terminal

Dy^{III} ion by three mono atomic μ -O bridges. The ab initio calculation established that the central Dy^{III} ferromagnetically coupled to other Dy^{III} ions, while the striking aspect is that intramolecular Dy-Dy ferromagnetic dipolar interaction is stronger than intramolecular Dy-Dy ferromagnetic coupling. The intramolecular ferromagnetic dipolar interaction is due to highly anisotropic nature of Dy^{III} ions.^{38d}

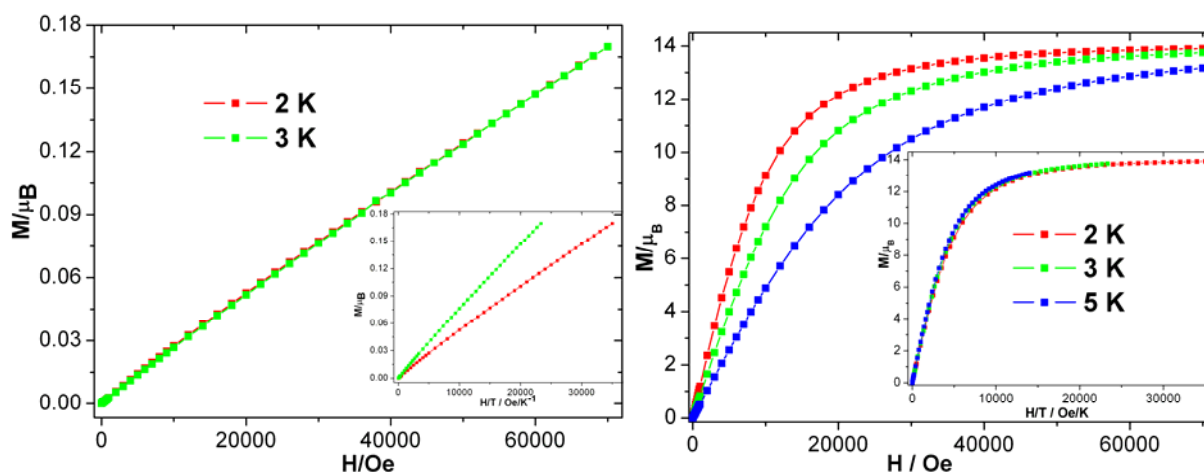


Fig. 4.3. Plots of M vs H and H/T (inset) of **22** (left) and **23** (right) at indicated temperatures.

The field dependence of magnetization (M) of **22** increases linearly with increasing magnetic field but only reaching very low values since the Eu^{III} ions are almost diamagnetic at 2 and 3 K.

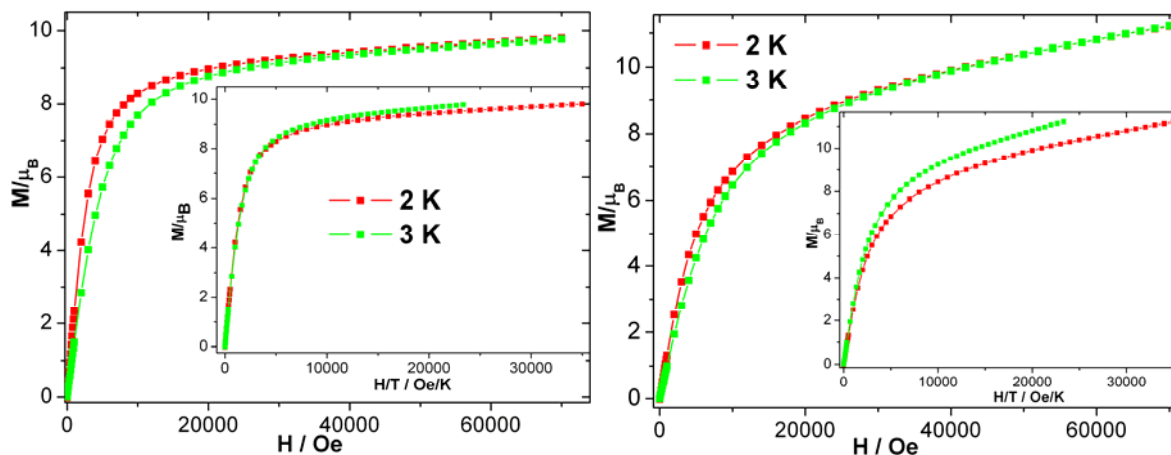


Fig. 4.4. Plots of M vs H and H/T (inset) of **24** (left) and **25** (right) at indicated temperatures.

The M value of **23** increases smoothly with the increase of H and reaches the expected saturation of magnetization (M_S) value of $14.0 \mu_B$, indicating the weak antiferromagnetic interaction can be overcome by applying a higher magnetic field. The M value of **21** (Fig. 4.2, right), **23** (Fig. 4.4, left) and **24** (Fig. 4.4, right) rapidly increases below 1 T and above that increases linearly without reaching true saturation. This indicates the presence of anisotropy in these systems. The reduced magnetization plots (Fig. 4.3, right) of **23** almost superposed on a single master curve because of isotropic nature of Gd^{III} ions. The M vs H/T plots at different temperatures of **21** (Fig. 4.2, right), **24** (Fig. 4.4, left) and **25** (Fig. 4.4, right) do not superpose on a single master curve indicating presence of magnetic anisotropy and/or low lying energy states in these systems.⁴³

4.2.3 Dynamic magnetic properties of 21-25

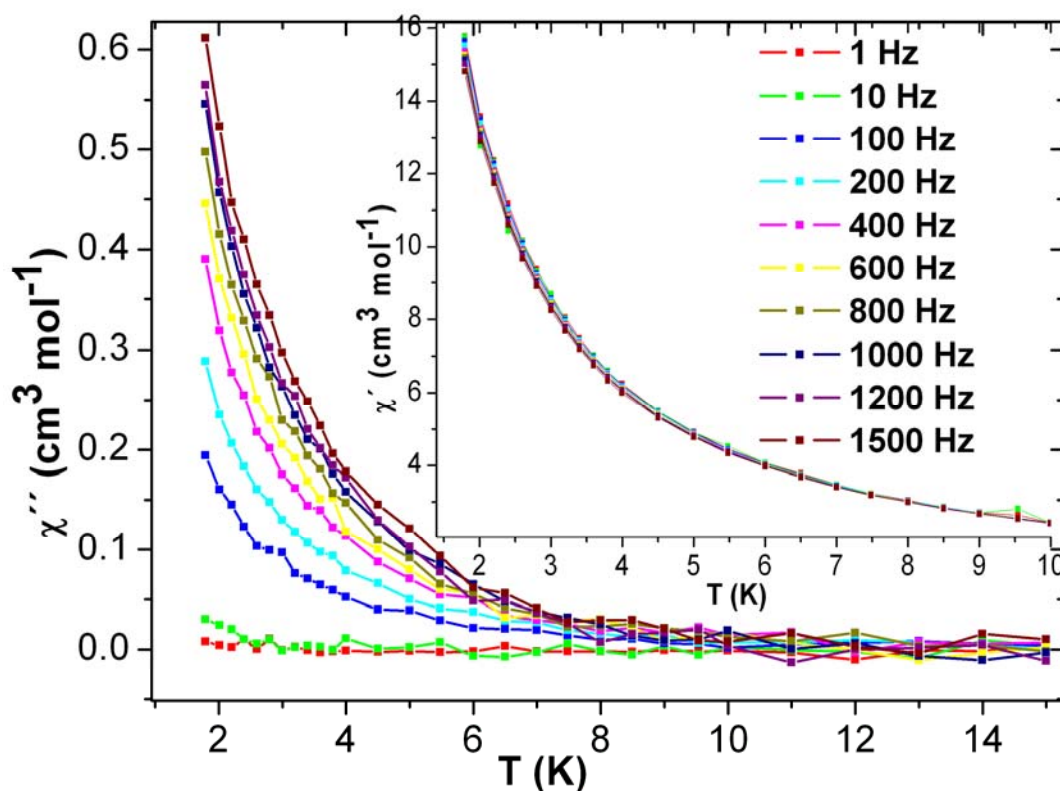


Fig. 4.5. Plots of out of phase susceptibility (χ'') and in phase (χ') and vs T of **21** at indicated frequencies under applied zero dc field.

The ac susceptibilities were measured on polycrystalline powder sample of compound **21-25** in the temperature range of 1.8 – 15 K at 1000 Hz. The only compound containing Dy (**21**) displays the frequency-dependent in-phase (χ') and out-of-phase (χ'') signals (Fig. 4.5) below 10 K, indicating slow relaxation of the magnetization in **21**. The presence of detectable in phase (χ') and out of phase signals (χ'') without a maximum suggests that **21** might be a SMM with a T_b below 1.8 K.

In the literature two Dy^{III}_2 SMMs were previously reported.^{37b} There are two single O-atom (μ -phenoxo) bridges in between two Dy^{III} ions and the average Dy-O-Dy bridging angles of two Dy^{III}_2 SMMs are 106.41° and 107.68° with corresponding energy barriers of 56 and 71 K respectively.^{37b} Dy_2Zn_3 complex (**21**) contains three mono atomic μ -O bridges between two Dy^{III} ions with an average bridging angle of 99.06° . If the bridging angle is correlated to the energy barrier it can be stated that energy barrier of doubly mono atomic (O) bridged Dy^{III}_2 SMMs, increases with the increase of Dy-O-Dy bridging angle. The large change ($8\text{-}9^\circ$) in the bridging angle may be reason of diminishing slow relaxation in **21** if compared with Dy^{III}_2 SMMs though more examples are required to accurately conclude this. Alternatively, cutting the linear trinuclear Dy^{III}_3 ^{38d} to dinuclear Dy^{III}_2 (**21**), leads to partially perish the slow relaxation behavior in **21**.

4.2.4 Fluorescence properties of 21-25

The yellow crystals of all the complexes (**21-25**) were dissolved in THF and fluorescence spectra were recorded in the wavelength range from 200 to 700 nm.

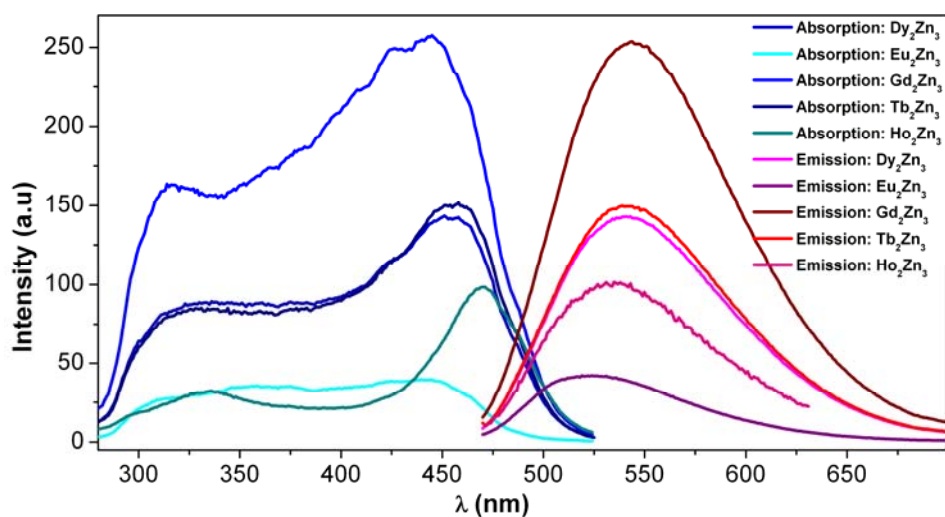


Fig. 4.6. Excitation (left) and emission spectra (right) of complexes **21-25** in THF solution.

Each of the complexes has two absorption peaks; first one at 300 – 350 nm and second one at 430 – 460 nm. The optical excitation in either peak (300 – 350 or 430 – 460 nm) leads to the emission at 500 – 600 nm. The absorption spectra originates from efficient energy absorption by organic ligand ($L1^{2-}$) followed by energy transfer from ligand to Zn^{II} ions. The emission band at 500 – 600 nm is most possibly due to emission from Zn^{II} centers. The complexes **21-25** ostentatiously emit yellow radiation upon simple irradiation by a UV-lamp.

4.3.1 Crystal structure of complex $[Dy_7Zn_4(OH)_4(L1)_8(Cl)_6(H_2O)_4]Cl_3 \cdot 35H_2O$ (**26**)

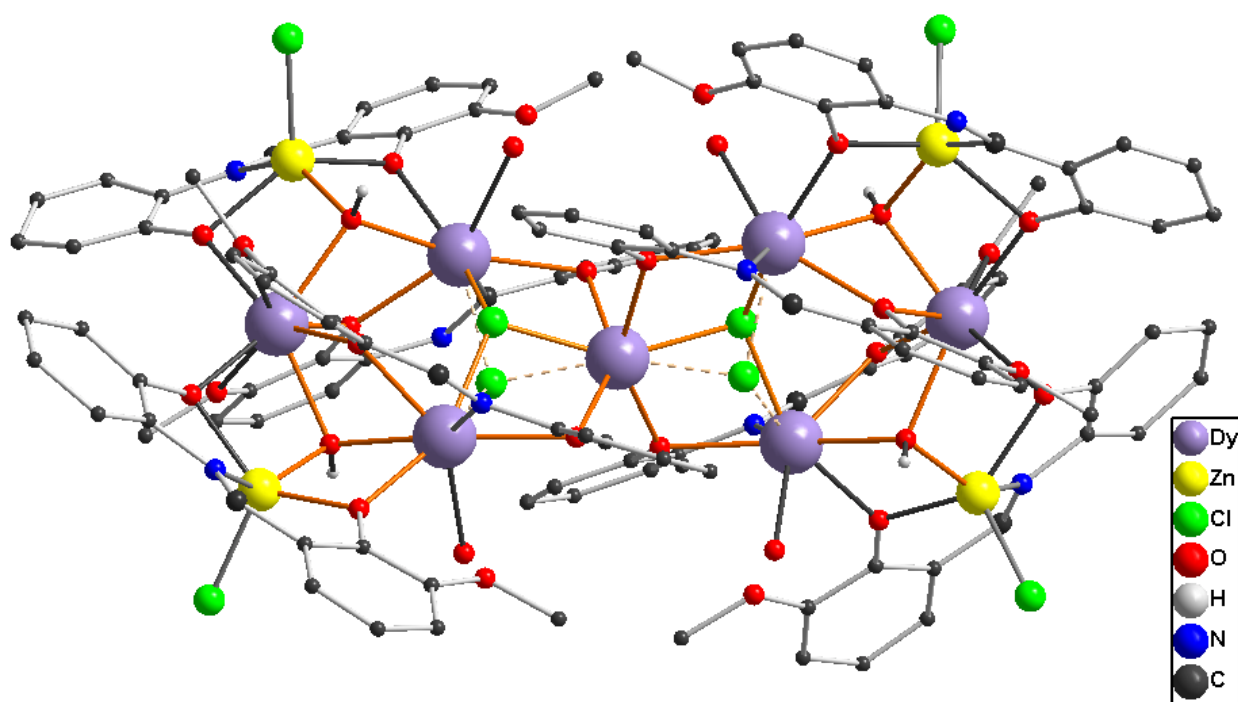


Fig. 4.7. Molecular structure of coordination cluster in compound **26**.

The undecanuclear heterometallic complex **26** crystallizes in space group $C2/c$. The crystallographic two-fold axis is approximately in the plane of the paper and vertical running through the central Dy1. The complex molecule consists of seven Dy^{III} ions, four Zn^{II} ions, four OH^- groups, and eight doubly deprotonated ligands ($L1^{2-}$), nine chloride anions (Cl^-) and four coordinated and 35 lattice water molecules (Fig. 4.7).

All four Zn^{II} ions adopt a distorted square pyramidal geometry with an O_3NCl donor set while the six Dy^{III} ions adopt an eight coordinated distorted square antiprismatic geometry with

an O_8 (Dy4) and an O_5NCl_2 (Dy2 and Dy3) donor sets, except the central Dy1 ion which adopts a distorted octahedral geometry with an O_4Cl_2 donor set. The $\{Dy^{III}_7(OH)_4(OR)_8Cl_2\}^{7+}$ core (Fig. 4.8) can be considered as two planar rhomboidal Dy_4 units sharing one common edge (Dy1) in the middle. The two halves of the molecule are related by a crystallographic two-fold axis passing through Dy1. The dihedral angle between two planar Dy^{III}_4 units is 75.24° .

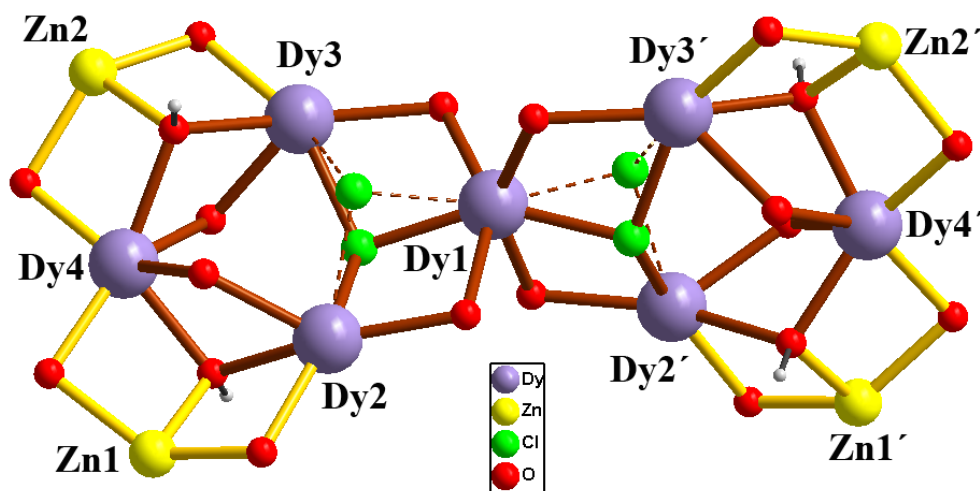


Fig.4.8. Molecular core of coordination cluster in compound 26.

The central Dy1 center is connected to its nearest four Dy^{III} centers (Dy2, Dy3, Dy2' and Dy3') by four phenoxide μ -O-atoms from the iminophenol part of the Schiff base ligands, each of which is coordinated to each Dy^{III} center (Dy2, Dy3, Dy2' or Dy3') into pocket-I (ONO), directing the pocket-II (OO) coordination site towards the Dy4 or Dy4' centers with one ligand from above and one below each Dy^{III}_4 . Each phenoxide O-atom of the o-vanillin part of these ligands acts as μ -bridge between Dy2 and Dy4 or Dy3 and Dy4. The ligand displays two kinds of bridging modes ($\eta^1:\eta^2:\eta^1:\eta^2:\mu_3$ and $\eta^2:\eta^1:\eta^2:\mu_3$) (Fig. 1.5). The two chloride ligands act as μ_3 -bridges to the Dy1–Dy2–Dy3 and Dy1–Dy2'–Dy3' triangular units. Each μ_3 -bridged chloride is disordered between positions above its respective Dy_3 triangle, displaced either 0.641 or 0.849 Å out of the Dy_3 plane. The two Zn^{II} ions (Zn1 and Zn2) are connected to each Dy_4 unit by two μ_3 -OH groups to Dy2–Dy4 or Dy3–Dy4 pairs. The Zn centers are close to the plane of the respective Dy_4 units, displaced ± 0.744 Å from it. The μ_3 -OH ligands are alternatively above and below the plane. The Zn1–Dy4 and Zn1–Dy2 edges (and similarly Zn2–Dy4 or Zn2–Dy3) are

also connected by phenoxide μ -O-atoms from aminophenol and o-vanillin parts of the Schiff base ligand respectively leaving pocket-II (OO) to accept H-bonding from water ligands coordinated to Dy2 and Dy3. The terminal chloride ligands coordinate one to each square pyramidal Zn^{II} ion in an apical site. Selected distances and angles are given in Table 4.4.

Table 4.4. Selected bond lengths (Å) and bond angles (°) within the coordination cluster in **26**.

Dy1—O8	2.329 (8)	Dy1—Cl1B ⁱ	2.326 (8)	Dy1—Cl1A	2.335 (7)
Dy1—O5 ⁱ	2.324 (8)	Dy1—Cl1B	2.326 (8)	Dy1—O5	2.324 (8)
Dy2—Cl1A	2.274 (7)	Dy2—O5	2.292 (8)	Dy2—O9	2.293 (9)
Dy2—O1	2.384 (8)	Dy3—O12	2.322 (8)	Dy2—O3	2.361 (8)
Dy2—O16	2.445 (9)	Dy2—Cl1B	2.484 (9)	Dy2—N1	2.435 (10)
Dy3—O8	2.339 (8)	Dy3—O2	2.358 (7)	Dy3—O6	2.355 (8)
Dy3—O17	2.426 (9)	Dy3—N2	2.456 (9)	Dy3—Cl1B	2.358 (8)
Dy3—Cl1A	2.388 (8)	Dy4—O3	2.399 (7)	Dy4—O1	2.267 (8)
Dy4—O14	2.291 (8)	Dy4—O6	2.438 (8)	Dy4—O4	2.499 (8)
Dy4—O11	2.271 (9)	Dy4—O2	2.308 (8)	Dy4—O7	2.495 (8)
Dy1—Dy2 ⁱ	3.6024 (9)	Dy1—Dy3	3.6351 (8)	Dy3—Zn2	3.4103 (16)
Dy1—Dy2	3.6025 (9)	Dy2—Zn1	3.3749 (18)	Dy3—Dy4	3.7928 (9)
Dy1—Dy3 ⁱ	3.6350 (8)	Dy2—Dy4	3.7514 (10)	Dy4—Zn1	3.3245 (19)
Dy4—Zn2	3.3287 (18)				
Dy2—Cl1A—Dy1	102.8 (3)	Dy4—O1—Dy2	107.5 (3)	Dy4—O2—Dy3	108.7 (3)
Dy2—Cl1A—Dy3	132.9 (3)	Dy2—O3—Dy4	104.0 (3)	Dy2—O5—Dy1	102.6 (3)
Dy1—Cl1A—Dy3	100.7 (3)	Dy3—O6—Dy4	104.6 (3)	Dy1—O8—Dy3	102.3 (3)
Dy1—Cl1B—Dy3	101.8 (3)	Dy1—Cl1B—	96.9 (3)	Dy3—Cl1B—Dy2	123.9 (3)

Symmetry code: (i) $-x+1, y, -z+1/2$.

4.3.2 Static magnetic properties of **26**.

The room temperature χT product of **26** is $98.18 \text{ cm}^3 \text{ K mol}^{-1}$ which is very close to the theoretically calculated value of $99.19 \text{ cm}^3 \text{ K mol}^{-1}$ for seven magnetically non-interacting Dy^{III} ions (with $^6\text{H}_{15/2}$, $g = 4/3$, $S = 5/2$). The χT product decreases on decreasing the temperature from room temperature to 8 K ($81.62 \text{ cm}^3 \text{ K mol}^{-1}$) below which it more rapidly decreases reaching $66.35 \text{ cm}^3 \text{ K mol}^{-1}$ at 1.8 K. The shape of χT vs T plot (Fig. 4.9, left) is consequence of

combination of the depopulation of Stark sub-levels at higher temperatures and/or weak intra molecular antiferromagnetic interaction and ZFS of Dy^{III} ions at low temperature.

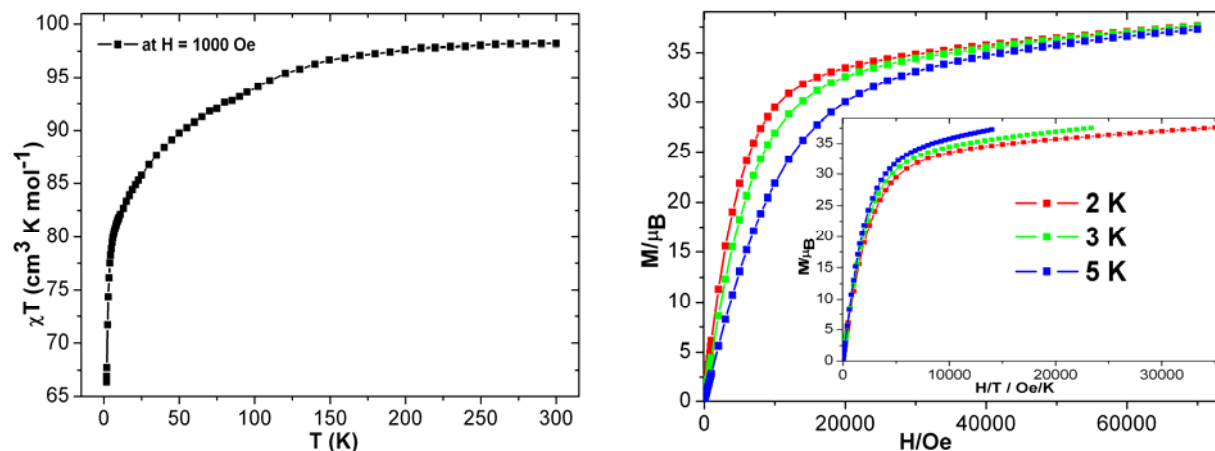


Fig. 4.9. Plots of χT vs T (left), M vs H (right) and M vs H/T (right, inset) of **26**.

The field dependent magnetization measurements show that M value of **26** increases more rapidly below 1 T and then increases linearly (Fig. 4.9, right-inset) at higher field without reaching true saturation indicating the presence of magnetic anisotropy in the system. The M_S value in between $5-6 \mu_B$ ³⁷⁻³⁸ per Dy^{III} ion is generally reported due to random orientation magnetic moments of each Dy^{III} ion in the powder sample. The maximum magnetization value of **26** is $37.59 \mu_B$ which is expected for 7 Dy^{III} ions ions ($7 \times 5.37 = 37.59 \mu_B$). Moreover, M vs H/T plots at different temperatures do not superpose (Fig. 4.9, right-inset) on a single master curve, also indicating the presence of low lying energy states and/or anisotropy in the system.⁴³

4.3.3 Dynamic magnetic properties of **26**.

The temperature dependent ac susceptibility measurements on polycrystalline sample of complex **26**, reveal the presence of ac (χ' and χ'') signal (Fig. 4.10) below 10 K but without a maximum in χ' and χ'' vs T plots. This kind of slow relaxation suggests that **26** may be a SMM with a blocking temperature below 1.8 K. Up to now, three defect-dicubane Dy₄ SMMs with two μ_3 -OH bridges, are reported.^{36b-d} The Dy₇ unit of **26** can be considered as combination of two Dy₄ units sharing a common Dy^{III} edge in the center, making a dihedral angle 75.24° between two coplanar Dy₄ units. The anisotropy may have been partially nullified the uniaxial magnetic momentum of **26** because of dihedral angle (75.24°), making T_b below 1.8 K.

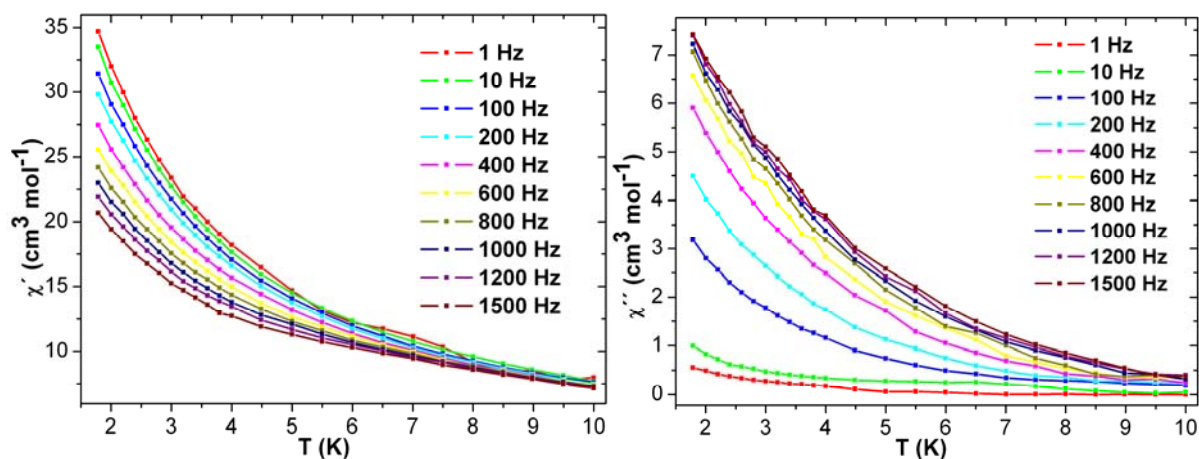


Fig. 4.10. Plots of χ' vs T (left) and χ'' vs T (right) of **26**.

4.3.4 Fluorescence properties of **26**.

The yellow-brown needle-shaped crystals (0.5 mg) of complex **26** were dissolved in THF (7.5 mL) and fluorescence spectra were recorded (Fig. 4.11) in the wave length range of 300 to 700 nm. First, two emission peaks are detected at 510 and 544 nm. Then absorption spectra have been recorded with a corresponding emission peaks at 510 and 544 nm respectively.

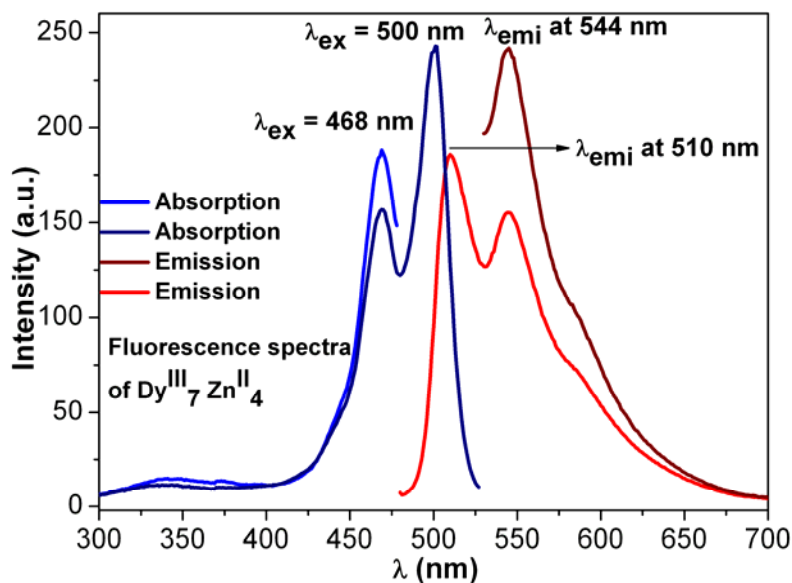


Fig. 4.11. The excitation and emission spectra of **26**.

The excitations with corresponding emission peak at 510 and 544 nm result from one absorption peak at 468 nm and two peaks at 468 and 500 nm respectively. Thus they have a

common absorption peak at 468 nm. The excitations at 468 and 500 nm led to the two bathochromic emission peaks at 510, 544 nm and one peak at 544 nm respectively. Both the excitations have a common bathochromic emission at 544 nm with a shoulder at 580 nm (Fig. 4.11). Two Zn^{II} centers are likely to be the corresponding emission centers.

4.4.1 Crystal structures of $[Ln_6Cd_6(CO_3)_2(OH)_4(\mu-Cl)_2(Cl)_2(L1)_8(OH_2)_{12}]Cl_2 \cdot 10THF$; [$Ln = Dy(27), Tb(28), Ho(29)$ and $Er(30)$]

The dodecanuclear complex **27** crystallizes in the space group $C2/m$. It contains six Cd^{II} ions, six Dy^{III} ions, two carbonates ($\mu_5-CO_3^{2-}$), eight dianionic ligands ($L1$)²⁻, four μ_3-OH groups, two μ -bridging Cl^- ions, two coordinated Cl^- , two free Cl^- ions, twelve coordinated water molecules and ten disordered THF molecules. The molecule occupies a site of $2/m$ symmetry. The two-fold axis passes through the central Dy of each Dy_3 unit, while the bridging chlorides and carbonate carbons are in the mirror plane which relates the two Dy_3 units. There are two crystallographically distinct eight coordinated Dy^{III} ($Dy1$ and $Dy2$) ions with a distorted square antiprismatic geometry. $Dy1$ and $Dy2$ are coordinated by an O_6N_2 and an O_7N donor sets respectively.

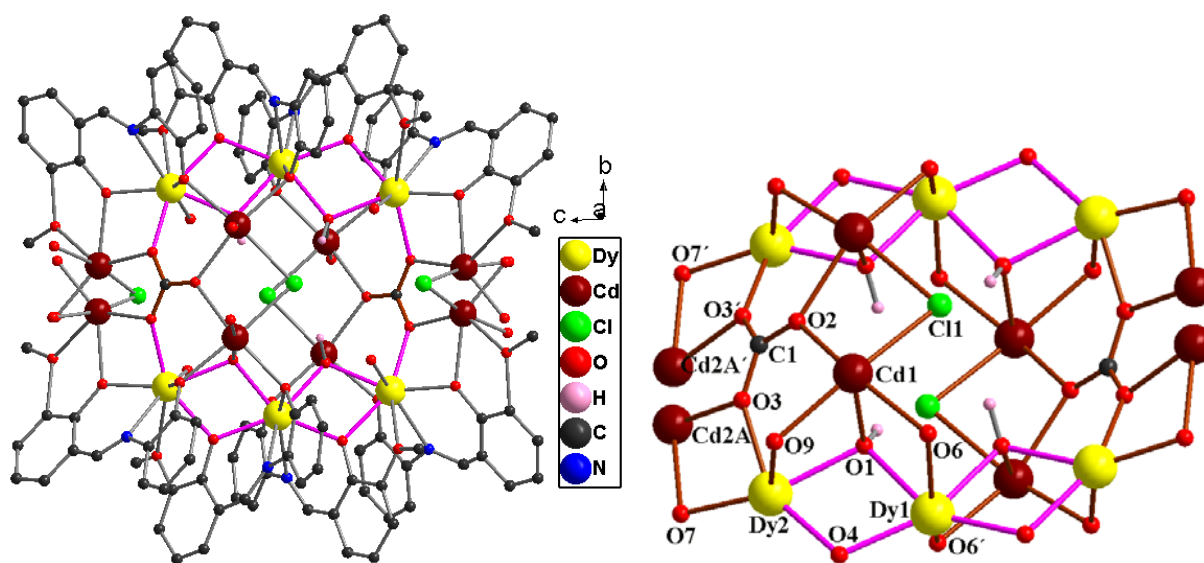


Fig. 4.12. Molecular structure (left) and core (right) of the coordination cluster in compound **27**.

There are two different types of Cd^{II} ions ($Cd1$ and $Cd2$) of which $Cd2$ ions are disordered over two positions on either side of the mirror plane, with the two sites 1.52 Å apart

as Cd2A and Cd2A' (Fig. 4.12). The Cd1 and Cd2A ions have a distorted octahedral geometry with an O₅Cl donor set. The "o-vanillin end" of one of the Schiff base ligands is also a bit disordered, to accommodate this Cd disorder. Attempts were made to refine the structure in C2 with the C2/m mirror plane now only a twin-low but the disorder Cd2A persisted.

The (μ_3 -OH) ligand O1 bridges between Dy1, Dy2 and Cd1. Iminophenol phenoxides also form μ_2 -bridges between Cd1 and Dy1, and Cd1 and Dy2. The chloride ligand Cl1 forms a μ_2 -bridge between Cd1 and Cd1', its equivalent from mirror symmetry. Chloride also accepts H-bond from symmetry-equivalents of the hydroxyl ligand O1. The carbonate ligand forms a (μ_5 -CO₃²⁻) bridge between Dy1, Cd1 and to their respective mirror symmetry equivalents. The non-planar dodecanuclear core {Dy₆Cd₆(μ_5 -CO₃)₂(μ_3 -OH)₄(μ -Cl)₂(μ -OR)₁₆}⁴⁺ (Fig. 4.12, right) contains two bent (Dy2–Dy1–Dy2' = 153.09°) Dy^{III}₃ units at the top and the bottom of the core. Each Dy1 center is coordinated by two dianionic ligands (L1)²⁻ through pocket-I (ONO) bridging through the vanillin phenoxides to Dy2/Dy2' which fit in the pocket-II. Dy2 is also chelated by pocket-II of another ligand which is also bridges through its vanillin phenoxides to Cd2A. The selected bond lengths and angles are given in Table 4.5.

Table 4.5. Selected bond lengths (Å) and bond angles (°) within the coordination cluster in **27**.

Dy1—O4 ⁱ	2.273 (6)	Dy1—O1 ⁱ	2.348 (5)	Dy1—N1	2.537 (6)
Dy1—O4	2.273 (6)	Dy1—O6 ⁱ	2.381 (5)	Dy1—N1 ⁱ	2.537 (6)
Dy1—O1	2.348 (5)	Dy1—O6	2.381 (5)	Dy2—O7	2.252 (6)
Dy2—O4	2.304 (5)	Dy2—O1	2.354 (5)	Dy2—N2	2.485 (7)
Dy2—O3	2.307 (5)	Dy2—O10	2.409 (6)	Dy2—O5	2.786 (6)
Dy2—O9	2.310 (5)	Dy1—O1—Dy2	106.78 (19)	Dy1—O4—Dy2	111.10 (19)

Symmetry codes: (i) $-x+1, y, -z+1$.

4.4.2 Static magnetic properties of **27-30**.

The temperature dependence of the dc susceptibility data of **27-30** are given in Table 4.6. The experimental data at 300 K are in good agreement with theoretical values. The χT vs T plots of all the complexes show similar trend (Fig. 4.13) except **27**. The χT product of Dy₆^{III}Cd₆^{II} (**27**) remains almost constant on decreasing the temperature from room temperature (24.70 cm³ K mol⁻¹) to 100 K (24.70 cm³ K mol⁻¹) followed by a steady decrease to 13 K (75.65 cm³ K mol⁻¹),

below which it steeply increases until the temperature reaches 1.8 K where χT has the value $89.52 \text{ cm}^3 \text{ K mol}^{-1}$. This shape of the χT vs T plot of **27** implies weak intramolecular ferromagnetic interactions below 13 K. The slow decrease of χT from 300-13 K is presumably due to depopulation of Stark sub-levels of Dy^{III} ions.

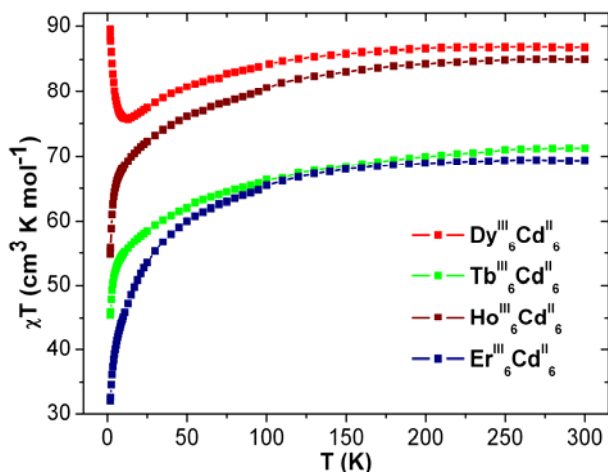


Fig. 4.13. Plots of χT vs T of **27-30** at 1000 Oe dc field.

Table 4.6. The dc magnetic data of compounds **27-30**.

Compound	Ground state of Ln^{III} ion	χT expected for non-interacting ions per complex ($\text{cm}^3 \text{Kmol}^{-1}$)	χT measured at 300 K per complex ($\text{cm}^3 \text{Kmol}^{-1}$)	χT measured at 1.8 K per complex ($\text{cm}^3 \text{Kmol}^{-1}$)	Magnetization at 2 K and 7 T (μ_B)
$\text{Dy}^{\text{III}}_6\text{Cd}^{\text{II}}_6$ (27)	${}^6\text{H}_{15/2}$	85.02	86.97	89.52	33.65
$\text{Tb}^{\text{III}}_6\text{Cd}^{\text{II}}_6$ (28)	${}^7\text{H}_6$	70.92	71.26	45.45	28.68
$\text{Ho}^{\text{III}}_6\text{Cd}^{\text{II}}_6$ (29)	${}^5\text{I}_8$	84.42	85.05	54.81	33.88
$\text{Er}^{\text{III}}_6\text{Cd}^{\text{II}}_6$ (30)	${}^4\text{T}_{15/2}$	68.88	69.36	31.99	30.28

A similar trend has been observed in reported Dy^{III}_3 compound ^{38d} with Dy-O-Dy angles ranging from $103.89(10)^\circ$ to $105.27(10)^\circ$. The ab initio calculation showed that the central Dy^{III} ferromagnetically coupled to other Dy^{III} ions, while the striking aspect is that intramolecular Dy-Dy ferromagnetic dipolar interaction is stronger than intramolecular Dy-Dy ferromagnetic coupling. ^{38d} The χT product of $\text{Tb}_6^{\text{III}}\text{Cd}_6^{\text{II}}$ (**28**), $\text{Ho}_6^{\text{III}}\text{Cd}_6^{\text{II}}$ (**29**) and $\text{Er}_6^{\text{III}}\text{Cd}_6^{\text{II}}$ (**30**) slowly decreases on decreasing the temperature from room temperature to 15 K and below which they

fall sharply until 1.8 K (Fig. 4.12, left) and reaches the values given in Table 4.6. The slow decrease of χT value at higher temperature is due to gradual depopulation of Stark sub-levels, while the sudden fall below 10 K is due to intramolecular antiferromagnetic interactions and/or ZFS of Ln^{III} ions. Since Dy (**27**) analogue can be magnetically more anisotropic in nature than that of the other rare-earth analogues, the intramolecular dipolar ferromagnetic coupling is stronger in **27** and the upturn of χT below 13 K, can be explained by this feature.

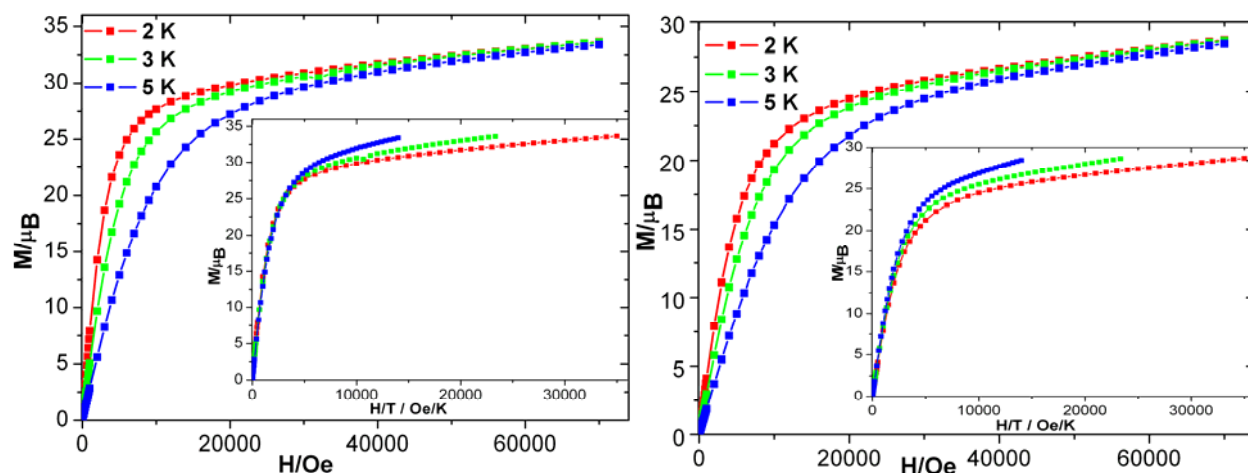


Fig. 4.14. Plots of M vs H and H/T (inset) of **27** (left) and **28** (right).

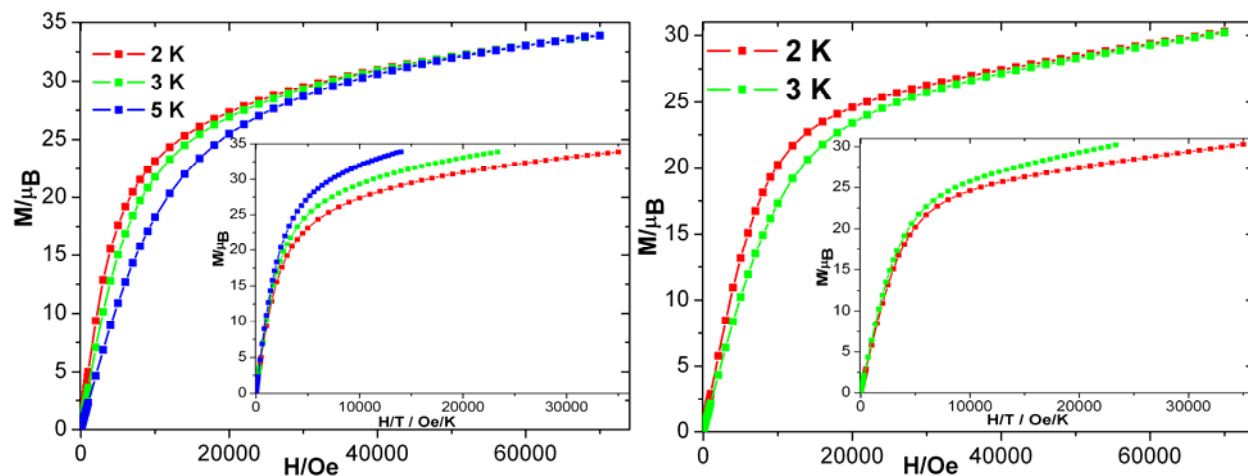


Fig. 4.15. Plots of M vs H and H/T (inset) of **29** (left) and **30** (right).

The field dependence of magnetization (Fig. 4.14-4.15) of all complexes (**27-30**) increases steeply below 1T at 2 K and reaches the values given in Table 4.6. Among all four

complexes, the M value of **27** increases relatively faster with increase of H as expected since it also has ferromagnetic interactions. Moreover, the M vs H/T plots of **27-30** at low temperatures (Fig. 4.14-4.15, inset) do not superposed on a single master-curve further indicating the presence of magnetic anisotropy and/or low lying excited states.⁴³

4.4.3 Dynamic magnetic properties of 27-30.

The temperature dependence of the ac susceptibilities of all four complexes (**27-30**) were measured under the applied frequency of 1000 Hz but only compound **27** shows slow relaxation of magnetization below 10 K (Fig. 4.16). Neither in-phase (χ') nor out-of-phase (χ'') vs T plots (Fig. 4.16) show any maxima, implies curtailment of relaxation of energy barrier through QTM or there may be more than one relaxation processes involved. A careful look at the out-of-phase (χ'') vs T plots at different frequencies reveals that the out-of-phase susceptibility (χ'') increases on decreasing the temperature in the frequency range 1-100 Hz but above 100 Hz, the rate of increase of χ'' decreases below 5 K. This kind of χ'' vs T signature suggests that the relaxation process is weakly temperature dependent and relaxation dynamic is taken by that of static. The in-phase and out-of-phase vs frequency measurements (Fig. 4. 17) at different temperatures were performed. On increasing temperature from 1.8 to 5.0 K, the maxima of χ'' vs frequency plots shift to higher frequency.

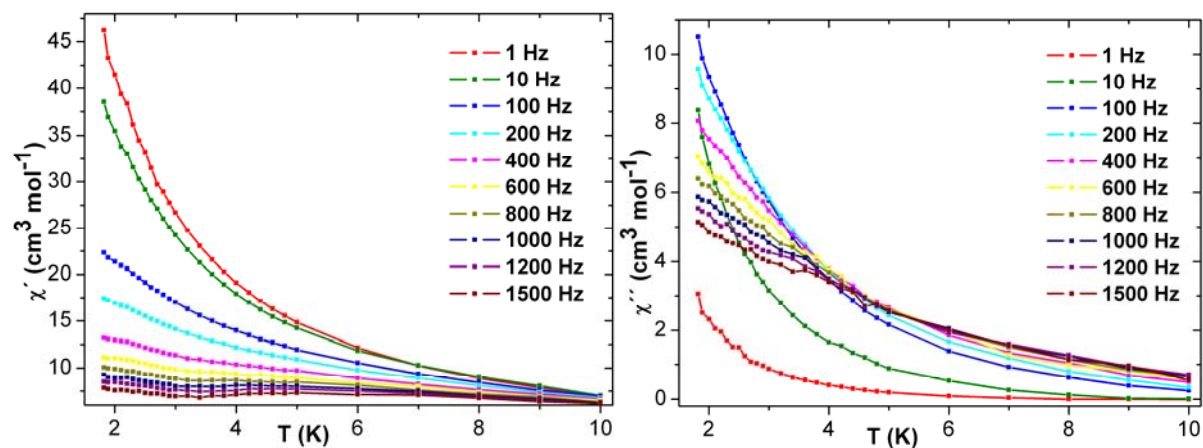


Fig. 4.16. Plots of χ' (left), χ'' (right) vs T of **27** at indicated frequencies.

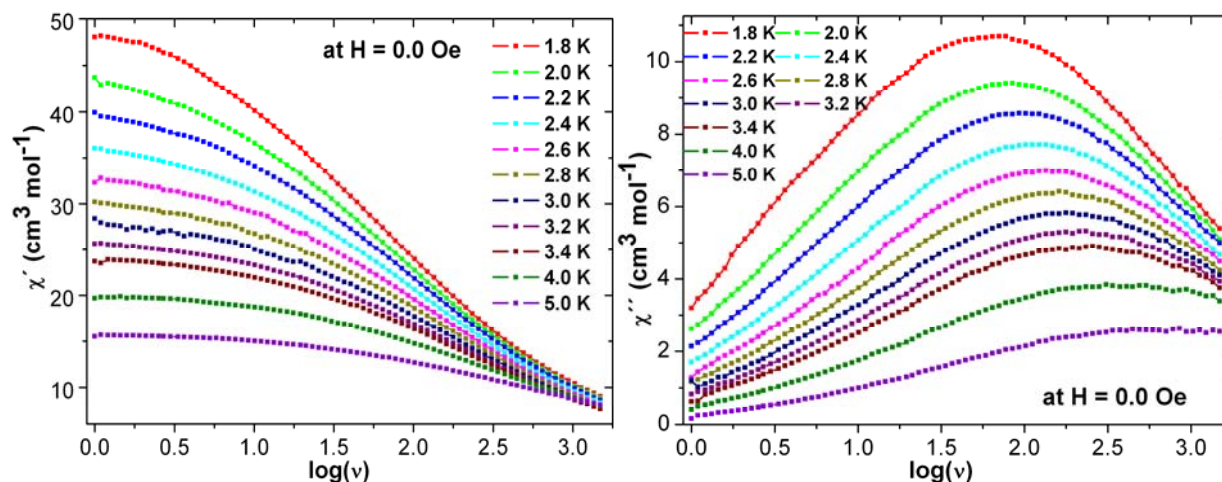


Fig. 4.17. Plots of χ' (left), χ'' (right) vs frequency of **27** at indicated temperatures.

The ac susceptibility vs frequency measurements (Fig. 4.18) under different applied magnetic fields at 1.8 K reveal the presence of no obvious QTM pathway. There is a maximum in χ'' vs frequency plots at 1.8 K under the magnetic field range of 0.0 Oe to 1.5 kOe but when the magnetic field is increased to 2 kOe the maximum appears to split into two, indicating the presence of more than one relaxation process.

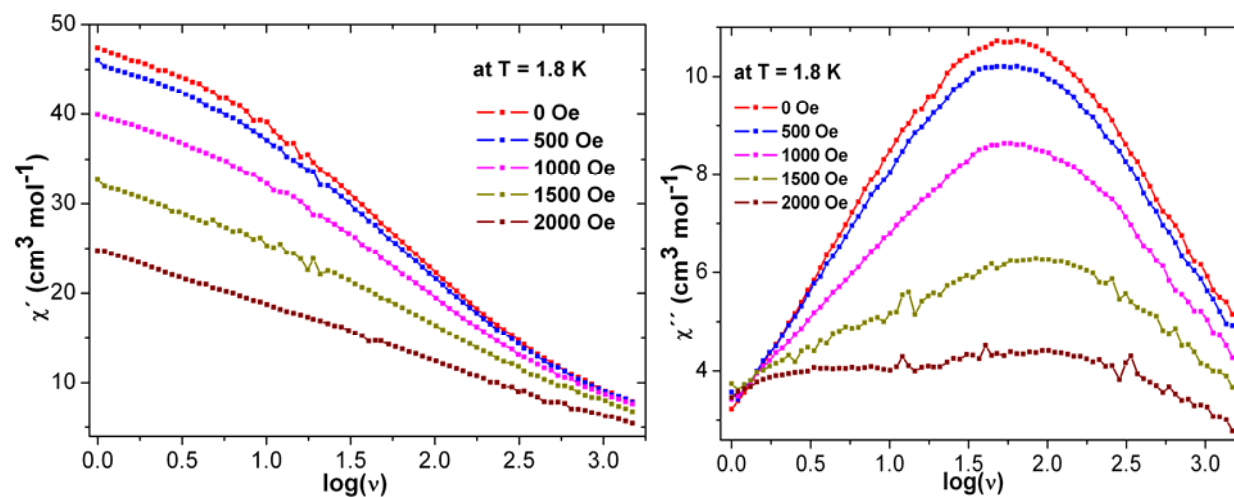


Fig. 4.18. Plots of χ' (left), χ'' (right) vs frequency of **27** at indicated dc magnetic fields.

The data of Fig. 4.17 are used for Cole-Cole and Arrhenius plots (Fig. 4.19) which suggest the presence of two relaxation processes and crossing temperature is close to 3.2 K. The linear

fittings on Arrhenius plots of **27** gave two energy barriers; first one is 4.82 K with $\tau_0 = 1.73 \times 10^{-4}$ s and second one is 14.89 K with $\tau_0 = 7.33 \times 10^{-6}$ s (Fig. 4.19, right).

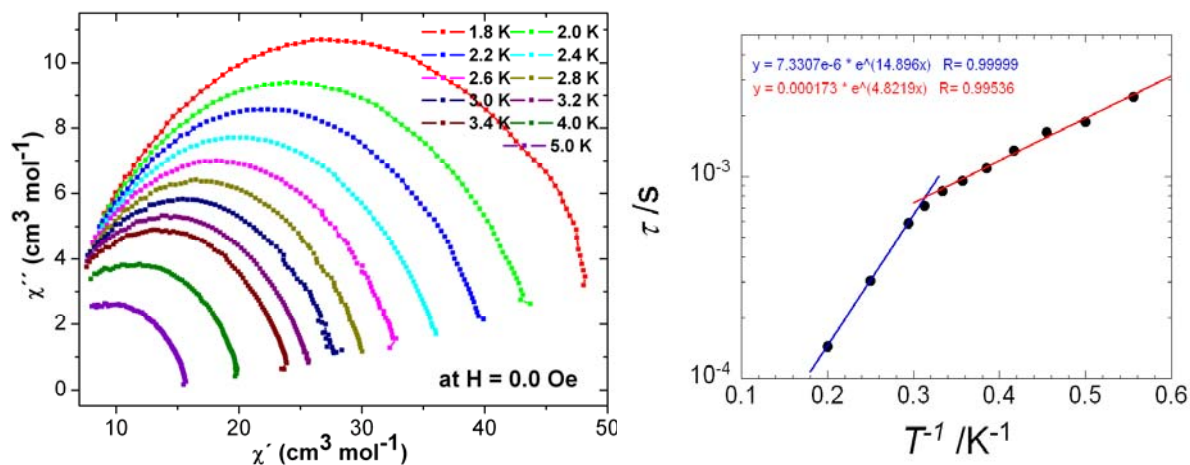


Fig. 4.19. The Cole-Cole (left) and Arrhenius plots (right) of **27** under applied zero dc field.

4.4.4 Fluorescence properties of 27-30.

The yellow rod-shaped crystals of complexes **27-30** were dissolved in THF and fluorescence spectra were recorded (Fig. 4.20 and 4.21) in the wavelength range from 275 to 700 nm. Multiple emission peaks were detected at wave lengths given in Table 4.7.

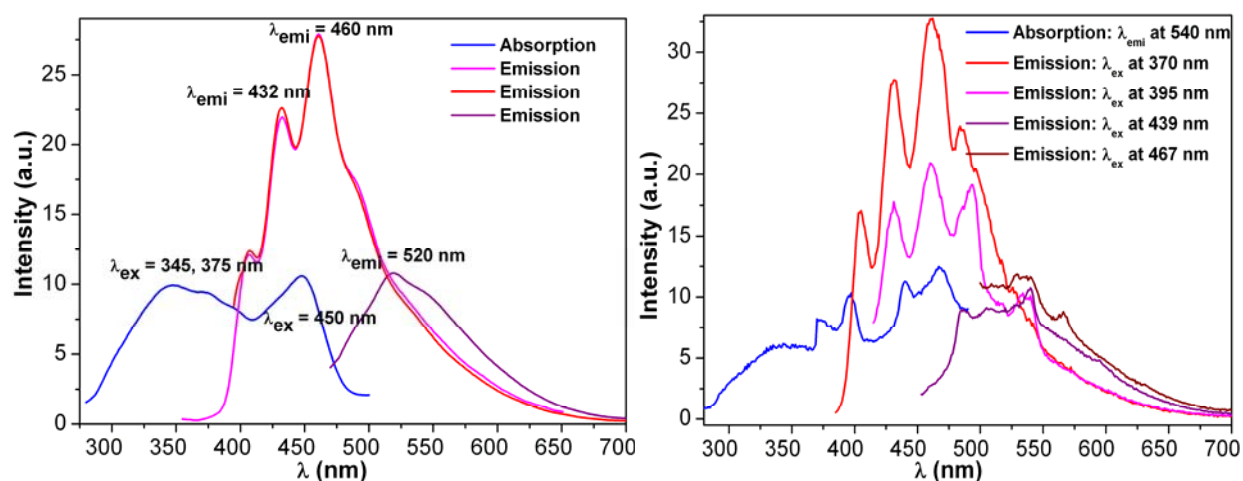


Fig. 4.20. The excitation and emission spectra of **27** (left) and **28** (right).

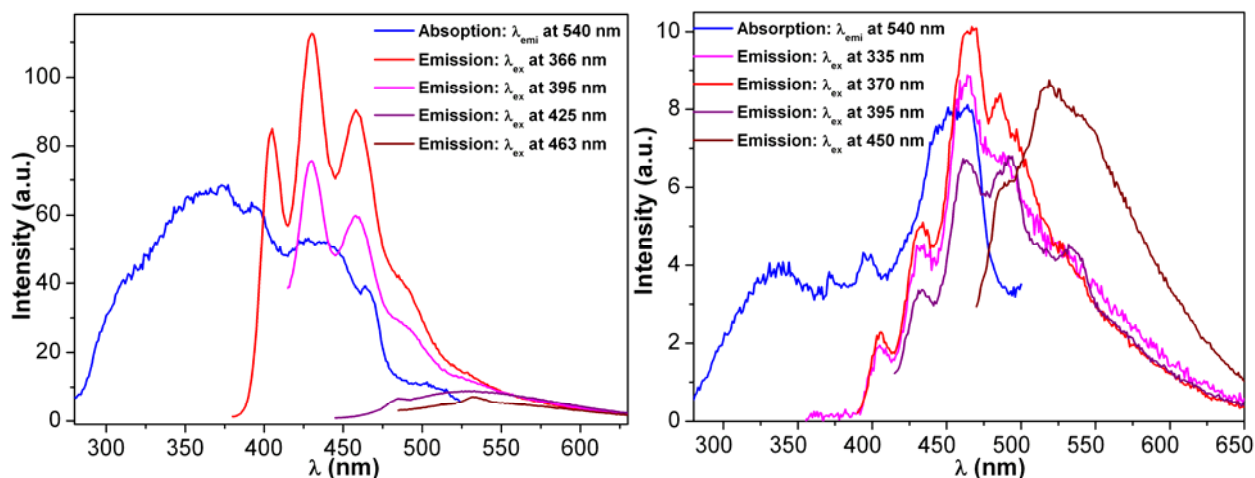


Fig. 4.21. The excitation and emission spectra of **29** (left) and **30** (right).

Table 4.7. The excitation and emission peaks of **27-30**.

compound	27	28	29	30
Absorption Peaks (nm)	345, 375, 450	370, 395, 439, 467	366, 395, 425, 463, 500	335, 370, 395, 450
Excitation wave length (λ_{ex}) (nm)	345, 375, 450	370, 395, 439, 467	366, 395, 425, 463	335, 370, 395, 450
Emission Peaks (λ_{em}) (nm)	345, 375: 406, 432, 460, 488, 527 450: 520	370: 405, 431, 460, 485, 525 395: 430, 460, 494, 534 439: 485, 505, 540 467: 540, 567	366: 405, 430 457, 488 395: 430 457, 488. 425: 485, 532. 463: 532	335: 405, 432, 466, 485 370: 405, 432, 466, 485 395: 432, 466 492, 533 450: 492, 520, 540

Absorption spectra were then recorded with corresponding emission peaks as given in Fig. 4.20 and 4.21. The excitation wavelengths and bathochromic emission peaks are listed in the Table 4.7. All four compounds (**27-30**) absorb in both UV and visible range and emit visible range with some common sets of values of wave lengths (Table 4.7). The Cd^{II} ions are likely to be responsible for the bathochromic emission spectra.

4.5.1 Crystal structures of $[\text{Ln}_3\text{Cu}_2(\mu_3\text{-OH})_2(\text{L1})_5(\text{NO}_3)(\text{MeOH})_2(\text{H}_2\text{O})]\cdot 3\text{MeOH}\cdot x\text{H}_2\text{O}$; $[\text{Ln} = \text{Dy}(31), \text{Gd}(32), \text{Tb}(33), \text{and Ho}(34), x = 0 \text{ for } 31, 32, 34 \text{ and } x = 1 \text{ for } 33]$

Compounds **31-34** crystallise isomorphously in the triclinic space group $P\bar{1}$. The molecular structure of **31** is depicted in Fig. 4.22, and selected bond distances and angles are listed in Table 4.8.

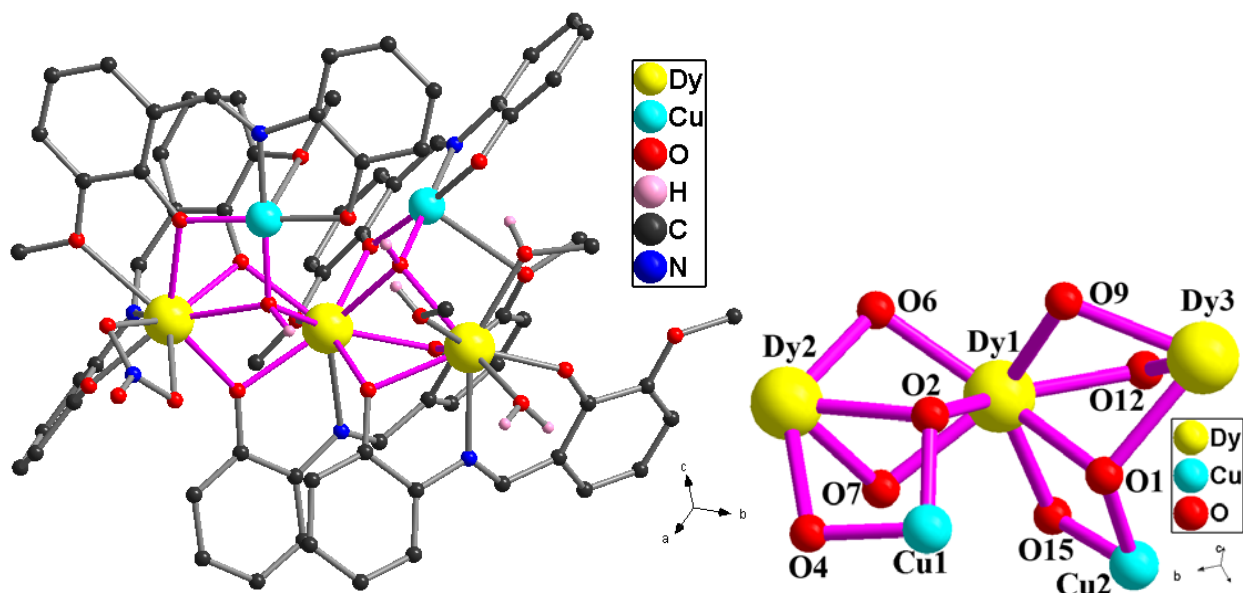


Fig. 4.22. Molecular structure (left) and core (right) of coordination cluster in compound **31**.

The pentanuclear compound consists of two Cu^{II} ions, three Dy^{III} , five dianionic ligands $(\text{L1})^{2-}$, two triply bridging hydroxyl groups, one coordinated water and two methanol. In the crystal lattice there are three MeOH solvent molecules for crystallization. The pentanuclear core of the coordination complex can be considered as two trinuclear $\{\text{Dy}^{\text{III}}_2\text{Cu}^{\text{II}}(\mu_3\text{-OH})\}$ units, sharing a common Dy vertex (Dy1) within the resulting $\text{Dy}_3\text{Cu}_2(\text{OH})_2$ core, the Dy2-Dy1-Dy3 angle of 132.3° is similar to that in **27**. The two $\mu_3\text{-OH}$ groups are 0.864 Å (O1-Cu1Dy1Dy2) and 0.857 Å (O2-Cu2Dy2Dy3) above the respective Dy_2Cu metal planes. The dihedral angle between Cu1Dy1Dy2 and Cu2Dy2Dy3 triangular planes is 78.40° . The heteropentanuclear core is held together by the five dianionic ligands $(\text{L1})^{2-}$ which show four different coordination modes; one chelating/bridging ($\eta^2:\eta^1:\eta^1:\mu_2$), one chelating/bridging ($\eta^2:\eta^1:\eta^1:\mu_3$), one chelating ($\eta^1:\eta^1:\eta^1:\mu_1$) and two chelating/bridging ($\eta^1:\eta^2:\eta^1:\eta^1:\mu_2$) ligands (Fig. 1.5), with the heterometallic Cu – Dy distances being Dy1 – Cu1 = 3.4359(3) Å, Dy2 – Cu1 = 3.863(3) Å, Dy2

– Cu2 = 3.3709(4) Å and Dy3 – Cu2 = 3.730(2) Å, and the Dy – Dy distances are Dy1 – Dy2 = 3.5494(2) Å and Dy2 – Dy3 = 3.5526(2) Å. Peripheral ligation is provided to Dy3 by two methanols and a water molecule and to Dy1 by one chelate nitrate molecule. Both Cu^{II} ions are four coordinated, in a square planar O₃N geometry; three positions are occupied by the ligand while the fourth equatorial position is occupied by a hydroxy oxygen atom belonging to a hydroxyl group. Dy1 and Dy2 are nona-coordinate with their coordination polyhedra best described as capped square antiprisms; N1 and O16 are capping the square antiprisms, respectively. Dy3 is octa-coordinate with a square antiprismatic geometry.

Table 4.8. Selected bond lengths (Å) and bond angles (°) within the coordination cluster in **31**.

Dy1—O5	2.2687 (17)	Dy1—N1	2.514 (2)	Dy2—O3	2.3365 (17)
Dy1—O8	2.3186 (17)	Dy1—O19	2.5523 (18)	Dy2—O8	2.3489 (16)
Dy1—O3	2.3393 (17)	Dy1—O13	2.6052 (17)	Dy2—O6	2.3824 (17)
Dy1—O12	2.4039 (16)	Dy1—N6	2.943 (2)	Dy2—O2	2.3850 (17)
Dy1—O1	2.4139 (16)	Dy1—Cu1	3.4360 (3)	Dy2—O11	2.3915 (17)
Dy1—O18	2.4950 (18)	Dy1—Dy2	3.5494 (2)	Dy2—O15	2.3964 (17)
Dy2—O1	2.5014 (17)	Dy3—O6	2.3380 (17)	Dy3—O22	2.4736 (19)
Dy2—N2	2.505 (2)	Dy3—O11	2.3477 (17)	Cu1—O12	1.9139 (17)
Dy2—O16	2.7057 (17)	Dy3—O2	2.3866 (18)	Cu1—O14	1.9281 (18)
Dy2—Cu2	3.3706 (3)	Dy3—O23	2.4158 (19)	Cu1—O1	1.9449 (16)
Dy2—Dy3	3.5526 (2)	Dy3—O21	2.4162 (19)	Cu1—N4	1.945 (2)
Dy3—O9	2.2159 (18)	Dy3—N3	2.470 (2)	Cu2—O15	1.9126 (17)
Cu2—O17	1.9215 (19)	Cu2—N5	1.946 (2)	Cu2—O2	1.9519 (18)
Cu1—O1—Dy1	103.53 (7)	Cu1—O1—Dy2	120.14 (8)	Dy1—O1—Dy2	92.44 (6)
Cu2—O2—Dy2	101.54 (7)	Cu2—O2—Dy3	118.24 (8)	Dy2—O2—Dy3	96.24 (6)
Dy2—O3—Dy1	98.77 (6)	Dy3—O6—Dy2	97.63 (6)	Cu2—O15—Dy2	102.35 (7)
Cu1—O12—Dy1	104.89 (7)	Dy3—O11—Dy2	97.11 (6)	Dy1—O8—Dy2	99.01 (6)

4.5.2 Static magnetic properties of 31-34

The temperature dependence of dc susceptibility data of **31-34** are given in Table 4.9. The experimental data at room temperature are in good agreement with theoretical values. The plots of χT vs T for all complexes (**31-34**) show similar trends (Fig. 4.23, left). The χT product of Gd₃^{III}Cu₂^{II} (**32**) remains almost constant on decreasing temperature between temperature

($24.70 \text{ cm}^3 \text{ K mol}^{-1}$) and 25 K ($24.70 \text{ cm}^3 \text{ K mol}^{-1}$) below which it rapidly decreases reaching $12.45 \text{ cm}^3 \text{ K mol}^{-1}$ at 1.8 K. The shape of the χT vs T plot of **32** indicates that paramagnetic behaviour in temperature range of 25-300 K and below 24 K weak intramolecular antiferromagnetic in **32**. The χT products of $\text{Dy}_3^{\text{III}}\text{Cu}_2^{\text{II}}$ (**31**), $\text{Tb}_3^{\text{III}}\text{Cu}_2^{\text{II}}$ (**33**) and $\text{Ho}_3^{\text{III}}\text{Cu}_2^{\text{II}}$ (**34**) slowly decrease from room temperature to 10 K, below which they fall sharply until temperature reaches 1.8 K (Fig. 4.23, left). The slow decrease of χT value at higher temperature (25-300 K) is due to gradual depopulation Stark sub-levels, and the sharp fall below 10 K is due to intramolecular antiferromagnetic interactions and/or ZFS of Ln^{III} ions.

Table 4.9. The dc magnetic data of compounds **31-34**.

Compound	Ground state of Ln^{III} ion	χT expected for non-interacting ions per complex ($\text{cm}^3 \text{ K mol}^{-1}$)	χT measured at 300 K per complex ($\text{cm}^3 \text{ K mol}^{-1}$)	χT measured at 1.8 K per complex ($\text{cm}^3 \text{ K mol}^{-1}$)	Magnetization at 2 K and 7 T (μ_B)
$\text{Dy}_3^{\text{III}}\text{Cu}_2^{\text{II}}$ (31)	$^6\text{H}_{15/2}$	43.26	44.25	27.50	19.48
$\text{Gd}_3^{\text{III}}\text{Cu}_2^{\text{II}}$ (32)	$^8\text{S}_{7/2}$	24.39	24.70	12.45	23.19
$\text{Tb}_3^{\text{III}}\text{Cu}_2^{\text{II}}$ (33)	$^7\text{H}_6$	36.21	37.06	21.96	17.88
$\text{Ho}_3^{\text{III}}\text{Cu}_2^{\text{II}}$ (34)	$^5\text{I}_8$	42.96	42.96	18.66	18.42

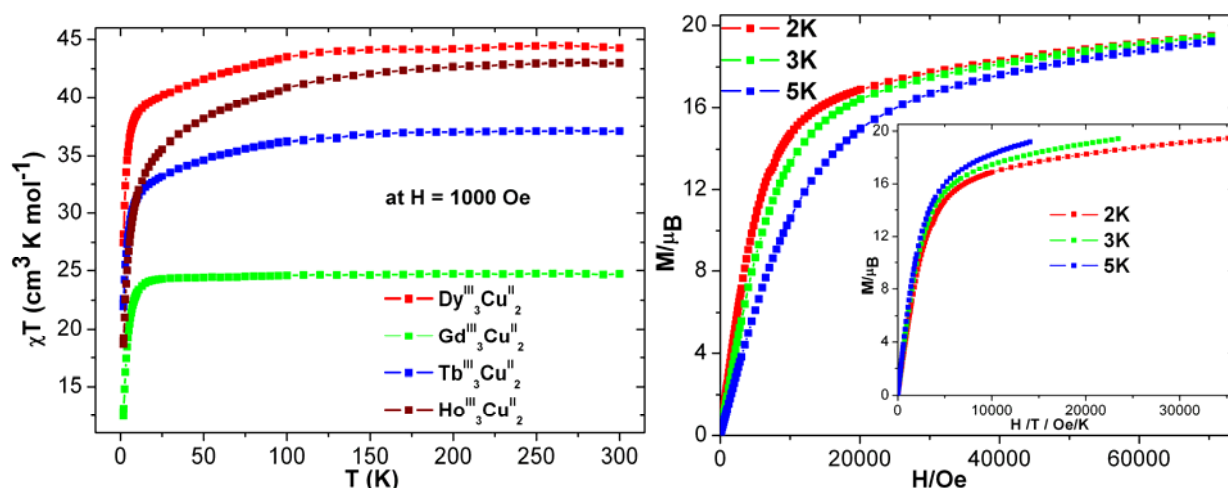


Fig. 4.23. Plots of χT vs T of **31-34** (left), M (right) and M vs H/T (right, inset) of **31**.

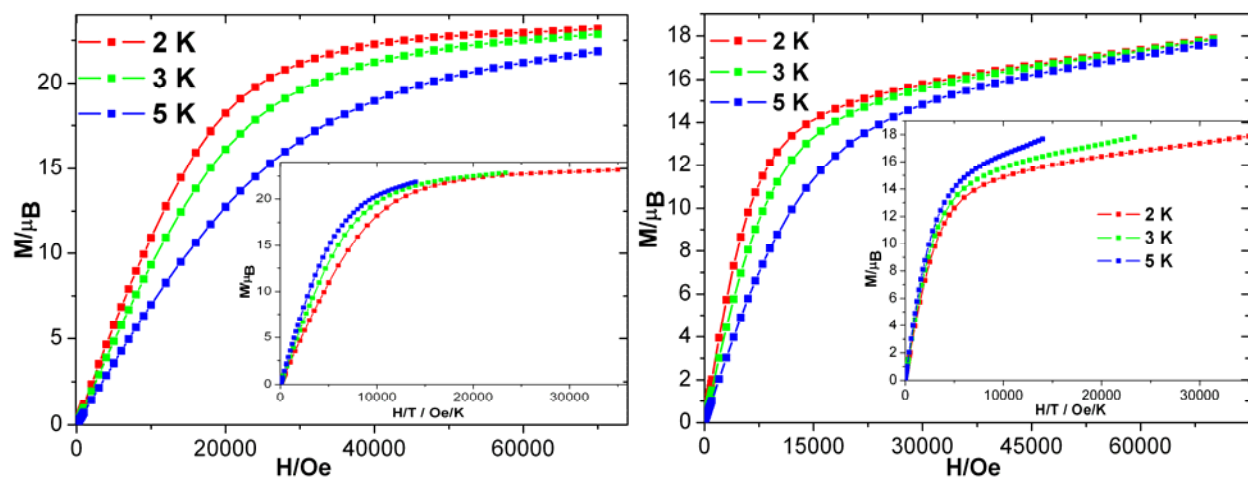


Fig. 4.24. Plots of H and M vs H/T (inset) of **32** (left) and **33** (right) at indicated temperatures.

At 2 K, the field dependence of the magnetizations for all the complexes (**31-34**) increase on increasing dc field to reach the maximum values without true saturation of magnetization except for **32**. The magnetization values of complexes (**31-34**) are given in Table 4.9. (Fig. 4.23, right; 4.24 and 4.25). The magnetization value of **32** reaches 23.19 at 2 K, which is expected for 3 Gd^{III} and 2 Cu^{II} ions. This infers that the intramolecular antiferromagnetic interactions in **32** are weak and could be overcome when the applied dc magnetic reaches more than 30 kOe (Fig. 4.24, left).

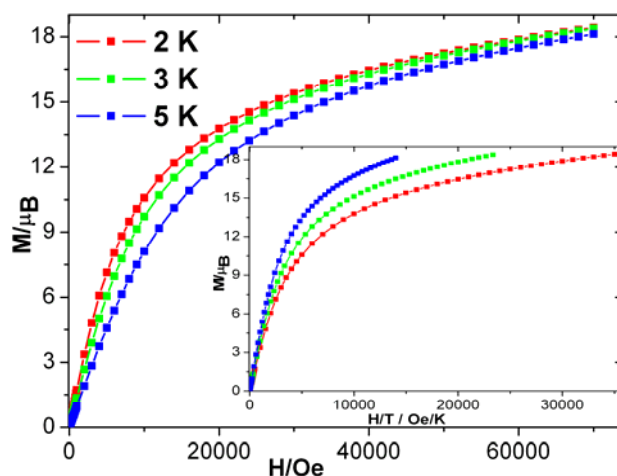


Fig. 4.25. Plots of H and M vs H/T (inset) of **34** (left).

Moreover, the M vs H/T plots at low temperatures (Fig. 4.23, right; 4.24 and 4.25; inset) of complexes **31**, **33** and **34** do not superpose on a single master-curve as expected for isotropic systems, further indicating the presence of magnetic anisotropy and/or low lying excited states. The same trend is observed in **32** indicating the presence of low lying excited states.

4.5.3 Dynamic magnetic properties of 31-34

The temperature dependence of ac susceptibility measurements on all the complexes (**31-34**) reveal the presence of detectable in-phase (χ') and out-of-phase (χ'') susceptibility below 10 K only for **31**. The out-of-phase susceptibility (χ'') of $\text{Dy}_3^{\text{III}}\text{Cu}_2^{\text{II}}$ (**31**) increases with increasing frequency (Fig. 4.26) below 6 K. The presence of out-of-phase susceptibility without a maximum indicates that complex **31** might be an SMM with blocking temperature below 1.8 K. The reported ^{38d} linear Dy^{III}_3 complex is ferromagnetically coupled and possesses two relaxation processes below 15 K. The magnetic core of $\text{Dy}^{\text{III}}_3\text{Cu}_2^{\text{II}}$ (**31**) is rather different, containing a bent Dy^{III}_3 unit with two Cu^{II} ions coupled to Dy^{III} ions through the two $\mu_3\text{-OH}$ bridges. The coupling of two Cu^{II} ions with linear Dy^{III}_3 may have changed the directions of easy axis and spin energy levels as well, resulting in changed relaxation behaviour (Fig. 4.26).

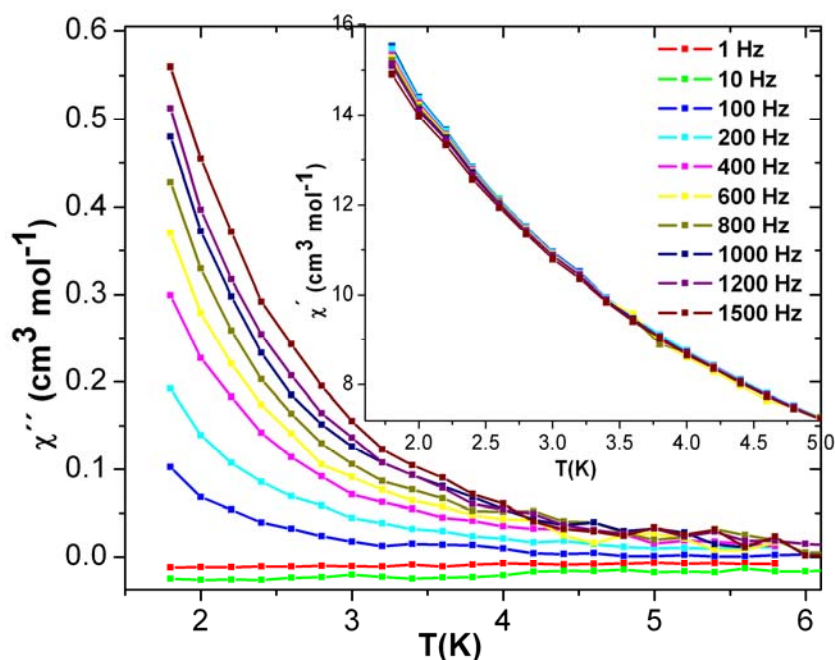


Fig. 4.26. Plots of χ'' and χ' (inset) vs T of **31** at indicated applied frequencies.

4.6.1 Crystal structures of $[\text{Ln}_2\text{Co}_2(\text{L1})_4(\text{NO}_3)_2(\text{THF})_2] \cdot 4\text{THF}$; $[\text{Ln} = \text{Dy}(\mathbf{35}), \text{Y}(\mathbf{36}), \text{Gd}(\mathbf{37}), \text{Tb}(\mathbf{38}), \text{Ho}(\mathbf{39}) \text{ and } \text{Er}(\mathbf{40})]$

All the tetranuclear Ln_2Co_2 complexes (**35-40**) are isomorphous, crystallizing in the space group $P-1$. The compounds **35** and **36** are fully crystallographically characterized while for the other the unit cell constants were checked. The structures of **35-40** are very similar to that of $[\text{Dy}_2\text{Ni}_2(\text{L1})_4(\text{NO}_3)_2(\text{DMF})_2]$ (**1**) or $[\text{Dy}_2\text{Ni}_2(\text{L1})_4(\text{NO}_3)_2(\text{MeOH})_2] \cdot 3\text{MeOH}$ (**2**) which has been described in chapter 3, and so their structures need not to be described in detail. The Dy_2Ni_2 (**1/2**) and Dy_2Co_2 (**35**) crystallizes in different space group. The coordinated 2 DMF/MeOH ligands in **1** or **2** are replaced by two THF ligands in **35-40** (Fig. 4.27). Selected bond lengths and angles are given in Table 4.10.

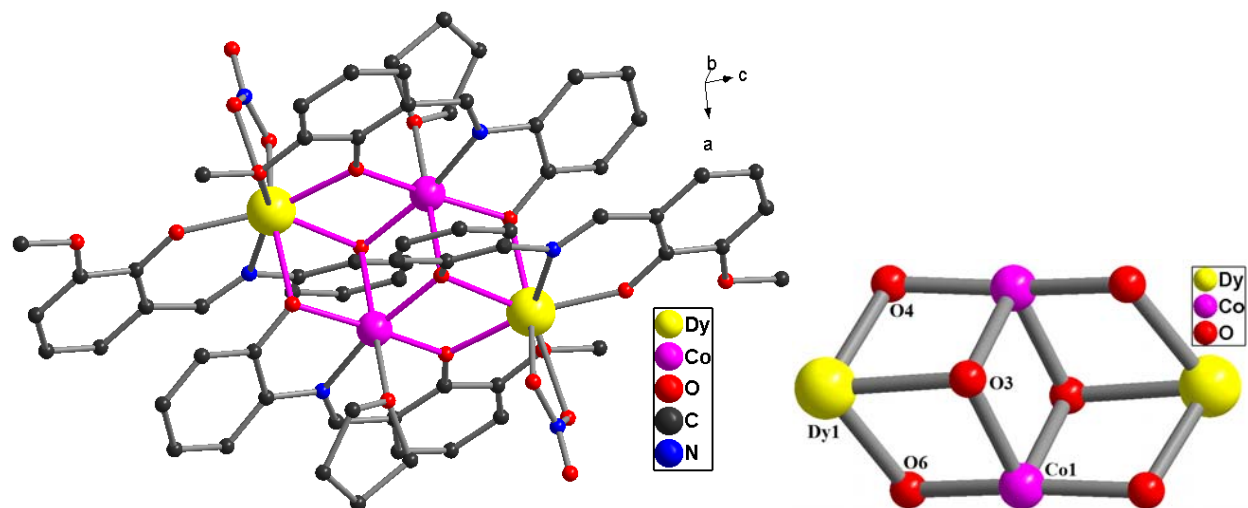


Fig. 4.27. Molecular structure (left) and core (right) of coordination cluster in compound **35**.

Table 4.10. Selected bond lengths (Å) and bond angles (°) within the coordination cluster in **35**.

Dy1—O1	2.155 (3)	Dy1—O7	2.441 (3)	Dy1—N3	2.892 (3)
Dy1—O4	2.306 (2)	Dy1—N1	2.454 (3)	Dy1—O5	2.518 (3)
Dy1—O6 ⁱ	2.343 (3)	Dy1—O8	2.480 (3)	Dy1—O3	2.390 (3)
Co1—O6	2.036 (3)	Co1—O3 ⁱ	2.261 (3)	Co1—O10	2.197 (3)
Co1—O4	2.038 (3)	Co1—O3	2.077 (2)	Co1—N2	2.062 (3)
Dy1—Co1	3.4962 (6)	Co1—Dy1 ⁱ	3.4886 (6)	O3—Co1Co1 ⁱ Dy1	1.069
Co1—O3—Dy1	102.77 (10)	Co1—O4—Dy1	107.03 (10)	Co1—O6—Dy1 ⁱ	105.41 (10)
C28—O6—Dy1 ⁱ	121.1 (2)	Co1 ⁱ —O3—Dy1	97.15 (9)		

Symmetry code: (i) $-x+1, -y+1, -z+1$.

4.6.2 Static magnetic properties of 35-40.

The magnetic data of **35-40** are summarized in Table 4.11. At room temperature, the χT value of $5.20 \text{ cm}^3 \text{ K mol}^{-1}$ for **36** is larger than the expected ($3.75 \text{ cm}^3 \text{ K mol}^{-1}$) spin-only value for two Co^{II} ions ($S = 3/2$ spin) and two diamagnetic Y^{III} ions (Fig. 4.28, inset).

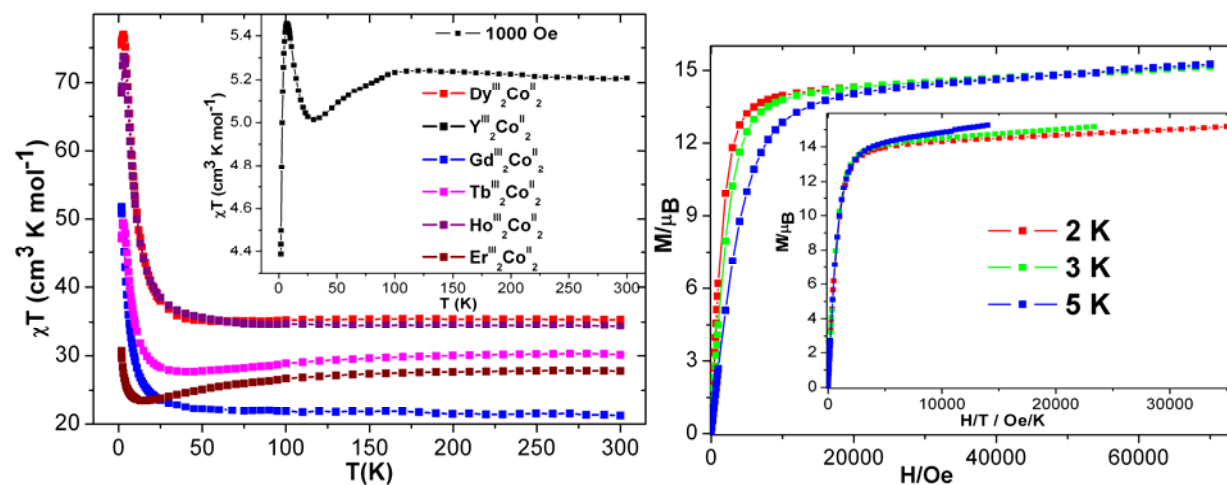


Fig. 4.28. Plots of χT vs T of **35-40** at 1000 Oe dc field. Plots of M vs H and H/T (inset) of **35** (right).

Table 4.11. dc magnetic data of compounds **35-40**.

Compound	Ground state of Ln^{III} ion	χT expected for non-interacting ions per complex ($\text{cm}^3 \text{ K mol}^{-1}$)	χT measured at 300 K per complex ($\text{cm}^3 \text{ K mol}^{-1}$)	χT measured at 1.8 K per complex ($\text{cm}^3 \text{ K mol}^{-1}$)	Magnetization at 2 K and 7 T (μ_B)
$\text{Dy}^{\text{III}}_2\text{Co}^{\text{II}}_2$ (35)	${}^6\text{H}_{15/2}$	32.09	35.34	75.42	15.17
$\text{Y}^{\text{III}}_2\text{Co}^{\text{II}}_2$ (36)	-	3.75	5.20	4.38	3.98
$\text{Gd}^{\text{III}}_2\text{Co}^{\text{II}}_2$ (37)	${}^8\text{S}_{7/2}$	19.51	21.19	51.71	20.16
$\text{Tb}^{\text{III}}_2\text{Co}^{\text{II}}_2$ (38)	${}^7\text{H}_6$	27.39	30.14	47.13	13.86
$\text{Ho}^{\text{III}}_2\text{Co}^{\text{II}}_2$ (39)	${}^5\text{I}_8$	31.89	34.40	68.40	16.47
$\text{Er}^{\text{III}}_2\text{Co}^{\text{II}}_2$ (40)	${}^4\text{I}_{15/2}$	26.71	27.77	30.71	13.74

This is often found for Co^{II} containing compounds, as a result of the orbital contribution of the high spin Co^{II} ions to the magnetization. On lowering the temperature the χT product of **36**

remains almost constant till 110 K and below that slowly decreases reaching a minimum value of $5.01 \text{ cm}^3 \text{ K mol}^{-1}$ at 29 K possibly due to depopulation higher of J levels ($5/2$, $3/2$ etc.). Below 29 K, χT product increases to a maximum of $6.66 \text{ cm}^3 \text{ K mol}^{-1}$ at 5.5 K due to ferromagnetic coupling between two Co^{II} ions, followed by a sharp fall to $4.38 \text{ cm}^3 \text{ K mol}^{-1}$ at 1.8 K due to ZFS of Co^{II} ions (Fig. 4.28, inset).

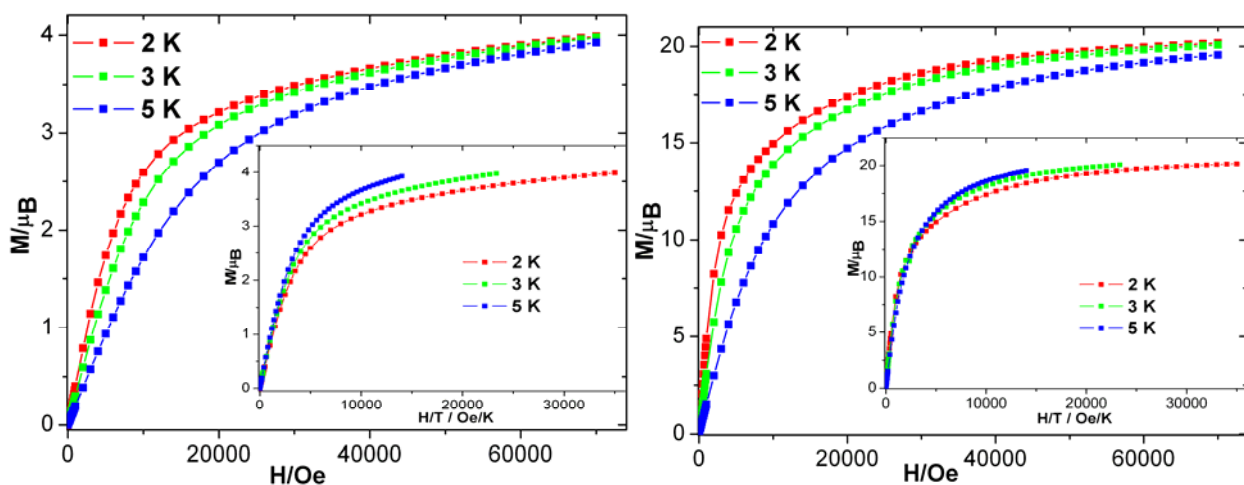


Fig. 4.29. Plots of H and M vs H/T (inset) of **36** (left) and **37** (right) at indicated temperatures.

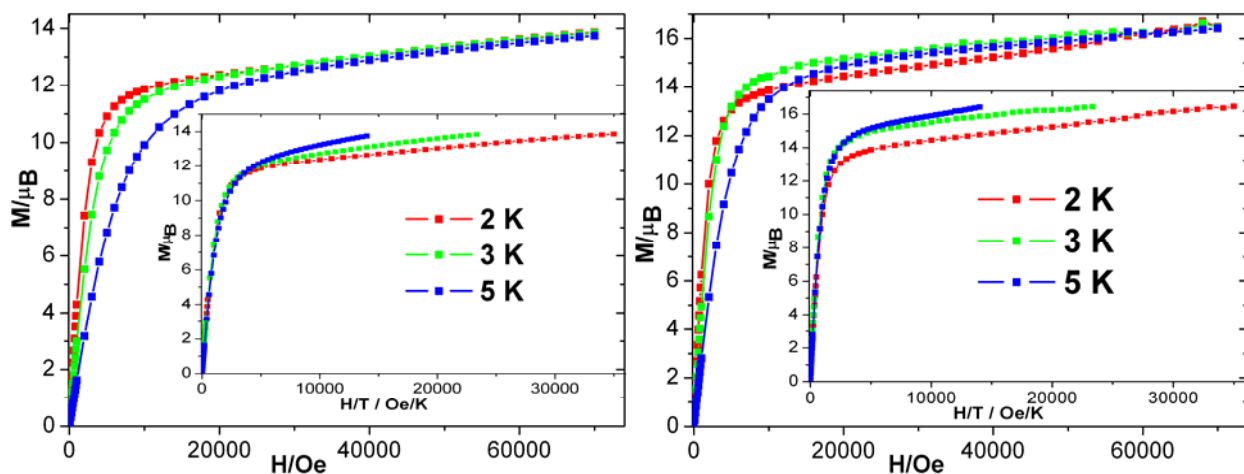


Fig. 4.30. Plots of H and M vs H/T (inset) of **38** (left) and **39** (right) at indicated temperatures.

The room temperature χT values of **35** and **37-40** are 35.34, 21.19, 30.14, 34.50 and $27.77 \text{ cm}^3 \text{ K mol}^{-1}$ respectively, which are in good agreement with the expected values for the sum of the experimental value of the Co^{II}_2 unit obtained from **36** and the Curie constants for two

respective Ln^{III} ions. On lowering the temperature, the χT products of **37** and **39** remain almost constant down to 50 K, below which they continuously increase to reach $51.71 \text{ cm}^3 \text{ K mol}^{-1}$ at 1.8 K and $73.71 \text{ cm}^3 \text{ K mol}^{-1}$ at 3 K, respectively. Below 3 K, the χT product of **39** falls sharply to $68.40 \text{ cm}^3 \text{ K mol}^{-1}$ at 1.8 K possibly due to ZFS of $\text{Co}^{\text{II}}/\text{Ho}^{\text{III}}$ ions (Fig. 4.28).

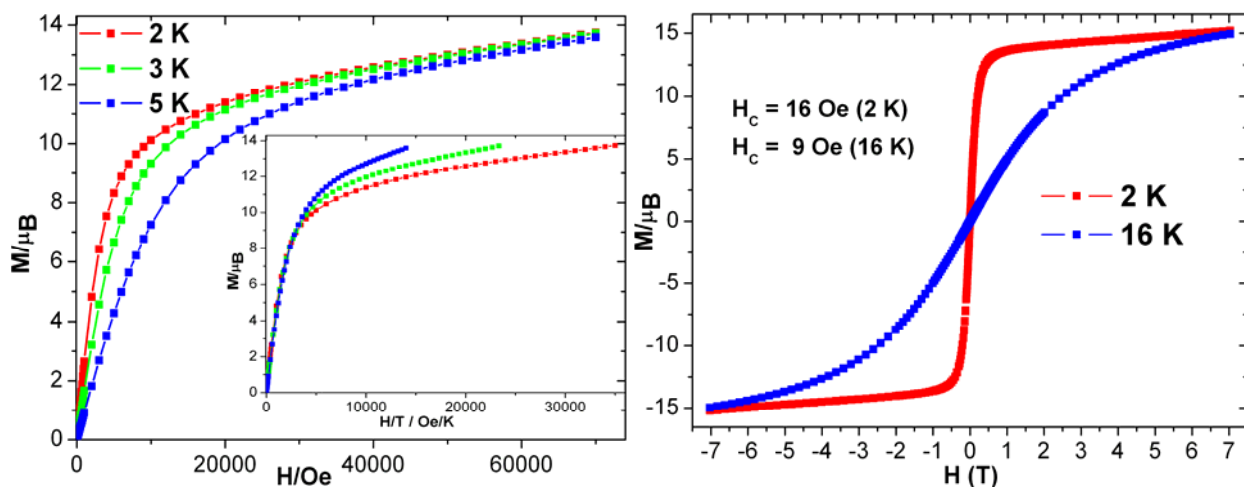


Fig. 4.31. Plots of H and M vs H/T (inset) of **40** (left) at indicated temperatures. Hysteresis loops of **35** at 2 and 16 K.

The χT products of **35**, **38** and **40** slowly decrease with decreasing temperature reaching minimum values of $35.15 \text{ cm}^3 \text{ K mol}^{-1}$ at 55 K (**35**), $27.75 \text{ cm}^3 \text{ K mol}^{-1}$ at 35 K (**38**) and $23.52 \text{ cm}^3 \text{ K mol}^{-1}$ at 17 K (**35**). Below these respective temperatures, the χT products of **35**, **38** and **40**, sharply increase to maximum values at 3 K (**35** and **38**) and 1.8 K (**40**), followed by sharp falls till 1.8 K (**35** and **38**). The gradual fall of χT products of **35**, **38** and **40** at higher temperatures, is due to depopulation of Stark sub-levels. The shape of the χT vs T plots of **35** and **37-40** indicates intramolecular ferromagnetic interaction between Co-Co and Co-Ln at low temperatures (Fig. 4.28).

The field dependence of the magnetization of compounds **35-40** measured at low temperatures shows a gradual increase of the magnetization for **36**, **37** and **40** with a lack of saturation even at 7 T. The magnetizations of **35**, **38** and **39** increase sharply below 0.5 T and increase linearly at higher fields (Fig. 4.28-4.31), indicating the presence of stronger ferromagnetic interactions within **35**, **38** and **39** compared to **36**, **37** and **40**. The M vs H/T curves (Fig. 4.28-4.31, inset) of **35-40** do not superpose on a single master-curve which further indicates

the presence of magnetic anisotropy and/or low lying energy states in all the complexes (**35-40**). The measurement of hysteresis loops on powder sample of **35** revealed appearance of very narrow hysteresis loops at 2 and 16 K with coercive field (H_C) of 16 and 9 Oe respectively (Fig. 4.31, right). Complex **35** reaches saturation of magnetization ($15.17 \mu_B$) value even at 16 K.

4.6.3 Dynamic magnetic properties of 35-40.

In order to detect any slow relaxation associated with SMM behavior, variable-temperature ac susceptibility measurements on **35-40** were performed with 1000 Hz frequency. There is no out-of-phase susceptibility detected above 1.8 K for **36** and **40**, while compounds **35**, **37**, **38** and **39** display a frequency-dependent out-of-phase signal (Fig. 4.32-4.34).

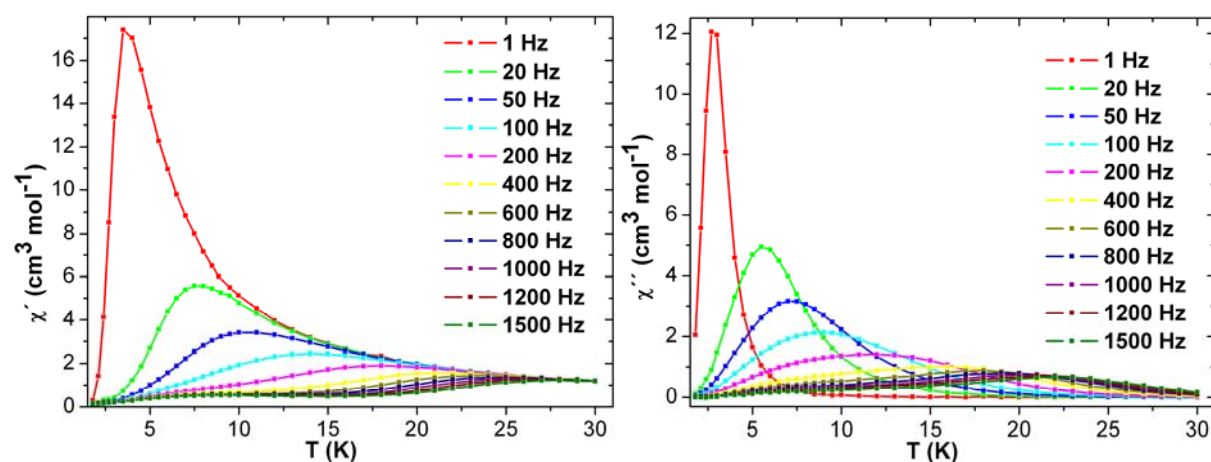


Fig. 4.32. Plots of χ' (left), χ'' (right) vs T of **35** at indicated frequencies.

Since no out-of-phase signal was observed for the Y_2Co_2 (**36**) or Er_2Co_2 (**40**) analogues, it can be concluded that the magnetic slow-relaxation behavior of Dy_2Co_2 (**35**), Tb_2Co_2 (**38**) and Ho_2Co_2 (**39**) complexes arises largely from the anisotropic contribution of respective Ln^{III} ions (Dy, Tb and Ho). However, the presence of weak out phase signals in χ'' vs T plots (Fig. 4.34, left) of Gd_2Co_2 (**37**) infers that anisotropic contribution from Co^{II} ions towards SMM behavior is not negligible.

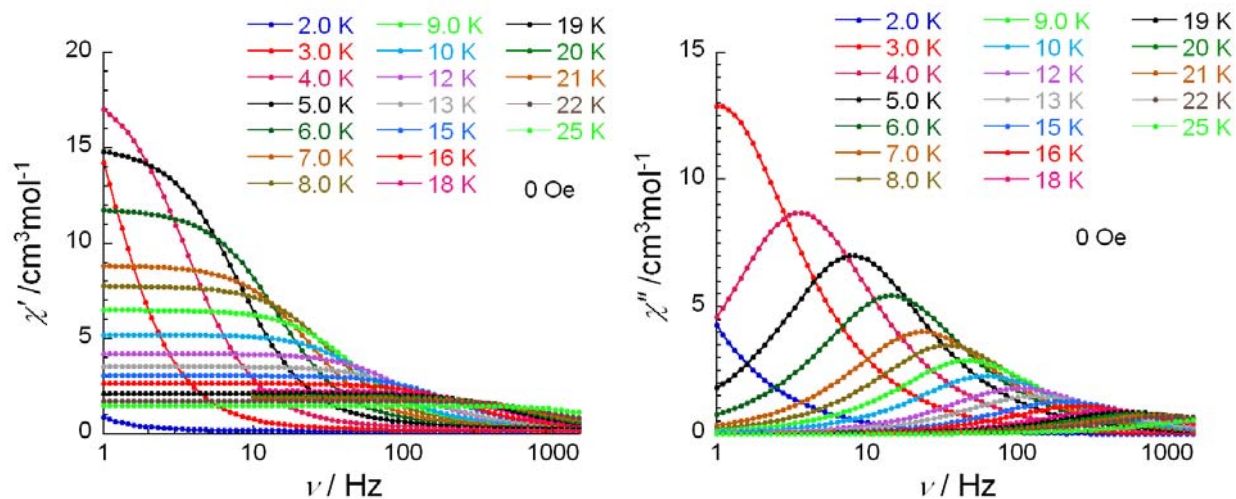


Fig. 4.33. Plots of χ' (left), χ'' (right) vs frequency of **35** at indicated temperatures.

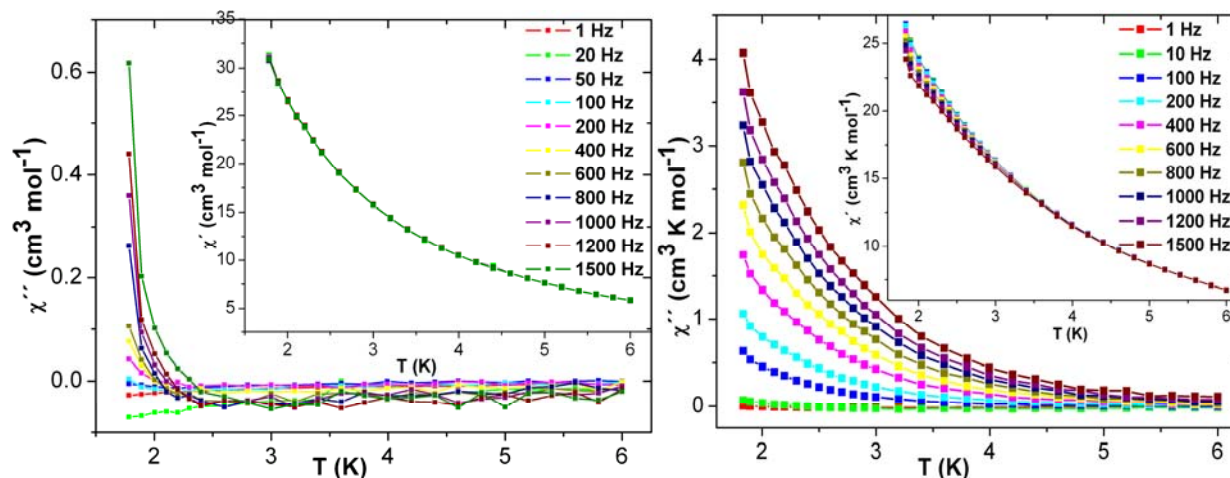


Fig. 4.34. Plots of χ'' (left), χ' (left, inset) vs T of **37** (left) and **38** (right).

There is no maxima in the χ'' vs T plots (Fig. 4.34) of **37** and **38** indicating that they may be SMM with T_b below 1.8 K. The slow relaxation of magnetization of **35** was observed at temperatures up to 30 K. In this series (**35-40**), Dy_2Co_2 (**35**) has the highest blocking temperature (T_b) of 22 K (maximum in χ'' vs T plot) at 1500 Hz (Fig. 4.32, right). The detectable ac signals were also observed in χ' and χ'' vs frequency plots (Fig. 4.33, right) in the temperature range of 1.8-25 K. All the above mentioned ac plots (Fig. 4.32-4.33) of **35** indicate more than one relaxation path ways are operating. The χ' and χ'' vs frequency measurements at different field indicate absence of QTM path ways in **35**. The linear fittings on the Arrhenius plot of **35** (Fig.

4.39, left) gave two energy barriers; one is 17.67 K with $\tau_0 = 4.9 \times 10^{-4}$ s and other one is 81.68 K with $\tau_0 = 3.9 \times 10^{-6}$ s.

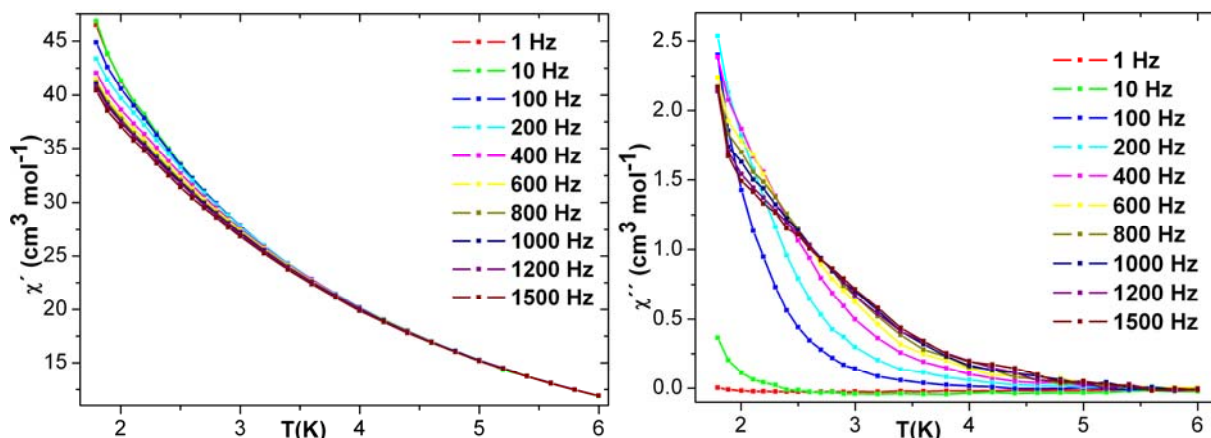


Fig. 4.35. Plots of χ' (left), χ'' (right) vs T of **39** at indicated frequencies.

The relaxation dynamics of **39** is little different than rests of this series. Both χ' and χ'' vs T plots of **39** (Fig. 4.35) do not show maxima, instead but a shoulder is visible, suggesting the presence of QTM or there may be more than one relaxation process involved. A careful look at χ'' vs T plots at different frequencies reveals that the out-of-phase susceptibility (χ'') increases with the decrease of T as the frequency increases from 1-400 Hz but above 400 Hz, the rate of increase of χ'' decreases below 2.5 K as the frequency increases from 400-1500. This kind of χ'' vs T signature suggests that the relaxation process is weakly temperature dependent and relation dynamic is taken by that of static and/or there may be more than one relaxation processes involved. The ac susceptibility vs frequency measurements (Fig. 4.36) under zero applied magnetic field in the temperature range of 1.8 to 3.5 K show the appearance of a further maximum at higher frequencies. The ac susceptibility vs frequency measurements (Fig. 4.37) under different applied magnetic fields at 1.8 and 2.5 K reveal the presence of QTM pathway.

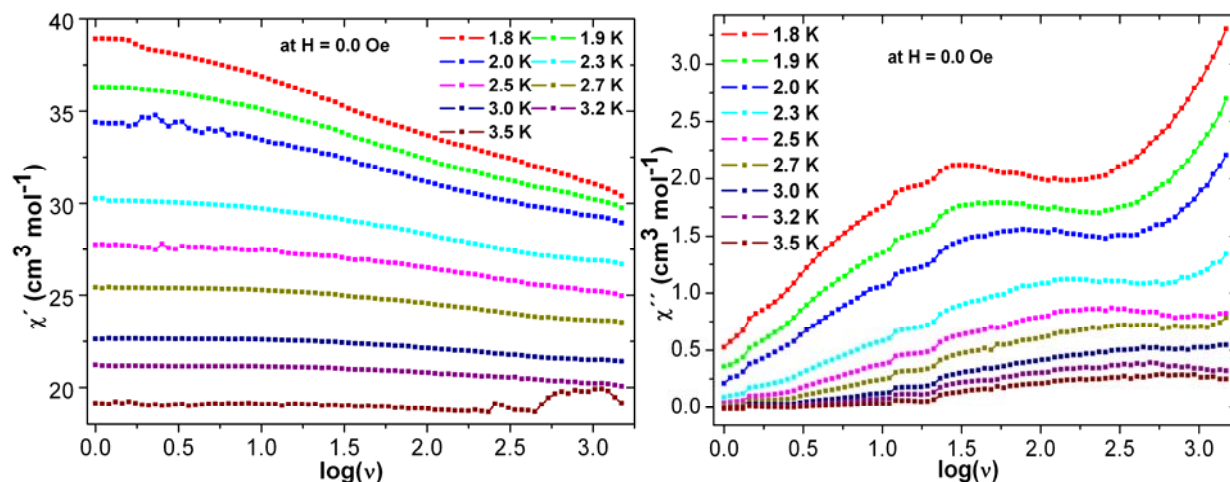


Fig. 4.36. Plots of χ' (left), χ'' (right) vs frequency of **39** at indicated temperatures.

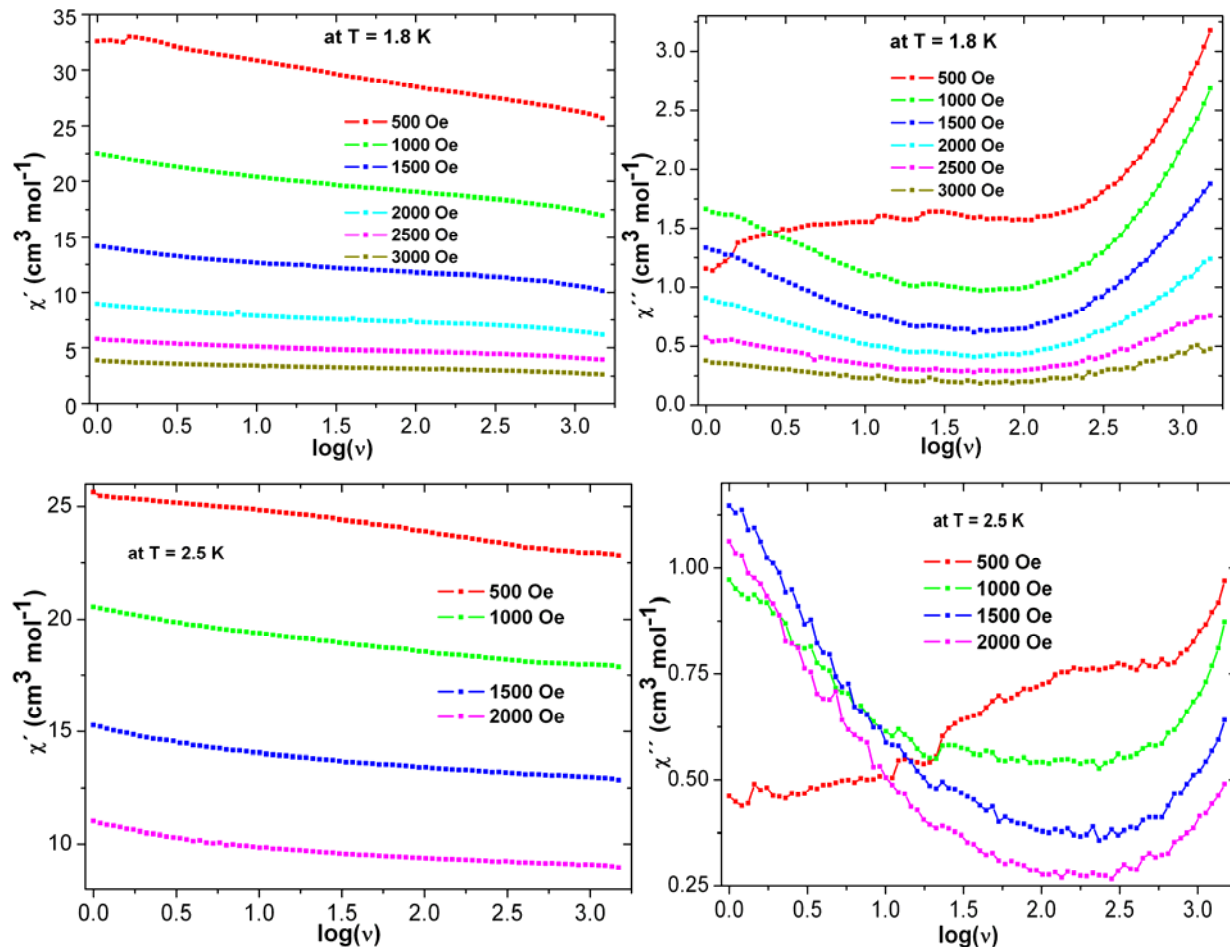


Fig. 4.37. Plots of χ' (left), χ'' (right) vs frequency of **39** at 1.8 (top) and 2.5 (bottom) K under indicated dc fields.

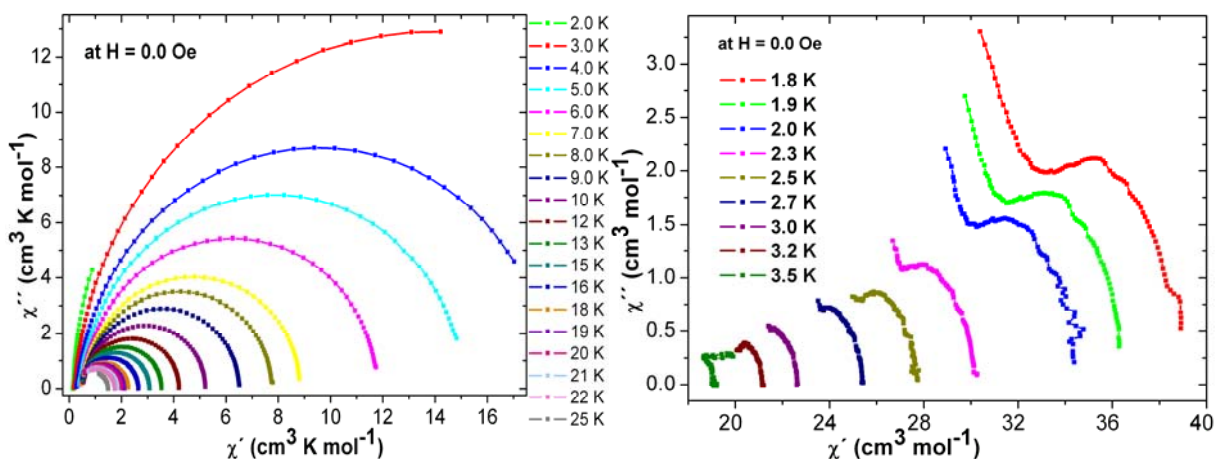


Fig. 4.38. Cole-Cole plots of **35** (left) and **39** (right) under zero dc field.

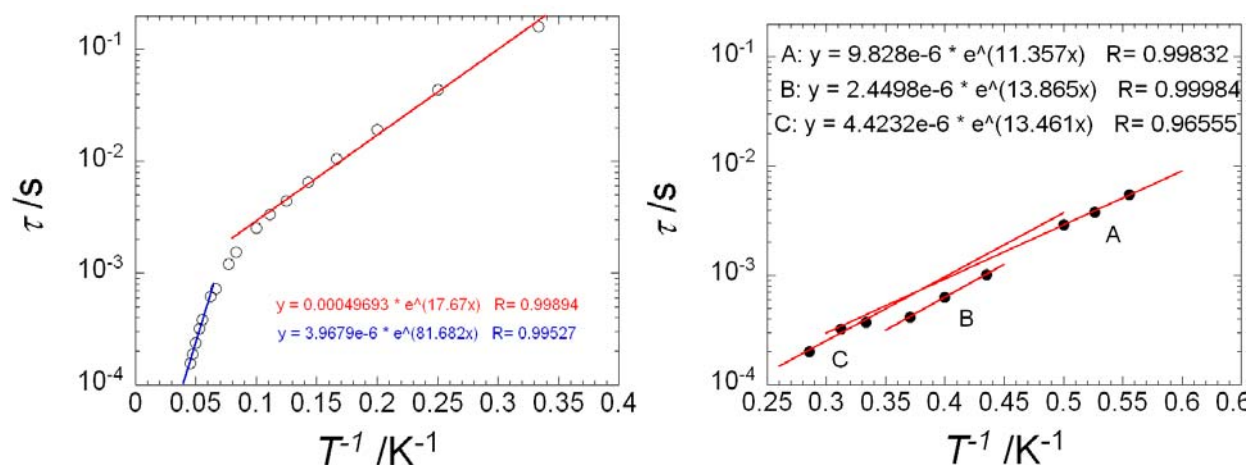


Fig. 4.39. Arrhenius plots of **35** (left) and **39** (right) under zero applied dc field.

This kind of shape of **39** originates from mixing of more than one relaxation processes which is bolstered by Cole-Cole (Fig. 4.38, right) and Arrhenius plots (Fig. 4.39, right). The linear fittings on the Arrhenius plot of **39** gave three energy barriers of similar magnitude; the first one is 11.35 K with $\tau_0 = 9.82 \times 10^{-4}$ s, the second one is 13.86 K with $\tau_0 = 2.44 \times 10^{-6}$ s and the third is 13.46 K with $\tau_0 = 4.42 \times 10^{-6}$ s (Fig. 4.39, right).

4.7 Conclusion:

In this chapter five different series of heterometallic $M^{II}-Ln^{III}$ ($M = Zn^{II}, Cd^{II}, Cu^{II}$ and Co^{II}) compounds have been obtained using similar molar ratios and reaction conditions. The five series are $[Ln_2Zn_3(OH)(L1)_5(MeOH)_{2.5}(OH_2)_{1.5}]Cl \cdot 3(MeOH) \cdot 2.5(H_2O)$; [$Ln = Dy$ (**21**), Eu (**22**), Gd (**23**), Tb (**24**) and Ho (**25**)], $[Dy_7Zn_4(OH)_4(L1)_8(Cl)_6(H_2O)_4]Cl_3 \cdot 35H_2O$ (**26**), $[Ln_6Cd_6(CO_3)_2(OH)_4(\mu-Cl)_2(Cl)_2(L1)_8(OH_2)_{12}]Cl_2 \cdot 10THF$ [$Ln = Dy$ (**27**), Tb (**28**), Ho (**29**) and Er (**30**)], $[Ln_3Cu_2(\mu_3-OH)_2(L1)_5(NO_3)(MeOH)_2(H_2O)] \cdot 3MeOH \cdot xH_2O$ [$Ln = Dy$ (**31**), Gd (**32**), Tb (**33**), and Ho (**34**), $x = 0$ for **31**, **32**, **34** and $x = 1$ for **33**] and $[Ln_2Co_2(L1)_4(THF)_2(NO_3)_2] \cdot 4THF$ [$Ln = Dy$ (**35**), Y (**36**), Gd (**37**), Tb (**38**), Ho (**39**) and Er (**40**)]. The cores of the most of the above mentioned different series are unprecedented. The nuclearity and topology of the final products has been found to be different with variation of M^{II} ions. A careful look at all the structures with consideration of the sizes, geometries and number of d-electrons of the M^{II} ions ($M = Zn^{II}, Cd^{II}, Cu^{II}$ and Co^{II}) led the following possible explanations.

The divalent zinc and cadmium ions have $3d^{10}$ and $4d^{10}$ electronic configurations respectively. The Cd^{II} ions are blatantly larger in size than that of Zn^{II} ions and hence their ionic radius and geometries are different. Thus their affinities towards the dianionic ligands ($L1^{2-}$) are different.

The Cu^{II} ions are found to display distorted square pyramidal geometries in **31-35** like Zn^{II} ions in **21-26**. But the equatorial Cu-O/N distances are always smaller than that of Zn-O/N and apical axes of Cu^{II} ions are longer than that of Zn^{II} ions resulting from the d^9 Jahn-Teller distortion. In $Ln^{III}_3Cu^{II}_2$ (**31-35**) complexes both the Cu^{II} ions sit in the plane of pocket-I (ONO) while Zn^{II} ions (Zn1 and Zn2) are found to be 0.739 and 0.760 Å respectively above the plane of pocket-I (ONO) in $Dy^{III}_7Zn^{II}_4$ (**26**). These immanent differences between the two ions (Cu^{II} and Zn^{II}) might have played pivotal role on the deciding fate of the final products (**21-26** and **31-35**). The imminent growth of pentanuclear $Ln^{III}_3Cu^{II}_2$ (**31-35**) is blocked by two terminal ligands. The Cd^{II} ions are far bigger in size than Zn^{II}/Cu^{II} ions but similar to the size of Na^+/Ln^{III} ions. As a consequence positive charge density is higher in Ln^{III} ions than that in Cd^{II} ions and hence dianionic ligands ($L1^{2-}$) may bind to more cationic Ln^{III} ions than Cd^{II} ions. Under the basic condition $\{Cd(OH)_2\}$ units might have trapped atmospheric CO_2 to convert it into carbonate (CO_3^{2-}) which joined the two $Ln^{III}_3Cd^{II}_3$ units of $Ln^{III}_6Cd^{II}_6$ (**27-30**), together with the $\mu-Cl$ ligands. When the M^{II} is octahedral (either Ni^{II} or Co^{II} ions) it produced Ln_2M_2 with a defect-

dicubane topology before it captures atmospheric CO₂. The synthetic strategies of preparation of five new series M-Dy (M = Zn^{II}, Cd^{II}, Cu^{II} and Co^{II}) have been illustrated in Table 4.1.

The magnetic and/or optical properties of all complexes (**21-40**) have been investigated. Among the Ln^{III}₂Zn^{II}₃ series the Dy (**21**) and Tb (**24**) analogues show intramolecular ferromagnetic interactions while the rest of this series possibly exhibit antiferromagnetic interaction. Only Dy (**21**) analogue of this series displays slow relaxation of magnetization below 10 K, but without a maximum in ac susceptibility vs T plots, implying T_b below 1.8 K. The fluorescence measurements at room temperature reveal bathochromic emission peak in between 475 to 650 nm when excited either at wavelength either of 300–350 or 430–460 nm. The complexes **21-25** ostentatiously emit yellow fluorescence radiation upon irradiation by UV-lamp.

The undecanuclear Dy^{III}₇Zn^{II}₄ (**26**) complex contains an unprecedented Dy^{III}₇ magnetic core which is connected to four {Zn^{II}L1} optical units connected by four μ₃-OH bridges. The dc magnetic measurements reveal possible weak intramolecular antiferromagnetic interactions. The ac measurements show frequency dependent ac signal below 15 K without a peak in ac susceptibility vs T plots, implying T_b below 1.8 K. The fluorescence measurements reveal interesting bathochromic emission peaks either at 510 and 544 nm or 544 nm when excited either at wavelength either of 468 or 500 nm respectively.

The dodecanuclear Ln₆Cd₆ [Ln = Dy(**27**), Tb(**28**), Ho(**29**) and Er(**30**)] clusters were found to have fixed atmospheric CO₂ during the reaction in ambient temperature and pressure. The dc magnetic measurements show that among this series, the Dy(**27**) analogue has intramolecular weak ferromagnetic coupling while the other (**28-30**) are possibly antiferromagnetically coupled. The ac measurements reveal the presence of ac signal and relaxation dynamic is weakly temperature dependence and taken by that of static. The fluorescence spectroscopy of all four (**27-30**) compounds show multiple bathochromic emission peaks in the visible range when excited in either UV or visible range. Thus bi-functional Dy₆Cd₆ (**27**) is a fluorescence SMM with two energy barriers of 4.82 and 14.89 K. Ln₆Cd₆ (**27-30**) are the highest nuclearity coordination clusters based on Cd^{II}-Ln^{III} ions.

The dc magnetic measurements on Ln^{III}₃Cu^{II}₂ [Ln = Dy(**31**), Gd(**32**), Tb(**33**), and Ho(**34**)] compounds reveal the presence of intramolecular weak intramolecular antiferromagnetic interactions and ac measurements show that only the Dy(**31**) analogue has slow relaxation of

magnetization below 10 K, without a maximum in ac susceptibility vs T plots, implying T_b below 1.8 K. The Gd-Cu magnetic interactions in Gd(32) have been found to be weakly antiferromagnetic.

The Ln_2Co_2 [$\text{Ln} = \text{Dy}$ (35), Y (36), Gd (37), Tb (38), Ho (39) and Er (40)] clusters with a defect-dicubane topology were found to be magnetically interesting though they are consisted of only two (36) or four (35 and 37-40) highly anisotropic magnetic centers. The dc magnetic measurements reveal the presence of dominant ferromagnetic coupling in all complexes (35-40). The magnetization increases very rapidly (below 0.5 T) with the increasing H at 2 K. The dynamic measurements reveal that Dy (35) analogue has engrossing slow relaxation of magnetization with a T_b of 22 K and two relaxation energy barriers (≈ 17 and 81 K), thus 35 has the highest blocking temperature and energy barrier among all 3d-4f based SMMs so far reported in the literature. The ac dynamics of 37 shows the presence of weak out-of-phase signal in Gd(37) analogue implying the anisotropic contributions from Co^{II} ions are not negligible. The Tb (38) analogue shows the presence of ac signals below 10 K without a maximum in ac susceptibility vs T plots, implying T_b below 1.8 K. The relaxation dynamics of Ho (39) analogue is more complicated by the mixing of more than one relaxation pathways. The fittings on Arrhenius plots produce three energy barriers ranging from 11 to 13 K.

Chapter 5

Tetranuclear 4f Coordination Clusters with (E)-2-(2-hydroxy-3-methoxybenzylidene-amino)phenol (H₂L1) and (E)-N'-(2-hydroxy-3-methoxybenzylidene)-(2-hydroxy)-benzohydrazide (H₃L3)

5.1 Introduction

Coordination chemistry has become an effective tool for designing and synthesizing new materials from zero dimensional⁷ molecular clusters to multidimensional polymeric networks.¹² The proper combination of organic ligands and metal ions results in the synthesis of compounds which possess various physical properties such as magnetism,^{7,12} catalysis,^{54a} porosity,^{54b-c} optical,^{54d} photo-luminescence⁵⁵ etc. Initially coordination compounds of 3d metal ions were employed for reaching some targeted properties in the materials. More recently 4f (lanthanide) ions have been found useful for some applications.^{54d} The 4f ions generally have higher coordination numbers than the 3d metal ions and thus different coordination compounds may be expected with same the ligand.⁵⁶

One of the most promising aspects of the 4f ions (Ln^{III}) is their optical properties.^{54d-55} By virtue of this they have been employed as dopants in the semiconductor GaN in order to produce visible-light emitting materials.⁵⁷ Some lanthanide compounds are also able to absorb UV radiation and emit in visible region.^{54d-55} Mixed lanthanide, for example Gd^{III} and Eu^{III}, compounds have also been found useful for their photoluminescence properties with high quantum yields.^{55a} Lighting devices such as eco-friendly luminescent lamps, light emitting diodes used in television and computer displays, optical fibers, optical amplifiers, lasers, as well as responsive luminescent stains for biomedical analysis, medical diagnosis, and cell imaging rely heavily on lanthanide ions.^{54d-55} Trivalent lanthanide ions are also employed to produce materials which emit in the Near Infra Red (NIR) region⁵⁸ as NIR photons can penetrate deep into tissues without causing damage and without significant loss of intensity owing to the low absorption of NIR photons in such media and NIR light also diffracts much less than visible light.⁵⁸

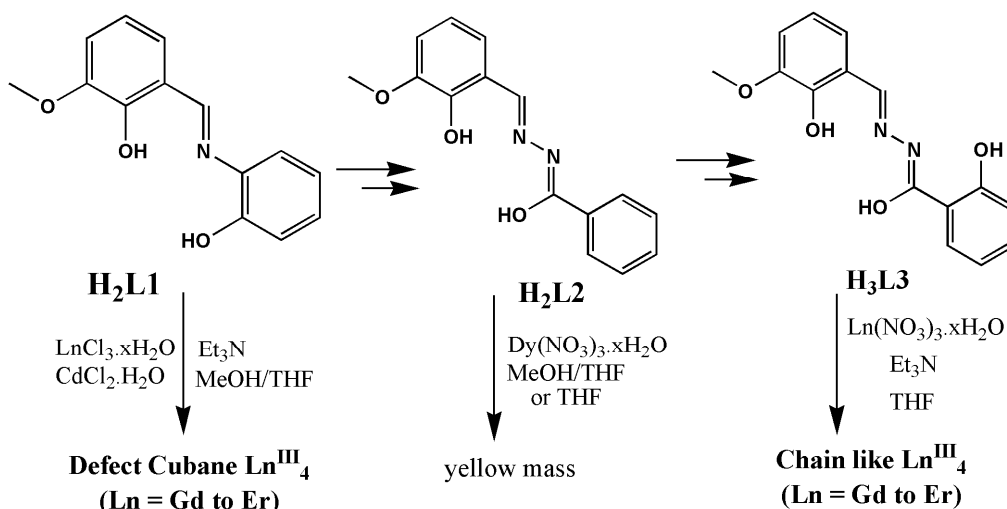
Probably the most interesting aspect of the 4f ions is their magnetic properties.⁴³ Some trivalent lanthanide (Dy^{III}, Tb^{III}, Ho^{III} etc.) ions have unquenched orbital angular momentum and display Ising type single-ion magnetic anisotropy,⁴³ so that magnetic clusters of these 4f ions can

display fascinating magnetic properties such as SMM behavior.^{5,6} As a result the nature of the 4f orbitals, exchange interactions between lanthanide ions, e.g. Dy^{III} ions in a purely Dy^{III} based clusters, is very weak. Nevertheless, because of their single ion anisotropy they can have higher blocking temperatures and energy barriers to reversal of magnetization and also often display multiple relaxation processes.⁴⁰ Thus lanthanide compounds give vast range of deeply engrossing materials with a broad range of physical properties.^{40,50,54d-58}

5.2 Synthetic strategy

In the previous two chapters, 3d-4f chemistry based on the H₂L1 ligand was described. The Schiff-base ligand H₂L1 was prepared through condensation of o-vanillin and 2-aminophenol. The H₂L1 has two phenolic –OH groups which are easier to deprotonate because of the increased acidity (compared with amide proton) resulting from the stabilization of phenolate anions through the aromatic ring structure. Similar ligands (H₂L2 and H₃L3) were synthesized in order to explore the coordinative analogies in this set of ligands. Thus, the ligands H₂L2 and H₃L3 are similar to H₂L1 (Scheme 5.1) but with the phenolic OH-group in H₂L1 replaced by the amide O-atom of a –CO–NH group (or OH group of –C(OH)=N–). Since the lone pair on amide O-atoms are more delocalized on conjugated π -electronic clouds, the donation tendency of lone pairs on amide O-atom decreases. In comparison to the H₂L2, the H₃L3 has an additional phenol –OH in the aromatic ring.

The reaction of LnCl₃·6H₂O and CdCl₂·H₂O with H₂L1 in the presence of base (Et₃N) in the molar ratio of 1:1:2:5 led to the formation of a series of defect-dicubane tetranuclear [Ln^{III}₄(OH)₂(L1)₄(HL1)₂]·2THF [Ln = Dy(**41**), Gd(**42**), Tb(**43**), Ho(**44**) and Er(**45**)] complexes from MeOH and THF solvent mixtures. The Cd^{II} salt apparently prevents further hydrolysis of lanthanide salts. After the successful isolation of compounds **41-45**, the H₂L2 ligand was reacted in a similar fashion but only an amorphous yellow mass was obtained. Thus, the ligand was modified to H₃L3. The H₂L2 was functionalized into its *ortho*-position of aromatic ring of the hydrazide part, by OH-group instead of H-atom to make H₃L3 (Scheme 5.1). The reaction of Ln(NO₃)₃·6H₂O with H₃L3 in the presence of base (Et₃N) in the molar ratio of 2:1:2 led to the formation of a series of chain like tetra nuclear (Et₃NH)₆[Ln₄(HL3)₂(NO₃)₁₀(H₂O)₄](NO₃)₄ [Ln = Er(**46**), Gd(**47**), Tb(**48**), Dy(**49**) and Ho(**50**)] complexes from THF solution upon ether diffusion.



Scheme 5.1. Synthetic strategy for preparation of two tetranuclear Ln^{III}_4 compounds.

In this chapter the synthesis of two different series of Ln^{III}_4 cluster (**41-50**), obtained by adjusting reaction conditions are described.

5.2.1 Crystal Structures of $[\text{Ln}_4(\text{OH})_2(\text{L1})_4(\text{HL1})_2] \cdot 2\text{THF}$ [$\text{Ln} = \text{Dy}(\mathbf{41})$, $\text{Gd}(\mathbf{42})$, $\text{Tb}(\mathbf{43})$, $\text{Ho}(\mathbf{44})$ and $\text{Er}(\mathbf{45})$]

The compounds from **41-45** are isomorphous and crystallize in the triclinic space group $P-1$, thus only the crystal structure of **41** will be described here. The identities of compounds **42-45** were established by checking their unit cells parameters as well as the X-ray powder diffraction patterns.

The asymmetric crystallographic unit contains two Dy^{III} ions, one $\mu_3\text{-OH}$, two fully deprotonated dianionic ligands $(\text{L1})^{2-}$, one zwitterionic ligand $\{\text{H}^+(\text{L1})^{2-}\}$ and one lattice THF molecule. All four Dy^{III} ions are coplanar forming a defect-dicubane core (Fig. 5.1), although two external Dy-Dy edges are bridged by two oxygen, not one. Dy1 and Dy2 have coordination number eight with a square antiprismatic O_7N donor set. Two triply bridging OH^- groups are situated $0.893(2)$ Å either above or below the plane of the four Dy^{III} ions. The ligand displays three different bridging modes ($\eta^1:\eta^2:\eta^1:\eta^2:\mu_3,\eta^1:\eta^1:\eta^2:\mu_2$ and $\eta^1:\eta^1:\eta^1:\mu_2$, Fig. 1. 5). All ligands act in a chelating and/or bridging mode; the first ligand joining $\text{Dy1}'\text{-Dy2-Dy1}$, the second with $\text{Dy1}'\text{-Dy2}$ and the third one Dy2-Dy1 . Between the Dy1-Dy2 and $\text{Dy1}'\text{-Dy2}'$ centers there are two μ_2 -phenoxide O-atom bridges. Both Dy1 and Dy2 centers are chelated by pocket-1 (ONO)

and pocket-II (OO). The mono deprotonated ligands are zwitterions with the two phenolic oxygens in each ligand as phenoxides, both accepting a hydrogen bond from the N-H of the protonated imine nitrogen (Fig. 5.1). These two ligands are nearly coplanar with Dy₄ plane whereas the fully deprotonated ligands are nearly perpendicular to it. The shortest intermolecular Dy1-Dy1 distance is 10.25Å. Selected bond lengths and angles were given in Table 5.1 along with three other similar reported Dy₄ defect-dicubanes.

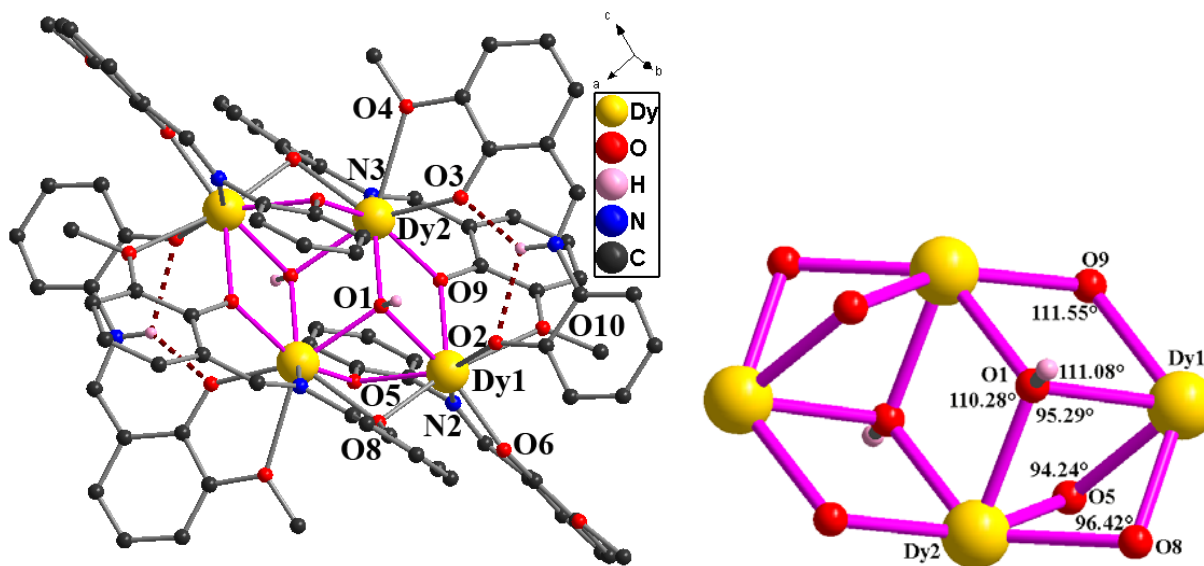


Fig. 5.1. Molecular structure (left) and core (right) of the coordination cluster in compound **41**.

Table 5.1. Selected bond lengths (Å) and bond angles (°) within the coordination cluster in **41** along with three other similar reported Dy₄.

Dy-X (41)	41	Dy ₄ ^{36b}	Dy ₄ ^{36c}	Dy ₄ ^{36d}
Dy1-O5	2.430(4)	2.358(4)	2.534(9)	2.543(4)
Dy1-O8 ¹	2.357(5)	2.488(4)	2.724(3)	2.299(5)
Dy1-O6	2.220(5)	2.557(4)	2.297(6)	2.458(4)
Dy1-O2	2.259(4)	2.354(6)	2.493(7)	2.410(5)
Dy1-N2	2.470(6)	2.369(5)	2.565(8)	2.576(5)
Dy1-O9	2.389(5)	2.369(4)	2.197(7)	2.286(5)
Dy1-O1	2.415(5)	2.370(4)	2.367(6)	2.334(4)
Dy1-O10	2.562(5)	2.358(4)	2.448(6)	2.258(4)
Dy2-O1 ¹	2.351(4)	2.346(4)	2.451(6)	2.447(4)
Dy2-O1	2.329(5)	2.337(4)	2.306(6)	2.373(4)
Dy2-O9	2.342(5)	2.306(4)	2.344(6)	2.284(4)
Dy2-O3	2.292(4)	2.351(4)	2.454(8)	2.372(5)
Dy2-N3	2.503(6)	2.467(5)	2.509(8)	2.402(5)

Dy2-O4	2.687(5)	2.388(4)	2.196(6)	2.397(5)
Dy-X (41)	41	Dy ₄ ^{36b}	Dy ₄ ^{36c}	Dy ₄ ^{36d}
Dy2-O8	2.370(4)	2.472(5)	2.592(6)	2.343(5)
Dy2-O5 ⁱ	2.293(5)	2.289(4)	2.312(6)	2.370(4)
Dy-O-Dy (41)	41	Dy ₄ ^{36b}	Dy ₄ ^{36c}	Dy ₄ ^{36d}
Dy2-O9-Dy1	111.6(2)	112.8(2)	114.8(3)	106.5(2)
Dy2-O1-Dy1	111.1(2)	110.3(2)	107.4(2)	101.7(2)
Dy2-O1-Dy2 ⁱ	110.3(2)	111.4(2)	105.4(2)	113.90(2)
Dy2 ⁱ -O1-Dy1	95.3(2)	94.78(14)	102.5(2)	107.0(2)
Dy2 ⁱ -O5-Dy1	96.3(2)	95.95(15)	106.2(2)	102.4(2)
Dy1 ⁱ -O8-Dy2	96.4(2)	94.46(14)	Dy1-N1N2-Dy2	Dy1-OCO-Dy2
O1- Dy ₃ (plane)	0.893(2)	0.922	0.905	0.872(4)
Dy(1) ... Dy(2)	3.9116(6)	3.8693(4)	3.883	3.8319(4)
Dy(1) ... Dy(2) ⁱ	3.5227(6)	3.4650(5)	3.737	3.6509(4)
Dy(2) ... Dy(2) ⁱ	3.8401(8)	3.8671(6)	3.786	4.0407(6)
Dy(1) geometry	SAP	SAP	SAP	DOD
Dy(2) geometry	distorted SAP	SAP	SAP	DOD-BCTP

Symmetry code: (i) $-x, -y+1, -z+1$. X = O/N/Cl-atom when viewed in similar orientations alike **41**.

5.2.2 Static magnetic properties of **41-45**:

The temperature dependent magnetic susceptibilities of **41-45** were measured on powdered samples in the temperature range 1.8-300 K under an applied dc magnetic field of 1000 Oe (Fig. 5.2). The data are summarized in Table 5.2. The experimental χT values at room temperature in most of the systems, are close to the expected theoretical ones for four non-interacting Ln^{III} ions^{11,43} although slight lower χT values are obtained for **41** and **43** possibly due to population of the low-lying orbitals with lower J values. For the theoretically isotropic complex Gd^{III}₄ (**42**), the χT product remains almost constant from room temperature to 25 K and then rapidly decreases to 13.66 cm³ K mol⁻¹ at 1.8 K indicating the presence of antiferromagnetic intramolecular interactions and/or small ZFS contributions of Gd^{III} ions. The temperature independent behavior suggests the coupling between the Gd^{III} ions is very weak, which is also supported by the small Weiss constant of -2.45 K obtained from the Curie-Weiss fit of the χT product above 15 K. The rapid decrease of the χT product of **42** below 20 K is probably due to the small ZFS and/or weak antiferromagnetic intermolecular interaction. The thermal evolution of the χT of Dy^{III}₄ (**41**) and Ho^{III}₄ (**44**) is similar, in which the χT product slowly decreases with the decrease of temperature to 46.37 (**41**) at 13 K and 48.35 (**44**) cm³ K mol⁻¹ at 15 K and then

rapidly increases to 62.32 (**41**) $\text{cm}^3 \text{K mol}^{-1}$ and 58.08 (**44**) $\text{cm}^3 \text{K mol}^{-1}$ at 1.8 K. This type of behavior suggests the presence of overall intramolecular ferromagnetic couplings among the Ln^{III} ions, but the decrease (Fig. 5.2) of the χT product in the higher temperature range (15-200 K) is likely due to the depopulation of Stark sublevels of Ln^{III} ions.⁴³ Additionally, for compounds Tb^{III}_4 (**43**) and Er^{III}_4 (**45**), the χT product decreases monotonically in the full temperature range, suggesting the presence of overall antiferromagnetic interactions, however, the depopulation of its Stark sublevels of these Ln^{III} ions can also contribute to the decrease of the χT product.

Looking at the static magnetic behavior of this family, the question presents itself as to why the overall interaction changes from antiferromagnetic to ferromagnetic on going from the Tb/Er and Dy/Ho cases? From the result of what might be considered as the isotropic case of the Gd^{III} analogue, the spin-spin magnetic exchange interactions between the Ln^{III} ions in this family are overall likely to be antiferromagnetic. However, as illustrated for the Dy^{III}_3 complex,^{38d} the dipolar interactions between the anisotropic Ln^{III} ions such as Dy^{III} or Ho^{III} ions can be ferromagnetic and rather large depending on the orientation of the easy axes. Since the magnetic exchange intramolecular interaction of this family is very weak we can expect that the dipolar contribution in the case of Dy^{III} and Ho^{III} complexes is sufficient to dominate the exchange interaction, thereby leading to the observed increase of the χT product.

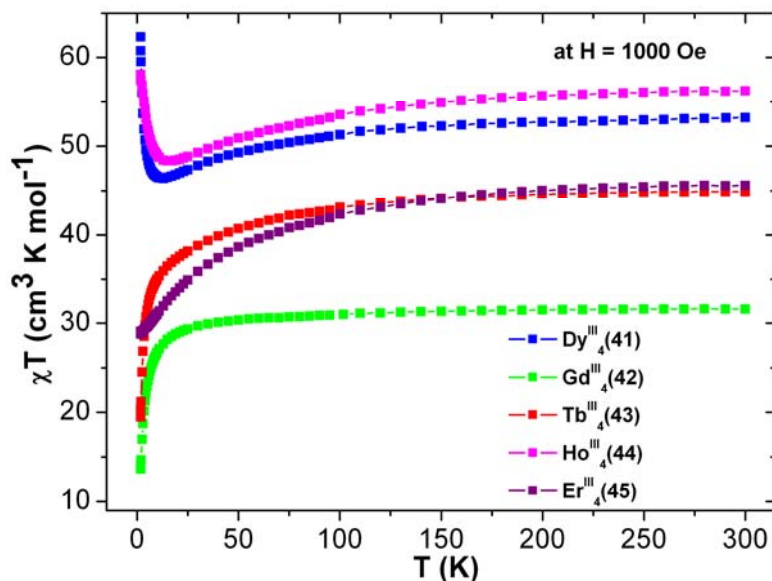


Fig. 5.2. Plots of χT vs T of **41-45** under 1000 Oe dc field.

Table 5.2. The dc magnetic data of compounds 41-45.

Compound	Ground state of Ln ^{III} ion	χT expected for non-interacting ions per complex (cm ³ Kmol ⁻¹)	χT measured at 300 K per complex (cm ³ Kmol ⁻¹)	Curie constant ^a C (cm ³ Kmol ⁻¹)	Weiss constant ^a θ (K)	Magnetization at 2 K and 7 T (μ_B)
Dy ^{III} ₄ (41)	⁶ H _{15/2}	56.68	53.21	53.81	-5.78	20.73
Gd ^{III} ₄ (42)	⁸ S _{7/2}	31.50	31.59	31.85	-2.45	28.03
Tb ^{III} ₄ (43)	⁷ H ₆	47.25	44.90	45.79	-5.63	18.38
Ho ^{III} ₄ (44)	⁵ I ₈	56.28	56.23	57.16	-5.57	22.41
Er ^{III} ₄ (45)	⁴ I _{15/2}	45.92	45.61	47.18	-10.15	19.51

a) Curie-Weiss fit is obtained above 15 K.

The field dependence of magnetization measurements at low temperatures reveals that the magnetization has a relative rapid increase below 1 T and then follows a steady increase up to 7 T. The magnitude of the magnetization is listed in Table 5.2.

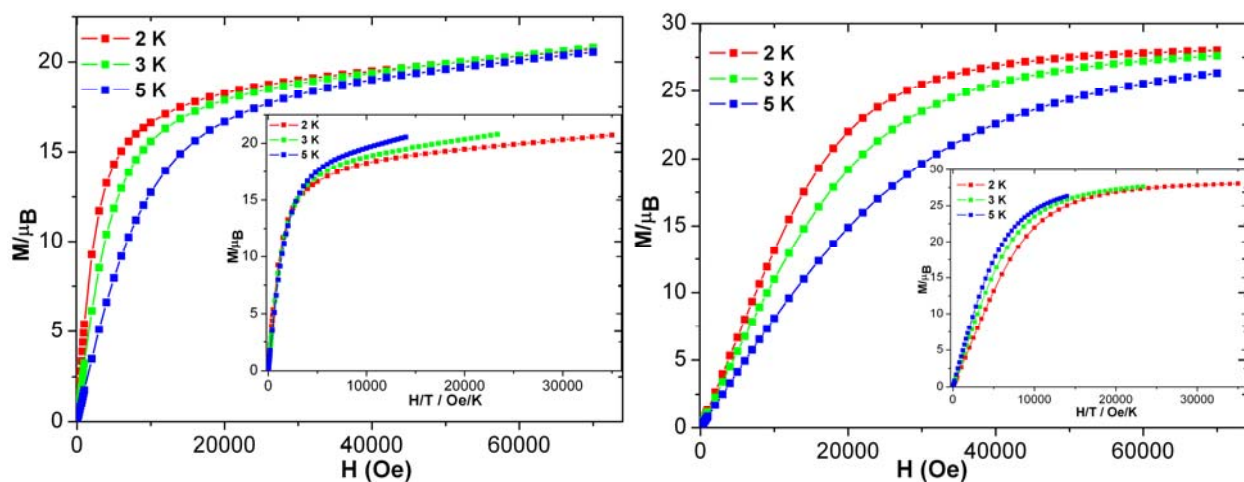


Fig. 5.3. Plots of M vs H and H/T (inset) of **41** (left) and **42** (right) at indicated temperatures.

The lack of true saturation in magnetization of complexes **41** and **43-45** indicates the presence of magnetic anisotropy and/or low lying excited states. However, in the case of

isotropic complex Gd^{III}_4 (**42**), the magnetization almost reaches a saturation of $28.0 \mu_{\text{B}}$, which is in good agreement with the expected value for four non-coupled Gd^{III} ions ($7.0 \mu_{\text{B}}$ per Gd^{III}).

This behavior further suggests that the interaction between Gd^{III} and Gd^{III} is very weak so that the antiferromagnetic interactions are easily overcome by the external field. Furthermore, the M vs H/T plots at low temperatures (Fig. 5.3-5.5, inset) for all the compounds are not superposed on a single master-curve as expected for isotropic systems further indicating the presence of magnetic anisotropy and/or low-lying excited states.⁴³ The slight deviation of M vs H/T at different temperatures for isotropic complex Gd^{III}_4 (**42**) is due to the population of low-lying excited states (Fig. 5.3, right, inset).

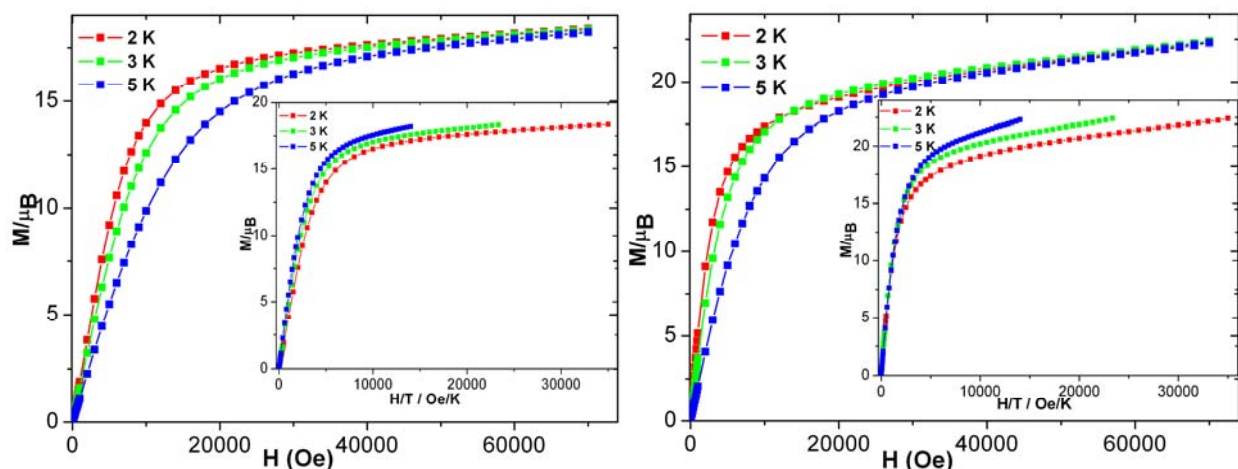


Fig. 5.4. Plots of M vs H and H/T (inset) of **43** (left) and **44** (right) at indicated temperatures.

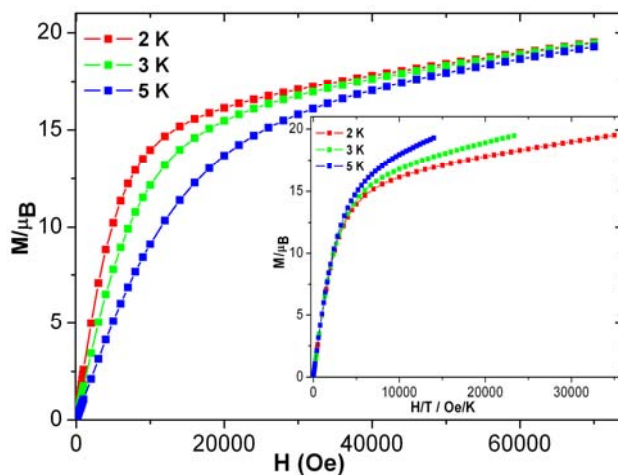


Fig. 5.5. Plots of M vs H and H/T (inset) of **45**.

If four isotropic Gd^{III} ions couple to each at low temperature (below 20 K), they can produce several (15) energy states with corresponding spin value ranging from $S = 0$ to $S = 14$. Since the magnetic coupling is very weak, several closely spaced low-lying energy states are possible. The spin energy states starting from lower S -values to higher S -values are gradually populated depending upon their energies of separations and strength of the applied dc magnetic field.

5.2.3 Dynamic properties of 41-45.

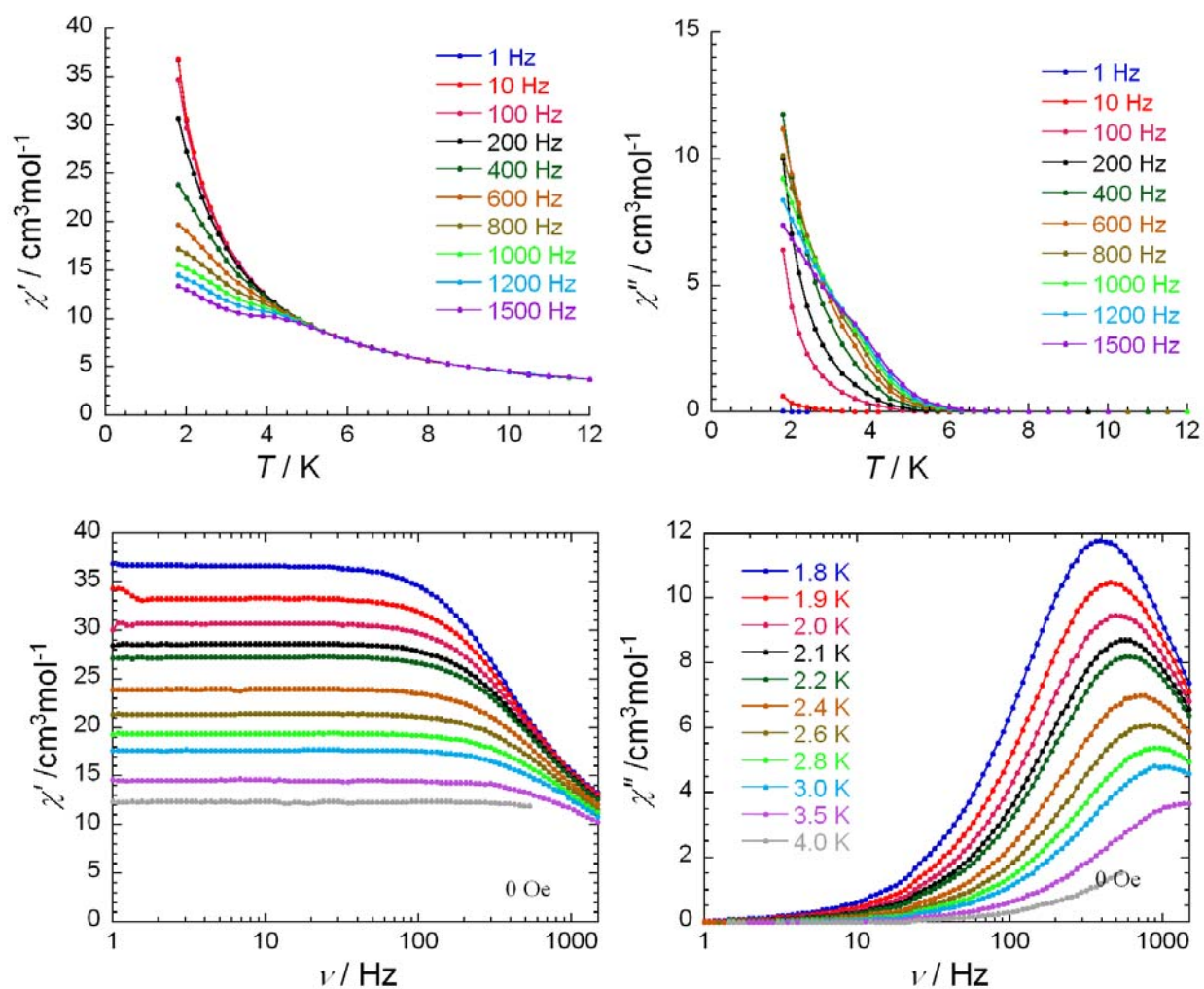


Fig. 5.6. Plots of In phase (χ') and out of phase susceptibility (χ'') vs T (top) and frequency (bottom) of **41** at indicated temperatures under applied dc field $H = 0$ Oe.

The ac measurements were carried out for all five compounds. Of these, only Dy compound **41** shows a non-zero out-of-phase component indicating the presence of slow relaxation of the magnetization. The captive ac susceptibilities of **41** are strongly frequency dependent below 6 K but no maximum could be detected up to 1500 Hz (Fig. 5.6).

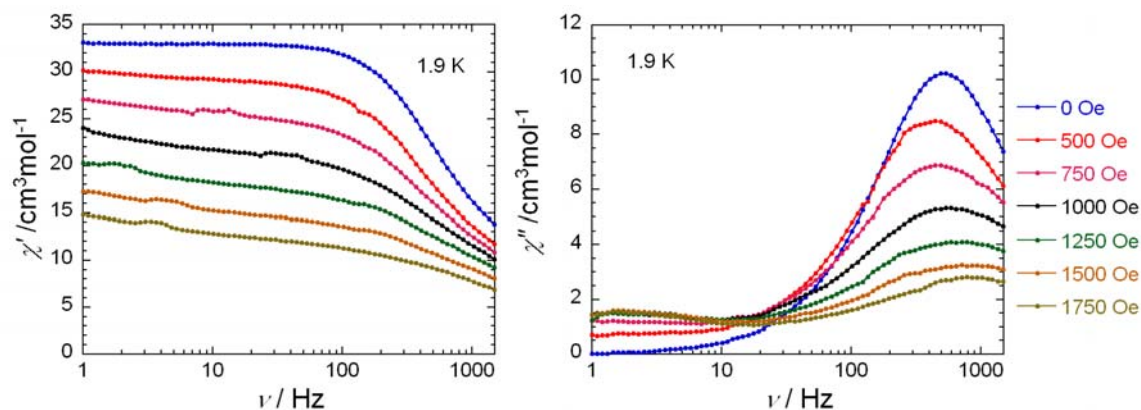


Fig. 5.7. Plots of in-phase (χ') and out-of-phase susceptibility (χ'') vs frequency of **41** under indicated external dc fields.

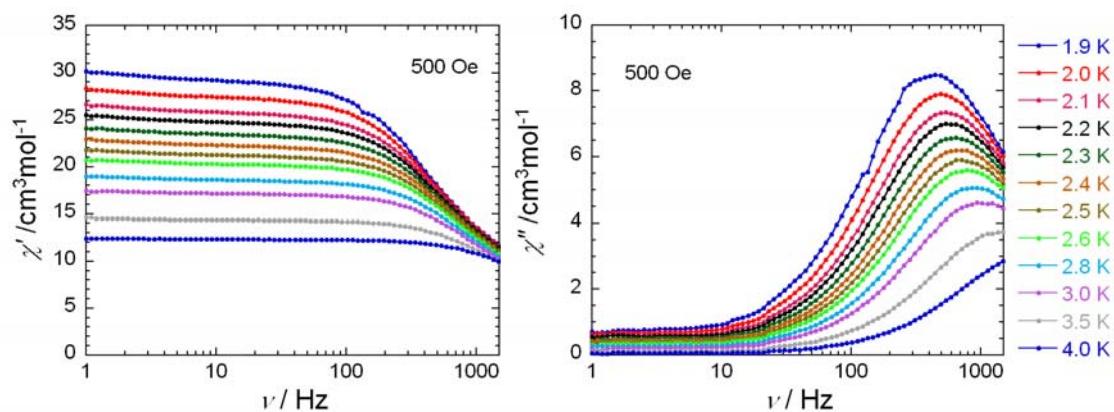


Fig. 5.8. Plots of χ' , χ'' vs frequency of **41** at indicated temperatures under applied dc field $H = 500$ Oe.

It is noticeable that the temperature dependence of out-of-phase susceptibilities are not increasing with the increase of the frequency as often observed in SMMs, suggesting that this complex has a very weak temperature dependence of the relaxation time, probably because tunneling is strong. In this case, the use of ac data vs T is not recommended as the change in the static components overwhelms that of the dynamic. Therefore, the frequency sweeping ac

susceptibilities were collected from 1.8 K to 3.5 K (Fig. 5.6). Both χ' and χ'' are frequency dependent with maxima detected up to 3.5 K. The relaxation time of **41**, deduced from those data (Fig. 5.6), follows an activated behavior with an energy gap (Δ) of 3.7 K and a pre-exponential factor (τ_0) of 4.8×10^{-5} s (5.9, left). The analysis of Cole-Cole plots of χ'' vs χ' exhibits a nearly semicircular shape (5.9, right). Fitting the data using a generalized Debye model^{59a} leads to α in the range of 0.04 - 0.07, which proves that there is one dominant relaxation process (Table 5.3).

Table 5.3. Analysis of Cole-Cole plots of **41**.

T (K)	α	χ_0 (cm ³ /mol)	χ_{inf} (cm ³ /mol)
1.8	0.046(2)	36.707(6)	10.757(78)
1.9	0.044(7)	33.315(15)	10.380(195)
2.0	0.048(8)	30.728(14)	9.946(228)
2.1	0.049(9)	28.650(14)	9.579(244)
2.2	0.058(11)	27.293(17)	9.144(304)
2.4	0.062(8)	24.002(10)	8.476(232)
2.6	0.057(0)	21.440(7)	7.990(146)
2.8	0.046(7)	19.388(6)	7.726(179)
3.0	0.041(0)	17.693(5)	7.421(130)

The frequency dependence of the ac susceptibility was also measured at 1.8 K in an applied dc field (Fig. 5.7). With increasing field the relaxation rate $1/\tau$ slightly decreases from 520 Hz at zero field to a minimum value of 430 Hz at 500 Oe and then increases. This slowing down of magnetic relaxation is typical for quantum tunneling in SMMs.^{59b} Therefore, frequency sweeping ac susceptibilities were performed again under a dc field of 500 Oe (Fig. 5.8). The parameters of the relaxation process now become an energy barrier of 4.9 K and relaxation time of 3.0×10^{-5} s (5.9, left), which are not very different from the one obtained in the absence of dc field. Overall, these experimental results have revealed that this compound indeed exhibits quantum tunneling effect but the dynamic component is not influenced much by an applied transverse field.

A literature survey shows that only three defect-dicubane Dy₄ complexes have been previously reported. In each case, the all four Dy^{III} ions are eight coordinated with an O₇N donor set in **41**, (O₆N₂)/(O₆N₂),^{36b} (O₅N₂Cl)/(O₆N₂),^{36c} and (O₇N)/(O₈)^{36d} donor sets. In all cases two μ_3 -OH groups are above and below the plane by 0.893 (2), 0.922 (2), 0.905 (2) and 0.872 (4) Å respectively (Table 2). However they differ around the periphery of the metal-hydroxide core.

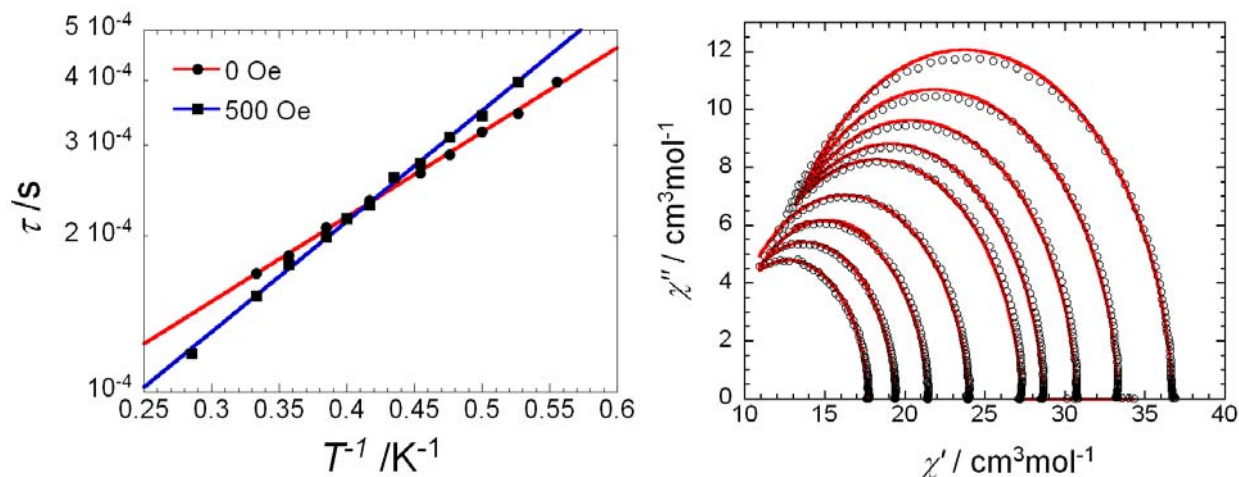


Fig. 5.9. τ vs $1/T$ plot for **41** obtained from frequency dependent ac susceptibility measurements both under a dc field of zero and 500 Oe. The solid lines represent the Arrhenius fits at $H = 0$ Oe (spots) and $H = 500$ Oe (squares) (left). Cole-Cole diagram of compound **41** in the temperature range of 1.8 – 3.0 K under zero dc field. The solid red lines represent the least-squares fit obtained with a generalized Debye model (right).

The *Wing-body* Dy-Dy of the Dy_4 of *Po-Heng Lin et. al.*^{36c} has alternative two single O-atom and two single O-atom plus one bi-atomic (-N-N-) bridges. The second Dy_4 of *Yan-Zhen et. al.*^{36b} has alternating two and three single O-atom bridges and that of *Abbas et. al.*^{36d} it has two single O-atom and one *syn-syn* carboxylate bridges. The structural parameters of the core of **41** more closely resemble that of Dy_4 of *Yan-Zhen et. Al.*^{36b} but their relaxation behaviors are different. The analysis of Cole-Cole plot **41** of χ'' vs χ' exhibits a nearly semicircular shape (Fig. 5.9, right). Fitting the data using a generalized Debye model^{59a} implies a single relaxation process (Table 5.4) while that of *Abbas et. al.*^{36d} does not produce good fit, infers more than one relaxation processes. Number of relaxation processes is not reported on Dy_4 of *Yan-Zhen et. al.*^{36b} The Dy_4 of *Po-Heng Lin et. al.*^{36c} has two clear dominant relaxation processes.

The difference in magnetic behavior between the previously reported complexes and the complex **41**, could be due to differences in ligand fields, bond lengths and slightly acute bridging angles in the central core of **41** as well as different orientations of the anisotropy axes. For comparison the structural parameters of all four complexes are given in Table 5.1. A careful look at both bond parameters and magnetic cores, led to the conclusion that single ion magnetic anisotropy of each Dy^{III} ion of all four Dy_4 complexes likely to play pivotal role on the ac

dynamics. This implies ligand field effect pivotal for Dy₄ of *Po-Heng Lin et. al.*^{36c} while QTM effect may have perished ac dynamic of rest three Dy₄ compounds. However, different ligand has been used in all four cases thus ligand field effect does not remain unaltered. Further comparative *ab* initio calculations are required to incisively elucidate this kind of experimental observations.

Table 5.4. The energy barriers and relaxation times of **41** and of previously reported Dy₄ compounds.

	41	Dy ₄ ^{36b}	Dy ₄ ^{36c}	Dy ₄ ^{36d}
QTM	observed	-	Not observed	observed
No. of relaxation processes	one	-	two	More than one
Δ (K)	4.9	7.0	9.7 and 170	6.9
τ_0 (s)	3.0×10^{-5}	3.8×10^{-5}	3.2×10^{-5} and 4×10^{-7}	4.8×10^{-5}

5.3.1 Crystal structures of (Et₃NH)₆[Ln₄(HL3)₂(NO₃)₁₀(H₂O)₄](NO₃)₄; [Ln = Er(46), Gd(47), Tb(48), Dy(49) and Ho(50)]

The compounds **46-50** are isomorphous, thus only the crystal structure of **46** will be described here while rest of the complexes (**47-50**) of this series were characterized by unit cell constants and X-ray powder diffraction. The complex **46** crystallizes in *P*-1 space group and the center of symmetry passes through the molecule. The total molecule contains four Er^{III} ions, two doubly deprotonated ligands (HL3)²⁻, ten coordinated nitrates (NO₃⁻) and four coordinated water molecules (Fig. 5.10). The crystal lattice in **46** also contains two (Et₃NH)⁺ ions for charge balance and four sets of (Et₃NH)⁺ (NO₃)⁻ rather than some solvent molecules.

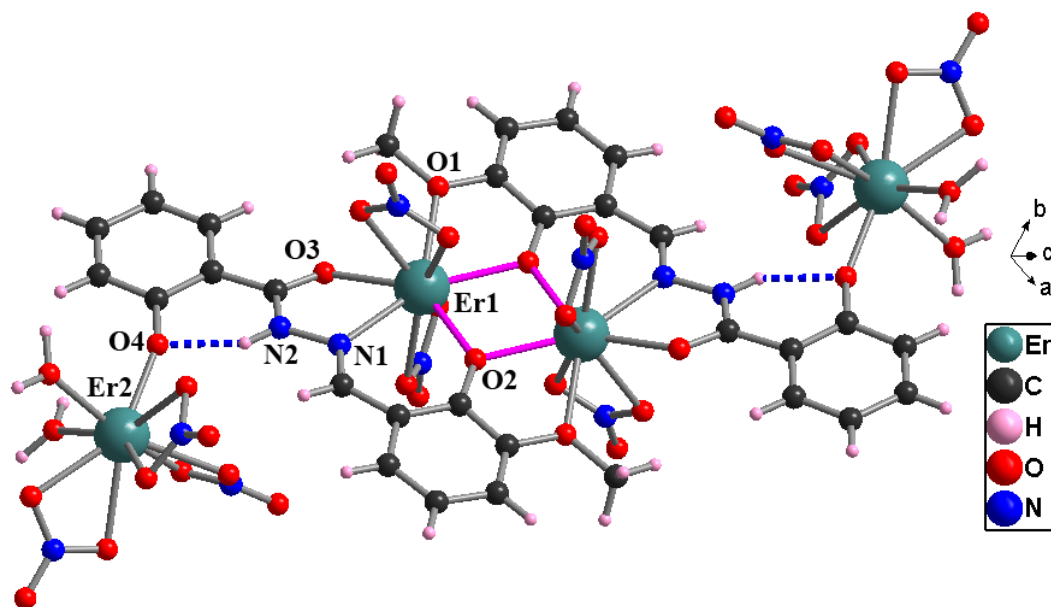


Fig. 5.10. Molecular structure of the coordination cluster in compound **46**.

In the crystal structure, the amide proton on N2 of the ligand is not deprotonated but both the phenolic OH-groups are deprotonated. In the center two Er^{III} ions are bridged by two μ_2 -phenoxide O-atoms (O2 and O2') and each ligand provides additional coordination through the methoxy oxygen O1, the imine nitrogen N1 and amide oxygen O3 with an overall bridging mode $\eta^1:\eta^2:\eta^1:\eta^1:\eta^1:\mu_3$ (Fig. 1.6, middle). There are two nitrate ions coordinated to each Er^{III} ions in chelating fashion perpendicular to the plane of aromatic ring of the ligands (Fig. 5.10). The central dimeric $\{\text{Er}^{\text{III}}_2(\text{HL}3)_2(\text{NO}_3)_4\}^{2-}$ unit is linked to the two more $\{\text{Er}^{\text{III}}(\text{NO}_3)_3(\text{H}_2\text{O})_2\}$ units from both sides of the $\{\text{Er}^{\text{III}}_2(\text{HL}3)_2(\text{NO}_3)_4\}^{2-}$ unit by with a two deprotonated phenolic O-atom (O4) (phenolic OH-group corresponding to amide part of H₃L3; Fig. 5.10) to form $\{\text{Er}^{\text{III}}_4(\text{HL}3)_2(\text{NO}_3)_{10}(\text{H}_2\text{O})_4\}^{2-}$ unit. The Er1-Er1' distance and Er1-O2-Er1' angle are 3.667(5) Å and 105.14(16)° respectively. The Er1-Er2 distance is 7.247 Å, and the mononuclear $\{\text{Er}^{\text{III}}(\text{NO}_3)_3(\text{H}_2\text{O})_2\}$ units can be magnetically isolated from the central Er₂ dimer. All four free NO₃⁻ ions are hydrogen-bonded to NH-protons on Et₃NH⁺ ions and coordinated water molecules on Er2 center. The Er1-O/N and Er2-O distances vary from 2.278(4) to 2.473(5) Å and 2.183(4) to 2.506(4) Å respectively. All four Er^{III} ions have adopted a distorted capped square antiprismatic geometry an O₈N (Er1) or O₉ (Er2) donor set. There is intramolecular H-bonding (Fig. 5.10, blue dotted line) between H2N2 and O4 (2.636(6) Å). The selected bond parameters of complex **46** are given in Table 5.5.

Table 5.5. Selected bond lengths (Å) and bond angles (°) within the coordination cluster in **46**.

Er1—O2	2.278 (4)	Er1—O10	2.458 (5)	Er2—O17	2.452 (4)
Er1—O3	2.290 (4)	O2—Er1 ⁱ	2.340 (4)	Er2—O13	2.453 (5)
Er1—O2 ⁱ	2.340 (4)	Er2—O4	2.183 (4)	Er2—O19	2.461 (5)
Er1—O1 ⁱ	2.392 (4)	Er2—O16	2.506 (4)	Er1—Er1 ⁱ	3.667(5)
Er1—O7	2.404 (5)	Er2—O6	2.298 (4)	N2...O4	2.636 (6)
Er1—O8	2.431 (5)	Er2—O5	2.325 (4)		
Er1—N1	2.446 (5)	Er2—O20	2.423 (4)	Er1—O2—	105.14 (16)
Er1—O11	2.473 (5)	Er2—O14	2.441 (5)		

Symmetry code: (i) $-x, -y, -z$.

5.3.2 Static magnetic properties of 46-50.

The susceptibility (Fig. 5.11) data of **46-50** are summarized in Table 5.6. The experimental χT values at room temperature in all cases are in good agreement with the theoretical ones for four non-interacting Ln^{III} ions.^{11,43} The χT products of compounds **46-50** all follow a similar trend, remaining almost constant down to a certain temperature (100-300 K) and then decreasing with the decrease of temperature (Fig. 5.11). For theoretically isotropic complex Gd^{III}₄ (**47**), the χT product remains almost constant from room temperature to 30 K and then rapidly decreases to 21.26 cm³ K mol⁻¹ at 1.8 K implying the presence of antiferromagnetic intramolecular interactions. The temperature independent behavior suggests the coupling between the Gd^{III} ions is very weak, which is also supported by a small Weiss constant of -1.09 K obtained from the Curie-Weiss fit of the χT product above 15 K. The rapid decrease of the χT product below 25 K is probably due to the small ZFS and/or intermolecular interaction. The thermal evolution of χT for Tb^{III}₄ (**48**) and Dy^{III}₄ (**49**) is similar, with the χT product remains almost constant until 100 K and then slowly decreases with the decrease of temperature to 19.41 (**48**) and 30.27 (**49**) cm³ K mol⁻¹ at 1.8 K respectively. The shape of χT plots suggest the presence of overall intramolecular weak antiferromagnetic interactions which is also accompanied by depopulation of Stark sublevels of Ln^{III} ions⁴³ (Fig. 5.11). For compounds Er^{III}₄ (**46**) and Ho^{III}₄ (**50**), the χT product decreases continuously over the full temperature range, also suggesting the presence of overall weak intramolecular antiferromagnetic interactions together with the depopulation of the Stark sublevels of these Ln^{III} ions. The similar trend has been

observed in previously reported triply μ -O bridged Ln^{III}_2 ^{53b} compounds (Ln = Gd, Tb and Eu) with bridging ranging from 98.86(8) to 103.36(9)°. In contrary, the intramolecular ferromagnetic interactions were observed in two Dy^{III}_2 ^{37b} complexes with Dy-O-Dy bridging angle of 106.41° and 107.68°. The geometries of the reported Ln^{III}_2 (Ln = Gd, Tb and Eu)^{53b} and Dy^{III}_2 ^{37b} are distorted capped square and square antiprismatic respectively. The central doubly single atomic bridged Dy1-O-Dy1 of **49** with distorted capped square anti-prism, is expected to be close to 105° since **49** is iso-structural to **46** (in **46**, Er1-OEr1 = 105.14(16)°). The change in geometry of Dy^{III} ions and Dy-O-Dy angle might be the reason why χT value of **49** monotonically decreases with the decrease of T.

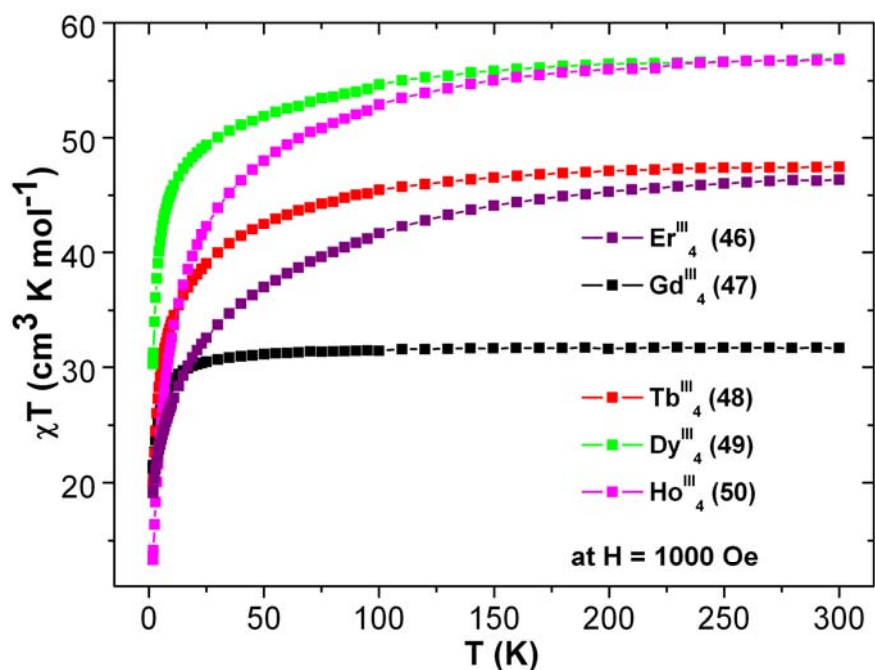


Fig. 5.11. Plots of χT vs T for **46-50** at 1000 Oe dc field.

The field dependence of magnetization at low temperatures shows that the magnetization has a relative rapid increase below 1 T and then follows a steady increase up to 7 T. The magnitude of the magnetization is listed in Table 5.5. The lack of true saturation in magnetization of complexes **46** and **48-50** indicates the presence of magnetic anisotropy and/or low lying excited states. However, in the case of isotropic complex Gd^{III}_4 (**47**), the magnetization almost reaches a saturation of 28.30 μ_B , which is in good agreement with the expected value for

four non-coupled Gd^{III} ions ($7.0 \mu_{\text{B}}$ per Gd^{III}). This further suggests that the interaction between Gd^{III} and Gd^{III} is very weak so that the antiferromagnetic interactions are easily overcome by the external field. Furthermore, the M vs H/T plots at low temperatures (Fig. 5.12-5.14, inset) for all compounds are not superposed on a single master-curve as expected for an isotropic system further indicating the presence of magnetic anisotropy and/or low-lying excited states.⁴³ The slight deviation of M vs H/T at different temperatures for isotropic complex Gd^{III}_4 (47) is due to the population of low-lying excited states (Fig. 5.13, left, inset).

Table 5.6. The dc magnetic data of compounds 46-50.

Compound	Ground state of Ln^{III} ion	χT expected for non-interacting ions per complex ($\text{cm}^3\text{Kmol}^{-1}$)	χT measured at 300 K per complex ($\text{cm}^3\text{Kmol}^{-1}$)	Curie constant ^a C ($\text{cm}^3\text{Kmol}^{-1}$)	Weiss constant ^a θ (K)	Magnetization at 2 K and 7 T (μ_{B})
Er^{III}_4 (46)	$^4\text{I}_{15/2}$	45.92	46.34	48.48	-14.39	19.73
Gd^{III}_4 (47)	$^8\text{S}_{7/2}$	31.50	31.69	31.85	-1.09	28.30
Tb^{III}_4 (48)	$^7\text{H}_6$	47.25	47.48	48.57	-6.59	19.78
Dy^{III}_4 (49)	$^6\text{H}_{15/2}$	56.68	56.87	57.77	-5.10	21.51
Ho^{III}_4 (50)	$^5\text{I}_8$	56.28	56.80	58.89	-10.66	20.87

(a) Curie-Weiss fit is obtained above 15 K.

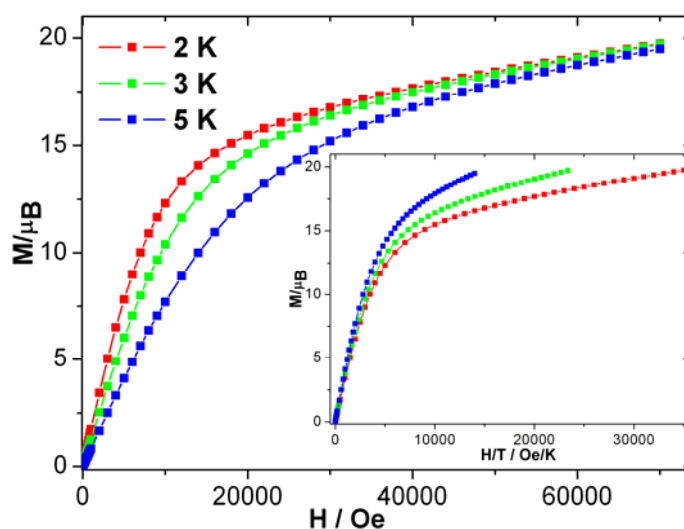


Fig. 5.12. Plots of M vs H and H/T (inset) of 46.

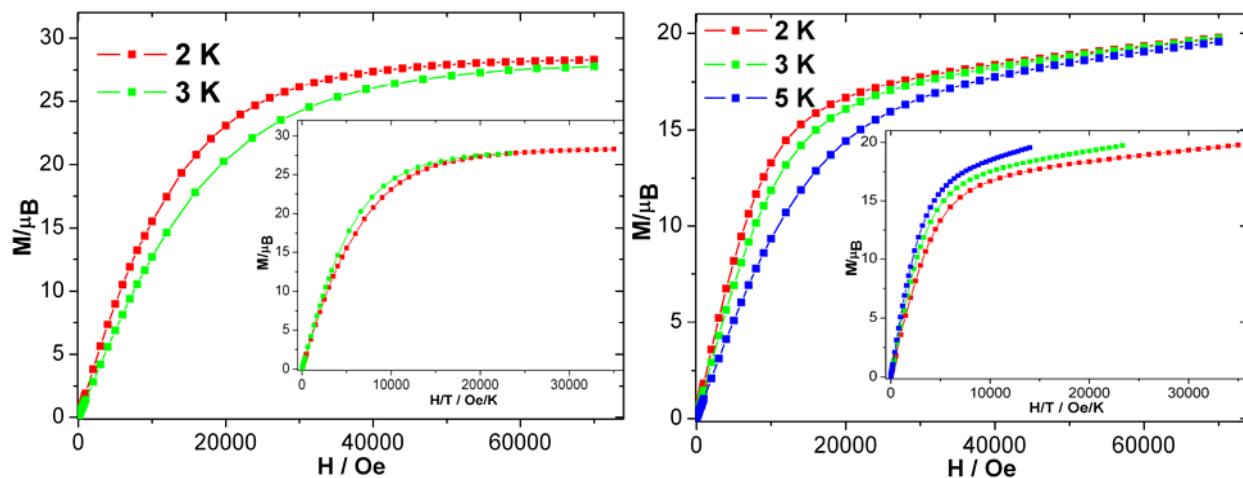


Fig. 5.13. Plots of M vs H and H/T (inset) of **47** (left) and **48** (right) at indicated temperatures.

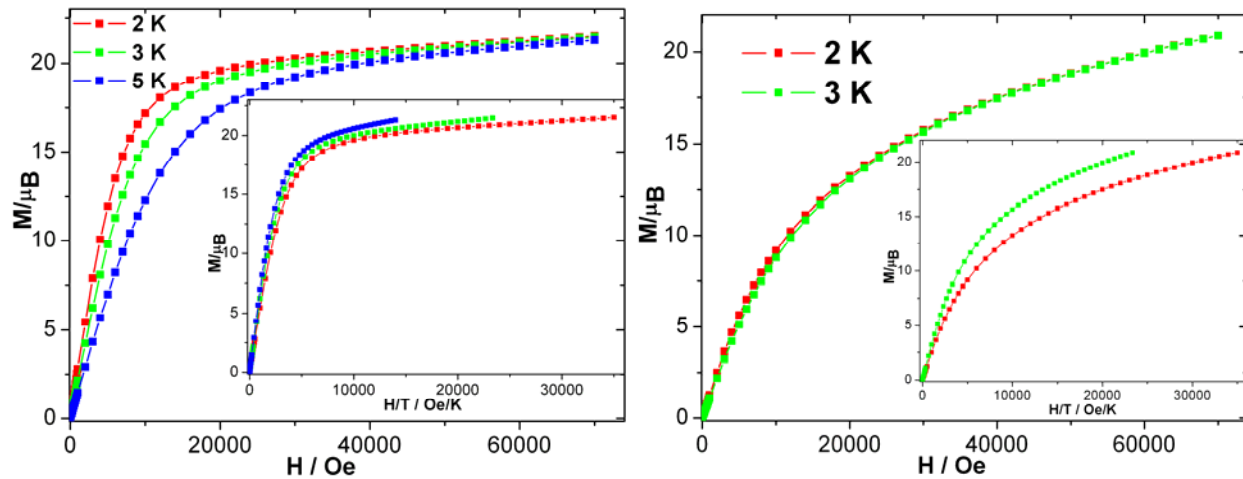


Fig. 5.14. Plots of M vs H and H/T (inset) of **49** (left) and **50** (right) at indicated temperatures.

5.3.3 Dynamic properties 46-50.

The ac measurements were carried out for all compounds. Out of the five compounds (**46-50**), only the Dy compound **49** shows a non-zero out-of-phase component indicating the presence of slow relaxation of the magnetization. The ac susceptibilities of **49** are strongly frequency dependent below 10 K with a detectable maxima around 4 K at 1500 Hz (Fig. 5.15). It is noticeable that the temperature dependence of out-of-phase susceptibilities are increasing with the increase of the frequency without a clear maxima as often observed in SMMs, suggesting that this complex has a very weak temperature dependence of the relaxation time, probably because tunneling is strong and/or associated with more than one relaxation process. Therefore, the

frequency sweeping ac susceptibilities were collected from 1.8 K to 4.0 K (Fig. 5.15). Both χ' and χ'' are frequency dependent with maxima detected up to 4 K.

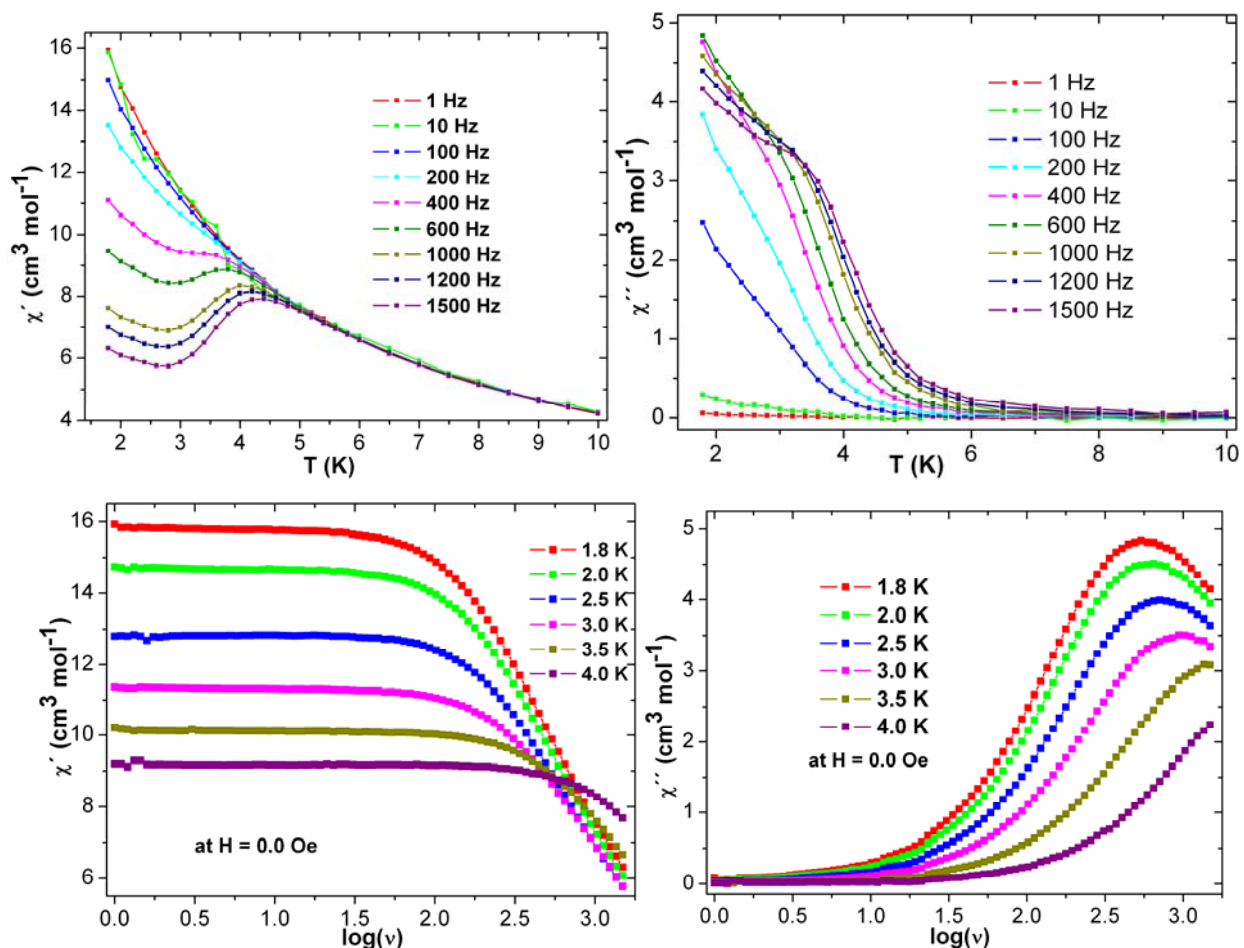


Fig. 5.15. Plots of In phase (χ') and out of phase susceptibility (χ'') vs T (top) and frequency (bottom) of **49** at indicated temperatures under applied dc field $H = 0.0$ Oe.

The χ' and χ'' vs frequency plots at 1.8 K (Fig. 5.16) indicates the possible presence of QTM. From χ' and χ'' vs T plots, it seems there are more than one relaxation process involved. The relaxation time of **49**, deduced from those data (Fig. 5.17, left), follows an activated behavior with energy gaps (Δ) of 1.59 and 11.85 K and pre-exponential factors (τ_0) of 1.1×10^{-4} and 3.1×10^{-6} s respectively (Fig. 5.17, left). The Cole-Cole plots of χ'' vs χ' show a nearly semicircular shape (Fig. 5.17, right).

In the literature there are two Dy^{III}₂ compounds reported.^{37b} In compound **49**, a Dy₂ unit can be found which is similar to the reported one.^{37b} The terminal Dy^{III} ions (Dy₂) of **49** are

separated by 7.247 (5) Å (Dy1-Dy2) from central Dy₂ unit. Thus, the magnetic interactions between Dy1 and Dy2 are likely to be very weak. The central doubly single atomic μ -bridged Dy1-O-Dy1 angle is expected to be close to 105° (Er1-OEr1 = 105.14(16)° in **46**). In this context, the Dy-O-Dy bridging angles of the Dy^{III}₂^{37b} SMMs are 106.41° and 107.68° and corresponding energy barriers are 56 and 71 K respectively.

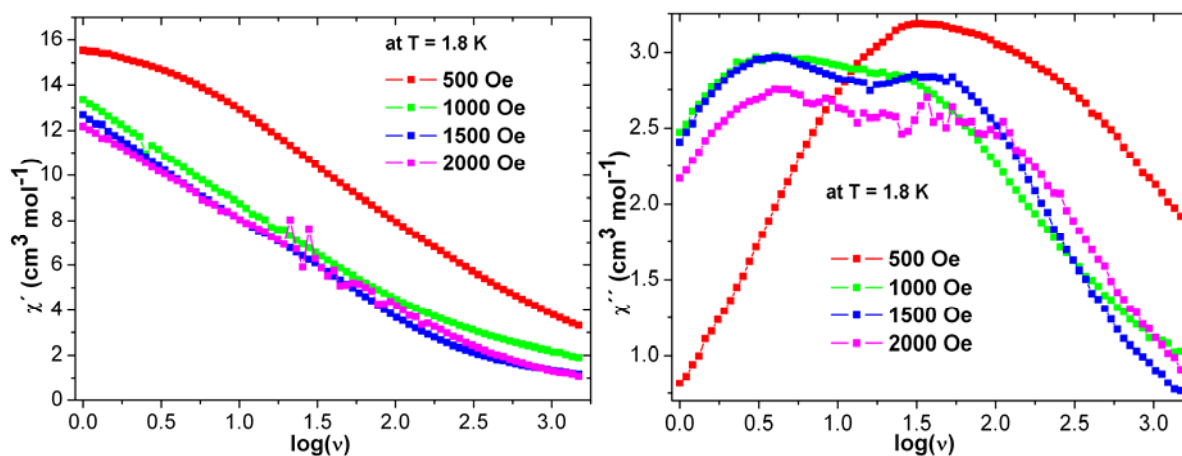


Fig. 5.16. Plots of in-phase (χ') and out-of-phase susceptibility (χ'') vs frequency of **49** under indicated external dc fields.

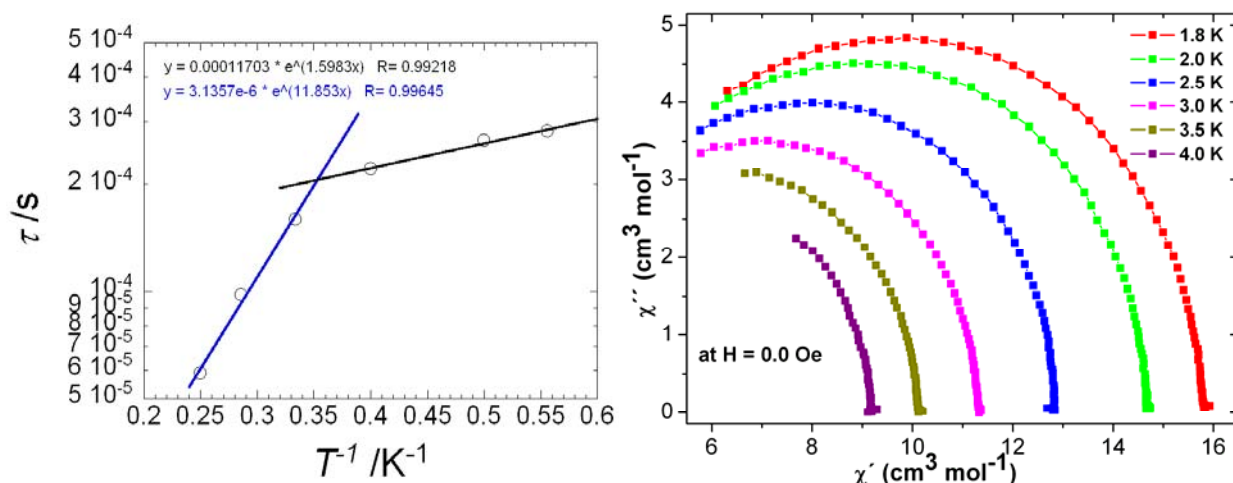


Fig. 5.17. τ vs $1/T$ plot for **49** obtained from frequency dependent ac susceptibility measurements both under a dc field of zero. The solid lines represent the Arrhenius fits at $H = 0$ Oe (left). Cole-Cole diagram (right) of compound **49** in the temperature range of 1.8 – 4.0 K under zero dc field.

5.4 Conclusion:

In this chapter syntheses, crystal structures and magnetic properties of two different series of tetranuclear lanthanide compounds are presented based on H₂L1 and H₃L3 with general formulae [Ln^{III}₄(OH)₂(L1)₄(HL1)₂]·2THF [Ln = Dy(**41**), Gd(**42**), Tb(**43**), Ho(**44**) and Er(**45**)] and (Et₃N)₆[Ln₄(HL3)₂(NO₃)₁₀(H₂O)₄](NO₃)₄ (**46-50**) respectively. But the topology of the coordination clusters is different with respect to each other. Crystal structures reveal that compounds **41-45** have a defect-dicubane while **46-50** have a non-planar chain-like topology. From structural comparison, it is found that deprotonated iminophenolic O-atom of H₂L1 coordinates and bridges thus producing tetra nuclear coordination cluster (**41-45**). The enol form of amide O-atom of H₃L3 only acted as coordinating atom (not bridging) to produce dinuclear unit which then binds two Ln^{III} ions by its functionalized deprotonated phenolic O-atom (**46-50**).

From magnetic point of view the Dy-analogues (**41** and **49**) of both the series are SMMs. Among the coplanar Ln^{III}₄ series (**41-45**), Dy(**41**) and Ho(**44**) analogues show over all weak intramolecular ferromagnetic interactions at low temperature while the other three compounds (Gd(**42**), Tb (**43**) and Er(**45**)) show weak antiferromagnetic interactions. Complex **41** shows slow relaxation of magnetization characteristic of SMM behavior with QTM relaxation pathways making lower energy barrier for magnetic relaxation. Generally, Ln complexes are in the weak limit of magnetic coupling. Among all three reported defect-dicubane Dy₄,^{36b-d} the exact nature of magnetic coupling (ferro or antiferro) has not been envisaged. In contrast, **41** has over all weak ferromagnetic coupling below 15 K within Dy₄ complex and in spite of that, the ac relaxation dynamic of **41** does not improved much when compared to that of *Yan-Zhen et. al.*^{36b} and *Abbas et. al.*^{36d} The absence of QTM and pivotal single-ion magnetic anisotropy are the impetus of higher energy barrier in Dy₄ of *Po-Heng Lin et. al.*^{36c}

The dc magnetic measurements reveal that all (**46-50**) compounds are weakly antiferromagnetically coupled. Dynamic magnetic property measurements show that compound Dy^{III}₄ (**49**) is a SMM with two energy barriers ($\Delta = 1.59$ and 11.85 K) with nice slow relaxation of magnetizations through two relaxation pathways below 7 K.

Chapter 6

Cu-Ln Coordination Clusters with (E)-N'-(2-hydroxy-3-methoxybenzylidene)-benzohydrazide (H₂L2) and bis-(E)-N,N'-(2-hydroxy-3-methoxy)-benzylhydrazone (H₂L4)

6.1 Introduction

Since the discovery of Single Molecule Magnet (SMM) behavior in Mn₁₂-Ac,^{4,5} considerable effort has been employed on developing the synthetic routes to a variety of homo-²⁰⁻²⁶ and hetero-metallic^{27,42,44-50} high spin coordination clusters. In order to observe SMM behavior it is necessary to combine a non-zero and preferably high spin state (S) with an Ising-type uniaxial magnetic anisotropy (D).^{4,5,60} Below the blocking temperature T_b, slow relaxation of the magnetization can be observed and the hope is to utilize this so that each molecule may function as a data storage or processing unit.¹⁹ The SMMs must have a negative axial zero-field splitting (D), which leads to a double-well potential with an energy barrier between “spin-up” (S_z = +S) and “spin-down” (S_z = -S) states.^{8a} On the other hand, the above mentioned double well formalism is not obeyed by the compounds containing highly anisotropic metal ions (such as Co^{II}, Dy^{III}, Tb^{III} etc.). The height of the barrier U_{eff} is related to the spin and anisotropy providing a giant spin model can be used and then given by the equation U_{eff} = |DS²|. Thus a logical goal seems to be to combine high total spin, S with a significant and negative uniaxial anisotropy, D. However, it has recently become clear that the attractive idea of achieving very high spin molecules in order to optimize barrier height fails if the combination with the anisotropy is to be taken into account. In fact, any significant orbital contribution (and thus single ion magnetic anisotropy) automatically implies that the quantum number for the total spin on the molecule, S, is no longer a good quantum number and since S is also a part of the description of for the zero-field splitting parameters this leads to a linear rather than quadratic dependency on S for the barrier height, suggesting that the more useful parameter to optimize is, in fact, the D parameter.⁶⁰ The giant spin model, implicated if we take S to be the dominant factor in increasing U_{eff}, is mostly valid for Mn and Ni-based SMMs, but is not valid for highly anisotropic systems.³⁵ It is apparently thought that adding together a lot of anisotropic single ions will give an anisotropic molecular system. This tends not to be working because of the difficulty of aligning the single-ion anisotropies close to parallel. Hence, it is better to use one strongly

anisotropic ion and try to give it an environment that will maximize the anisotropy of a particular magnetic center. Since Ln^{III} (4fⁿ) metal ions such as Tb^{III}, Dy^{III}, Ho^{III}, Tm^{III}, Er^{III} etc. contain large unquenched orbital angular momentum because of the internal nature of valence f orbitals, they are rich source of large and inherent single ion magnetic anisotropy.⁴³ This is also one of the reasons why rare earths are widely used in magnet technology. Some examples of this are provided by the SmCo₅ and Nd₂Fe₁₄B permanent magnets, which have found large market use in the past few years.⁴³ It is well known that f orbitals are deeply buried, so the interactions between f electrons are expected to be small producing measurable effects at extremely low temperatures. This is one of the reasons for the intense recent efforts to produce systems containing both 3d and 4f metal ions as the hope is that this will result in a stronger magnetic interaction of the f electrons with more expanded d orbitals and also measurable effect at higher temperatures.⁴³

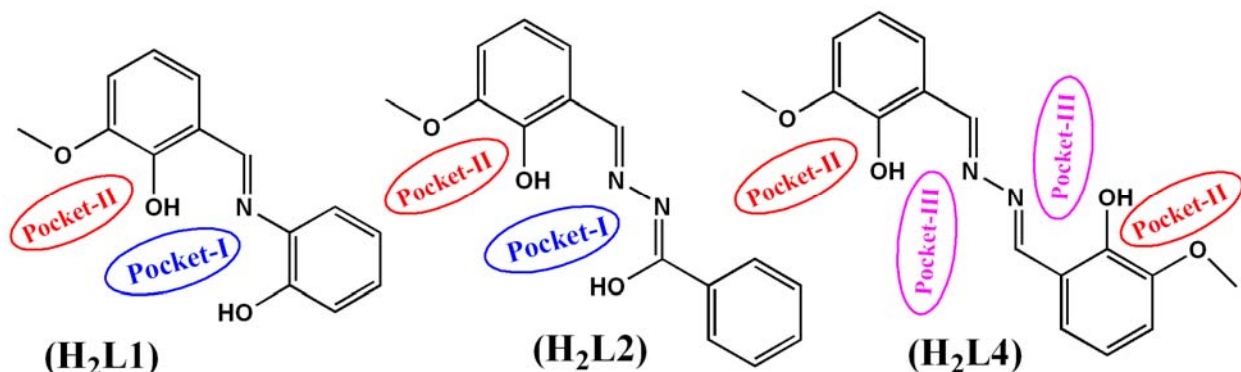
In most cases, the Gd^{III}-Cu^{II} magnetic interaction is found to be ferromagnetic.^{43,44d,61a} However, replacing Gd^{III} by highly anisotropic Tb^{III} or Dy^{III} ions can give an anisotropic spin pair with an easy axis,⁴⁴ In the literature several engrossing Ln^{III}-Cu^{II} SMMs (TbCu,^{44c,h} Tb₂Cu₂,^{44a} Dy₂Cu₂,^{44a} Dy₂Cu,^{44b} Dy₂Cu₂,^{44e,h} Dy₆Cu₆,⁴⁴ⁱ Dy₆Cu₆,^{44j} Cu₂₄Dy₈,^{61b} etc.) are reported. The Dy₂Cu^{44b} has the highest energy barrier (46 K) among the Ln^{III}-Cu^{II} based SMMs.

6.2 Synthetic strategy

Ln₃Cu₂ complexes synthesized using the H₂L1 ligand, have been discussed in chapter 4. Here the synthesis of Ln-Cu complexes using the H₂L2 ligand is described. From the coordination chemistry point of view both H₂L1 and H₂L2 are similar (Scheme 6.1). Each diprotic ligand (H₂L2) can be described in terms of possessing two pockets (I and II) (Scheme 6.1). The first provides ONO (a phenolic O from the vanillin part of the ligand, an imine N and an amide O) and the second provides two oxygen donors from the phenol O-atom and an O from the OMe group of o-vanillin part of the ligand. As before, the phenolic O-atom can also bridge between metal ions in the two pockets. The H₂L4 ``double-ligand`` now has two pockets of type II (OO), but instead of pocket-I, we now have two pocket-III (ON) such that metal ions in these pockets are bridged by the hydrazine linkage.

It is well-known that the ratio, metal salt, temperature, solvent, and the time of reaction can all affect the nature of the final product. Bearing this in mind, these parameters were

modified and the influence influence on the resulting structural characteristics of the final products noted (Table 6.1).



Scheme 6.1. View of H₂L1 (left), H₂L2 (middle) and H₂L4 (right).

The reaction of Dy(NO₃)₃·6H₂O, Cu(NO₃)₂·2.5H₂O and H₂L2 in 20 mL of MeOH in the presence of base (Et₃N) in the ratio of 2.5:2.5:1:7.8 led to the isolation of needle-shaped green crystals of [DyCu(L2)(OMe)(NO₃)₂(H₂O)(MeOH)]·2MeOH (**51**). When the above ratio was changed to 2.5:2.5:1:6, block shaped green crystals of [DyCu₂(L2)₂(OMe)₂(NO₃)(H₂O)₂]·H₂O·1.5MeOH (**52**) is obtained. Utilization of sodium azide in the previous reaction, produces black color block-shaped crystals of [DyCu₂(L2)₂(N₃)₃(MeOH)(H₂O)]·3MeOH·1.5H₂O (**53**).

The reaction of Dy(NO₃)₃·6H₂O, Cu(NO₃)₂·2.5H₂O and H₂L2 in 20 mL of MeOH in the presence of triethylamine (Et₃N) as a base in the ratio of 1:1:2:5 led to the isolation of needle-shaped green crystals of [LnCu₃(L2)₃(OMe)₃]·xMeOH·yH₂O [Ln = Dy(**54**), x = 1.5, y = 0.215; Tb(**55**) and Gd(**56**) x = 1, y = 0; Ho(**57**) and Er(**58**) x = 1.5, y = 0.215].

After the isolation and characterization of propeller shape DyCu₃ (**54**) complex, H₂L4 was formed in situ to connect two DyCu₃ (**54**) magnetic units giving [Dy₂Cu₆(OMe)_{2.76}(N₃)_{1.24}(L2)₆(H₂O)(MeOH)(L4)]·10MeOH·2H₂O (**59**). In the crystal structure there are two partially disordered OMe/N₃ bridges between Dy^{III} and Cu^{II} within the molecule. The reaction without addition of sodium azide has been attempted but no such compound is obtained with pure methoxide (OMe) bridges.

In order to investigate the influence of solvent, the reaction which produced the propeller shaped Dy^{III}Cu^{II}₃ (**54**) molecule with three μ-OMe bridges, was performed in EtOH instead of MeOH, but instead of a propeller system, hexagonal-shaped light green crystals of

$[\text{Ln}_9\text{Cu}_2(\text{L}2)_4(\text{HL}2)_4(\text{OH})_8(\text{CO}_3)_3(\text{NO}_3)_3(\text{H}_2\text{O})_4(\text{EtOH})](\text{NO}_3)_2 \cdot 9\text{EtOH} \cdot 6\text{H}_2\text{O}$ [$\text{Ln} = \text{Dy}(\mathbf{60})$ and $\text{Er}(\mathbf{61})$] were obtained. The carbonate (CO_3^{2-}) originates from the fixation of carbon dioxide which transforms into carbonate in the presence of base. If the reaction is carried out in inert atmosphere no crystals containing Dy^{III} ions can be obtained.

The similar reaction, but using $\text{DyCl}_3 \cdot 6\text{H}_2\text{O}$ instead of $\text{Dy}(\text{NO}_3)_3 \cdot 6\text{H}_2\text{O}$ in EtOH, gave block-shaped green-brown crystals of the μ_3 -OH bridged $[\text{Dy}_2\text{Cu}(\text{OH})(\text{L}2)_2(\text{HL}2)_2(\text{H}_2\text{O})]\text{Cl} \cdot 5\text{EtOH} \cdot 2.5\text{H}_2\text{O}$ ($\mathbf{62}$) triangle, the core of which seems to be a fragment of the much larger $\text{Dy}^{\text{III}}_9\text{Cu}^{\text{II}}_2$ ($\mathbf{60}$). In this chapter the syntheses, crystal structures and magnetic properties of these novel complexes ($\mathbf{51}$ - $\mathbf{62}$) are presented.

Table. 6.1. Comparison of Dy^{III} - Cu^{II} products ($\mathbf{51}$, $\mathbf{52}$, $\mathbf{53}$, $\mathbf{54}$, $\mathbf{59}$, $\mathbf{60}$ and $\mathbf{62}$) with various reaction conditions.

Ratio ^a	Solvent	Atmosphere /temperature	Time of stir (min.)/ Crystallization(days)	Compound
A:B:C:G = 2.5:2.5:1:7.8	MeOH	air/rt	15/14	DyCu ($\mathbf{51}$)
A:B:C:G = 2.5:2.5:1:6	MeOH	air/rt	15/14-21	DyCu_2 ($\mathbf{52}$)
A:B:C:F:G = 1:1:1:3.8:2.4	MeOH	air/rt	15/60	DyCu_2 ($\mathbf{53}$)
A:B:C:G = 1:1:2:5	MeOH	air/rt	10/2-3	DyCu_3 ($\mathbf{54}$)
A:B:C:E:F:G = 6:15:12:1.02:19.38:24.23	MeOH	air/rt	15/14-21	Dy_2Cu_6 ($\mathbf{59}$)
A:B:C:G = 1:1:2:5	EtOH	air/rt	20/21	Dy_9Cu_2 ($\mathbf{60}$)
D:B:C:G = 1:1:2:5	EtOH	air/rt	20/21	Dy_2Cu ($\mathbf{62}$)

(a) A = $\text{Dy}(\text{NO}_3)_3 \cdot 6\text{H}_2\text{O}$, B = $\text{Cu}(\text{NO}_3)_2 \cdot 2.5\text{H}_2\text{O}$, C = $\text{H}_2\text{L}2$, D = $\text{DyCl}_3 \cdot 6\text{H}_2\text{O}$, E = $\text{H}_2\text{L}4$, F = NaN_3 , G = Et_3N , Volume of solvent = 20 mL.

6.2.1 Crystal structure of complex $[\text{DyCu}(\text{L}2)(\text{OMe})(\text{NO}_3)_2(\text{H}_2\text{O})(\text{MeOH})] \cdot 2\text{MeOH}$ ($\mathbf{51}$).

The complex $\mathbf{51}$ crystallizes in the orthorhombic space group $Pbca$ with $Z = 8$. The asymmetric unit of $\mathbf{51}$ contains one Cu^{II} ion, one Dy^{III} ion, one dianionic ligand ($\text{L}2^{2-}$), one μ - OMe^- , two chelating nitrates (NO_3^-), one coordinated MeOH and one H_2O . The Cu^{II} ion has adopted distorted a square planar geometry with an O_3N donor set while the Dy^{III} ion has adopted a nine coordinate distorted capped square antiprism geometry with an O_9 donor set (Fig. 6.1).

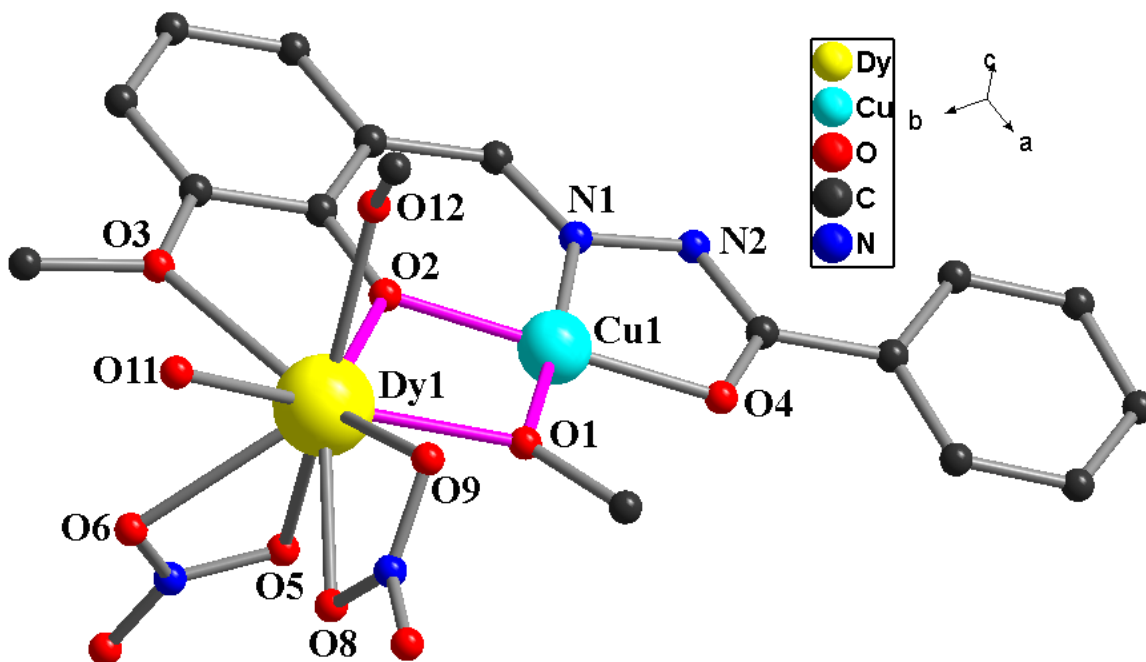
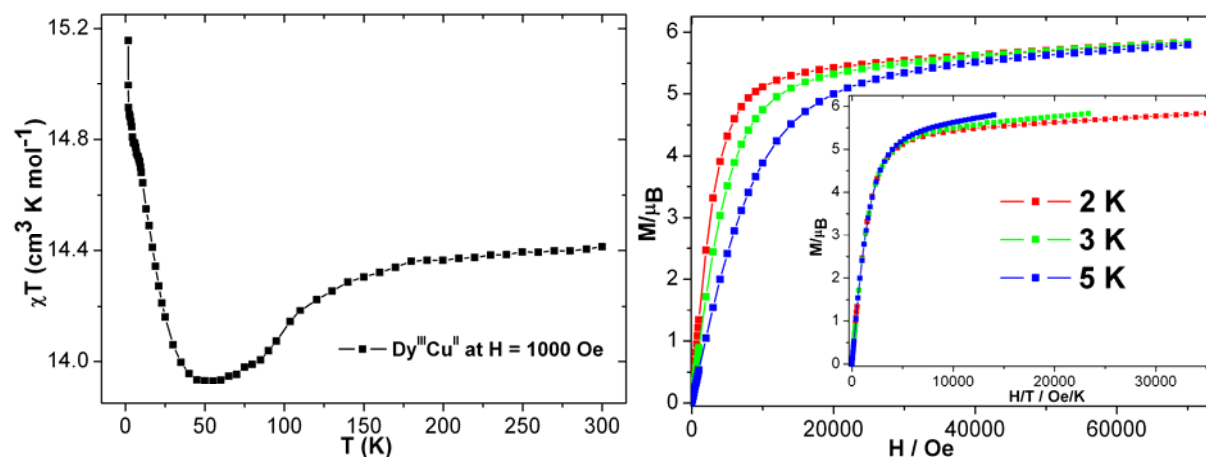


Fig. 6.1. Molecular structure of the coordination cluster in compound **51**; Cu1 and Dy1 centers in pocket-I and -II respectively.

The square planar Cu^{II} ion is ligated into pocket-I(ONO) of the dianionic ligand (L^{2-}) while Dy^{III} ion is ligated into pocket-II(OO) and they are linked by the phenoxy oxygen O2. Thus the ligand displays a $\eta^1:\eta^2:\eta^1:\eta^1:\mu_2$ coordination mode (Fig. 1.6). The fourth coordination site of the square planar Cu^{II} ion is completed by the bridging μ -methoxide oxygen (O1) which also bridges between the Cu^{II} and Dy^{III} ions (Fig. 6.1). In addition to the two oxygens from this bridge, the coordination sphere of the Dy^{III} ion is completed by four O-atoms of two chelating mono anionic nitrates, one H_2O oxygen and one MeOH oxygen. The Dy-O bond distances vary from 2.264(3) to 2.578(3) Å while Cu-O/N bond distances vary from 1.910(3) to 1.934(3) Å. The Cu1-Dy1 distance is 3.3499(5) Å and Cu1-O1-Dy1 and Cu1-O2-Dy1 bridging angles are 106.44(13) and 104.30(13)° respectively. The crystal lattice in **51** also contains two MeOH solvent molecules which are hydrogen-bonded to coordinated nitrate and water molecules on the dysprosium (O11-O21 = 2.643(5) Å and O8-O22 = 2.769 Å). There are also π - π stacking interactions between the aromatic parts of the ligand. Selected bond lengths and angles are provided in Table 6.2.

Table 6.2 Selected bond lengths (Å) and bond angles (°) within the coordination cluster in **51**.

Dy1—O1	2.264 (3)	Dy1—O12	2.354 (3)	Dy1—O6	2.495 (4)
Dy1—O2	2.315 (3)	Dy1—O8	2.410 (4)	Dy1—O9	2.526 (3)
Dy1—O11	2.348 (3)	Dy1—O5	2.478 (4)	Dy1—O3	2.578 (3)
Cu1—O1	1.910 (3)	Cu1—O2	1.916 (3)	Cu1—O4	1.919 (3)
Dy1—N1	1.934 (3)	Dy1—Cu1	3.3499 (5)		
Cu1—O2—Dy1	104.30 (13)	Cu1—O1—Dy1	106.44 (13)		

6.2.2 Static magnetic properties of 51.**Fig. 6.2.** Plots of χT vs T (left), M vs H (right) and H/T (right, inset) of **51**.

The temperature dependence of the magnetic susceptibility was measured on a powdered sample of **51** in the temperature range 1.8–300 K under an applied dc magnetic field of 1000 Oe (Fig. 6.2). The experimental χT value ($14.41 \text{ cm}^3 \text{ K mol}^{-1}$) at room temperature, is in good agreement with the theoretical value ($14.51 \text{ cm}^3 \text{ K mol}^{-1}$) for one Dy^{III} and one Cu^{II} ions.^{11,43} The χT product of **51** slowly decreases on decreasing temperature to reach a value of $13.93 \text{ cm}^3 \text{ K mol}^{-1}$ at 50 K, after which it rapidly increases to $15.15 \text{ cm}^3 \text{ K mol}^{-1}$ at 1.8 K. This type of behavior (increase below 50 K) suggests the presence of intramolecular ferromagnetic couplings between the Dy^{III} and Cu^{II} ions, with the decrease of the χT product in the high temperature range is more likely due to the depopulation of Stark sublevels of the Dy^{III} ion.⁴³ The field dependence of the magnetization at low temperatures (Fig. 6.2) reveals that the magnetization has a relative rapid increase below 1 T and then follows a steady increase up to 7 T. The M_S value at 7 T is $5.84 \mu_B$, lower than expected value of $6.5 \mu_B$, indicating lack of saturation.

Furthermore, the M vs H/T plots at low temperatures (Fig. 6.2, right inset) for **51**, are not superposed on to a single master-curve as expected for isotropic system further indicating the presence of magnetic anisotropy and/or low-lying excited states.⁴³ Ac measurements did not show any out-of-phase signals indicating that there is no SMM behavior above 1.8 K.

6.3.1 Crystal structures of the complexes $[\text{DyCu}_2(\text{L2})_2(\text{OMe})_2(\text{NO}_3)(\text{H}_2\text{O})_2]\cdot\text{H}_2\text{O}\cdot 1.5\text{MeOH}$ (**52**) and $[\text{DyCu}_2(\text{L2})_2(\text{N}_3)_3(\text{MeOH})(\text{H}_2\text{O})]\cdot 3\text{MeOH}\cdot 1.5\text{H}_2\text{O}$ (**53**)

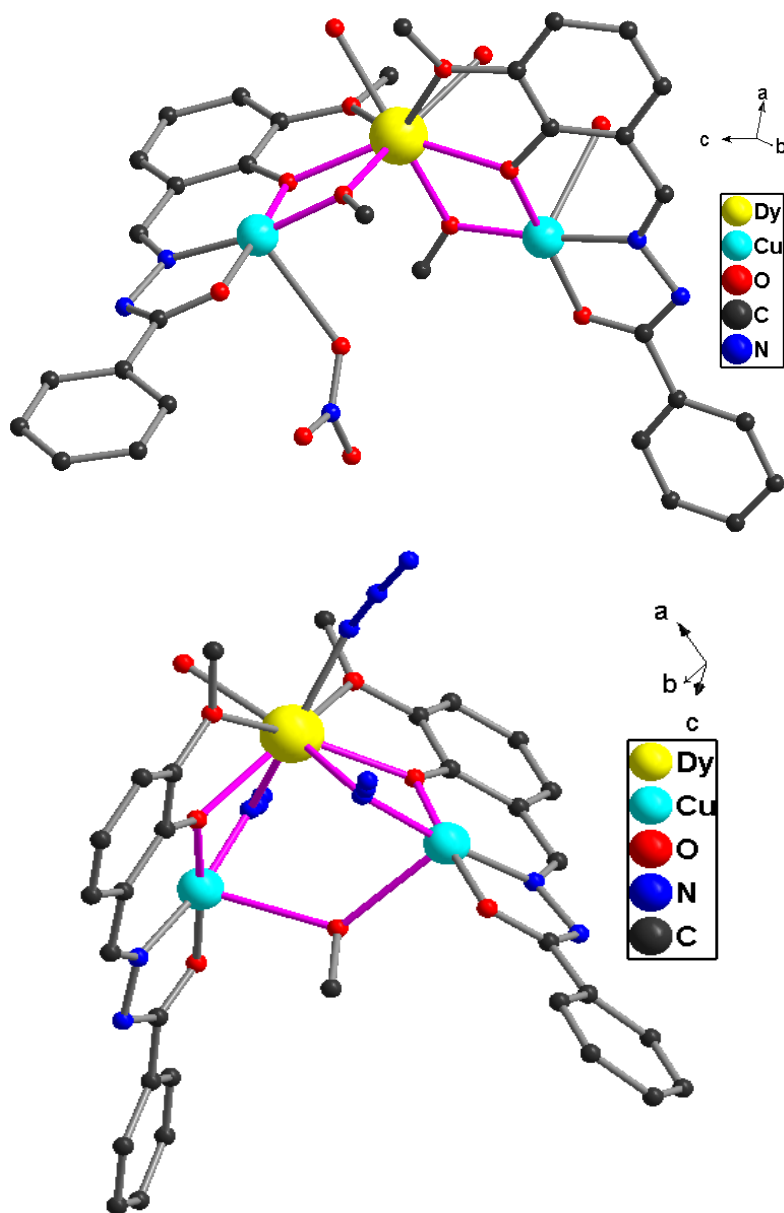


Fig. 6.3. Molecular structure of the coordination cluster in compounds **52** (top) and **53** (bottom).

The complex **52** crystallizes in monoclinic space group $P2_1/n$ with $Z = 4$. The asymmetric unit of **52** contains two Cu^{II} ions, one Dy^{III} ion, two dianionic ligands ($\text{L}2^{2-}$), two $\mu_2\text{-OMe}^-$ groups, one coordinating nitrate and two coordinated H_2O molecules. Both the Cu^{II} ions have distorted square pyramidal geometry with O_4N donor sets while the Dy^{III} ion with an O_8 donor set has a distorted square antiprismatic geometry (Fig. 6.3, top).

Table 6.3 Selected bond lengths (Å) and bond angles ($^\circ$) within the coordination cluster in **52**.

Dy1—O2	2.254 (3)	Dy1—O6	2.337 (3)	Dy1—O7	2.551 (3)
Dy1—O1	2.256 (3)	Dy1—O10	2.342 (3)	Dy1—O4	2.652 (3)
Dy1—O3	2.316 (3)	Dy1—O9	2.344 (3)	O41...N2 ⁱⁱⁱ	2.846 (5)
Cu1—N1	1.920 (3)	Cu2—O6	1.925 (3)	O10...O13 ⁱ	2.741 (5)
Cu1—O3	1.930 (3)	Cu2—O2	1.910 (3)	O9...O12 ⁱ	2.661 (5)
Cu1—O5	1.935 (3)	Cu2—N3	1.921 (3)	O9...O41	2.718 (5)
Cu1—O11	2.629 (5)	Cu2—O8	1.936 (3)	O10...N4 ⁱⁱ	2.713 (4)
Cu1—O1	1.914 (3)	Cu2—O41	2.694 (4)		
Cu2—O6—Dy1	102.78 (12)	Cu1—O3—Dy1	103.49 (12)	Cu1—Dy1	3.3403(10)
Cu2—O2—Dy1	106.36 (12)	Cu1—O1—Dy1	106.32 (12)	Cu2—Dy1	3.3431(10)

Symmetry codes: (i) $x+1, y, z$; (ii) $x+1/2, -y+1/2, z+1/2$; (iii) $x+1/2, -y+1/2, z-1/2$.

Two square pyramidal Cu^{II} ions of **52** are ligated into pocket-I(ONO) of two dianionic ligands ($\text{L}2$)²⁻. The central Dy^{III} ion is ligated by two pocket-II(OO) and linked by the phenoxy $\mu\text{-O}$ -atoms O3 and O6 to Cu1 and Cu2 respectively. Thus both the ligands display a $\eta^1:\eta^2:\eta^1:\eta^1:\mu_2$ coordination mode (Fig. 1.6) as observed in **51**. The fourth coordination site of each Cu^{II} ion occupied a $\mu\text{-OMe}$ ligand (O1 or O2) each of which also bridges between the respective Cu and Dy1 (Fig. 6.1). Thus, central Dy^{III} ion is doubly coupled to each of two adjacent Cu^{II} ions ($\text{Cu1-Dy1-Cu2} = 110.93(2)^\circ$) through one $\mu\text{-OMe}$ and one $\mu\text{-O}$ phenoxide bridges (Fig. 6.3, top). The fifth coordination site of each Cu^{II} ion is completed by one O-atom of either a unidentate nitrate or a water ligand ($\text{Cu1-O11} = 2.629(5)$ Å and $\text{Cu2-O41} = 2.694(4)$ Å). The square anti-prism geometry of Dy1 is completed by two coordinating H_2O oxygens. The Dy-O bond distances vary from 2.254 (3) to 2.652 (3) Å. Selected bond distances and angles are given in Table 6.3. Two coordinated H_2O molecules make intra complex hydrogen-bonding with

water molecule on Cu1 (O9-O14 = 2.717 Å) and inter complex hydrogen-bonding (O9-O13 = 2.663 and O10-O12 = 2.728 Å) with coordinated NO₃⁻ on Cu2 center and non coordinated N-atom (N4-O10 = 2.714(3) Å) on the amide part of the ligand of another complex. There are also π - π stacking interactions between the aromatic parts of the ligand.

The complex **53** crystallizes in the triclinic space group *P*-1. The asymmetric unit of **53** contains two Cu^{II} ions, one Dy^{III} ion, two dianionic ligands (L2)²⁻, two μ -N₃⁻, one μ -MeOH, one terminally coordinating azide (N₃⁻) and one coordinated water molecule (Fig. 6.3, bottom). Both the Cu^{II} ions have a distorted square pyramidal geometry with an O₃NO donor set while the Dy^{III} ion adopts a distorted square antiprismatic geometry with an O₅N₃ donor set. Both the square pyramidal Cu^{II} ions are placed in pocket-I of each ligand (L2)²⁻ and coordinated by ONO sites of each dianionic ligand (L)²⁻ while Dy^{III} ion sits in both pocket-II (OO) and linked to each Cu^{II} by a μ -phenoxide O-atom. The fourth equatorial coordination site of square plane of each Cu^{II} ion is occupied by one *end-on* μ_2 -N₃⁻ anion which bridges between the Cu^{II} and the Dy^{III}.

Table 6.4 Selected bond lengths (Å) and bond angles (°) within the coordination cluster in **53**.

Dy1—O4	2.304 (2)	Dy1—O7	2.329 (2)	Dy1—O5	2.551 (2)
Dy1—N31	2.315 (3)	Dy1—N21	2.436 (3)	Dy1—O2	2.578 (2)
Dy1—O1	2.318 (2)	Dy1—N11	2.454 (3)	O7...N2 ⁱ	2.753 (4)
Cu1—O1	1.940 (2)	Cu2—N21	1.962 (3)	O31...O41	2.711 (6)
Cu1—N1	1.926 (3)	Cu2—N3	1.920 (3)	O7...O45A ⁱⁱ	2.660 (11)
Cu1—O3	1.932 (2)	Cu2—O6	1.920 (3)	O7...O45B ⁱⁱ	2.660 (13)
Cu1—N11	1.958 (3)	Cu2—O4	1.929 (2)	Dy1—Cu2	3.3976 (5)
Cu1—O31	2.490 (3)	Cu2—O31	2.618 (3)	Dy1—Cu1	3.3944 (5)
Cu1—Dy1—Cu2	83.376 (12)	Cu1—O31—Cu2	124.34 (10)	Cu2—N21—Dy1	100.58 (12)
Cu1—O1—Dy1	105.39 (9)	Cu1—N11—Dy1	99.99 (11)	Cu2—O4—Dy1	106.45 (10)

Symmetry codes: (i) $-x+2, -y+1, -z+1$; (ii) $x+1, y, z$.

The Jahn-Teller axial sites of the square pyramidal Cu1 and Cu2 centers are completed by one μ_2 -O-atom of MeOH (Cu1-O31-Cu2 = 124.34 (10)°, Cu-O31 = 2.490(3) Å and Cu2-O31 = 2.618(3) Å). Thus, Dy^{III} ion is doubly coupled to two adjacent Cu^{II} ions through one *end-on* μ -N₃ and one μ -O phenoxide bridges (Fig. 6.3, bottom). The bridging methanol ligand has pulled the two Cu^{II} centers close together so that the Cu1-Dy1-Cu2 angle is 83.376(12)° compared to

110.93(2)° in **52**. Selected bond distances and bond angles are given in Table 6.4. Two complex molecules remain close to form an intermolecular dimer through H-bonding (N⋯HO) and π - π stacking interactions between aromatic parts of the ligand. The H₂O molecules on the dysprosium center make inter complex hydrogen-bonding with one of the non coordinated N-atoms of other complex (N2-O7 = 2.753(4) Å). The intramolecular Cu1-Cu2, inter molecular Cu1-Cu1' and Cu1-Cu2' distances are 4.517, 4.298 and 6.027 Å respectively. There are also π - π stacking interactions between aromatic parts of ligand.

6.3.2 Static magnetic properties of **52-53**.

The magnetic cores of **52** and **53** are closely related. The two μ -OMe bridges in **52** are replaced by two μ_2 -N₃ bridge in **53**. Additionally, there is a μ -HOMe bridge between Cu1 and Cu2 centres in **53**, so that the Cu1-Dy1-Cu2 angle is much smaller in **53** than in **52** (Fig. 6.4, left).

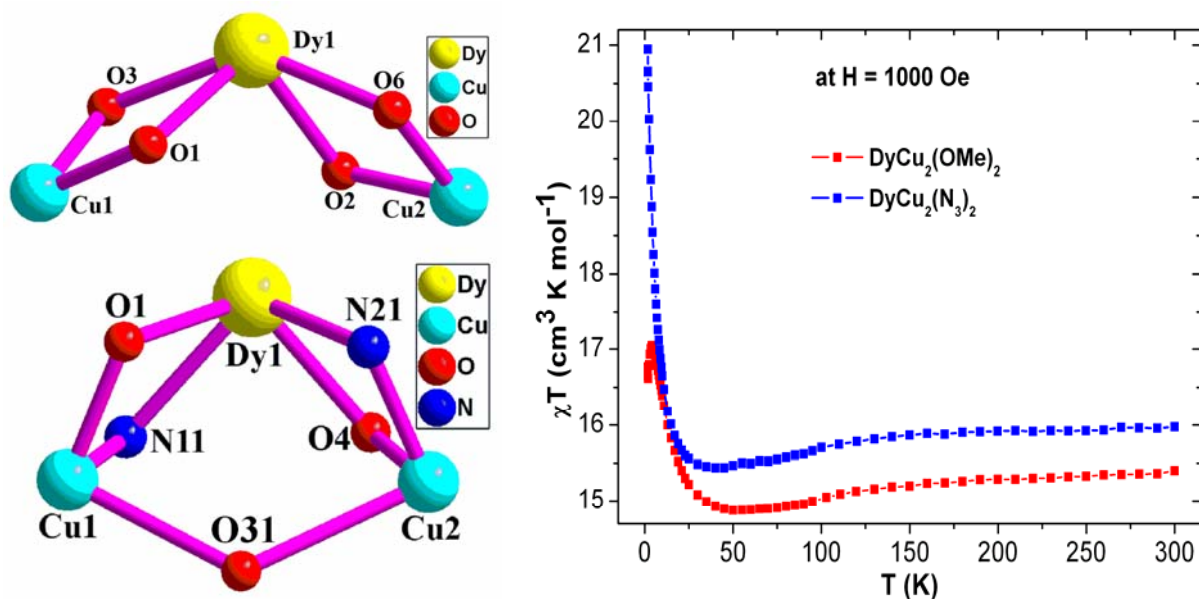


Fig. 6.4. The magnetic cores (left) of **52** (top) and **53** (bottom). Plots of χT vs T of **52** and **53** under 1 kOe applied dc magnetic field (right).

The room temperature χT products of **52** and **53** are 15.40 and 15.97 cm³ K mol⁻¹ respectively which are slightly larger than that of theoretically calculated value of 14.92 cm³ K mol⁻¹ for non-interacting 2 Cu^{II} ions (with $S = 1/2$, $g = 2.0$) and one Dy^{III} ions (with ⁶H_{15/2}, $g =$

4/3, $S = 5/2$). The χT products of both the complexes gradually decrease on decreasing the temperature to reach values of $14.87 \text{ cm}^3 \text{ K mol}^{-1}$ at 50 K (**52**) and $15.44 \text{ cm}^3 \text{ K mol}^{-1}$ at 35 K (**53**), followed by rapid increase to $17.0 \text{ cm}^3 \text{ K mol}^{-1}$ at 3 K (**52**) and $20.94 \text{ cm}^3 \text{ K mol}^{-1}$ at 1.8 K (**53**). Below 3 K, the χT product of **52** falls to $16.76 \text{ cm}^3 \text{ K mol}^{-1}$ at 1.8 K while **53** does not. The shape of the χT vs T plots (Fig. 6.4, right) is due to a combination of depopulation of Stark sub-levels at higher temperatures, weak ferromagnetic interactions between the Cu^{II} and Dy^{III} at low temperature. The fall of χT of **52** below 3 K is due to ZFS of Dy^{III} ion. The stronger ferromagnetic coupling in **53** at low temperature dominates the depopulation of Stark sub-levels and/or ZFS of Dy^{III} ion. Since azide bridges are well known for mediating stronger magnetic coupling than OMe bridges, the χT value of **53** reaches higher values at 1.8 K than that of **52** (Fig. 6.4, right).

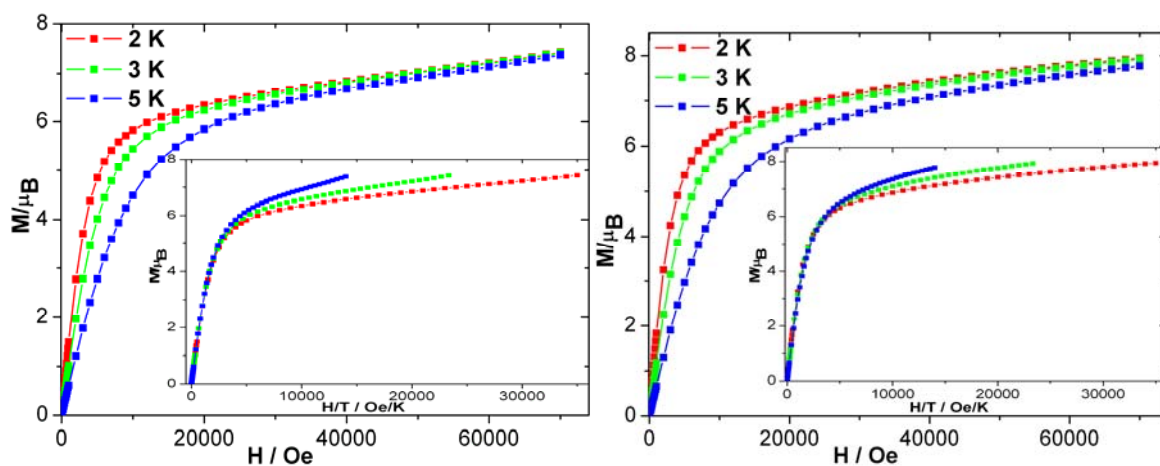


Fig. 6.5. Plots of M vs H and M vs H/T (inset) of **52** (left) and **53** (right) at indicated temperatures.

The field dependence of the magnetizations of **52** and **53** show that M values of both increase rapidly below 1 T and then increase linearly at higher field without reaching true saturation, indicating the presence of magnetic anisotropy in the systems. At 2 K and under an applied dc magnetic field of 7 T, the maximum magnetization values are 7.42 (**52**) and 7.94 (**53**) μ_{B} which are close to the expected value for two Cu^{II} ($S = 1/2$, $g = 2.0$) and one Dy^{III} ($5.58 \mu_{\text{B}}$) ions ($2 + 5.58 = 7.58 \mu_{\text{B}}$) with spins parallel. Moreover, M vs H/T plots of either **52** or **53** at

different temperatures do not superpose (Fig. 6.5, inset) on to a single master curve, also indicating the presence of low lying energy states and/or anisotropy in the systems.⁴³

6.3.3 Dynamic magnetic properties of **52** and **53**.

The temperature dependent ac susceptibility measurements on complex of **52** and **53**, reveal the presence of strong ac (χ' and χ'' vs T) signal (Fig. 3.34, left) in both compounds below 10 K under zero applied dc field.

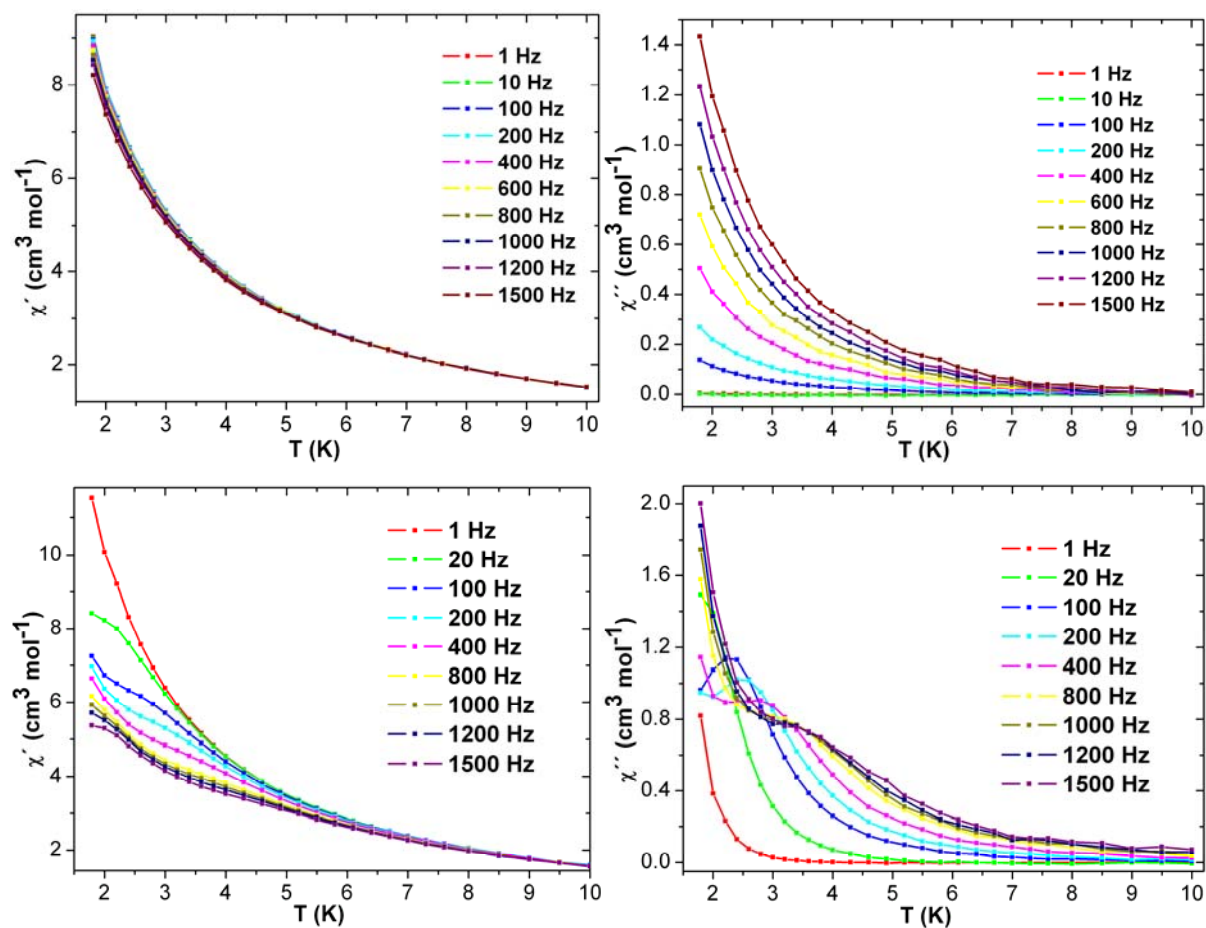


Fig. 6.6. Plots of χ' (left), χ'' (right) vs T of **52** (top) and **53** (bottom) at indicated frequencies.

There was no maximum observed (Fig. 6.6, top) for **52**. However, the shape of the χ' and χ'' vs T plots for **53** indicates that there could be two associated relaxation processes (Fig. 6.6, bottom).

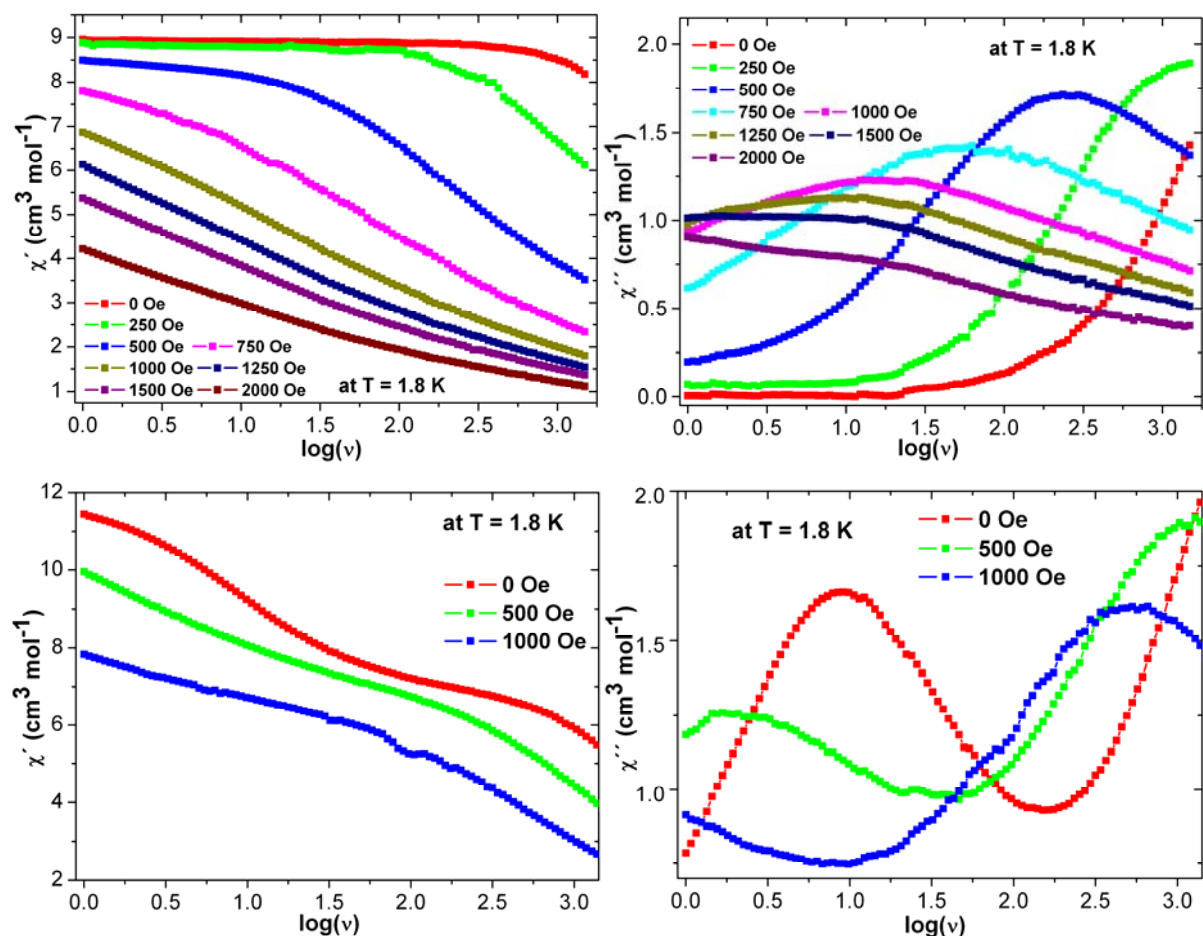


Fig. 6.7. Plots of χ' (left), χ'' (right) vs frequency of **52** (top) and **53** (bottom) under indicated applied dc fields.

The blocking (T_b) temperatures (the maxima of χ'' vs T plot) of **52** and **53** are below 1.8 K (**52**) and 3.5 K (**53**) at 1500 Hz respectively (Fig. 6.6) under zero dc field. The slow relaxation behavior of **52** and **53** are different with respect to each other. The frequency dependent ac measurements (Fig. 6.7) at 1.8 K with different applied magnetic fields revealed that there might be some QTM effect. The plots of ac (χ' and χ'') susceptibilities of **52** and **53** reveal there is one maximum (Fig. 6.7, top) for **52** and two maxima (Fig. 6.7, bottom) for **53** instead. From the plots in Fig. 6.7, top, it was clear that the applied dc field of 1 kOe field is sufficient to suppress the QTM pathways in **52**, while the critical field was not clear in **53**. This suggests that there might be two relaxation pathways in **53** but relaxation time might be too fast at higher fields. Thus, ac (χ' and χ'') susceptibilities of **52** and **53** were recorded under 1 kOe (Fig. 6.8, top) and zero Oe applied dc magnetic field (Fig. 6.8, bottom).

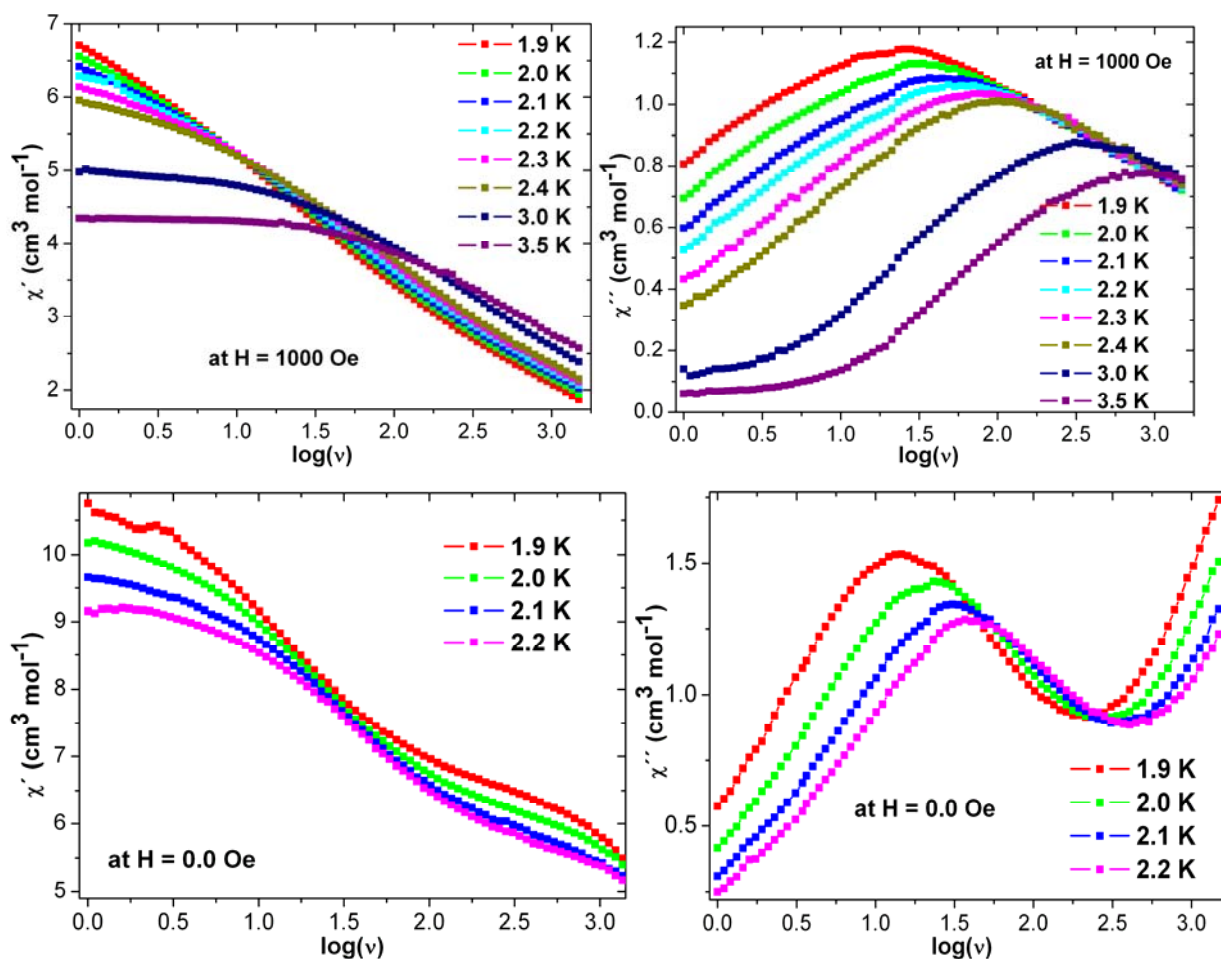


Fig. 6.8. Plots of χ' (left), χ'' (right) vs T of 52 (top) and 53 (bottom) at indicated temperatures.

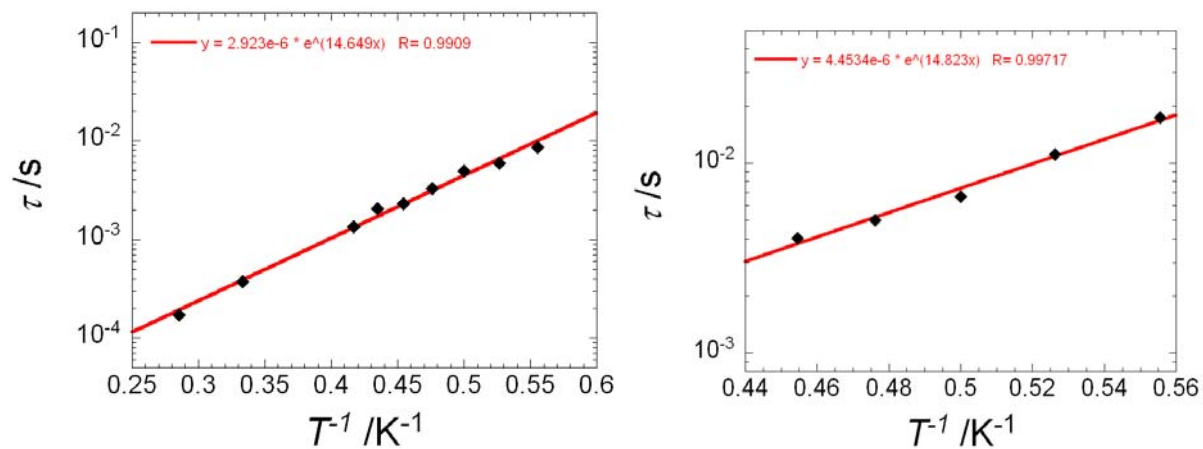
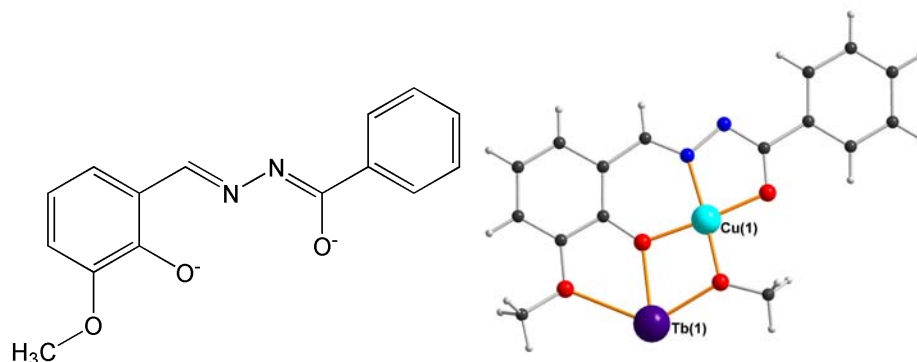


Fig. 6.9. Arrhenius plots of 52 (left) at 1 kOe and 53 (right) at zero applied dc field respectively.

The linear fitting on Arrhenius plot (τ vs $1/T$) for **52** (Fig. 6.9, left) gave an energy barriers of 14.64 K with relaxation time $\tau_0 = 2.9 \times 10^{-6}$ s under 1 kOe and zero applied dc magnetic field and corresponding values of 14.82 K and 4.4×10^{-6} s for **53** under zero dc field. Thus, both the SMMs **52** and **53** have similar energy barriers but different relaxation behavior. and **53** (Fig. 6.9, right)

6.4.1 Crystal Structure of $[\text{LnCu}_3(\text{L2})_3(\text{OMe})_3] \cdot x\text{MeOH} \cdot y\text{H}_2\text{O}$; [Ln = Dy(**54**), $x = 1.5$, $y = 0.215$; Tb(**55**) and Gd(**56**) $x = 1$, $y = 0$; Ho(**57**) and Er(**58**) $x = 1.5$, $y = 0.215$].

The complexes **54-58** are structurally similar, although **55** and **56** crystallize very differently from **54**, **57** and **58**. The structure of **55**, which crystallizes in the monoclinic space group $P2_1/n$ with the TbCu_3 complex on a general position, will be described in detail, and is shown in Fig. 6.10. Compounds **55** and **56** are isomorphous confirmed by measuring the unit cell constants of **56**.



Scheme 6.2. The dianionic ligand (L2^{2-}) (left) and $\{\text{Tb}(\text{OMe})(\text{L2})\}^-$ unit (right) of **55**.

The central Tb(1) is surrounded by three of the $\{\text{CuL2}(\text{OMe})\}^-$ metalloligands shown in Scheme 6.2, in each of which the ligand (L2^{2-}) chelates the corresponding Cu^{II} cation through its two deprotonated oxygens and the imine nitrogen, with a methoxo ligand derived from deprotonation of the methanol solvent completing the square-planar O_3N environment of the Cu^{II} ion. The organic phenoxo and methoxy oxygens of each metalloligand then in turn chelate Tb1, with the methoxo ligand forming an additional Cu·Tb bridge. The Cu-O and Cu-N bond lengths are all in the range 1.898(4)-1.937(4) Å, typical for square-planar Cu^{II} cations.

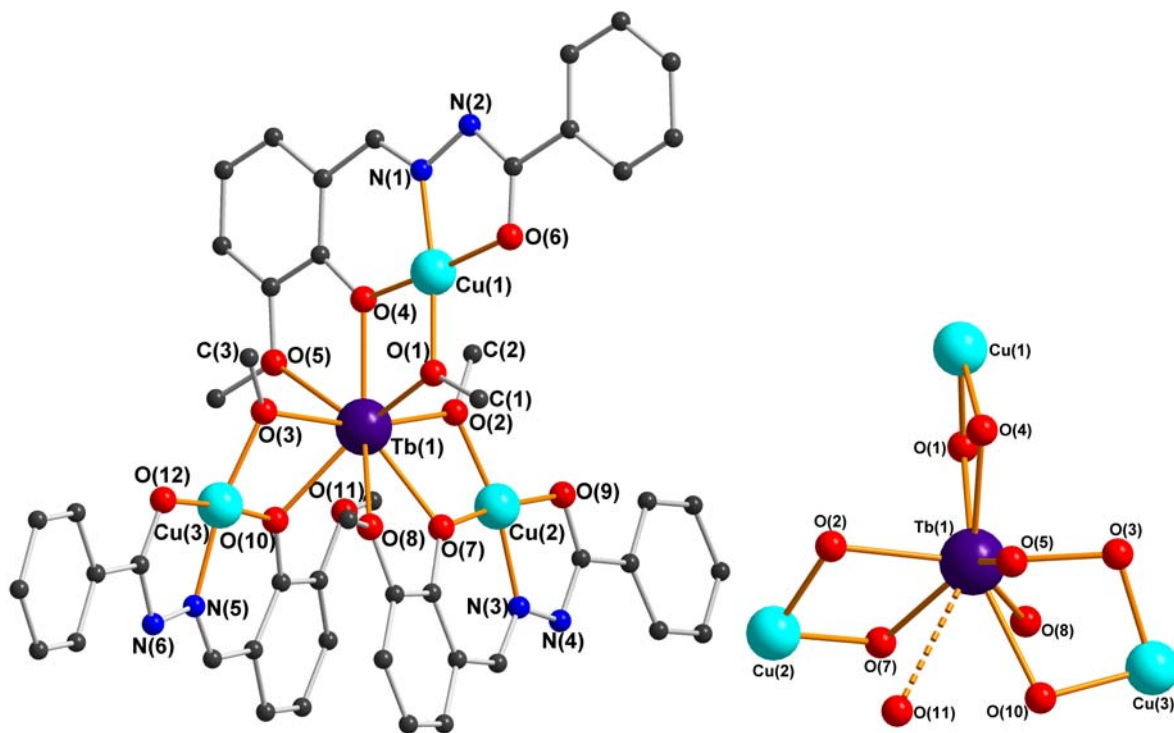


Fig. 6.10. Molecular structure of the $[\text{TbCu}_3(\mu\text{-OH})_3(\text{L}2)_3]$ complex in **55**, H-atoms omitted for clarity (left); the core of the complex projected onto the TbCu_3 mean plane, with the very long Tb1-O11 bond shown as a dashed line (right).

The Tb(1)-O bond distances involving the bridging methoxo ligands, 2.285(3)-2.310(3) Å, are slightly shorter than those to the phenoxo oxygens, 2.349(3)-2.393(3) Å. Those to the organic methoxy groups are, however, considerably longer, with Tb1-O5 and Tb1-O8 2.663(4) and 2.770(4) Å, respectively, while $\text{Tb1}\cdots\text{O11}$ at 3.006(4) Å constitutes at most a very weak interaction; it is shown dotted in Fig. 6.10. O8 is aligned with an axial site on Cu3, and O11 similarly with Cu2, but the corresponding $\text{Cu}\cdots\text{O}$ distances are both over 2.9 Å and there can therefore be no significant interactions. The six Tb-O-Cu angles are all in the range 98.62(15)-105.96(15)°.

In transition metal complexes with a hexa-coordinate central metal cation, such a construction often results in a rather regular “three-bladed propeller” core with three-fold symmetry. In the present complex this is not the case, as a consequence of the higher coordination number of Tb1, eight rather than six. Two of the metallo-ligands, those involving Cu2 and Cu3 are arranged mutually antiparallel, such that they are related by an approximate

twofold axis through Tb1, while the third one, that involving Cu1, lies close to perpendicular to the other two with its phenoxo oxygen O4 close to the twofold axis relating the other two ligands. The $\{\text{Tb}(\mu\text{-OR})_6\text{Cu}_3\}$ propeller core thus deviates significantly from threefold symmetry. Although the three Tb··Cu distances are not that different, at 3.3480(8), 3.3398(6) and 3.3038(7) Å, the Tb_3Cu unit deviates from planarity, with Tb1 0.393 Å out of the plane through the three Cu centres. More significantly, the three $\{\text{Tb}(\mu\text{-OR})_2\text{Cu}\}$ linkages make very different angles to the TbCu_3 mean plane; with the three individual TbO_2Cu mean planes involving Cu1, Cu2 and Cu3 subtending dihedral angles of 83.38(8)°, 47.94(12)° and 10.44(12)°, respectively, to the TbCu_3 plane. The coordination geometry of the eight-coordinate Tb1 can best be described as a distorted bicapped trigonal prism, with O(4) and O(8) forming the caps; if O(11) were within bonding distance of Tb1, then it would form a third cap to the prism.

Compounds **54**, **57** and **58** are isostructural to **55** and **56**, but have a very different crystal structure. The structure of **54** will be described here. The unit cell constants for **57** and **58** are very similar to those of **54**. At first, sight **54** crystallizes in a C-centered monoclinic unit cell with one molecule in the asymmetric unit. But after structure solution in $C2/c$ and initial refinement of the molecule it became apparent that the metalloligand involving Cu1 showed rather ill-defined twofold disorder, corresponding to rotation about the Tb1-O4 axis, with a *ca.* 3:1 occupancy ratio. Furthermore the temperature factors of the other atoms were higher than expected, and it proved impossible to refine the structure in any satisfactory manner. Noting that the systematic absences for the *c* glide were not very clean, and that the mean value of $|E^2 - 1|$ was rather low, the possibility that the apparent monoclinic cell was the result of *pseudo*-merohedral twinning was investigated.

After transformation of the unit cell to primitive triclinic, the structure could again be solved, this time with two molecules in the asymmetric unit. One of these, centred around Dy1, was ordered (apart from one of the phenyl groups), while the other showed the same disorder as before, with a 57:43 occupancy ratio. Now, after allowing for the twinning (“TWIN 1 0 0 1 -1 0 0 0 -1 2”), the structure could be refined satisfactorily; a modest use of similarity restraints (both geometrical and for thermal parameters of closely adjacent partial atoms from different disorder components) allowed refinement of the disordered metalloligand in molecule 2. The structures of the two molecules are shown in Fig. 6.11. It may be noted that, if the phenyl substituent is ignored, the external shape of the metallo-ligand involving Cu4A/Cu4B conforms rather well to

the twofold symmetry of the rest of the molecule, as does its ligation of Dy²; the resulting structural flexibility is presumably the cause of the twinning and disorder. The Dy¹ and Dy² centers of **54**, are situated 0.392 and 0.511/0.557 Å above Cu₁Cu₂Cu₃ and Cu₄ACu₅Cu₆/Cu₄BCu₅Cu₆ planes respectively. Both of the two molecules are closely iso-structural to complex **55**.

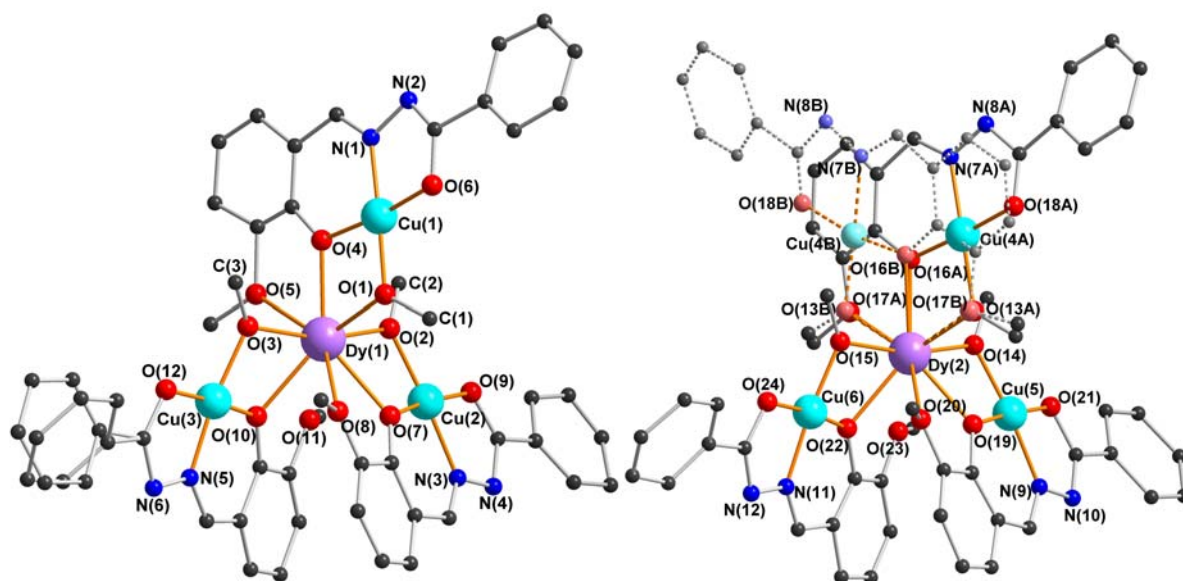


Fig. 6.11. Molecules 1 (left) and 2 (right) in the crystal structure of **54**. Atoms from the second disorder component in molecule 2 are drawn smaller and paler than for those in the first component; bonds in the second component are drawn dashed.

6.4.2 Static magnetic properties of **54** -**58**.

The dc magnetic data of **54**-**58** are summarized in Table 6.5. The room temperature χT values for Dy^{III}Cu^{II}₃ (**54**) and Tb^{III}Cu^{II}₃ (**55**) are 16.31 and 14.78 cm³ K mol⁻¹, respectively, which are slightly greater than those calculated for the Dy^{III} or Tb^{III} ion and three Cu^{II} ions: 15.30 for **54** and 12.95 cm³ K mol⁻¹ for **55**. On lowering the temperature, the χT value of **54** stays almost constant from 300 K to 80 K and then continuously increases to reach 26.22 cm³ K mol⁻¹ at 1.8 K, however, that of **55** decreases slowly between 300 K and 60 K, and then rapidly increases to reach a maximum of 17.67 cm³ K mol⁻¹ at 7 K with a final fall to 15.70 cm³ K mol⁻¹ at 1.8 K (Fig. 6.12). These features of χT vs T plots of **54** and **55** indicate the presence of overall

ferromagnetic interactions. The fall of χT of **55** below 7 K is probably due to zero field splitting of the Tb^{III} ion.

Table 6.5. The dc magnetic data of compounds **54-58**.

Compound	Ground state of Ln^{III} ion	χT expected for non-interacting ions per complex ($\text{cm}^3\text{Kmol}^{-1}$)	χT measured at 300 K per complex ($\text{cm}^3\text{Kmol}^{-1}$)	χT measured at 1.8 K per complex ($\text{cm}^3\text{Kmol}^{-1}$)	Magnetization at 2 K and 7 T (μ_B)
$\text{Dy}^{\text{III}}\text{Cu}^{\text{II}}_3$ (54)	$^6\text{H}_{15/2}$	15.30	16.37	26.22	8.2
$\text{Tb}^{\text{III}}\text{Cu}^{\text{II}}_3$ (55)	$^7\text{H}_6$	12.95	14.54	15.70	7.6
$\text{Gd}^{\text{III}}\text{Cu}^{\text{II}}_3$ (56)	$^8\text{S}_{7/2}$	9.0	9.37	14.0	10.33
$\text{Ho}^{\text{III}}\text{Cu}^{\text{II}}_3$ (57)	$^5\text{I}_8$	15.19	15.48	13.68	8.36
$\text{Er}^{\text{III}}\text{Cu}^{\text{II}}_3$ (58)	$^4\text{I}_{15/2}$	12.60	12.50	10.16	8.32

For anisotropic Dy^{III} and Tb^{III} ions, the thermal depopulation of the excited Stark sublevels can contribute to a decrease of the χT product, and results in the decrease of χT in the higher temperature regime in **55**, but this effect is not obviously observed in the Dy compound. Although the magnetic cores of the two compounds has a simple topology ‘three-bladed propeller’, it is known that the coupled systems including at least one ion with an orbital momentum contribution are not amenable to a quantitative analysis and the symmetry of these propeller is low.

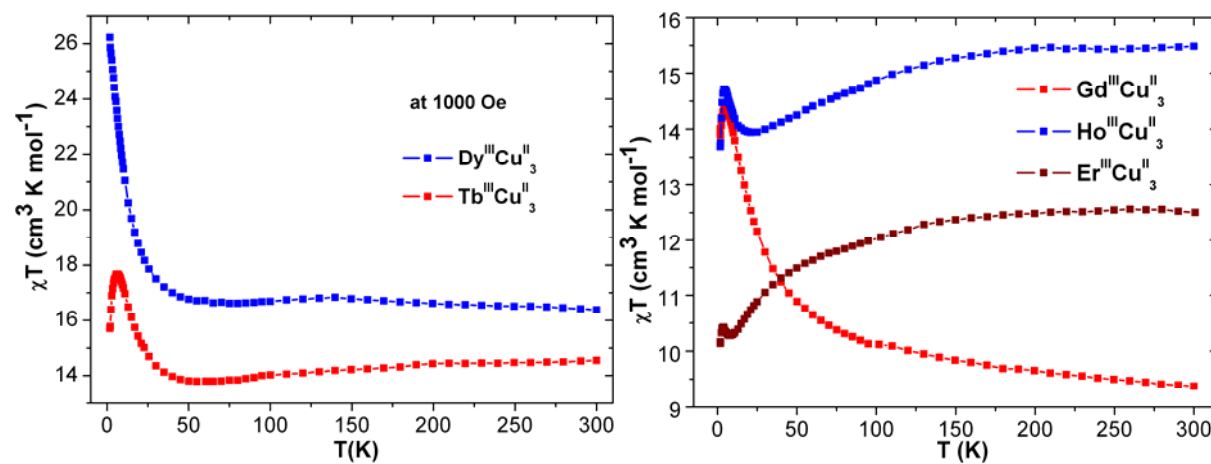


Fig. 6.12. Plots of χT vs T of **54-55** (left) and **56-58** (right) under indicated applied magnetic field.

The χT product of **56** increases from room temperature to 4 K where it reaches a maximum before falling slightly to $14.0 \text{ cm}^3 \text{ K mol}^{-1}$ at 1.8 K. The shape of the curve indicates strong ferromagnetic interaction between Gd^{III} and Cu^{II} ions. While the χT products of **57** and **58** decrease steadily between room temperature and 20 (**57**) K and 8 K (**58**) (due to the depopulation of Stark sub-levels) followed by an increase to a maximum at 4 K (**57**) and 3 K (**58**) (due to weak intramolecular ferromagnetic coupling) and finally fall till temperature reaches 1.8 K (due to ZFS of Ho^{III} / Er^{III}) (Fig. 6.12, right). The field dependence of the magnetizations of both **54** and **55** (Fig. 6.13) reveal that the magnetization rapidly increases below 10 kOe, as expected for a ferromagnetically coupled system above which slowly increases to 8.2 and $7.6 \mu_{\text{B}}$ at 2 K for **54** and **55** respectively in a linear fashion till the dc magnetic field reaches 7 T.

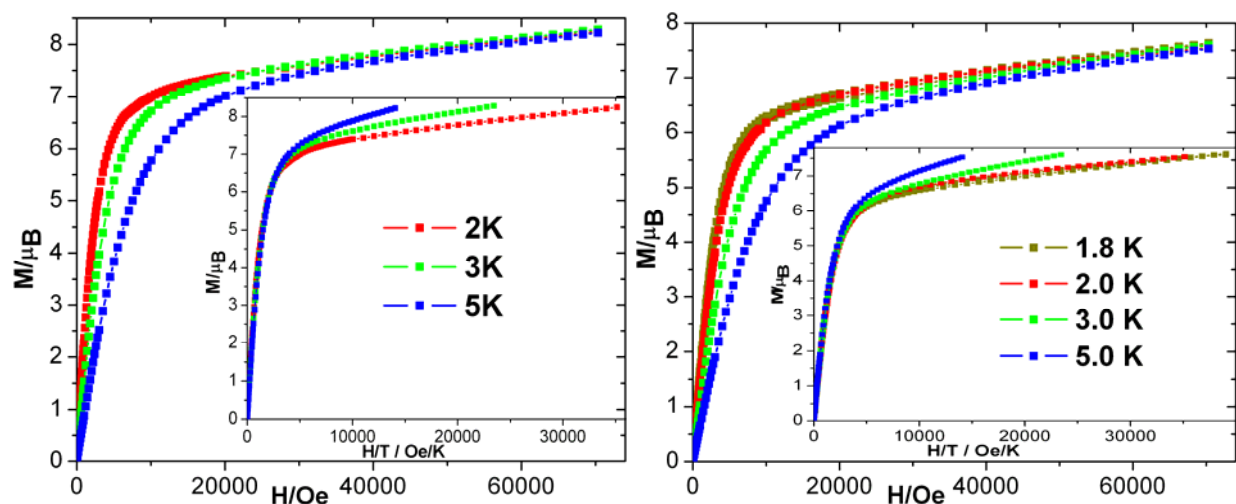


Fig. 6.13. The M vs H and M vs H/T (inset) plots of **54** (left) and **55** (right) at the indicated temperatures.

The lack of saturation of M and the non-superposed M vs H/T plots of **54**, **55**, **57** and **58** indicate the presence of anisotropy and/or low lying excited states in the system.⁴³ At 2 K, the magnetization of **56** saturates to $10.33 \mu_{\text{B}}$ at 7 T as expected for ferromagnetically coupled one Gd^{III} (with $S = 7/2$ and $g = 2.0$) and three Cu^{II} ions (with $S = 1/2$ and $g = 2.0$) ($10.0 \mu_{\text{B}}$). The M vs H/T plots of **56** almost superposed on to a single master curve as expected for an isotropic system (Fig. 6.14, left).

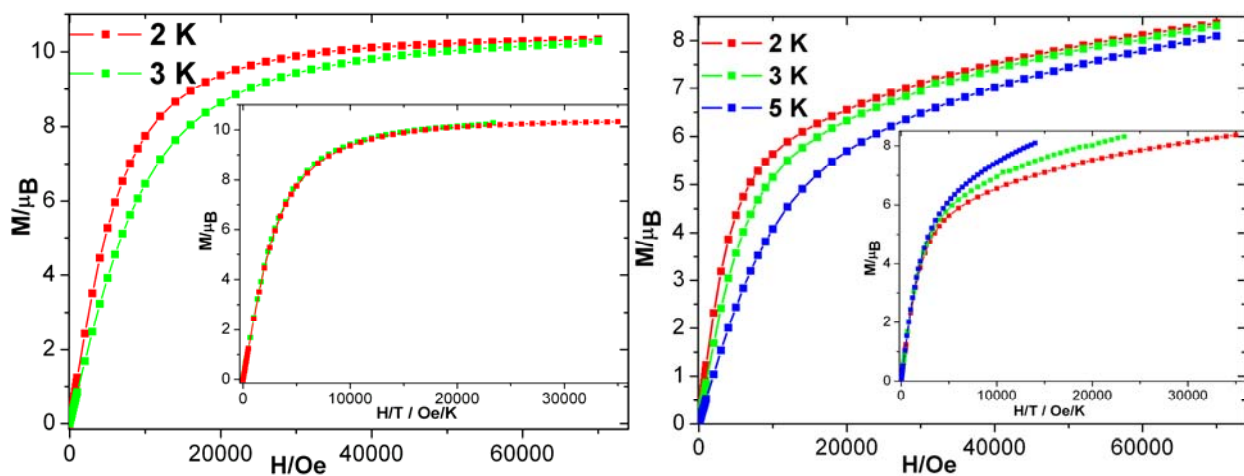


Fig. 6.14. The M vs H and M vs H/T (inset) plots of **56** (left) and **57** (right) at the indicated temperatures.

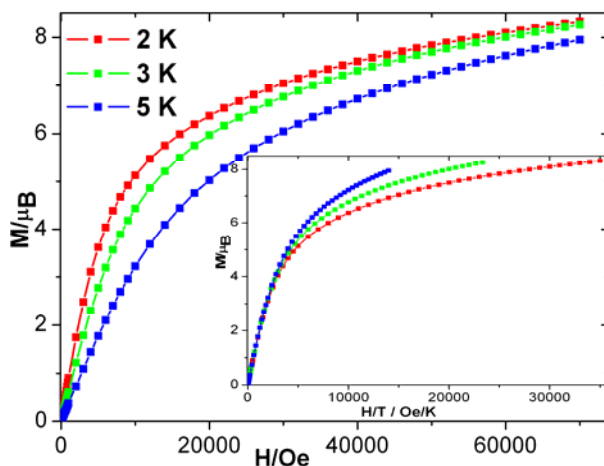


Fig. 6.15. The M vs H and M vs H/T (inset) plots of **58**.

6.4.3 Dynamic magnetic properties of 54-58.

The dynamic properties of all compounds **54-58** have been investigated at 1 kHz under zero dc field in the temperature range of 1.8-10 K. Only compounds **54**, **55** and **57** exhibit detectable in-phase (χ') and out-of-phase (χ'') signals. The χ' and χ'' vs T data are plotted in Fig. 6.16-6.17. There is no maximum in χ' and χ'' vs T plots of **57** indicating that **57** may be a SMM with T_b below 1.8 K (Fig. 6.17). The ac susceptibilities of both real and imaginary components for **54** and **55** exhibit strong frequency- and temperature-dependence below 10 K suggesting (Fig. 6.16-6.18) both these compounds are better SMMs compared to **57**. The maxima of the out-of-phase susceptibilities (**54** and **55**) were extracted to quantify the energy

barriers Δ and relaxation times τ_0 . The thermally activated regimes in **54** and **55** could be observed from 1.8 K up to 4.4 and 3.8 K, respectively, in which the fit to the Arrhenius equation leads to the following parameters: $\Delta = 19.6$ K and $\tau_0 = 2.4 \times 10^{-6}$ s for **54** and $\Delta = 18.7$ K and $\tau_0 = 1.0 \times 10^{-6}$ s for **55** (Fig. 6.19). Another important parameter α , the width of the distribution of the relaxation time, could be obtained by analyzing the Cole-Cole diagrams of **54** and **55** (Fig. 6.20).

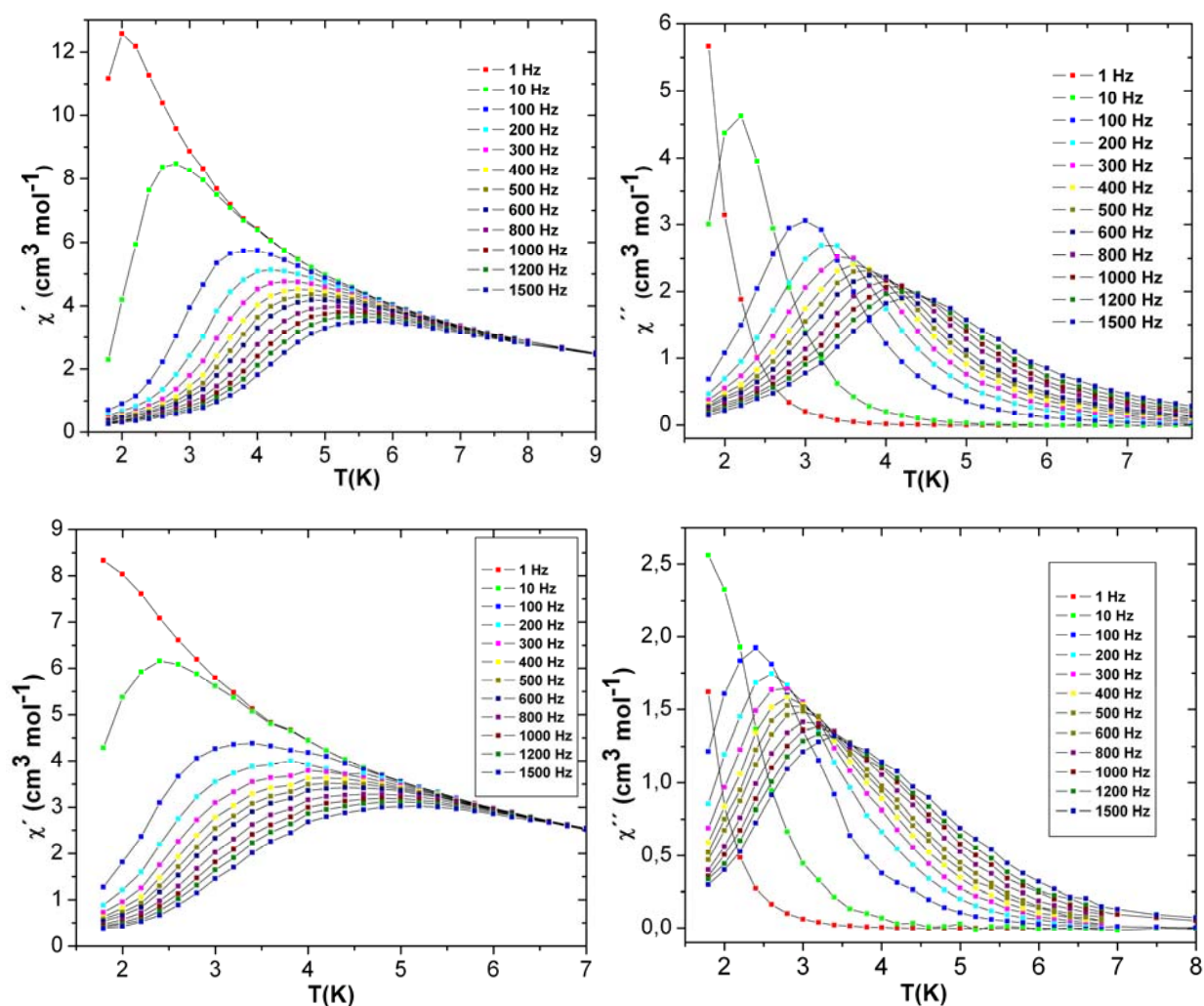


Fig. 6.16. Plots of in-phase (χ') and out-of-phase (χ'') susceptibilities vs T of **54** (top) and **55** (bottom) at indicated frequencies under zero dc applied magnetic field.

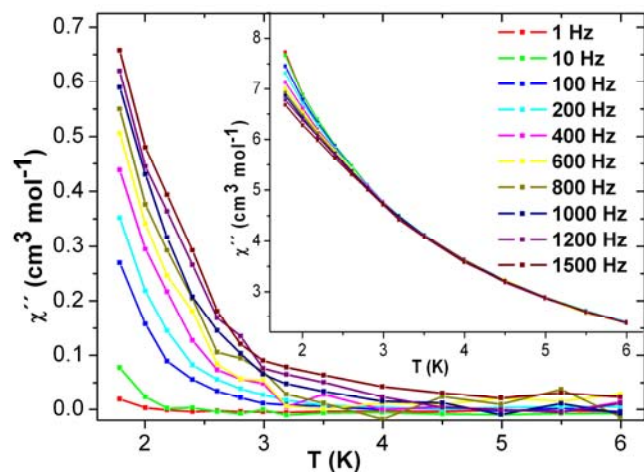
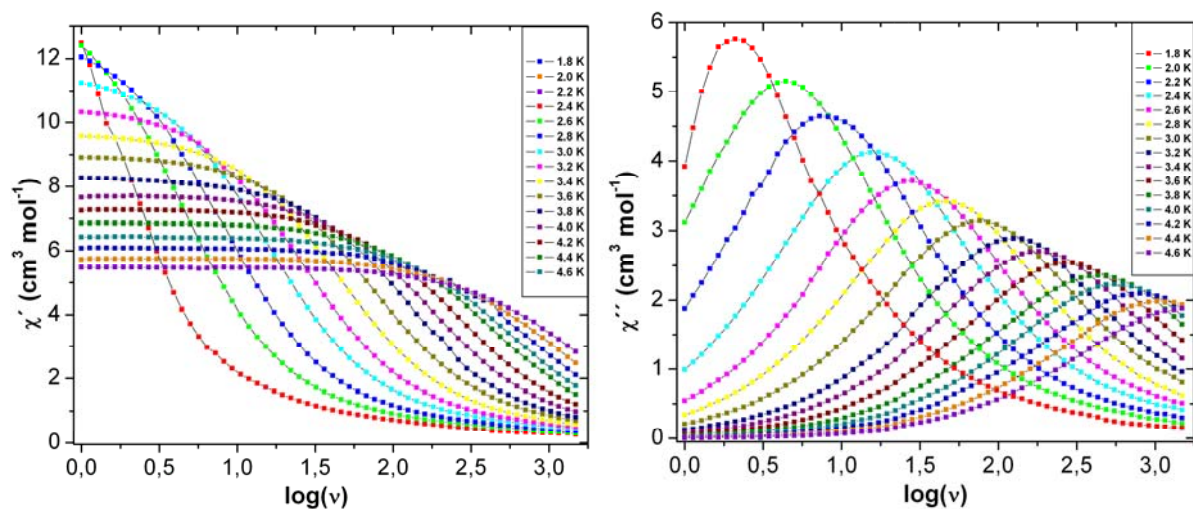


Fig. 6.17. Plots of χ'' and χ' (inset) vs T of **57**.

The fits to a generalized Debye model^{59a} result in the α parameters between 0.18 and 0.24 for **54**, and 0.30 and 0.39 for **55**, respectively (Table 6.6). Such values are comparable to that reported in some 3d-4f SMMs.^{44,50} The frequency dependence of the ac susceptibilities of **54** and **55** were also measured with an applied static field.



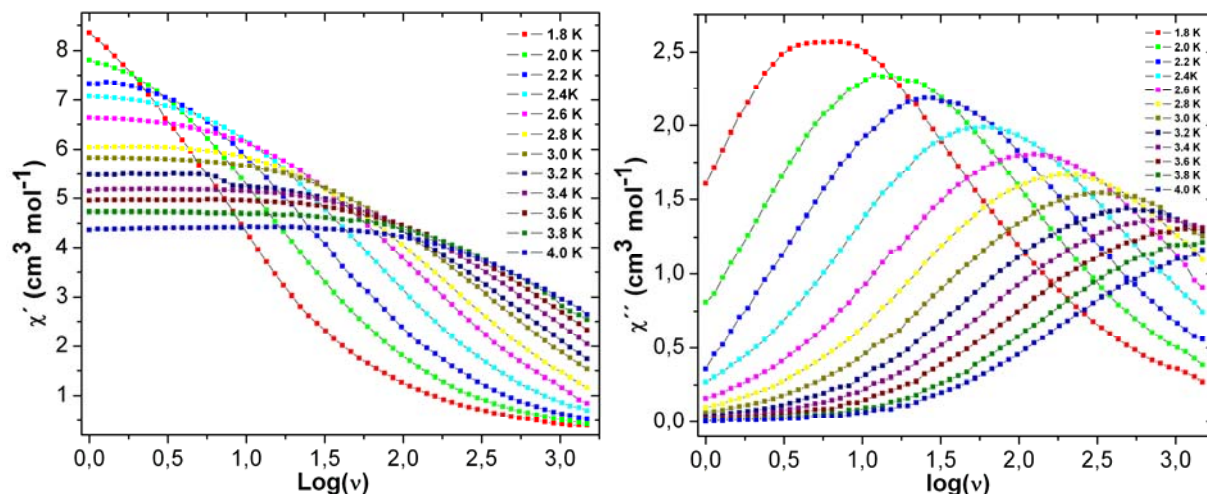


Fig. 6.18. Plots of in-phase (χ') and out-of-phase (χ'') susceptibilities vs $\text{log}(\nu)$ of **54** (top) and **55** (bottom) with ν in the range of 1-1500 Hz at indicated temperatures under zero dc applied magnetic field.

This effect is indeed experimentally observed in both compounds. The optimum field to slow down the relaxation process was found to be 1.5 kOe in both cases (Fig. 6.21). Therefore, the frequency dependence of the ac susceptibility measurements were remeasured under 1.5 kOe external dc field (Fig. 6.22). The thermally-activated regimes observed under 1.5 kOe extended to higher temperatures: 5.0 and 4.2 K for **54** and **55**, respectively.

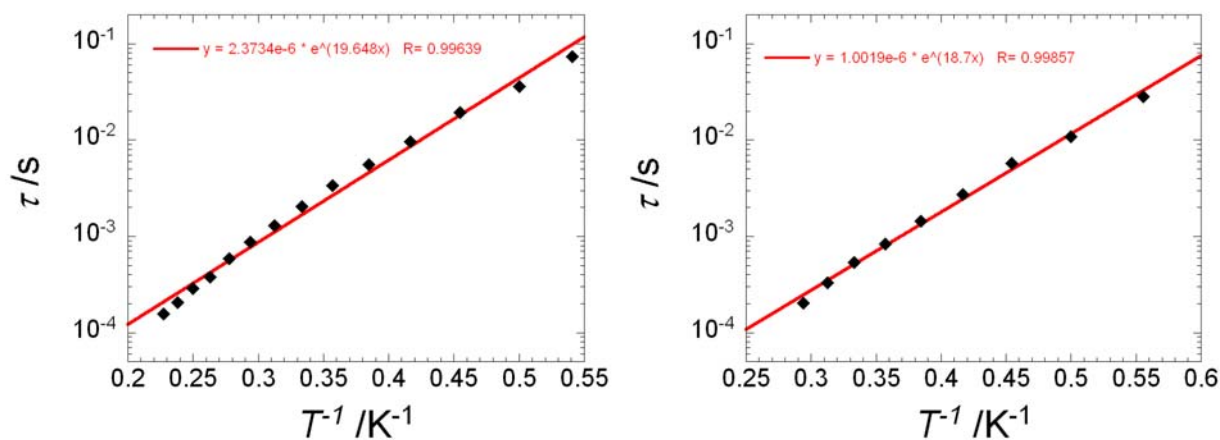


Fig. 6.19. Arrhenius plots of complexes **54** (left) and **55** (right) under zero dc field. The red lines indicate the best fits.

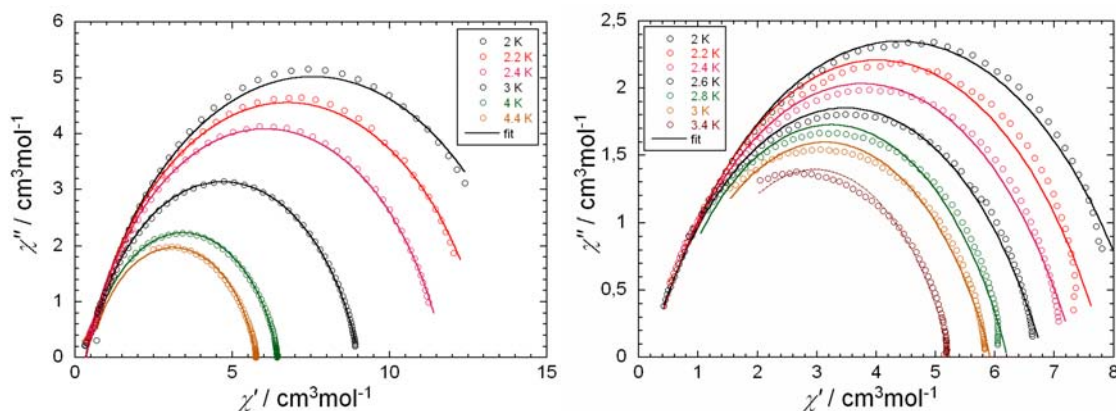


Fig. 6.20. Cole-Cole plots using the frequency dependence of ac susceptibility data shown in Fig. 6.15 for **54** (left) and **55** (right). The solid lines are the best fit obtained with a generalized Debye model with the parameters listed in the following two Tables.

The effective energy barriers of spin reversal and the relaxation times are now found to be 30.8 K and 3.8×10^{-7} s for **54** and 22.5 K and 5.3×10^{-7} s for **55**, respectively (Fig. 6.23). The observation that the energy barrier for spin reversal is higher and its relaxation time is shorter under static field than those under zero dc field is consistent with that of a system possessing a relaxation process influenced by quantum tunneling.

Table 6.6. The ac parameters of DyCu₃ (**54**) and TbCu₃ (**55**).

54	54	54	54	55	55	55	55
T (K)	α	χ_0 (cm ³ /mol)	χ_{inf} (cm ³ /mol)	T (K)	α	χ_0 (cm ³ /mol)	χ_{inf} (cm ³ /mol)
1.8	0.239(11)	16.484(32)	0.341(25)	1.8	0.389(2)	10.154(28)	0.165(7)
2.0	0.227(6)	14.790(10)	0.325(15)	2.0	0.352(4)	8.602(27)	0.172(15)
2.2	0.214(4)	13.173(4)	0.338(10)	2.2	0.335(8)	7.867(35)	0.186(32)
2.4	0.207(3)	11.741(17)	0.358(8)	2.4	0.345(5)	7.362(17)	0.167(26)
3.0	0.199(1)	9.016(4)	0.385(8)	2.6	0.355(5)	6.820(13)	0.143(32)
4.0	0.187(3)	6.450(2)	0.423(3)	2.8	0.329(8)	6.216(14)	0.271(54)
4.4	0.183(5)	5.770(2)	0.484(6)	3.0	0.337(7)	5.926(9)	0.351(55)
				3.4	0.302(10)	5.244(8)	0.679(85)

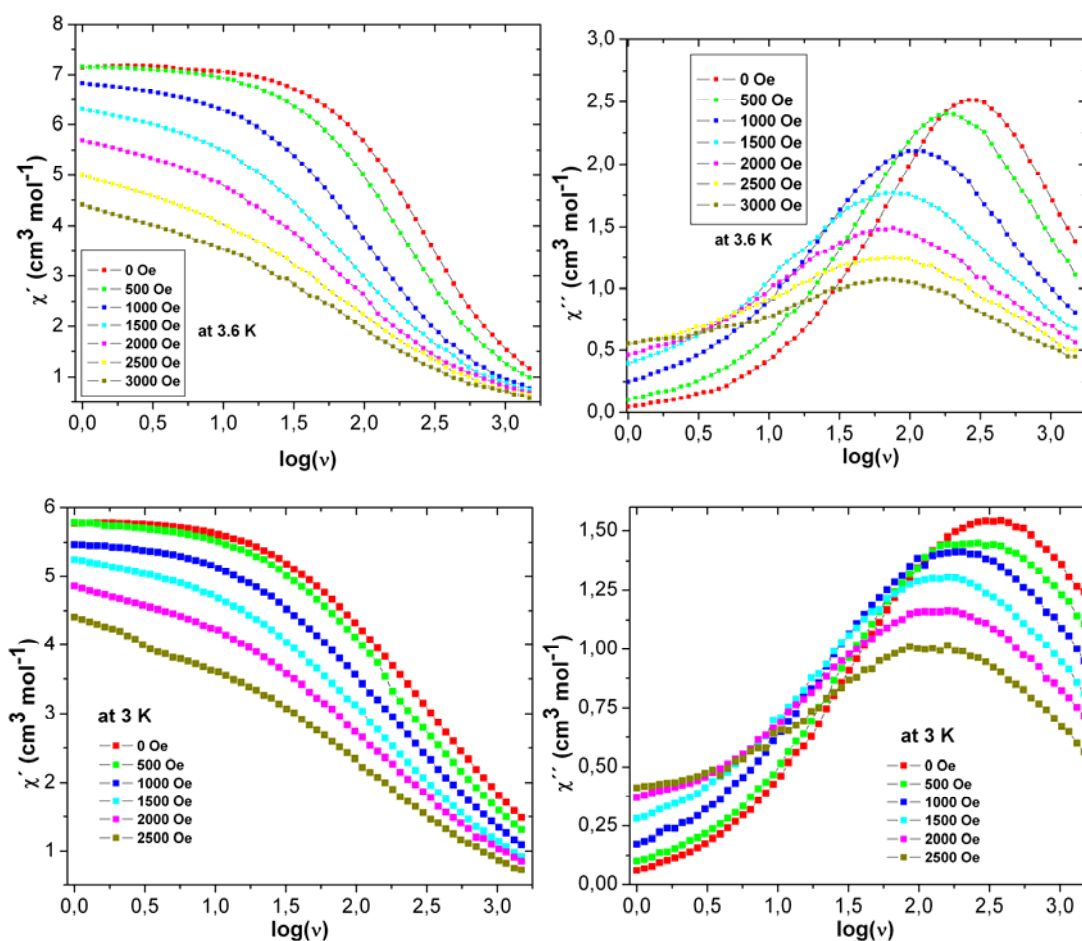


Fig. 6.21. Plots of in-phase (χ') and out-of-phase (χ'') susceptibilities vs $\log(\nu)$ of **54** (top) and **55** (bottom) at different applied dc fields.

To confirm the SMM behavior, magnetization measurements on a polycrystalline sample of **54** show hysteresis loops opening at 2 K with a field sweep rate of 0.46 T/s. The measurements were performed at 1.49 K with different field sweep rates and at different temperatures with a fixed sweep rate of 0.46 T/s. Both experiments show strong temperature- and field-sweep rate-dependent hysteresis (Fig. 6.24). The step-like features in hysteresis loops due to resonant quantum tunneling, which are characteristic for SMMs, are not clearly present in these data. However, this is a common finding in experiments on powder samples at temperatures just below the blocking temperature.

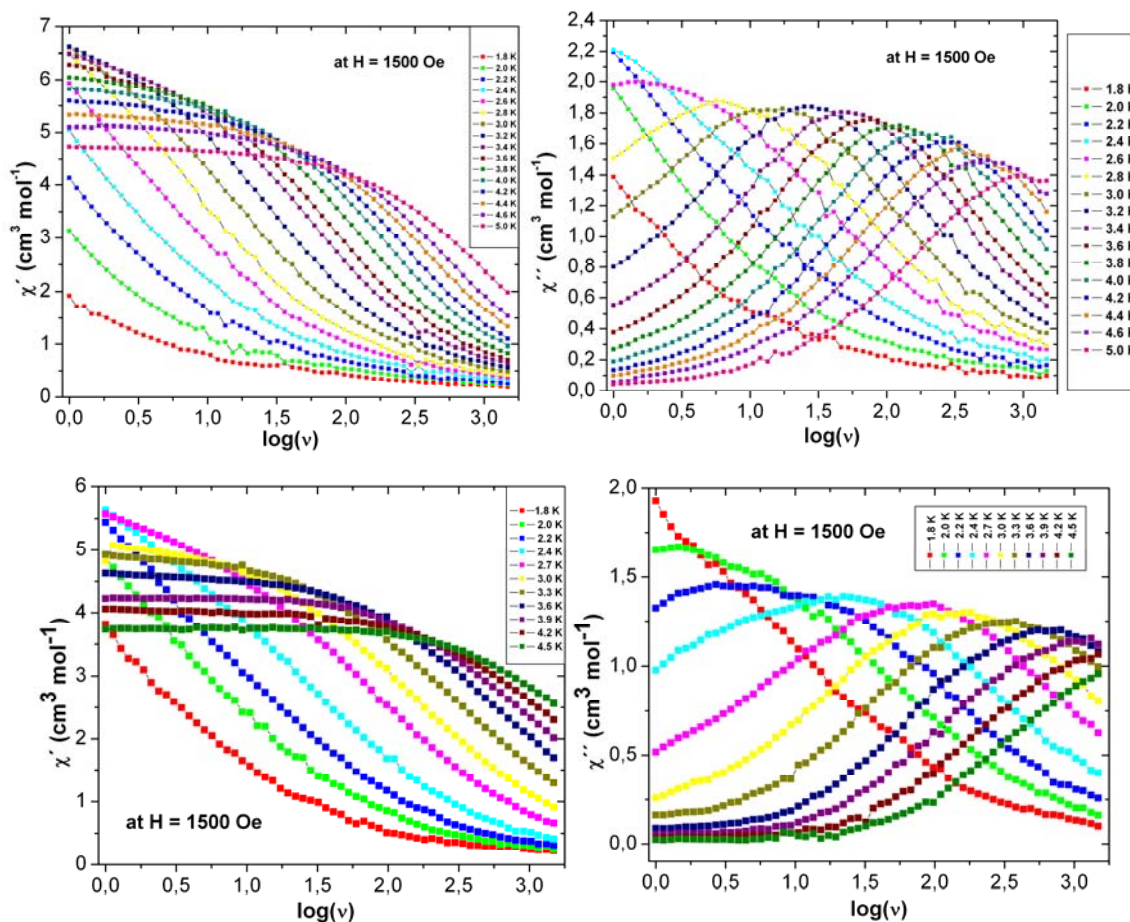


Fig. 6.22. Plots of in-phase (χ') and out-of-phase (χ'') susceptibilities vs $\log(\nu)$ of **54** (top) and **55** (bottom) with ν in the range of 1-1500 Hz at indicated temperatures under a dc applied magnetic field of 1.5 kOe.

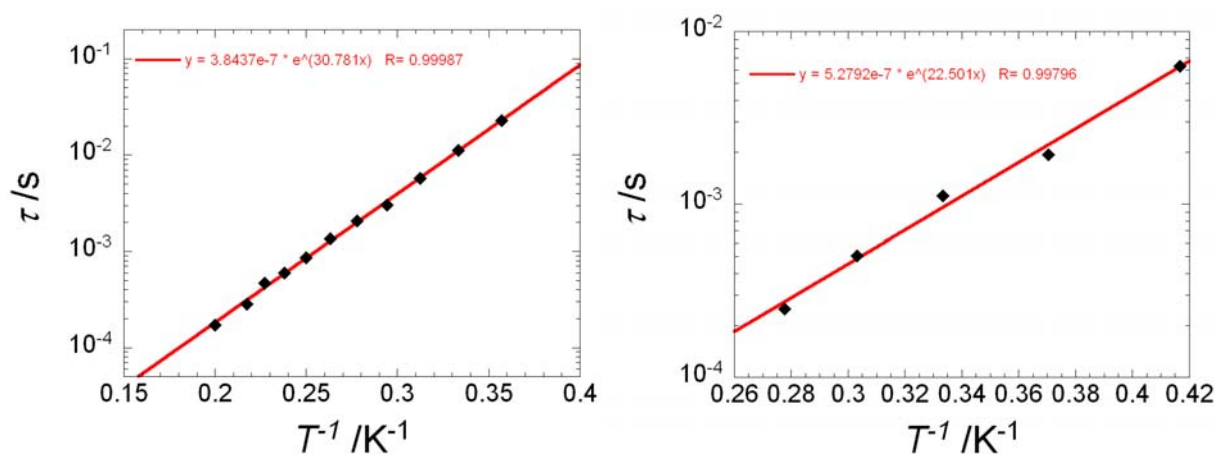


Fig. 6.23. Arrhenius plots of complexes **54** (left) and **55** (right) at a dc field of 1.5 kOe. The red lines indicate the best fits.

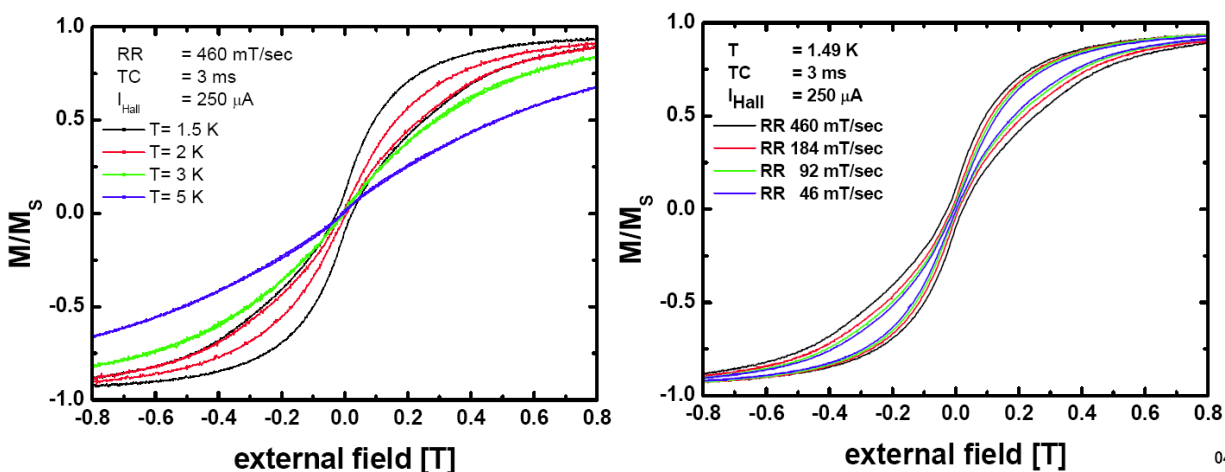


Fig. 6.24. Hysteresis loop measurements of **54** at different temperatures with a fixed field sweep rate of 0.46 T/s (left) and at different field sweep rates at 1.49 K (right). The magnetization is normalized to the saturation value M_s .

6.5.1 Crystal structure of $[\text{Dy}_2\text{Cu}_6(\text{OMe})_{2.76}(\text{N}_3)_{1.24}(\text{L}2)_6(\text{H}_2\text{O})(\text{MeOH})(\text{L}4)] \cdot 10\text{MeOH} \cdot 2\text{H}_2\text{O}$ (**59**)

The complex **59** crystallizes in the centrosymmetric space group $P-1$ with a center of symmetry within the molecule. The asymmetric crystallographic unit contains three Cu^{II} ions, one Dy^{III} ion, three $(\text{L}2)^{2-}$, one $\mu_2\text{-OMe}^-$, one disordered $\mu_2\text{-(OMe)}_{0.69}/(\text{N}_3)_{0.31}$ and half a $(\text{L}4)^{2-}$ ligand. The crystal lattice of **59** also contains ten MeOH and two H_2O solvent molecules. All three Cu^{II} ions have elongated Jahn-Teller axes. The Cu2/Cu3, Cu1 and Dy1 centers adopt distorted octahedral, square pyramidal and square antiprismatic geometry respectively.

Each half of the Dy_2Cu_6 complex has structural a similarity (Fig. 6.25) to the propeller-shape DyCu_3 complex (**54**). In the center of the propeller, there is again a Dy^{III} ion with Cu^{II} ions at the three vertices. Each blade (Cu3-Dy1, Cu2-Dy1 and Cu1-Dy1) is double μ_2 - bridged by OMe-phenoxide, mixed azide/OMe-phenoxide and phenoxide-phenoxide combinations. Cu1 and Cu2 are ligated into pocket-I (ONO) and Dy^{III} ion into pocket-II (OO) of the ligand $(\text{L}2)^{2-}$. However, Cu3 and Cu3' are now both ligated by pocket-III of $(\text{L}4)^{2-}$ ligand, and these two Cu^{II} centers are now by the =N-N= linkage. The bridging ligand $(\text{L}4)^{2-}$ not only connects two propeller shaped DyCu_3 units but also replaces one $\mu_2\text{-OMe}$ by one $\mu_2\text{-phenoxide}$ bridge in each

DyCu₃ unit of Dy₂Cu₆ complex **59**. Thus the L⁴ displays $\eta^1: \eta^2: \eta^2: \eta^1: \eta^2: \eta^1: \mu_6$ (Fig. 6.25, bottom). The two DyCu₃ units are therefore joined magnetically, with Cu3-Cu3' 5.185 Å.

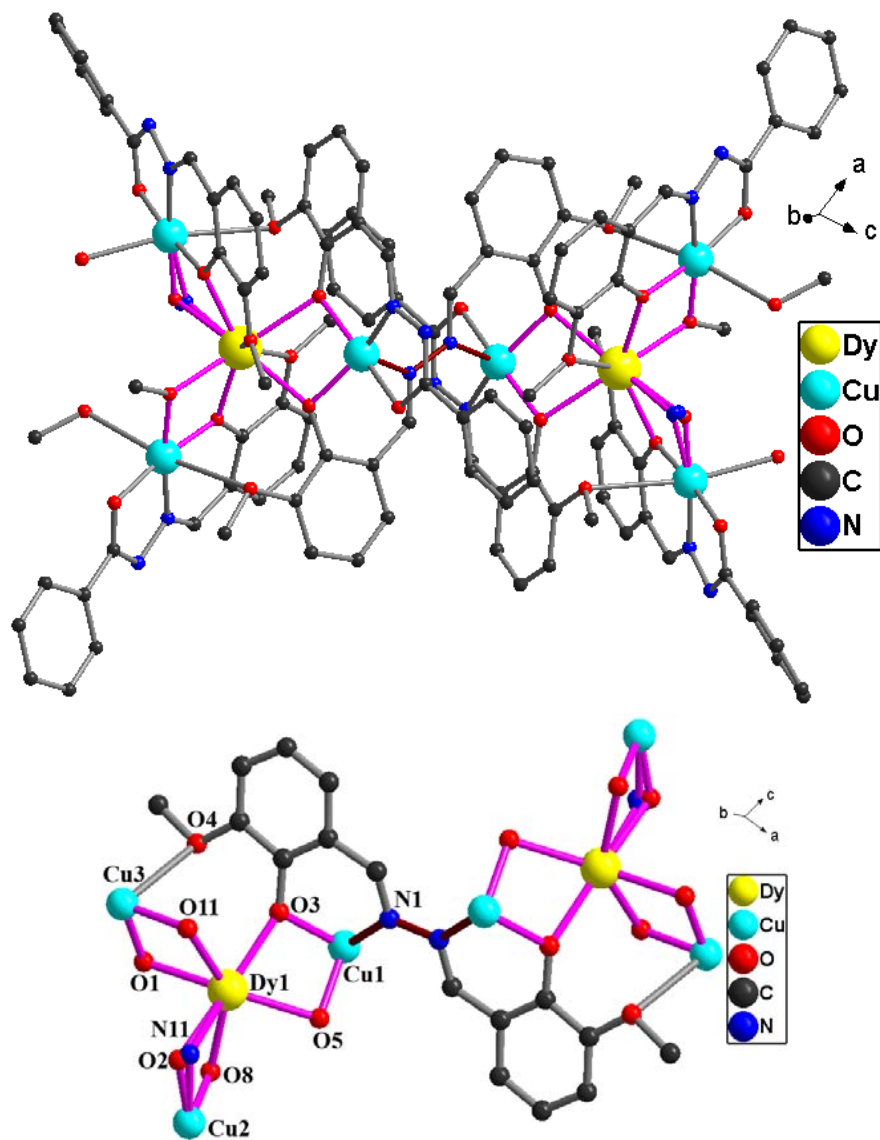


Fig. 6.25. Molecular structure (top) and core (bottom) of the coordination cluster in compound **59**.

Thus, the magnetic core (Fig. 6.25, bottom) has been distorted with respect to the original propeller shape DyCu₃ core, and the geometries of the Cu^{II} ions have also changed in complex **59**. One MeOH/H₂O molecule and a methoxy (-OMe) group are coordinated to each of Cu2 and Cu3 centers in their respective Jahn-Teller axial sites. The Dy-O/N bond distances range from 2.248(6) to 2.595(6) Å. The *equatorial* and *axial* Cu-O/N bond distances range from 1.920(7) to 1.985(6) Å and 2.249(6) to 2.839(6) Å respectively. The Dy1-Cu1, Dy1-Cu2 and Dy1-Cu3

distances are 3.3049(11), 3.3309(12) and 3.3258(12) Å respectively. Since Dy1 is only slightly displaced 0.253 Å out of the coplanar Cu₃ unit, each Cu-Dy-Cu angle only deviates slightly from 120° (Cu1-Dy1-Cu3 = 121.66(3), Cu1-Dy1-Cu2 = 125.02(3) and Cu3-Dy1-Cu2 = 111.58(3)°). The Cu-O/N-Dy bridging angles are in the range of 97.6(2) to 106.2(3).

6.5.2 Static magnetic properties of **59**.

The room temperature χT value for the Dy^{III}₂Cu^{II}₆ unit (**59**) is 34.81 cm³ K mol⁻¹, which is slightly greater than the expected value of 30.60 for **59** containing two Dy^{III} ($S = 5/2$, $L = 5$, ${}^6\text{H}_{15/2}$, $g = 4/3$, $C = 14.17$ cm³ K mol⁻¹) and six Cu^{II} ions ($S = 1/2$ and $g = 2.0$). On lowering the temperatures, the χT value of **59** continuously decreases from 300 K to 50 K, and rapidly increases to reach a maximum of 36.56 cm³ K mol⁻¹ at 7.5 K, and finally falls to 27.08 cm³ K mol⁻¹ at 1.8 K (Fig. 6.26, left). The shape of the χT vs T plot indicates ferromagnetic interactions, which are probably weaker in **59** than that in **54**. The magnetic core of **59** can be considered as two three-bladed propellers magnetically connected through a (*trans*-) =N-N= pathway (Fig. 6.25, right) which may have mediated an antiferromagnetic interaction between the two units.

The field dependence of the magnetization of **59** (Fig. 6.26, right) reveals that the magnetization rapidly increases with dc field up to 1 T, as expected for a ferromagnetically coupled system. Above 1 T, the magnetization slowly increases in a linear fashion up to 7 T to reach 15.84 μ_B at 2 K. Both the lack of saturation of M and the non-superposed M vs H/T plots, indicate the presence of anisotropy and/or low lying excited states in the system.⁴³

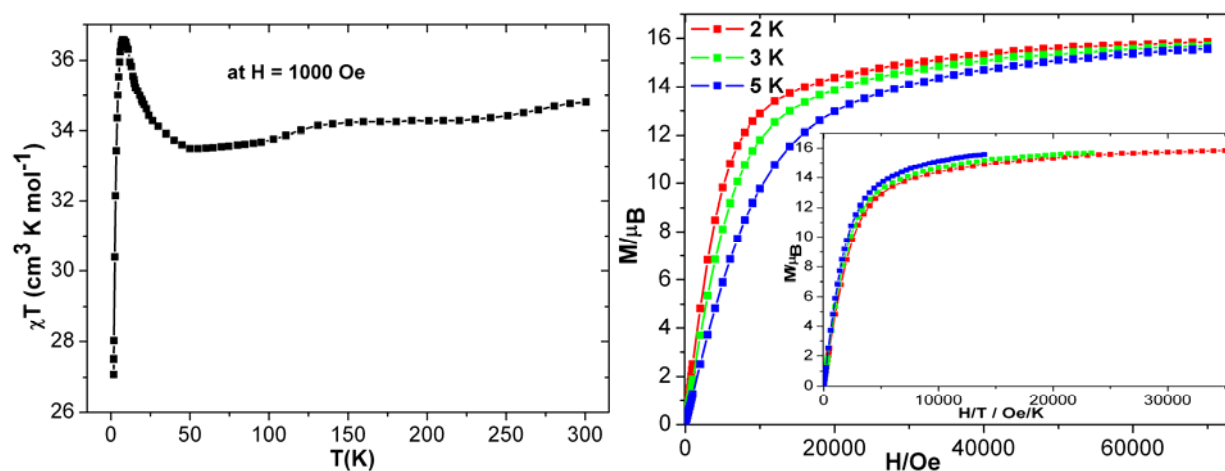


Fig. 6.26. Plots of χT vs T, M vs H (right), M vs H/T (right, inset) of **59** (left).

6.5.3 Dynamic magnetic properties of **59**.

Below 10 K, compound **59** exhibits detectable in-phase (χ') and out-of-phase (χ'') signals. The presence of temperature (Fig. 6.27) and frequency (Fig. 6.28) dependent in-phase (χ') and out-of-phase (χ'') signals, suggests SMM behavior in **59**. At 1.8 K, the χ' and χ'' vs frequency plots under the dc magnetic field range 0.0-2.0 kOe indicate the presence of QTM in the system (Fig. 6.29).

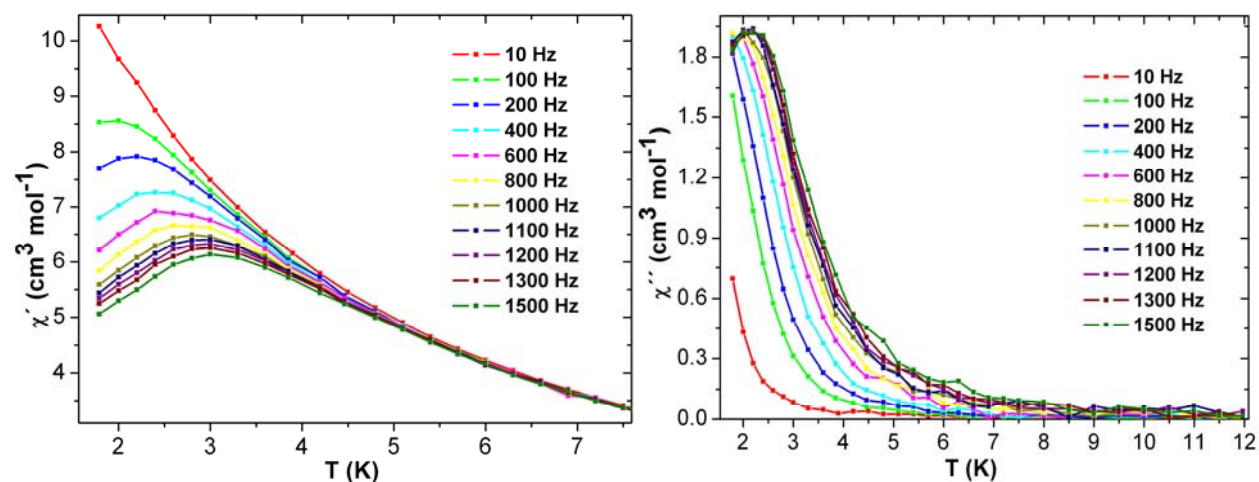


Fig. 6.27. Plots of χ' (left) and χ'' (right) vs T of **59**.

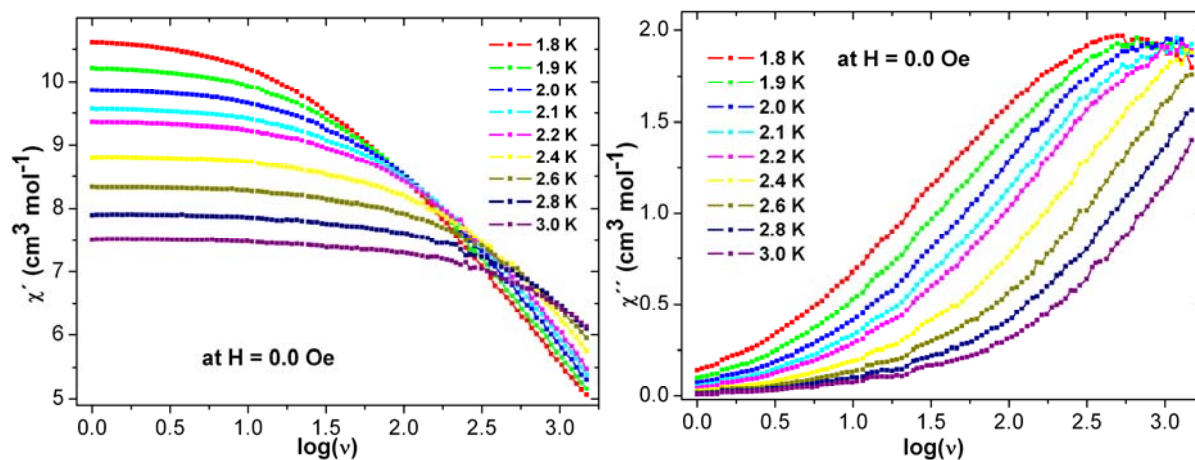


Fig. 6.28. Plots of χ' (left) and χ'' (right) vs frequency of **59**.

The χ'' vs frequency plots suggest the application of a dc field of 1.5 kOe could be sufficient to suppress the QTM pathways (Fig. 6.29, right). Thus, frequency dependent in-phase

(χ') and out-of-phase (χ'') susceptibilities were measured under 1.5 kOe dc field in the temperature range of 1.8-3.0 K (Fig. 6.30). The blocking temperature (T_b) was found to be increased from 2.5 to 3.0 K. The Cole-Cole plots under zero and 1.5 kOe dc magnetic field look semicircular (Fig. 6.31), indicating the involvement of a single relaxation process. The data of Fig. 6.28 and 6.30 were utilized for Arrhenius plots (Fig. 6.32) and linear fitting gave an energy barrier of $\Delta = 10.33$ K with $\tau_0 = 1 \times 10^{-6}$ s under zero dc field and $\Delta = 18.39$ K and $\tau_0 = 1.7 \times 10^{-7}$ s under 1.5 kOe applied dc field (Fig. 6.32).

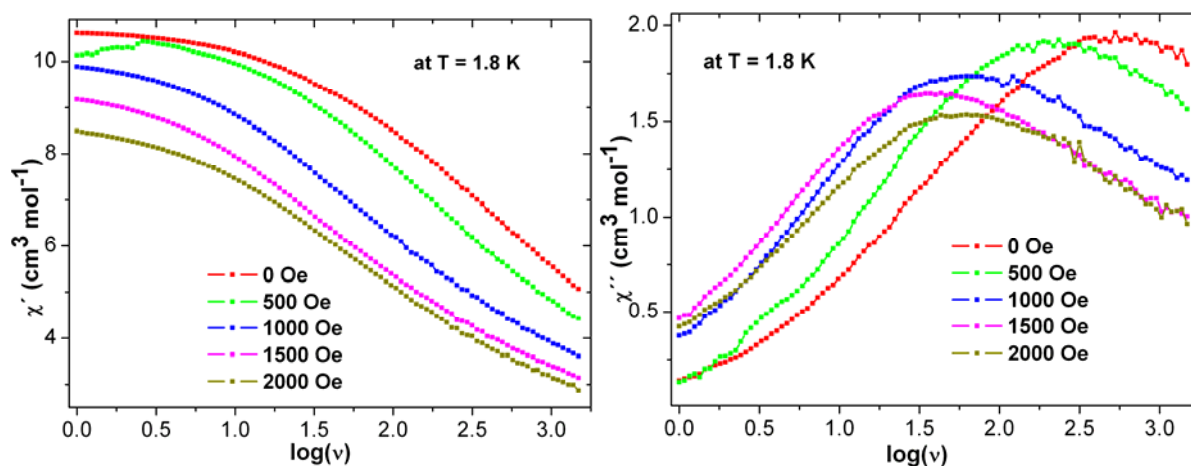


Fig. 6.29. Plots of χ' (left) and χ'' (right) vs frequency of **59** at 1.8 K under indicated applied dc magnetic fields.

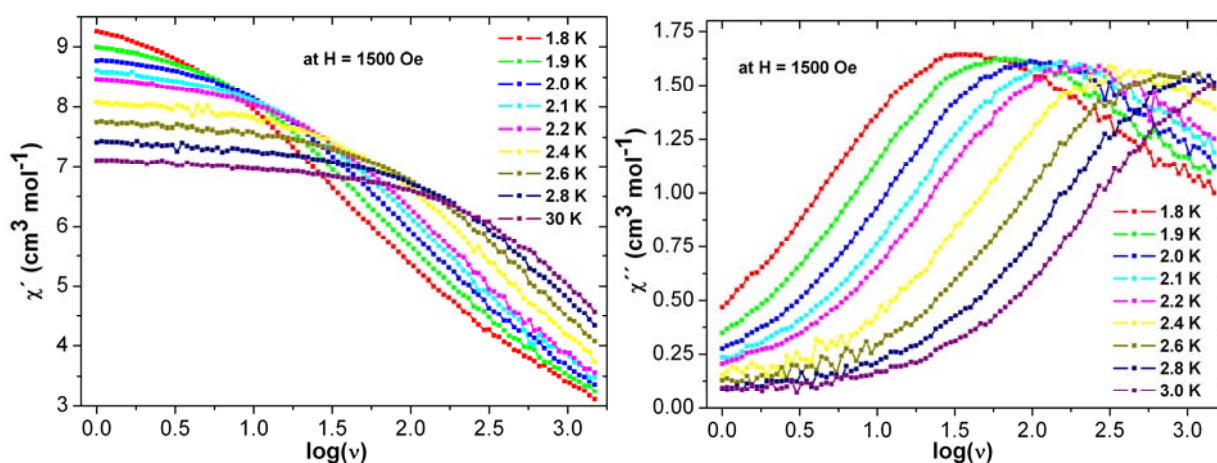


Fig. 6.30. Plots of χ' (left) and χ'' (right) vs frequency of **59** under 1.5 kOe applied dc magnetic field.

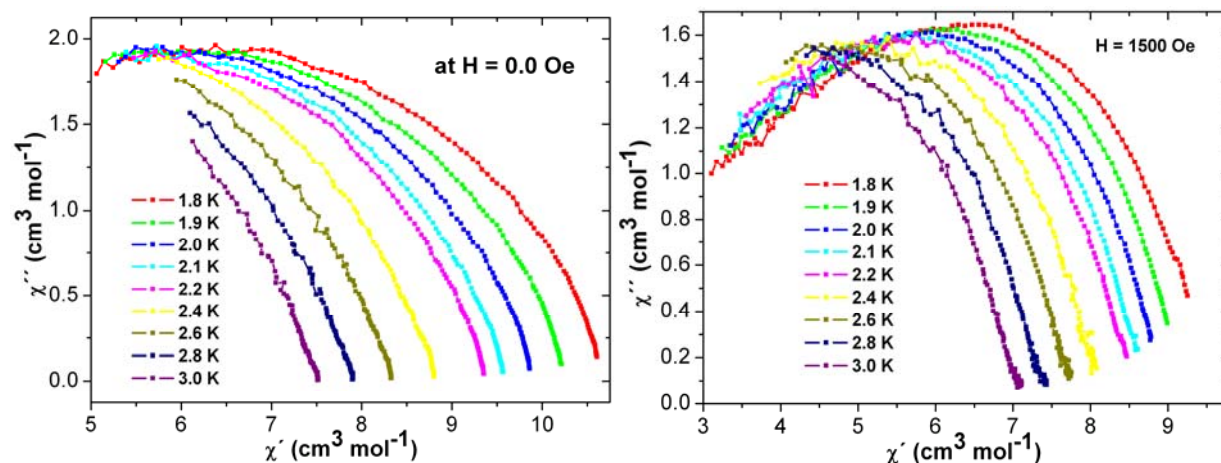


Fig. 6.31. Cole-Cole plots for **59** under zero (left) and 1.5 kOe (right) dc magnetic fields.

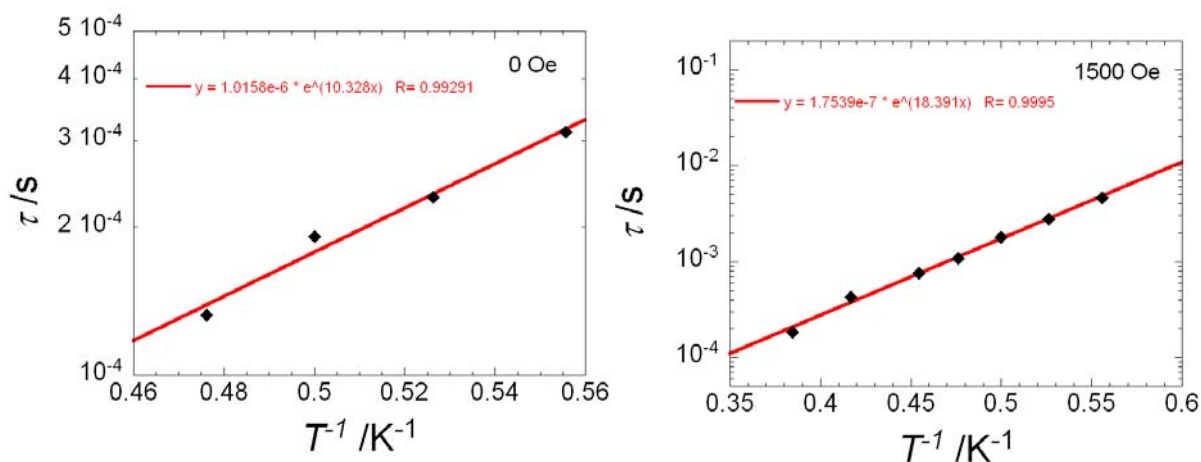


Fig. 6.32. The Arrhenius plots for **59** under zero (left) and 1.5 kOe (right) dc magnetic fields.

6.6.1 Crystal structures of $[\text{Ln}_9\text{Cu}_2(\text{L}2)_4(\text{HL}2)_4(\text{OH})_8(\text{CO}_3)_3(\text{NO}_3)_3(\text{H}_2\text{O})_4(\text{EtOH})](\text{NO}_3)_2 \cdot 9\text{EtOH} \cdot 6\text{H}_2\text{O}$ [$\text{Ln} = \text{Dy}(\mathbf{60})$ and $\text{Er}(\mathbf{61})$]

Both **60** and **61** are isomorphous, which was confirmed by checking the unit cell constants of **61**. The structure of **60** was fully determined and will be described here; it crystallizes in monoclinic space group $C2/c$. The molecule contains nine Dy^{III} ions, two Cu^{II} ions, four dianionic ligands $(\text{L}2)^{2-}$, four monoanionic ligands $(\text{HL}2)^-$, eight $\mu_3\text{-OH}$, three carbonate dianions, three chelating nitrates, four coordinated H_2O and one ethanol molecule (Fig. 6.33, top). The lattice of **60** contains two nitrate counter ions for charge balance and solvent molecules (9 EtOH and 6 H_2O) of crystallization.

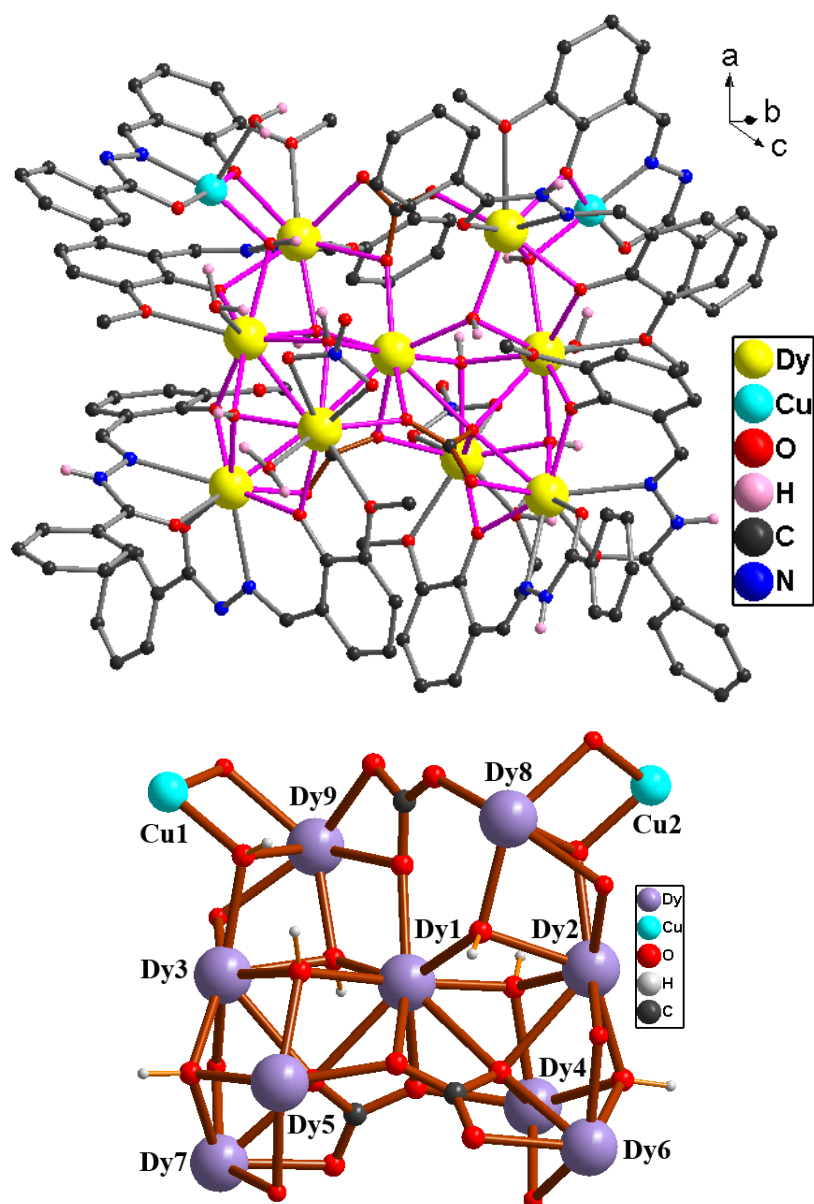


Fig. 6.33. Molecular structure (top) and core (bottom) of the coordination cluster in compound 60.

The coordination geometry of Cu1 and Cu2 are distorted square planar and square prism. The Dy8 center has an eight-coordinate square-antiprismatic geometry with an O₇N donor set, while the other Dy^{III} ions are all nine-coordinate with distorted capped square-antiprismatic geometries. Dy1, Dy2, Dy3, Dy4, Dy5 are coordinated by nine O-atoms, Dy9 by an O₈N donor set, while Dy6 and Dy7 are coordinated by seven O-atoms and two N-atoms (O₇N₂).

The metal-oxygen core (Fig. 6.33, bottom) can be described as follows. Dy3, Dy1 and Dy2 form an almost linear Dy₃ unit (Dy3-Dy1-Dy2 = 173.2°) through the centre of the molecule.

To one side of this, Dy3 and Dy1, and Dy1 and Dy2, are linked by μ_3 -OH bridges to Dy9 and Dy8 respectively. Between these two triangles, a $\eta^2:\eta^1:\eta^1:\mu_3$ carbonate forms a rather unsymmetrical bridge between Dy1, Dy8 and Dy9. Dy3 and Dy9, and Dy2 and Dy8, are then linked by further μ_3 -OH bridges to the Cu^{II} centres Cu1 and Cu2, respectively. On the other side of the linear unit, Dy3 and Dy1, and Dy1 and Dy2, are similarly linked by μ_3 -OH bridges to Dy5 and Dy4 respectively, with further μ_3 -OH bridges linking Dy3 and Dy5 to Dy7, and Dy2 and Dy4 to Dy6. The Dy3/Dy1/Dy5/Dy4 and Dy2/Dy1/Dy4/Dy6 unit form rather open tetrahedral units, with additional bridging from two $\eta^2:\eta^2:\eta^1:\eta^1:\eta^1-\mu_5$ carbonates.

Alternatively, the central section of the core can be considered as being composed of two Dy₄(μ_3 -OH)₂ butterfly units that share a common “body” Dy center, Dy1. Each of the two Dy₄ units is itself close to planar, but the two butterflies are far from mutually coplanar, making a dihedral angle of 77° between them. Four external Dy-Dy edges of this “fused di-butterfly” Dy₇(μ_3 -OH)₄ unit are then bridged by μ_3 -OH ligands to two Cu^{II} and two Dy^{III} centres, which form a distorted external rectangle about the Dy₇(μ_3 -OH)₄ core.

Peripheral ligation is provided mainly by four mono-deprotonated ligands (HL2)⁻ and four doubly-deprotonated ligands (L2)²⁻. The ligands display two types of bridging mode ($\eta^1:\eta^2:\eta^1:\eta^1:\mu_2$ and $\eta^2:\eta^1:\eta^1:\mu_2$ Fig. 1.6). In each ligand, the phenoxy oxygen bridges between two metal atoms, providing further bridging around the edge of the core, while the amide oxygens each ligate only one metal centre. Both the Cu1 and Cu2 ions are coordinated within the pocket-I (ONO) of doubly-deprotonated ligands (L2)²⁻. The Dy^{III} centres are coordinated by pocket-I and/or pocket-II (OO) of the ligands. There are two chelating nitrates, coordinated to Dy4 and Dy5, while four water ligands are coordinated to Cu2, Dy3, Dy4 and Dy5 and one ethanol ligand coordinates to Dy4.

6.6.2 Static magnetic properties of **60** and **61**.

The room temperature χT values for **60** and **61** per Dy^{III}₉Cu^{II}₂ (**60**) and Er^{III}₉Cu^{II}₂ (**61**) units are 126.23 and 104.70 cm³ K mol⁻¹ respectively, which are in good agreement with expected values of 128.28 for **60** containing nine Dy^{III} ($S = 5/2$, $L = 5$, ${}^6H_{15/2}$, $g = 4/3$) and two Cu^{II} ions, and 104.07 cm³ K mol⁻¹ for **61** containing nine Er^{III} ($S = 3/2$, $L = 6$, ${}^4I_{15/2}$, $g = 6/5$) with and Cu^{II} ions. On lowering the temperatures, the χT values of **60** and **61** continuously decrease

from room temperature to 25 K and then rapidly decrease more rapidly to reach the values of 63.27 (**60**) and 33.54 $\text{cm}^3 \text{K mol}^{-1}$ (**61**) at 1.8 K (Fig. 6.34). The feature of χT vs T plots of **60** and **61** indicates the presence of overall weak intramolecular antiferromagnetic interactions though it is difficult to quantify the interactions.⁴³ For anisotropic Dy^{III} and Er^{III} ions, the thermal depopulation of their excited Stark sublevels can contribute to the decrease of the χT product at higher temperature.

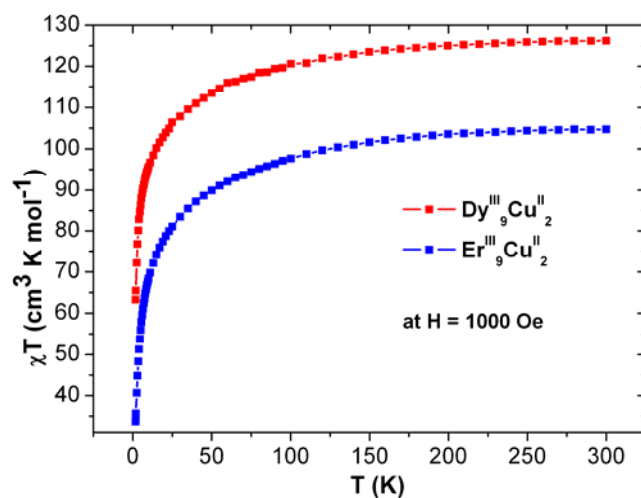


Fig. 6.34. Plots of χT vs T of **60** and **61** under applied dc magnetic field of 1 kOe.

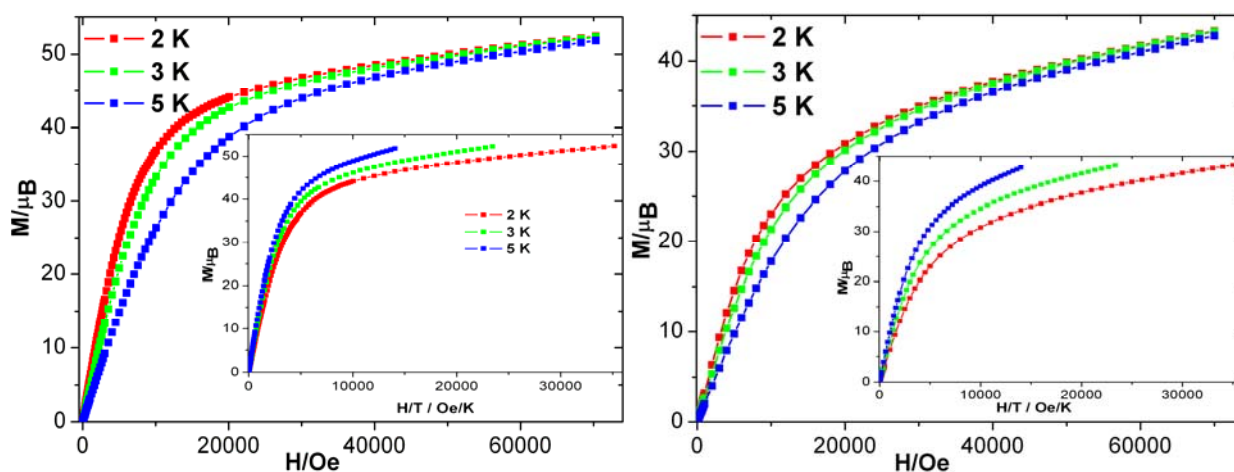


Fig. 6.35. Plots of M vs H and M vs H/T (inset) of **60** (left) and **61** (right) at indicated temperatures.

The field dependence of the magnetizations of **60** (Fig. 6.35) reveal that the magnetization increases more rapidly up to dc field of 10 kOe compared to that of **61**, since Dy^{III} ions are more anisotropic than Er^{III} ions. Above 10 kOe, the magnetization slowly increases in a linear fashion up to 7 T and reaches 52.36 and 43.25 μ_B at 2 K for **60** and **61**, respectively. The M vs H/T plots at different temperatures do not superpose on to single master curves (Fig. 6.35) indicating the presence of anisotropy and/or low lying excited states in the systems.⁴³

6.6.3 Dynamic magnetic properties of **60** and **61**.

Below 10 K, compound **60** exhibits slow relaxation of magnetization while **61** does not. The presence of temperature dependent in-phase (χ') and out-of-phase (χ'') signals (Fig. 6.36), suggests **60** might be a SMM with T_b below 1.8 K. The preliminary magnetic measurements indicate the absence of QTM in the system. To confirm the SMM behavior in **60**, micro-SQUID measurements were performed on a single crystal of **60**. The presence of temperature and sweep rate dependent hysteresis loops below 0.6 K (Fig. 6.37), confirms SMM behavior in **60**.

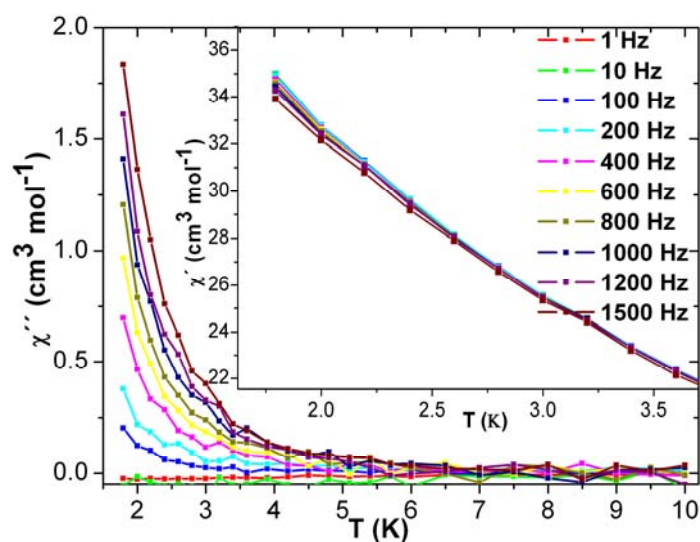


Fig. 6.36. Plots of χ'' and χ' (inset) vs T of **60**.

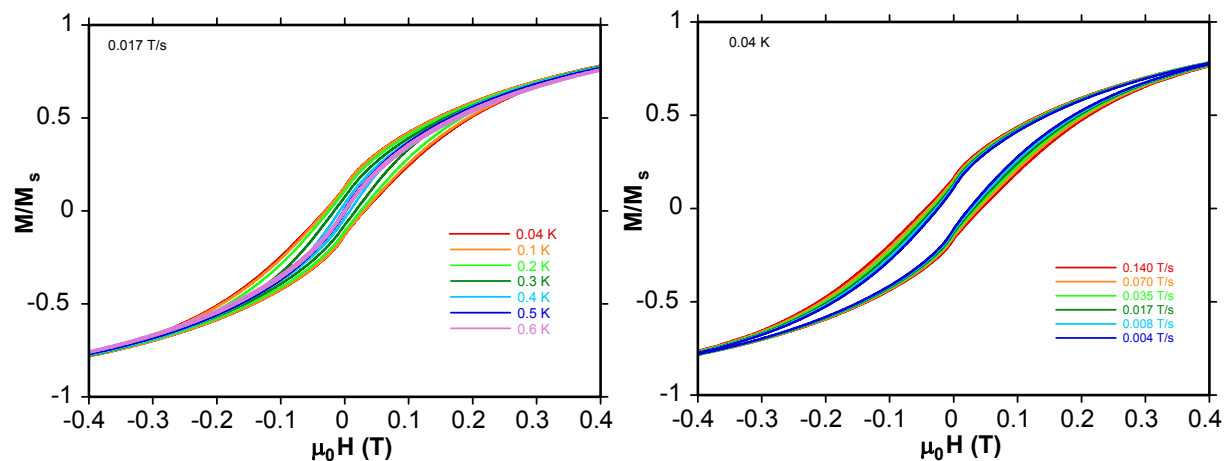


Fig. 6.37. The temperature (left) and sweep rate (right) dependence hysteresis loops of **60**.

6.7.1 Crystal structure of $[\text{Dy}_2\text{Cu}(\text{OH})(\text{L}2)_2(\text{HL}2)_2(\text{H}_2\text{O})]\text{Cl}\cdot 5\text{EtOH}\cdot 2.5\text{H}_2\text{O}$ (**62**).

The complex **62** crystallizes in the space group $P-1$. The asymmetric unit contains two Dy^{III} ions, one Cu^{II} ions, three doubly deprotonated ligands $(\text{L}2)^{2-}$, one mono deprotonated ligand $(\text{HL}2)^{-}$ and one water molecule coordinated to Dy^{III} ion (Fig. 6.38, left).

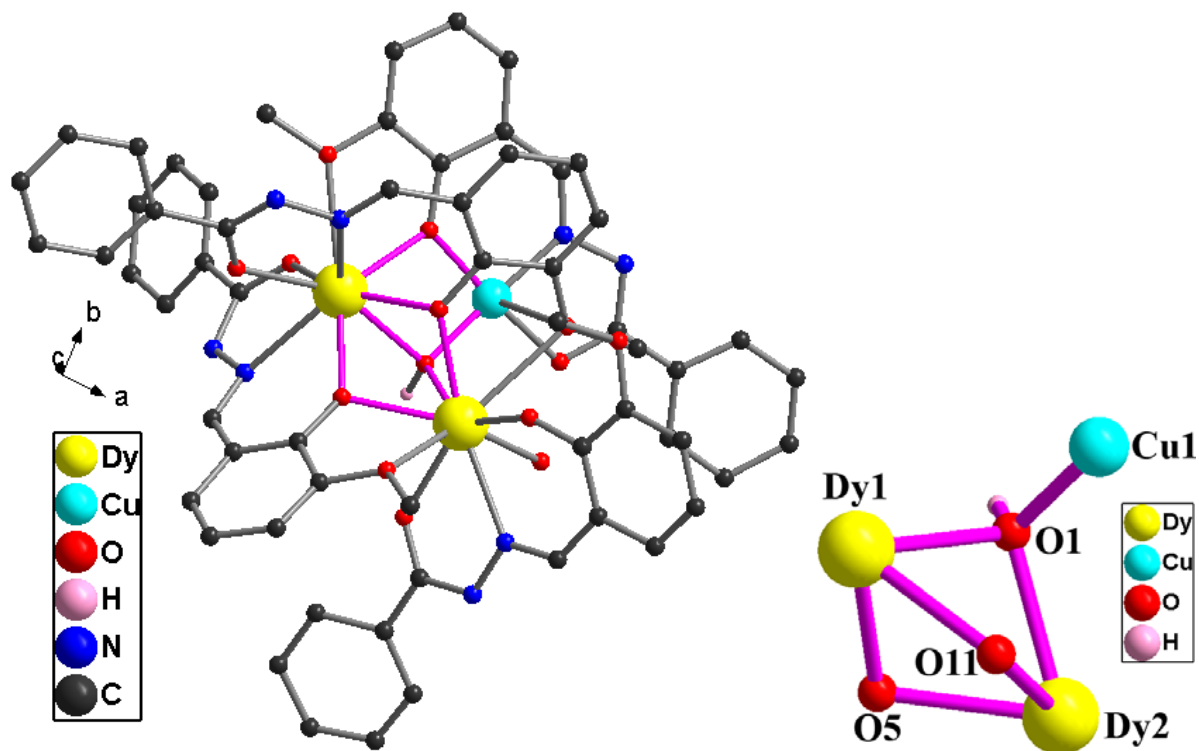


Fig. 6.38. Molecular structure (left) and core (right) of the coordination cluster in compound **62**.

Both the Dy1 and Dy2 centers are nine coordinated with an O₇N₂ (Dy1) and O₈N (Dy2) donor sets with a distorted capped square antiprismatic geometry. The Cu^{II} ion has adopted a distorted square planar geometry with an O₃N donor set. The crystal lattice in **62** contains five EtOH and two and half water molecules.

The metal-hydroxide core (Fig. 6.38, right) is a hetero-atomic triangle (Dy^{III}₂Cu^{II}) with a μ₃-OH which is 0.955 Å above the Dy1Dy2Cu1 triangular plane. The first two vertexes are occupied by two nine coordinated Dy^{III} ions and third vertex is by one Cu^{II} ions, which is shielded by organic ligands bridging among the metal ions. Dy1 is coordinated by three doubly deprotonated ligands; two pocket I (ONO) and one pocket II (OO) while Dy2 is coordinated by one mono deprotonated ligand (HL2)⁻ into pocket II (OO) and one doubly deprotonated ligand (L2)²⁻ into pocket I (ONO). The ligands display η¹:η¹:η¹:μ₁ and η¹:η²:η¹:η¹:μ₂ (Fig. 1.6) bridging modes. There is a water molecule coordinated to Dy2 center. Other than μ₃-OH bridge, the Cu1-Dy1 and Dy1-Dy2 edges are bridged by an additional one and two μ-phenoxide bridges, respectively. The Dy1-Cu1, Dy1-Dy2 and Dy2-Cu1 distances are 3.4106(10), 3.6285(5) and 3.6322(10) Å. The Cu1-O-Dy1 angles are 105.1(2) and 101.9(2)°. The Dy1-O-Dy2 angles are 94.7(2), 102.3(2) and 102.18(18)° and Dy2-O-Cu1 angle is 111.4(2)°. The Cu-N/O distances vary from 1.903(6) to 1.953(5) Å. Dy1-O/N and Dy2-O/N bond distances ranges from 2.268(5) to 2.702(5) Å and 2.189(6) to 2.817(6) Å respectively.

6.7.2 Static magnetic properties of **62**.

The room temperature χT values of per Dy^{III}₂Cu^{II} (**62**) is 29.09 cm³ K mol⁻¹, which is in good agreement the expected value of 29.09 for **62** containing two Dy^{III} (*S* = 5/2, *L* = 5, ⁶H_{15/2}, *g* = 4/3) and one Cu^{II} ions (*S* = 1/2 and *g* = 2.0). On lowering the temperature, the χT value of **62** continuously decreases from 300 K to 13 K, and rapidly decreases to reach a minimum of 25.47 cm³ K mol⁻¹, followed by slight increase to reach 25.69 cm³ K mol⁻¹ at 4 K (Fig. 6.39, left) and finally a decrease to 25.23 cm³ K mol⁻¹ at 1.8 K. The ferrimagnetic shape of χT vs T plots of **62** may suggest the presence of overall weak intramolecular ferromagnetic interactions though it is difficult to predict the exact nature of interaction.⁴³

The field dependence of the magnetization of **62** (Fig. 6.39, right) reveals that the magnetization rapidly increases below 10 kOe above which slowly increases in a linear fashion up to 7 T, reaching 11.69 μ_B at 2 K. The lack of saturation of M (Fig. 6.39, right) indicates the

presence of anisotropy and/or low lying excited states in the system.⁴³ Moreover, the M vs H/T plots at different temperatures do not superpose on to a single master curve indicating the presence of anisotropy and/or low lying excited states in the system.⁴³

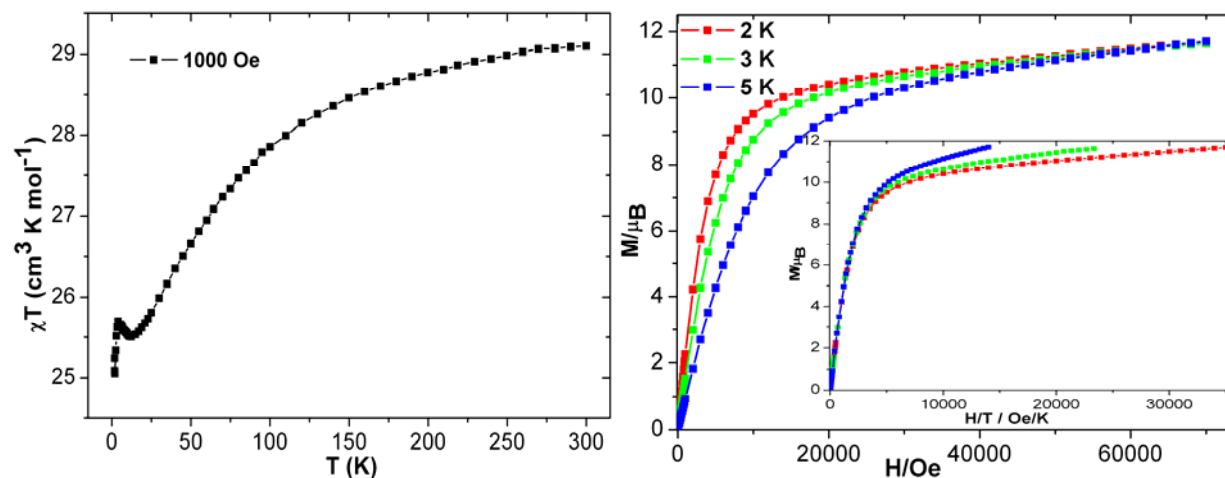


Fig. 6.39. Plots of χT vs T (left), M vs H (right) and M vs H/T (right, inset) of **62**.

6.7.3 Dynamic magnetic properties of **62**.

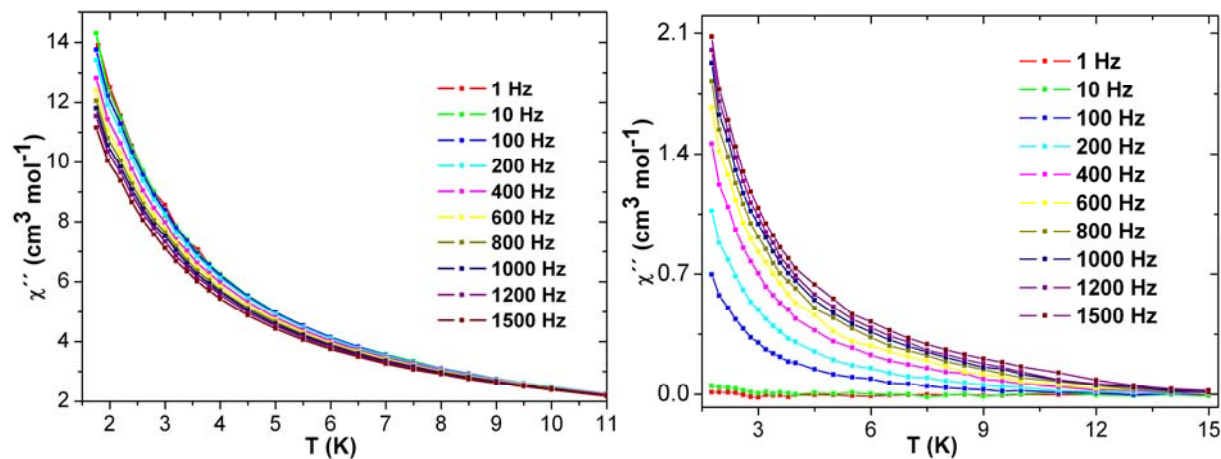


Fig. 6.40. Plots χ' (left) and χ'' (right) susceptibilities vs T of **62** at indicated frequencies under zero dc applied magnetic field.

Below 15, compound **62** exhibits slow relaxation of magnetization. The presence of temperature dependent in-phase (χ') and out-of-phase (χ'') signals (Fig. 6.40), suggests **62** might be a SMM with T_b below 1.8 K. The additional ac measurements indicate the absence of QTM in **62**.

6.8 Conclusion:

In this chapter twelve new Ln-Cu complexes (**51-62**) of seven different nuclearities, are reported. The syntheses are carried out under aerobic condition and products are crystallized either from MeOH or EtOH by slow evaporation in air. By changing the reaction conditions, the nuclearity of the compounds can be increased; starting from dinuclear (DyCu; **51**) to undecanuclear (Dy₉Cu₂; **60**). The structure of complexes from **51-58** can be understood in terms of coordination of one, two or three {Cu(L₂)X} metalloligands to a central Ln^{III} ion, where X is bridging methoxy or azide ligand. The number of {Cu(L₂)X} units is dependent on the amount of base in the reaction. In situ condensation of (L₄)²⁻ resulted in the dimerisation of the two DyCu₃ propeller into a Dy₂Cu₆ system (**59**) with two Cu^{II} centers are linked through a hydrazine bridge.

Since there are three μ-OMe⁻ bridges in the propeller shaped DyCu₃ (**54**), it was attempted to replace OMe⁻ bridges by OEt⁻ bridges, by carrying out the reaction in EtOH instead of MeOH. However, instead Dy₉Cu₂ (**60**) was resulted. The crystal structure revealed that there are eight μ₃-OH bridges and three carbonate (CO₃²⁻) per Dy₉Cu₂ unit. When the reaction is performed in inert atmosphere, it produces known a Cu^{II}₄^{52e} cluster. If other solvents (ⁱPrOH, ⁿBuOH, DMF and DMSO) were used as a reaction medium, the known Cu^{II}₄^{52e} compound was again always encountered in each case from the identical reaction ratio. The reaction which produces **60** is performed using DyCl₃·6H₂O instead of Dy(NO₃)₃·6H₂O, it produces Dy₂Cu (**62**), the {Dy₂Cu(μ₃-OH)}⁴⁺ core of which can be considered as a small part of Dy₉Cu₂ (**60**).

All the complexes (**51-62**) were magnetically investigated. The dc magnetic measurements reveal that complexes **51-59** show intramolecular ferromagnetic interactions. The exact nature of coupling (ferro-or antiferro-) in **60-62**, cannot be determined because of concurrent thermal depopulation of Stark sub-levels of the corresponding Ln^{III} ions. The M value of each complex increases rapidly at smaller magnetic fields and then increases almost linearly (except **56**) at higher field. The increase of the M value at low temperature is faster for systems where ferromagnetic coupling is stronger (**51, 52, 53, 54, 55, 56** and **59**). The M vs H/T plots of all the complexes (except isotropic GdCu₃; **56**) do not superpose on single master curve, indicating presence of low-lying energy states and/or anisotropy in the systems.⁴³ The saturation

of M value of **56** in M vs H plot is observed at 2 K and M vs H/T plots are superposed on a single master curve as expected for this isotropic system.

The dynamic magnetic property measurements reveal that the majority (**52**, **53**, **54**, **55**, **57**, **59**, **60** and **62**) of these complexes, exhibit interesting slow relaxation of magnetization. The evaluated ac parameters of these compounds (**52**, **53**, **54**, **55**, **59**, **60** and **62**) are given in Table 6.7. The dinuclear DyCu (**51**) does not show slow relaxation of magnetization which might be due to insufficient effective energy barrier. With coupling of more than one Cu^{II} ions (2Cu^{II} in **52/53** or 3Cu^{II} in **54**) to the central Dy^{III} ion, slow relaxation of magnetization in **52-54**, is observed in the experimental temperature range (above 1.8 K). The slow relaxation dynamics of **52**, are accompanied by QTM effects and no maximum is observed in χ' and χ'' vs T plots for **52** due to the curtailment of energy barrier of relaxation through QTM pathways.

The application of small dc field (1 kOe), removed the degeneracy of the energy levels of **52** and QTM is switched off and the effective energy barrier is increased (Table 6.7). Two μ -OMe⁻ groups are replaced by two μ -N₃⁻ and additionally the two Cu^{II} ions are further connected by one μ -MeOH upon introduction of azide in the system (**53**). Consequently, DyCu₂(N₃)₂ (**53**) is not only strongly more ferromagnetically coupled but also slow relaxation dynamics become better and the maximum in χ'' vs T plots are observed at 3.5 K (T_b). Moreover, more than one slow relaxation processes are implicated in both temperature and frequency dependent ac susceptibility plots of **53**, though both the SMMs **52** and **53** have comparable energy barriers under 1 kOe and 0.0 kOe applied dc fields respectively (Table 6.7). The energy barrier of other relaxation processes of **53**, could not be resolved because of very low value of relaxation time of thermally activated energy states and/or faster quantum relaxation.

The Dy (**54**), Tb (**55**) and Ho (**57**) analogue of propeller LnCu₃ series (**54-58**) exhibit slow relaxation of magnetization either with a maximum [χ'' vs T; T_b = 4.4 (**54**) and 3.8 (**55**) K] in **54** and **55** or without a maximum (in χ'' vs T plots; T_b < 1.8 K) in **57**. Both Dy (**54**) and Tb (**55**) show QTM in their slow relaxation of magnetization and the application of a small dc field (1.5 kOe) led to the increase of their blocking temperatures to 5.0 (**54**) and 4.2 (**54**) K respectively. The Dy (**54**) analogue is found to be the best among this series from the point of view of blocking temperatures and energy barriers (Table 6.7). Moreover, DyCu₃ (**54**) displays temperature and sweep rate dependent hysteresis loop below 1.49 K, confirming the SMM behavior in **54**.

Upon linking two DyCu₃ (**54**) units into Dy₂Cu₆ (**59**), the blocking temperature is reduced to 2.5 (**59**) K from 4.4 (**54**) K under zero applied dc field. The QTM remains the common feature between DyCu₃ (**54**) and Dy₂Cu₆ (**59**), with the same optimum magnetic field of 1.5 kOe. The application of 1.5 kOe magnetic field, led to the increase of the effective energy barrier from 19.6 to 30.8 K for **54** and 10.32 to 18.39 K for **59**. This may result from the distortion of magnetic core of **59**, with respect to that of **54** and weak antiferromagnetic coupling between two DyCu₃ units in **59**.

The magnetic core of Dy₉Cu₂ (**60**), is more complicated (with several magnetic pathways) being composed of several triangular Dy₃ units and two Dy₂Cu units. The latter unit has been isolated in Dy₂Cu (**62**). Both the complexes show slow relaxation below 7 (**60**) and 15 (**62**) K respectively without a maximum in χ' and χ'' vs T plots, implying both might be SMMs with blocking temperature below 1.8 K, though slow relaxation is comparatively perished in **60** than that of **62**. To prove that micro-SQUID measurements were performed on a single crystal of **60**, which show both temperature and sweep rate dependent hysteresis loops below 0.5 K, confirming the SMM behaviour in **60**.

Table 6.7. The ac data of Dy^{III}/Tb^{III}-Cu^{II} complexes (**52**, **53**, **54**, **55**, **59**, **60** and **62**).

Compound	DyCu ₂ (52)	DyCu ₂ (53)	DyCu ₃ (54) /TbCu ₃ (55)	Dy ₂ Cu ₆ (59)	Dy ₉ Cu ₂ (60)	Dy ₂ Cu (62)
QTM	observed	observed	observed	observed	Not observed	Not observed
No. of processes	one	More than one	one	one	-	-
T _b (K) ^A	< 1.8	4.2	4.4/3.8	2.5	0.5	< 1.8
Δ (K) ^A	-	14.82	19.6/18.7	10.33	-	-
Δ (K) ^B	14.64	-	30.8/22.5	18.39	-	-
τ ₀ (s) ^A	-	4.4×10 ⁻⁶	2.4×10 ⁻⁶ /1.0×10 ⁻⁶	1×10 ⁻⁶	-	-
τ ₀ (s) ^B	2.9×10 ⁻⁶	-	3.8×10 ⁻⁷ /5.3×10 ⁻⁷	1.7×10 ⁻⁷	-	-

(A) Under Zero dc field and (B) When QTM is switched off.

Chapter 7

Conclusion and outlook:

This research has produced novel compounds exhibiting a wide range of structural motifs (Fig. 7.1), fascinating magnetic and/or fluorescence properties.

In **Chapter 3**, twenty heterometallic Ni^{II}-Ln^{III} coordination compounds (**1-20**) of five different series have been successfully synthesized using the H₂L1 ligand by varying either the reaction conditions or changing the molar ratio. All these compounds were crystallographically characterized and magnetically studied. Compounds **1-7** possess a defect-dicubane core topology. In some of the compounds, carbonate (CO₃²⁻) ligands are incorporated into the structure, changing the topology by opening out the defect-dicubane Ln₂Ni₂ core (**1-7**) into a distorted non-planar U-shaped Ln₂Ni₂ (**8-12**) conformation. Since further growth of nuclearity of the Ln₂Ni₂ core in **8-12** was apparently prevented by two terminal ligands, these were deliberately removed by gradually decreasing the amount of ligands and base, resulting in non-planar ring-like high nuclearity Ln₄Ni₈ (**13-18**) compounds. To study the effect of incorporation of carbonate into the structural motif, the synthetic reaction which produced Dy₄Ni₈ (**13**) was performed under N₂-atmosphere instead of air, leading to the isolation of the semicircular Dy₂Ni₄ complex (**19**) which contains no carbonate ligand. **19** contains four chelating nitrate ligands on the same edge of the cluster, and it was possible to replace these by bridging oxalate (C₂O₄²⁻) ligands, to give the Dy₄Ni₈ compound (**20**) in which two Dy₂Ni₄ units as found in **19** are bridged by two oxalates into a ring-like structure.

From a magnetic point of view, the Dy^{III}-Ni^{II} compounds (**1, 2, 8, 13, 19** or **20**) of each series have been more magnetically interesting than that of the other rare-earth analogues. The ac measurements suggest that all these Dy^{III}-Ni^{II} compounds are SMMs, with energy barriers U_{eff} in the range 7-28.5 K, with the defect-dicubane Dy₂Ni₂ (**2**) possessing the highest energy barrier (28.5 K) of the Ni-Ln based SMMs reported to date. Complex **19** also shows two well-resolved relaxation modes.

In **Chapter 4**, twenty heterometallic M^{II}-Ln^{III} compounds [Ln^{III}₂Zn^{II}₃ (**21-25**), Dy^{III}₇Zn^{II}₄ (**26**), Ln^{III}₆Cd^{II}₆ (**27-30**), Ln^{III}₃Cu^{II}₂ (**31-34**) and Ln^{III}₂Co^{II}₂ (**35-40**)] which form five different series have been synthesized employing the ligand (H₂L1), with similar molar ratios and reaction conditions to the synthesis of Dy₂Ni₂ (**2**) but replacing Ni^{II} ions by different M^{II} ions. The nuclearity and topology of the final products were found to vary with the M^{II} ions, depending on

the ionic radius and the preferred geometry and coordination number of the ion. The series of dodecanuclear $\text{Ln}^{\text{III}}_6\text{Cd}^{\text{II}}_6$ compounds (**27-30**) are the highest nuclearity Cd-Ln based coordination clusters to date. From a magnetic point of view, all five $\text{M}^{\text{II}}\text{-Dy}^{\text{III}}$ (**21**, **26**, **27**, **31** and **35**) compounds are again magnetically more interesting than their analogues. The $\text{Dy}^{\text{III}}_7\text{Zn}^{\text{II}}_4$ compound (**26**) displays rich fluorescence spectra and exhibits both in-phase and out-of-phase signals below 15 K suggesting SMM behavior. The Dy (**27**) analogue of the $\text{Ln}^{\text{III}}_6\text{Cd}^{\text{II}}_6$ series is ferromagnetically coupled and is probably a SMM. The fluorescence spectra of all four $\text{Ln}^{\text{III}}_6\text{Cd}^{\text{II}}_6$ (**27-30**) compounds display multiple bathochromic emission peaks in the visible range when excited in either UV or visible range. Thus the $\text{Dy}^{\text{III}}_7\text{Zn}^{\text{II}}_4$ (**26**) and $\text{Dy}^{\text{III}}_6\text{Cd}^{\text{II}}_6$ (**27**) compounds can be considered as bifunctional fluorescent SMMs.

The Ln_2Co_2 [Dy(**35**), Y(**36**), Gd(**37**), Tb(**38**), Ho(**39**) and Er(**40**)] compounds are ferromagnetically coupled and most exhibit slow relaxation of magnetization, indicating SMM behavior. Within this series, Dy_2Co_2 (**35**) has the highest blocking temperature (T_b) of 22 K at 1500 Hz. Two well-resolved strong ac signals were observed in χ' and χ'' vs frequency plots in the temperature range of 1.8-25 K, and two energy barriers could be derived: one is 17.7 K with $\tau_0 = 4.9 \times 10^{-4}$ s and the other 81.7 K with $\tau_0 = 3.9 \times 10^{-6}$ s. Thus Dy_2Co_2 (**35**) possesses the highest blocking temperature (22 K) and energy barrier (81 K) of any 3d-4f based SMM to date. The Ho_2Co_2 (**39**) also exhibits SMM behavior with three energy barriers ranging from 11 to 13 K.

In **Chapter 5**, eight compounds forming two different series of tetranuclear lanthanide complexes are presented based on the ligands $\text{H}_2\text{L1}$ or $\text{H}_3\text{L3}$, with general formulae $[\text{Ln}_4(\text{OH})_2(\text{L})_4(\text{HL1})_2] \cdot 2\text{THF}$ [$\text{Ln} = \text{Dy}$ (**41**), Gd(**42**), Tb(**43**), Ho(**44**) and Er(**45**)] and $(\text{Et}_3\text{N})_6[\text{Ln}_4(\text{HL3})_2(\text{NO}_3)_{10}(\text{H}_2\text{O})_4](\text{NO}_3)_4$ (**46-50**) respectively. However the topology of the tetranuclear units is different between the two series. Compounds **41-45** have a defect-dicubane core while **46-50** have a non-planar chain-like topology. Compound **41** and **44** are ferromagnetically coupled while their analogues (**42**, **43** and **45**) and also all the compounds (**46-50**) of the other series are antiferromagnetically coupled. The Dy analogues (**41** and **49**) of both series are SMMs with modest energy barriers.

In **Chapter 6**, twelve $\text{Ln}^{\text{III}}\text{-Cu}^{\text{II}}$ complexes (**51-62**) of seven different nuclearities, based on the ligands $\text{H}_2\text{L2}$ and $\text{H}_2\text{L4}$, are reported. By varying the reaction conditions, the nuclearity of the compounds could be increased, from dinuclear (DyCu ; **51**) up to undecanuclear (Dy_9Cu_2 ; **60**). The number of Cu^{II} ions around the Dy^{III} ion could be sequentially increased from one in **51**

(DyCu) to two in **52** (DyCu₂) and three in **54** (DyCu₃). All three compounds **51**, **52** and **54** are ferromagnetically coupled. The slow relaxation of magnetization gradually improved on increasing the number of Cu^{II} ions (**51**, **52** and **54**), with the energy barrier increasing from 14.6 K (**52**) to 30.8 K (**54**). On replacing Dy(**54**) by Tb(**55**), the energy barrier decreased from 30.8 K (**54**) to 22.5 K in **55** (TbCu₃). Two of the propeller-shaped DyCu₃ units were successfully connected into a Dy₂Cu₆ complex (**59**) by *in-situ* synthesis of H₂L4, with the two DyCu₃ units magnetically coupled through the *trans*-diimine =N–N= bridge. However, on linking the two DyCu₃ (**54**) units into Dy₂Cu₆ (**59**), the zero-field blocking temperature was reduced from 4.4 to 2.5 K. In both compounds, QTM could be suppressed by the same optimum dc field of 1.5 KOe, significantly increasing the effective energy barriers of **54** and **59** from 19.6 to 30.8 K, and from 10.3 to 18.4 K, respectively.

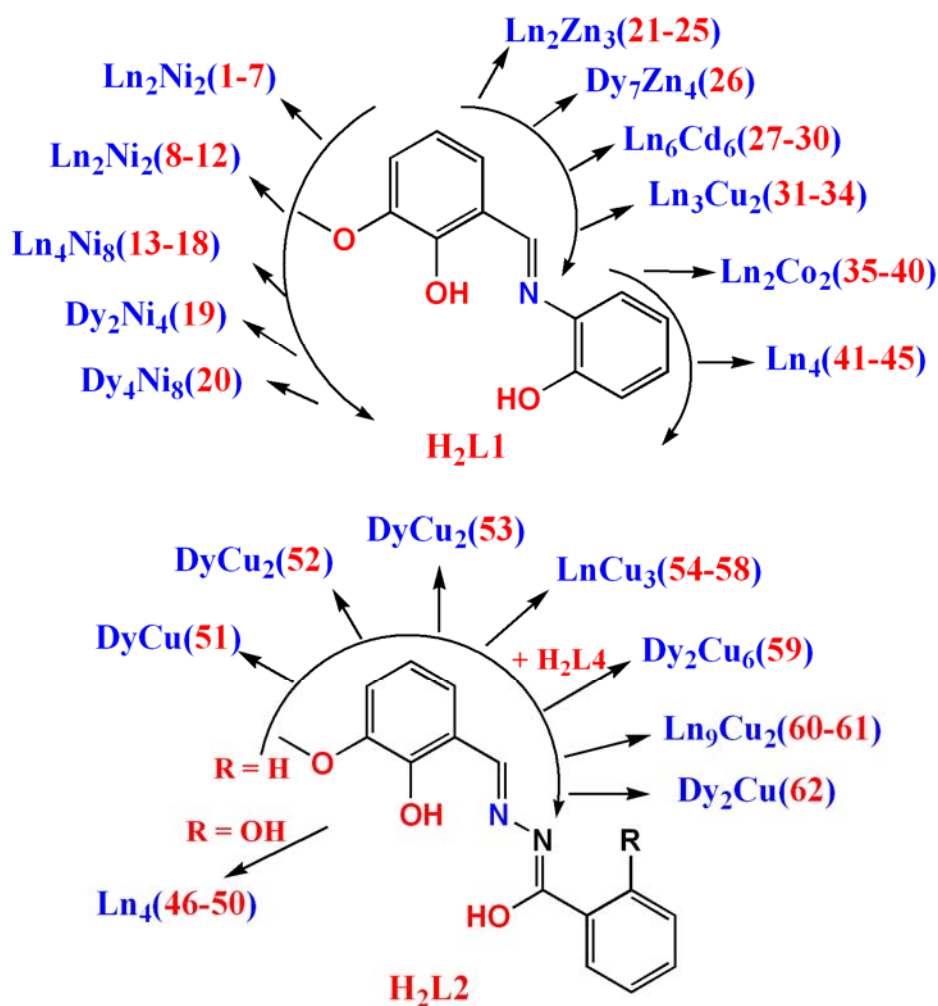


Fig. 7.1. Schematic representation of all compounds (1-62).

The attempt to replace the methoxy bridges by ethoxy resulted in the high-nuclearity Dy_9Cu_2 complex (**60**), in which the core is built up from several triangular Dy_3 units and two Dy_2Cu units. Micro-SQUID measurements were performed on a single crystal of **60**, which showed both temperature and sweep rate dependent hysteresis loops below 0.5 K, confirming SMM behaviour in **60**.

Chapter 8: Experimental

This chapter presents the syntheses of the reported compounds in addition to various analytical techniques utilized to characterize and investigate the properties of these compounds. All the analytical experiments mentioned were not applied to all of the compounds due to different experimental requirements or stability considerations.

8.1 NMR spectroscopy

^1H NMR and ^{13}C NMR spectroscopy were used to identify the ligands that were synthesized. The organic ligands were analyzed on the Bruker AC 250 spectrometer at the Inorganic Chemistry Department of the Campus South, Karlsruhe Institute of Technology (KIT). The deuterated solvents used were DMSO- d_6 and CDCl_3 .

8.2 Elemental analysis

Elemental analysis for C, H and N were carried out at the Inorganic Chemistry Department of the KIT.

8.3 Infra-red spectroscopy

Infra-red spectroscopy is a useful technique for identifying organic ligands and thus helps to verify the presence of organic ligands in the metal-ligand complexes. In addition, it provides a unique fingerprint of the molecule and enables identification of similar structures involving the same ligand. A small amount of the sample to be measured was ground into a fine powder together with absolutely dry KBr. This was then pressed into a transparent disk while under vacuum using a force of 10 N. Fourier Transform IR measurements were carried out on a Perkin-Elmer Spectrum instrument. The spectra were taken in the normal range between 4000 cm^{-1} to 400 cm^{-1} using 8 scans at a resolution of 4 cm^{-1} .

8.4 X-ray powder diffraction (PXRD)

PXRD was used to deduce the structure of compounds by comparing the spectra of similar systems in addition to unit cell check. The samples were grinded into fine powder, mounted on a round disk with grease between two plastic sheets and placed on the STOE STADI P X-ray powder diffractometer. The measurements were made using Cu- $K\alpha_1$ radiation with $\lambda = 1.5406\text{ \AA}$. The collected data were analyzed with the software WinX^{Pow}, which gives plots of the diffraction intensities as a function of the 2θ values.

8.5 X-ray single crystal measurement

The most powerful method for analyzing and confirming the structure of molecules is by single crystal X-ray structural analysis. The data were collected at 150/180 K (INT) on a Stoe IPDS II area detector diffractometer or at 100 K on a Bruker SMART Apex CCD diffractometer using graphite-monochromated Mo-K α radiation. The structures were solved using SHELXTL software. The following factors are important while refining the structures. First, the residual factors, R_1 and R_2 are defined as :

$$R_1 = \{ \sum \| F_0 \| - \| F_c \| \} / \{ \sum \| F_0 \| \}$$

$$wR_2 = \{ \sum [w(F_0^2 - F_c^2)^2] / \sum [w(F_0^2)^2] \}^{1/2}$$

$|F_0|$ is the data of the diffraction intensity and background exposure time obtained from the raw data after collection, reduction and correction. $|F_c|$ is the corresponding calculated data after structural analysis. $R_1 < 0.05$ normally indicates good structural analysis. The value w is the weight for each diffraction point and depends on the accuracy with which F_0^2 was measured. It is defined as: $w = 1/\sigma^2$

wR_2 is sensitive to the little differences in the structural analysis, such as the disorder of atoms and the defined H atoms. Normally wR_2 should be lower than 0.15 when the data is reasonable, but 0.2 is still acceptable. The goodness-of-fit is another important factor for the quality of the structural analysis, and is defined as:

$$S = \{ \sum [w(F_0^2 - F_c^2)^2] / (n - p) \}^{1/2}$$

where n and p are the number of the unique reflections and the number of parameters involved in the refinement, respectively. When S is far from 1.0, it indicates that the weighing scheme could be wrong and should be made better if the collected data is adequate.

8.6 Magnetic Measurements

Magnetic susceptibility measurements were obtained using a Quantum Design SQUID magnetometer MPMS-XL susceptometer. This magnetometer works between 1.8 and 400 K for dc applied fields ranging from -7 to +7 T. Measurements were performed on finely ground polycrystalline samples. Ac susceptibility measurements have been measured with an oscillating ac field of 3.5 Oe and ac frequencies ranging from 1 to 1500 Hz. The magnetic data were

corrected for sample holder contributions and for diamagnetic contributions calculated from Pascal's constants.

8.7 Fluorescence Spectroscopy

Fluorescence measurements were performed on Cary-Eclipse Fluoreszenzspektrometer at INT, KIT. The THF solutions of required complexes were measured in a standard 10 mm cuvette in a 90° geometry. PL was collected at a ~30° angle relative to the excitation light beam.

8.8 Syntheses

All chemicals and solvents used for synthesis were obtained from commercial sources and were used as received without further purification. The most of reactions were carried out in aerobic conditions and some were performed in N₂ atmosphere.

8.8.1 Ligand synthesis

8.8.1.1 Preparation of (E)-2-(2-hydroxy-3-methoxy-benzylideneamino)phenol (H₂L1): The equimolar mixture of o-vanillin (1520 mg, 10 mmol) and 2-Aminophenol (1230 mg, 10 mmol) was refluxed for 30 minutes in 20 mL of methanol. The resultant dark orange-red crystalline precipitate was filtered and washed well with cold methanol and followed by ether and dried in oven at 60°C and further purified by recrystallization from hot methanol. Yield is 92%. Anal. Calc. for C₁₄N₁H₁₃O₃ (found); C 69.12 (69.15), N 5.76 (5.70), H 5.38 (5.40), found. IR data (KBr disc, cm⁻¹): 3449(b), 2991(w), 2902(w), 2817(w), 2644(w), 1627(s), 1616(s), 1541(m), 1509(s), 1461(s), 1361(s), 1333(m), 1305(m), 1278(m), 1245(s), 1166(w), 1104(m), 1064(m), 1032(m), 1970(m), 923(w), 849(w), 738(s), 723(m), 575(w), 431(w).

8.8.1.2 Preparation of (E)-N'-(2-hydroxy-3-methoxybenzylidene)-benzohydrazide (H₂L2): An equimolar mixture of o-vanillin (1520 mg, 10 mmol) and benzoylhydrazide (1520 mg, 10 mmol) was refluxed in 20 mL of methanol for 20 min. The whitish yellow precipitate obtained was filtered off and washed well with cold methanol followed by ether, and was then dried in an oven at 60°C. Yield is 92%. Calc. (%) for C₁₅N₂H₁₄O₃ (found): C 66.65 (66.50), N 10.37 (10.40), H 5.22 (5.15). IR (KBr, cm⁻¹): 3546(m), 3473(m), 3414(m), 3079(w), 2942(w), 2890(w), 2857(w), 1660(s), 1600(s), 1575(s), 1468(s), 1451(s), 1411(s), 1377(m), 1349(s), 1251(m), 1166(m), 1091(w), 1077(m), 971(w), 946(w), 786(m), 776(m), 732(w), 716(w), 698(w) 636(w), 577(m), 550(m). ¹H-NMR (DMSO-d⁶) (δ ppm): (12.09 (singlet), 1H), (10.99 (singlet), 1H),

(8.66 (singlet), 1H), (9.96(triplet), 2H), (7.57 (quadrant), 3H), (7.16 (doublet), 1H), (7.03 (doublet), 1H), (6.87 (triplet), 1H), (2.5 (singlet), 3H).

8.8.1.3 Preparation of (E)-N'-(2-hydroxy-3-methoxybenzylidene)-(2-hydroxy)-benzohydrazide (H₃L3): An equimolar mixture of o-vanillin (1520 mg, 10 mmol) and salicylhydrazide (1520 mg, 10 mmol) was refluxed in 20 mL of methanol for 45 min. The whitish yellow precipitate obtained was filtered and thoroughly washed with cold methanol followed by ether, and dried in an oven at 60°C. Yield is 88%. Anal. Calc. (%) for C₁₅N₂H₁₄O₄ (found): C 62.93 (62.85), N 9.79 (9.82), H 4.93 (4.75). IR (KBr, cm⁻¹): 3230(w), 3200(w), 2995(w), 2937(w), 2837(w), 2664(w), 2573(w), 1607(s), 1583(s), 1565(s), 1482(m), 1455(m), 1376(m), 1312(s), 1257(s), 1236(s), 1155(m), 1103(w), 1038(w), 974(w), 905(w), 838(w), 781(w), 747(m), 733(w), 666(w), 730(w), 575(w), 5532(w), 470(w). ¹H-NMR (DMSO-d⁶) (δ ppm): (12.09 (singlet), 1H), (10.97 (singlet), 1H), (7.85 (dd), 1H), (7.45(triplet of triplet), 1H), (7.15 (dd), 2H), (7.05 (dd), 1H), (6.95 (quadrant), 1H), (6.85 (triplet), 1H), (2.5 (singlet), 3H). ¹³C-NMR (DMSO-d⁶) (δ ppm): 164.49, 158.82, 148.93, 147.93, 147.18, 134.01, 128.62, 120.78, 119.18, 119.13, 118.80, 117.27, 115.70, 113.99, 55.83.

8.8.1.4 Preparation of bis-(E)-N,N'-(2-hydroxy-3-methoxy)-benzylhydrazone (H₂L4): The mixture of o-vaniline (1520 mg, 10 mmol) and hydrazinehydrate (255 mg, 5 mmol) was refluxed for 45 min in 15 mL of methanol. The light yellow solution was left in air for crystallization. After two days, long rod shape yellow crystals obtained, was filtered and thoroughly washed with ether and dried in oven at 60°C. Yield is 93%. Anal. Calc. (%) for C₁₆N₂H₁₆O₄ (found); C 64.0 (63.92), N 9.33 (9.29), H 5.37 (5.40). IR (KBr, cm⁻¹): 3006(w), 2964(w), 2940(w), 2937(w), 2839(w), 1624 (s), 1578(w), 1464(s), 1380(w), 1319(m), 1262(s), 1350(s), 1220(m), 1091(m), 964(s), 836(w), 785(w), 745(m), 735(s), 657(w).

8.8.2 Syntheses of coordination compounds

8.8.2.1 Preparation of [Dy₂Ni₂(L1)₄(NO₃)₂(DMF)₂] (1): The mixture of Dy(NO₃)₃.6H₂O (45 mg, 0.1 mmol), Ni(NO₃)₂.6H₂O (29 mg, 0.1 mmol) and H₂L1 (48.6 mg, 0.2 mmol) was stirred in 10 mL of DMF for 10-20 minutes in the presence of Et₃N (48 mg, 0.48 mmol). The red-brown color block-shaped crystals of **1** were grown up after two weeks in 90% yield. Anal. Calc. (%) for C₆₂H₅₈O₂₀N₈Dy₂Ni₂ (found): C 44.39 (44.45), N 6.68 (6.65), H 3.48 (3.50). IR (cm⁻¹): 3546(m), 3478(s), 3414(s), 3232(w), 2924(w), 1660(s), 1605(s), 1584(m), 1548(m), 1474(s),

1455(s), 1383(s), 1398(m), 1384(m), 1297(m), 1228(s), 1181(s), 1108(w), 1032(w), 958(w), 870(w), 819(m), 744(m), 729(m), 685(w), 637(w), 584(w), 517(w).

8.8.2.2 Preparation of $[\text{Dy}_2\text{Ni}_2(\text{L1})_4(\text{NO}_3)_2(\text{MeOH})_2]\cdot 3\text{MeOH}$ (2): The same procedure was employed to prepare all complexes (2-7) and hence synthesis of only **2** is described here in detail. The mixture of $\text{Dy}(\text{NO}_3)_3\cdot 6\text{H}_2\text{O}$ (45 mg, 0.1 mmol), $\text{Ni}(\text{NO}_3)_2\cdot 6\text{H}_2\text{O}$ (29 mg, 0.1 mmol) and $\text{H}_2\text{L1}$ (48.6 mg, 0.2 mmol) was stirred in 10 mL of MeOH for 5-10 minutes in the presence of Et_3N (48 mg, 0.48 mmol). The yellow-green solution was left undisturbed and small hexagonal plate like greenish-yellow crystals of **2** were grown up after 12 h. Yield is 90%. Anal. Calc. (%) for $\text{C}_{61}\text{H}_{64}\text{N}_6\text{O}_{23}\text{Dy}_2\text{Ni}_2$ (found): C 43.31 (43.23), N 4.97 (5.02), H 3.81 (3.75). IR (KBr, cm^{-1}); 3414(b), 3057(w), 2942(w), 2835(w), 1606(s), 1586(s), 1546(m), 1517(s), 1481(s), 1459(s), 1439(s), 1386(s), 1331(m), 1290(m), 1255(m), 1225(s), 1182(w), 1108(w), 1075(w), 1019(w), 966(m), 822(w), 737(s), 642(w), 588(w), 520(w).

8.8.2.3 Preparation of $[\text{Y}_2\text{Ni}_2(\text{L1})_4(\text{NO}_3)_2(\text{MeOH})_2]\cdot 3\text{MeOH}$ (3): A similar procedure which gave **2** was followed for the preparation of **3**, using $\text{Y}(\text{NO}_3)_3\cdot 6\text{H}_2\text{O}$. Yield is 90%. Anal. Calc. (%) for $\text{C}_{61}\text{H}_{64}\text{N}_6\text{O}_{23}\text{Y}_2\text{Ni}_2$ (found): C 47.43 (47.55), N 5.44 (5.32), H 4.17 (4.25). IR (KBr, cm^{-1}); 3415(b), 3055(w), 2943(w), 2835(w), 1606(s), 1585(s), 1546(m), 1517(s), 1481(s), 1459(s), 1439(s), 1386(s), 1331(m), 1290(m), 1255(m), 1225(s), 1182(w), 1108(w), 1075(w), 1019(w), 966(m), 822(w), 737(s), 642(w), 588(w), 520(w).

8.8.2.4 Preparation of $[\text{Gd}_2\text{Ni}_2(\text{L1})_4(\text{NO}_3)_2(\text{MeOH})_2]\cdot 3\text{MeOH}$ (4): A similar procedure which gave **2** was followed for the preparation of **4**, using $\text{Gd}(\text{NO}_3)_3\cdot 6\text{H}_2\text{O}$. Yield is 92%. Anal. Calc. (%) for $\text{C}_{61}\text{H}_{64}\text{N}_6\text{O}_{23}\text{Gd}_2\text{Ni}_2$ (found): C 43.58 (43.52), N 5.00 (5.15), H 3.84 (3.60). IR (KBr, cm^{-1}); 3414(b), 3057(w), 2942(w), 2835(w), 1606(s), 1586(s), 1546(m), 1517(s), 1481(s), 1459(s), 1439(s), 1386(s), 1331(m), 1290(m), 1255(m), 1225(s), 1182(w), 1108(w), 1075(w), 1020(w), 966(m), 822(w), 735(s), 642(w), 588(w), 521(w).

8.8.2.5 Preparation of $[\text{Tb}_2\text{Ni}_2(\text{L1})_4(\text{NO}_3)_2(\text{MeOH})_2]\cdot 3\text{MeOH}$ (5): A similar procedure which gave **2** was followed for the preparation of **5**, using $\text{Tb}(\text{NO}_3)_3\cdot 6\text{H}_2\text{O}$. Yield is 91%. Anal. Calc. (%) for $\text{C}_{61}\text{H}_{64}\text{N}_6\text{O}_{23}\text{Tb}_2\text{Ni}_2$ (found): C 43.50 (43.45), N 4.99 (5.15), H 3.83 (3.55). IR (KBr, cm^{-1}); 3414(b), 3055(w), 2942(w), 2835(w), 1606(s), 1585(s), 1546(m), 1517(s), 1482(s), 1459(s), 1439(s), 1386(s), 1331(m), 1291(m), 1255(m), 1225(s), 1182(w), 1108(w), 1075(w), 1019(w), 966(m), 822(w), 734(s), 644(w), 589(w), 520(w).

8.8.2.6 Preparation of $[\text{Ho}_2\text{Ni}_2(\text{L1})_4(\text{NO}_3)_2(\text{MeOH})_2]\cdot 3\text{MeOH}$ (6): A similar procedure which gave **2** was followed for the preparation of **6**, using $\text{Ho}(\text{NO}_3)_3\cdot 6\text{H}_2\text{O}$. Yield is 85%. Anal. Calc. (%) for $\text{C}_{61}\text{H}_{64}\text{N}_6\text{O}_{23}\text{Ho}_2\text{Ni}_2$ (found): C 43.19 (43.15), N 4.95 (5.10), H 3.80 (3.55). IR (KBr, cm^{-1}); 3414(b), 3055(w), 2942(w), 2835(w), 1606(s), 1586(s), 1545(m), 1517(s), 1481(s), 1459(s), 1439(s), 1386(s), 1332(m), 1290(m), 1255(m), 1225(s), 1182(w), 1108(w), 1075(w), 1019(w), 966(m), 822(w), 737(s), 642(w), 588(w), 523(w).

8.8.2.7 Preparation of $[\text{Er}_2\text{Ni}_2(\text{L1})_4(\text{NO}_3)_2(\text{MeOH})_2]\cdot 3\text{MeOH}$ (7): A similar procedure which gave **2** was followed for the preparation of **3**, using $\text{Er}(\text{NO}_3)_3\cdot 6\text{H}_2\text{O}$. Yield is 90%. Anal. Calc. (%) for $\text{C}_{61}\text{H}_{64}\text{N}_6\text{O}_{23}\text{Er}_2\text{Ni}_2$ (found): C 43.07 (42.95), N 4.94 (5.05), H 3.79 (3.50). IR (KBr, cm^{-1}); 3415(b), 3057(w), 2942(w), 2835(w), 1606(s), 1585(s), 1545(m), 1516(s), 1481(s), 1459(s), 1439(s), 1386(s), 1331(m), 1290(m), 1255(m), 1225(s), 1182(w), 1108(w), 1075(w), 1019(w), 966(m), 825(w), 737(s), 642(w), 590(w), 520(w).

8.8.2.8 Preparation of

$[\text{Dy}_2\text{Ni}_2(\text{CO}_3)(\text{L1})_4(\text{MeOH})_6]_2[\text{Dy}_2\text{Ni}_2(\text{CO}_3)(\text{L1})_4(\text{MeOH})_5(\text{H}_2\text{O})]\cdot 14\text{MeOH}$ (8): The same procedure was employed to prepare all complexes (**8-12**) and hence synthesis of only **8** is described here in detail. The mixture of $\text{Dy}(\text{NO}_3)_3\cdot 6\text{H}_2\text{O}$ (45 mg, 0.1 mmol), $\text{Ni}(\text{NO}_3)_2\cdot 6\text{H}_2\text{O}$ (29 mg, 0.1 mmol) and $\text{H}_2\text{L1}$ (48.6 mg, 0.2 mmol) was stirred in 10 mL of MeOH for 1-2 minutes in the presence of Et_3N (48 mg, 0.48 mmol). The yellow-green solution was left undisturbed and small hexagonal plate like greenish-yellow crystals of **8** were grown up after 12 h. Yield is 25%. Anal. Calc. (%) for $\text{C}_{63}\text{H}_{78}\text{Dy}_2\text{N}_4\text{Ni}_2\text{O}_{26}$ corresponding to replacement of some MeOH by H_2O leading to $[\text{Dy}_2\text{Ni}_2(\text{CO}_3)(\text{L1})_4(\text{MeOH})_6]\cdot 5\text{H}_2\text{O}$ (found): C 43.24 (43.35), N 3.20 (3.25), H 4.47 (4.45). IR (KBr, cm^{-1}); 3430(b), 3037(w), 3014(w), 2929(w), 2829(w), 1606(s), 1583(s), 1543(w), 1481(s), 1452(s), 1385(s), 1291(s), 1223(s), 1179(w), 1099(w), 1078(w), 1073(w), 969(m), 873(w), 821(w), 734(s), 637(w), 573(w), 514(w), 414(w).

8.8.2.9 Preparation of

$[\text{Sm}_2\text{Ni}_2(\text{CO}_3)(\text{L1})_4(\text{MeOH})_6]_2[\text{Sm}_2\text{Ni}_2(\text{CO}_3)(\text{L1})_4(\text{MeOH})_4(\text{H}_2\text{O})_2]\cdot 15\text{MeOH}$ (9): A similar procedure which gave **8** was followed for the preparation of **9**, using $\text{Sm}(\text{NO}_3)_3\cdot 6\text{H}_2\text{O}$. Yield is 60%. Anal. Calc. (%) for $\text{C}_{62}\text{H}_{76}\text{Sm}_2\text{N}_4\text{Ni}_2\text{O}_{26}$ corresponding to replacement of some MeOH by H_2O leading to $[\text{Sm}_2\text{Ni}_2(\text{CO}_3)(\text{L1})_4(\text{MeOH})_5(\text{H}_2\text{O})]\cdot 5\text{H}_2\text{O}$ (found): C 43.51 (43.55), N 3.27 (3.26), H 4.47 (4.53). IR (KBr, cm^{-1}); 3430(b), 3037(w), 3015(w), 2929(w), 2829(w), 1606(s),

1583(s), 1545(w), 1481(s), 1452(s), 1385(s), 1291(s), 1223(s), 1179(w), 1099(w), 1078(w), 1073(w), 969(m), 873(w), 821(w), 735(s), 637(w), 573(w), 514(w), 415(w).

8.8.2.10 Preparation of

[Eu₂Ni₂(CO₃)(L1)₄(MeOH)₆]₂[Eu₂Ni₂(CO₃)(L1)₄(MeOH)₄(H₂O)₂]·15MeOH (10)**: A similar procedure which gave **8** was followed for the preparation of **10**, using Eu(NO₃)₃·6H₂O. Yield is 70%. Anal. Calc. (%) for C₆₂H₇₆Sm₂N₄Ni₂O₂₆ corresponding to replacement of some MeOH by H₂O leading to [Eu₂Ni₂(CO₃)(L1)₄(MeOH)₅(H₂O)]·5H₂O (found): C 43.43 (43.54), N 3.27 (3.21), H 4.46 (4.55). IR (KBr, cm⁻¹); 3430(b), 3037(w), 3014(w), 2929(w), 2829(w), 1605(s), 1583(s), 1543(w), 1482(s), 1452(s), 1385(s), 1291(s), 1223(s), 1179(w), 1099(w), 1078(w), 1073(w), 969(m), 873(w), 821(w), 734(s), 637(w), 573(w), 515(w), 413(w).**

8.8.2.11 Preparation of

[Gd₂Ni₂(CO₃)(L1)₄(MeOH)₆]₂[Gd₂Ni₂(CO₃)(L1)₄(MeOH)₄(H₂O)₂]·17MeOH (11)**: A similar procedure which gave **8** was followed for the preparation of **11**, using Gd(NO₃)₃·6H₂O. Yield is 75%. Anal. Calc. (%) for C₆₂H₇₈Gd₂N₄Ni₂O₂₇ corresponding to replacement of some MeOH by H₂O leading to [Gd₂Ni₂(CO₃)(L1)₄(MeOH)₅(H₂O)]·6H₂O (found): C 42.71 (42.65), N 3.21 (3.20), H 4.51 (4.50). IR (KBr, cm⁻¹); 3430(b), 3037(w), 3014(w), 2929(w), 2829(w), 1606(s), 1583(s), 1543(w), 1481(s), 1452(s), 1385(s), 1291(s), 1223(s), 1179(w), 1099(w), 1078(w), 1073(w), 969(m), 873(w), 821(w), 734(s), 637(w), 573(w), 514(w), 414(w).**

8.8.2.12 Preparation of

[Tb₂Ni₂(CO₃)(L1)₄(MeOH)₆]₂[Tb₂Ni₂(CO₃)(L1)₄(MeOH)₅(H₂O)]·14MeOH (12)**: A similar procedure which gave **8** was followed for the preparation of **12**, using Tb(NO₃)₃·6H₂O. Yield is 30%. Anal. Calc. (%) for C₆₃H₇₈Tb₂N₄Ni₂O₂₆ corresponding to replacement of some MeOH by H₂O leading to [Tb₂Ni₂(CO₃)(L1)₄(MeOH)₆]₂·5H₂O (found): C 43.42 (43.05), N 3.21 (3.24), H 4.51 (4.40). IR (KBr, cm⁻¹); 3430(b), 3037(w), 3015(w), 2929(w), 2829(w), 1606(s), 1584(s), 1543(w), 1481(s), 1452(s), 1385(s), 1291(s), 1223(s), 1180(w), 1099(w), 1078(w), 1073(w), 969(m), 873(w), 821(w), 734(s), 637(w), 575(w), 514(w), 414(w).**

8.8.2.13 Preparation of [Dy₄Ni₈(CO₃)₄(L1)₈(NO₃)₂(H₂O)₈(MeOH)₄](NO₃)₂·5MeOH·4H₂O

(13): The same procedure was employed to prepare all complexes (**13-18**) and hence synthesis of only **13** is described here in detail. The mixture of Dy(NO₃)₃·6H₂O (45 mg, 0.1 mmol), Ni(NO₃)₂·6H₂O (58 mg, 0.2 mmol) and H₂L1 (48.6 mg, 0.2 mmol) was stirred in 10 mL of MeOH for 5-10 minutes in the presence of Et₃N (48 mg, 0.54 mmol). The yellow-green solution

gradually turned to red-brown over the period of standing in air and red-brown color prism shaped crystals of **13** were grown up after one week. Yield is 45%. Anal. Calc. (%) for $C_{120}H_{138}Dy_4N_{12}Ni_4O_{69}$ corresponding to replacement of some MeOH by H_2O leading to $[Dy_4Ni_8(CO_3)_4(L1)_8(NO_3)_2(H_2O)_8(MeOH)_4](NO_3)_2 \cdot 9H_2O$ (found): C 36.28 (36.07), N 4.23 (4.15), H 3.50 (3.42). IR (KBr, cm^{-1}); 3393(b), 3058(w), 3019(w), 2922(w), 2845(w), 1618(m), 1587(w), 1509(w), 1480(s), 1460(s), 1459(s), 1408(s), 1386(s), 1307(m), 1255(m), 1225(m), 1182(m), 1108(w), 1096(w), 1076(w), 969(w), 823(w), 733(s), 641(w), 576(w), 517(w), 444(w).

8.8.2.14 Preparation of $[Y_4Ni_8(CO_3)_4(L1)_8(NO_3)_2(H_2O)_8(MeOH)_4](NO_3)_2 \cdot 5MeOH \cdot 4H_2O$ (14**):** A similar procedure which gave **13** was followed for the preparation of **14**, using $Y(NO_3)_3 \cdot 6H_2O$. Yield is 30%. Anal. Calc. (%) for $C_{120}H_{138}Y_4N_{12}Ni_4O_{69}$ corresponding to replacement of some MeOH by H_2O leading to $[Y_4Ni_8(CO_3)_4(L1)_8(NO_3)_2(H_2O)_8(MeOH)_4](NO_3)_2 \cdot 9H_2O$ (found): C 39.19 (39.15), N 4.57 (4.65), H 3.78 (3.75). IR (KBr, cm^{-1}); 3393(b), 3058(w), 3019(w), 2922(w), 2845(w), 1618(m), 1587(w), 1510(w), 1480(s), 1462(s), 1460(s), 1408(s), 1386(s), 1307(m), 1255(m), 1225(m), 1182(m), 1108(w), 1096(w), 1075(w), 969(w), 823(w), 733(s), 641(w), 576(w), 517(w), 445(w).

8.8.2.15 Preparation of $[Gd_4Ni_8(CO_3)_4(L1)_8(NO_3)_2(H_2O)_8(MeOH)_4](NO_3)_2 \cdot 5MeOH \cdot 4H_2O$ (15**):** A similar procedure which gave **13** was followed for the preparation of **15**, using $Y(NO_3)_3 \cdot 6H_2O$. Yield is 30%. Anal. Calc. (%) for $C_{120}H_{138}Gd_4N_{12}Ni_4O_{69}$ corresponding to replacement of some MeOH by H_2O leading to $[Gd_4Ni_8(CO_3)_4(L1)_8(NO_3)_2(H_2O)_8(MeOH)_4](NO_3)_2 \cdot 9H_2O$ (found): C 36.47 (36.35), N 4.25 (4.18), H 3.52 (3.62). IR (KBr, cm^{-1}); 3395(b), 3059(w), 3019(w), 2922(w), 2845(w), 1618(m), 1587(w), 1509(w), 1480(s), 1460(s), 1459(s), 1408(s), 1386(s), 1305(m), 1255(m), 1225(m), 1182(m), 1108(w), 1096(w), 1076(w), 969(w), 823(w), 733(s), 641(w), 576(w), 517(w), 445(w).

8.8.2.16 Preparation of $[Tb_4Ni_8(CO_3)_4(L1)_8(NO_3)_2(H_2O)_8(MeOH)_4](NO_3)_2 \cdot 5MeOH \cdot 4H_2O$ (16**):** A similar procedure which gave **13** was followed for the preparation of **16**, using $Tb(NO_3)_3 \cdot 6H_2O$. Yield is 30%. Anal. Calc. (%) for $C_{120}H_{138}Dy_4N_{12}Ni_4O_{69}$ corresponding to replacement of some MeOH by H_2O leading to $[Dy_4Ni_8(CO_3)_4(L1)_8(NO_3)_2(H_2O)_8(MeOH)_4](NO_3)_2 \cdot 9H_2O$ (found): C 36.41 (36.47), N 4.25 (4.20), H 3.51 (3.52). IR (KBr, cm^{-1}); 3393(b), 3059(w), 3020(w), 2922(w), 2845(w), 1618(m), 1587(w), 1509(w), 1480(s), 1460(s), 1459(s), 1408(s), 1386(s), 1305(m), 1255(m), 1225(m), 1182(m), 1108(w), 1096(w), 1076(w), 969(w), 823(w), 734(s), 641(w), 576(w), 517(w), 444(w).

8.8.2.17 Preparation of $[\text{Ho}_4\text{Ni}_8(\text{CO}_3)_4(\text{L1})_8(\text{NO}_3)_2(\text{H}_2\text{O})_8(\text{MeOH})_4](\text{NO}_3)_2 \cdot 5\text{MeOH} \cdot 4\text{H}_2\text{O}$ (17):

A similar procedure which gave **13** was followed for the preparation of **17**, using $\text{Ho}(\text{NO}_3)_3 \cdot 6\text{H}_2\text{O}$. Yield is 30%. Anal. Calc. (%) for $\text{C}_{120}\text{H}_{138}\text{Ho}_4\text{N}_{12}\text{Ni}_4\text{O}_{69}$ corresponding to replacement of some MeOH by H_2O leading to $[\text{Ho}_4\text{Ni}_8(\text{CO}_3)_4(\text{L1})_8(\text{NO}_3)_2(\text{H}_2\text{O})_8(\text{MeOH})_4](\text{NO}_3)_2 \cdot 9\text{H}_2\text{O}$ (found): C 36.20 (36.16), N 4.22 (4.11), H 3.49 (3.44). IR (KBr, cm^{-1}); 3393(b), 3058(w), 3019(w), 2922(w), 2845(w), 1620(m), 1587(w), 1509(w), 1480(s), 1460(s), 1461(s), 1408(s), 1386(s), 1307(m), 1255(m), 1225(m), 1182(m), 1108(w), 1096(w), 1076(w), 970(w), 823(w), 733(s), 641(w), 576(w), 515(w), 444(w).

8.8.2.18 Preparation of $[\text{Er}_4\text{Ni}_8(\text{CO}_3)_4(\text{L1})_8(\text{NO}_3)_2(\text{H}_2\text{O})_8(\text{MeOH})_4](\text{NO}_3)_2 \cdot 5\text{MeOH} \cdot 4\text{H}_2\text{O}$ (18):

A similar procedure which gave **13** was followed for the preparation of **18**, using $\text{Er}(\text{NO}_3)_3 \cdot 6\text{H}_2\text{O}$. Yield is 30%. Anal. Calc. (%) for $\text{C}_{120}\text{H}_{138}\text{Er}_4\text{N}_{12}\text{Ni}_4\text{O}_{69}$ corresponding to replacement of some MeOH by H_2O leading to $[\text{Er}_4\text{Ni}_8(\text{CO}_3)_4(\text{L1})_8(\text{NO}_3)_2(\text{H}_2\text{O})_8(\text{MeOH})_4](\text{NO}_3)_2 \cdot 9\text{H}_2\text{O}$ (found): C 36.11 (36.05), N 4.21 (4.27), H 3.48 (3.62). IR (KBr, cm^{-1}); 3393(b), 3058(w), 3019(w), 2924(w), 2845(w), 1618(m), 1587(w), 1509(w), 1480(s), 1460(s), 1460(s), 1408(s), 1386(s), 1307(m), 1255(m), 1225(m), 1182(m), 1108(w), 1096(w), 1076(w), 969(w), 823(w), 733(s), 641(w), 575(w), 517(w), 445(w).

8.8.2.19 Preparation of $[\text{Dy}_2\text{Ni}_4(\text{OH})_2(\text{L1})_4(\text{MeOH})_4(\text{NO}_3)_4] \cdot 4\text{MeOH}$ (19):

If the reaction which produces **13** is performed in same ratio (1:2:2:5.4) in MeOH under N_2 atmosphere, produces green color needle shaped crystals of **19** in 80% yield. Anal. Calc. (%) for $\text{C}_{60}\text{H}_{70}\text{Dy}_2\text{N}_8\text{Ni}_4\text{O}_{34}$ corresponding to replacement of four lattice MeOH by four H_2O leading to $[\text{Dy}_2\text{Ni}_4(\text{OH})_2(\text{L1})_4(\text{MeOH})_4(\text{NO}_3)_4] \cdot 4\text{H}_2\text{O}$ (found): C 35.90 (35.85), N 5.58 (5.45), H 3.51 (3.57). IR (KBr, cm^{-1}); 3440(b), 3060(w), 2941(w), 2844(w), 1607(s), 1584(m), 1481(s), 1465(s), 1437(s), 1385(s), 1295(s), 1225(s), 1180(m), 1100(w), 1075(w), 966(m), 824(m), 739(m), 641(m), 583(w), 515(w), 443(w).

8.8.2.20 Preparation of $[\text{Dy}_4\text{Ni}_8(\text{OH})_4(\text{L1})_8(\text{MeOH})_4(\text{H}_2\text{O})_4(\text{C}_2\text{O}_4)_2](\text{NO}_3)_4 \cdot 4\text{H}_2\text{O} \cdot 8\text{MeOH}$ (20):

The mixture of $\text{Dy}(\text{NO}_3)_3 \cdot 6\text{H}_2\text{O}$ (45 mg, 0.1 mmol), $\text{Ni}(\text{NO}_3)_2 \cdot 6\text{H}_2\text{O}$ (29 mg, 0.1 mmol), $\text{H}_2\text{L1}$ (15 mg, 0.061 mmol) and $\text{H}_2\text{C}_2\text{O}_4 \cdot 2\text{H}_2\text{O}$ (7 mg, 0.055 mmol) was dissolved in 15 mL of MeOH. The color of the solution changed from red to green on addition of triethylamine (Et_3N) (24 mg, 0.24 mmol) and then the solution was stirred for 5 min and left in air for slow evaporation. After one week green color needle shaped crystals of **20** were isolated in 25% yield.

Anal. Calc. (%) for $C_{128}H_{156}O_{68}N_{12}Dy_4Ni_8$ (found): C 37.75 (37.45), N 4.12 (4.15), H 3.91 (3.85), IR (KBr, cm^{-1}): 3437(b), 3062(w), 2921(w), 2850(w), 16871(m), 1638(s), 1617(s), 1589(m), 1565(w), 1484(m), 1464(m), 1384(s), 13058(w), 1233(m), 1183(m), 1111(w), 1093(w), 1072(w), 965(w), 821(w), 732(w), 620(w), 481(w).

8.8.2.21 Preparation of $[Dy_2Zn_3(OH)(L1)_5(MeOH)_{2.5}(OH_2)_{1.5}]Cl \cdot 3MeOH \cdot 2.5H_2O$ (21): The same procedure was employed to prepare all complexes (21-25) and hence synthesis of only 21 is described here in detail. Mixture of $DyCl_3 \cdot 6H_2O$ (38 mg, 0.1 mmol), $ZnCl_2$ (13 mg, 0.1 mmol) and H_2L1 (48.6 mg, 0.2 mmol) in 20 mL of MeOH was stirred for 25 minutes in the presence of Et_3N (0.48 mmol, 48 mg). The yellow fluorescence color block shaped crystals of 21 were obtained in 55% yield after one week from dark yellow solution from slow evaporation in air. Anal. Calc. (%) for $C_{75.50}H_{86}ClN_5O_{25.50}Dy_2Zn_3$ (found): C 44.37 (44.40), N 3.45 (3.50), H 4.27 (4.25). IR (KBr, cm^{-1}): 3640(s), 3430(w), 3047(w), 3002(w), 2985(w), 2936(w), 2836(w), 1608(s), 1585(s), 1545(m), 1479(s), 1460(s), 1446(s), 1438(s), 1398(m), 1385(m), 1280(s), 1279(s), 1242(s), 1226(s), 1180(s), 1152(m), 1109(m), 1078(w), 1040(w), 970(m), 873(w), 855(w), 820(m), 736(s), 622(w), 636(w), 577(w), 514(w), 437(w).

8.8.2.22 Preparation of $[Eu_2Zn_3(OH)(L1)_5(MeOH)_{2.5}(OH_2)_{1.5}]Cl \cdot 3MeOH \cdot 2.5H_2O$ (22): A similar procedure which gave 21 was followed for the preparation of 22, using $EuCl_3 \cdot 6H_2O$. Yield is 45%. Anal. Calc. (%) for $C_{75.50}H_{86}ClN_5O_{25.50}Eu_2Zn_3$ (found): C 44.84 (44.85), N 3.49 (3.55), H 4.49 (4.30). IR (KBr, cm^{-1}): 3640(w), 3435(b), 3050(w), 3008(w), 2985(w), 2939(w), 2838(w), 1609(s), 1584(s), 1544(m), 1478(s), 1447(s), 1437(s), 1398(m), 1384(m), 1323(w), 1289(s), 1279(s), 1242(s), 1225(s), 1180(s), 1152(m), 1109(m), 1080(w), 1040(w), 971(m), 872(w), 854(w), 819(m), 736(s), 635(w), 622(w), 576(w), 512(w), 436(w).

8.8.2.23 Preparation of $[Gd_2Zn_3(OH)(L1)_5(MeOH)_{2.5}(OH_2)_{1.5}]Cl \cdot 3MeOH \cdot 2.5H_2O$ (23): A similar procedure which gave 21 was followed for the preparation of 23, using $GdCl_3 \cdot 6H_2O$. Yield is 45%. Anal. Calc. (%) for $C_{75.50}H_{86}ClN_5O_{25.50}Gd_2Zn_3$ (found): C 44.60 (44.40), N 3.47 (3.45), H 4.29 (4.35). IR (KBr, cm^{-1}): 3641(w), 3435(b), 3050(w), 3008(w), 2985(w), 2939(w), 2838(w), 1609(s), 1584(s), 1544(m), 1478(s), 1447(s), 1437(s), 1398(m), 1384(m), 1323(w), 1289(s), 1279(s), 1242(s), 1225(s), 1180(s), 1152(m), 1109(m), 1080(w), 1040(w), 971(m), 872(w), 854(w), 819(m), 734(s), 635(w), 622(w), 576(w), 513(w), 435(w).

8.8.2.24 Preparation of $[Tb_2Zn_3(OH)(L1)_5(MeOH)_{2.5}(OH_2)_{1.5}]Cl \cdot 3MeOH \cdot 2.5H_2O$ (24): A similar procedure which gave 21 was followed for the preparation of 24, using $TbCl_3 \cdot 6H_2O$.

Yield is 47%. Anal. Calc. (%) for $C_{75.50}H_{86}ClN_5O_{25.50}Tb_2Zn_3$ (found): C 44.53 (44.45), N 3.46 (3.50), H 4.28 (4.25). IR (KBr, cm^{-1}): 3640(w), 3435(b), 3039(w), 3009(w), 2985(w), 2939(w), 2838(w), 1609(s), 1584(s), 1545(m), 1478(s), 1447(s), 1437(s), 1398(m), 1384(m), 1323(w), 1289(s), 1279(s), 1242(s), 1225(s), 1180(s), 1152(m), 1110(m), 1080(w), 1043(w), 971(m), 873(w), 855(w), 820(m), 737(s), 636(w), 622(w), 577(w), 513(w), 439(w).

8.8.2.25 Preparation of $[Ho_2Zn_3(OH)(L1)_5(MeOH)_{2.5}(OH_2)_{1.5}]Cl_3 \cdot 3MeOH \cdot 2.5H_2O$ (25): A similar procedure which gave **21** was followed for the preparation of **25**, using $HoCl_3 \cdot 6H_2O$. Yield is 50%. Anal. Calc. (%) for $C_{75.50}H_{86}ClN_5O_{25.50}Ho_2Zn_3$ (found): C 44.27 (44.25), N 3.44 (3.39), H 4.26 (4.25). IR (KBr, cm^{-1}): 3640(w), 3435(b), 3039(w), 3009(w), 2985(w), 2939(w), 2838(w), 1610(s), 1584(s), 1545(m), 1478(s), 1447(s), 1437(s), 1398(m), 1384(m), 1323(w), 1289(s), 1279(s), 1242(s), 1225(s), 1179(s), 1152(m), 1110(m), 1080(w), 1043(w), 971(m), 873(w), 855(w), 821(m), 737(s), 636(w), 622(w), 577(w), 515(w), 440(w).

8.8.2.26 Preparation of $[Dy_7Zn_4(OH)_4(L1)_8(Cl)_6(H_2O)_4]Cl_3 \cdot 35H_2O$ (26): Mixture of $DyCl_3 \cdot 6H_2O$ (67 mg, 0.175 mmol), $ZnCl_2$ (13 mg, 0.1 mmol) and H_2L1 (48.6 mg, 0.2 mmol) in 20 ml of MeOH was stirred for 25 minutes in the presence of Et_3N (0.48 mmol, 48 mg). The yellow solution slowly turned to red-brown in air on standing in air for two weeks. When the volume of the solution reduces to 15 mL, the solution isolated from air by covering the mouth of the vial. The red-brown color needle shaped crystals of **26** were obtained after four weeks in 50% yield. Anal. Calc. (%) for $C_{112}H_{170}Cl_9N_8O_{67}Dy_7Zn_4$ (found): C 30.34 (30.40), N 2.54 (3.52), H 3.88 (3.95). IR (KBr, cm^{-1}): 3437(b), 2962(w), 2928(w), 2850(w), 1617(s), 1575(m), 1545(m), 1481(s), 1457(s), 1450(s), 1389(m), 1292(m), 1284(m), 1225(m), 1175(s), 1107(w), 1070(s), 911(w), 825(w), 739(w), 666(w), 615(w), 505(w).

8.8.2.27 Preparation of $[Dy_6Cd_6(CO_3)_2(OH)_4(\mu-Cl)_2(Cl)_2(L1)_8(H_2O)_{12}]Cl_2 \cdot 10THF$ (27): The same procedure was employed to prepare all complexes (**27-30**) and hence synthesis of only **27** is described here in detail. The mixture of $DyCl_3 \cdot 6H_2O$ (38 mg, 0.1 mmol), $CdCl_2 \cdot H_2O$ (22 mg, 0.11 mmol) and H_2L1 (48.6 mg, 0.2 mmol) was dissolved in 20 mL of methanol and stirred for 20 min in the presence of Et_3N (36 mg, 0.36 mmol) to get yellow crystalline precipitate. The precipitate was filtered out and dissolved in 10 mL of THF. The yellow color rod shaped crystals of **27** were obtained after two weeks in 15% yield. Anal. Calc. (%) for $C_{138}H_{172}Dy_6Cd_6N_8Cl_6O_{56}$ corresponding to replacement of four lattice THF by four H_2O leading to $[Dy_6Cd_6(CO_3)_2(OH)_4(\mu-Cl)_2(Cl)_2(L1)_8(H_2O)_{12}]Cl_2 \cdot 6THF \cdot 4H_2O$ (found): C 35.25 (35.27), N 2.38

(2.25), H 3.68 (3.72). IR (KBr, cm^{-1}): 3445(w), 3034(b), 2965(w), 2935(w), 2830(w), 1665(s), 1613(m), 1585(s), 1551(s), 1494(s), 1484(s), 1261(m), 1255(w), 1175(m), 1110(w), 1071(m), 1034(m), 972(m), 860(w), 827(w), 735(m), 635(w), 586(w).

8.8.2.28 Preparation of $[\text{Tb}_6\text{Cd}_6(\text{CO}_3)_2(\text{OH})_4(\mu\text{-Cl})_2(\text{Cl})_2(\text{L1})_8(\text{OH}_2)_{12}]\text{Cl}_2\cdot 10\text{THF}$ (28): A similar procedure which gave **27** was followed for the preparation of **28**, using $\text{TbCl}_3\cdot 6\text{H}_2\text{O}$. Yield is 15%. Anal. Calc. (%) for $\text{C}_{138}\text{H}_{172}\text{Tb}_6\text{Cd}_6\text{N}_8\text{Cl}_6\text{O}_{56}$ corresponding to replacement of four lattice THF by four H_2O leading to $[\text{Tb}_6\text{Cd}_6(\text{CO}_3)_2(\text{OH})_4(\text{Cl})_4(\text{L1})_8(\text{H}_2\text{O})_{12}]\text{Cl}_2\cdot 6\text{THF}\cdot 4\text{H}_2\text{O}$ (found): C 35.42 (35.45), N 2.39 (2.35), H 3.70 (3.75). IR (KBr, cm^{-1}): 3445(w), 3031(b), 2965(w), 2932(w), 2830(w), 1665(s), 1613(m), 1585(s), 1551(s), 1493(s), 1484(s), 1260(m), 1255(w), 1175(m), 1111(w), 1080(m), 1034(m), 973(m), 862(w), 735(m), 637(w), 585(w).

8.8.2.29 Preparation of $[\text{Ho}_6\text{Cd}_6(\text{CO}_3)_2(\text{OH})_4(\mu\text{-Cl})_2(\text{Cl})_2(\text{L1})_8(\text{OH}_2)_{12}]\text{Cl}_2\cdot 10\text{THF}$ (29): A similar procedure which gave **27** was followed for the preparation of **29**, using $\text{HoCl}_3\cdot 6\text{H}_2\text{O}$. Yield is 15%. Anal. Calc. (%) for $\text{C}_{138}\text{H}_{172}\text{Ho}_6\text{Cd}_6\text{N}_8\text{Cl}_6\text{O}_{56}$ corresponding to replacement of four lattice THF by four H_2O leading to $[\text{Ho}_6\text{Cd}_6(\text{CO}_3)_2(\text{OH})_4(\text{Cl})_4(\text{L1})_8(\text{H}_2\text{O})_{12}]\text{Cl}_2\cdot 6\text{THF}\cdot 4\text{H}_2\text{O}$ (found): C 35.15 (35.31), N 2.37 (2.32), H 3.67 (3.66). IR (KBr, cm^{-1}): 3445(w), 3032(b), 2965(w), 2935(w), 2830(w), 1665(s), 1613(m), 1585(s), 1551(s), 1493(s), 1484(s), 1260(m), 1255(w), 1175(m), 1110(w), 1079(m), 1034(m), 972(m), 860(w), 735(m), 637(w), 586(w).

8.8.2.30 Preparation of $[\text{Er}_6\text{Cd}_6(\text{CO}_3)_2(\text{OH})_4(\mu\text{-Cl})_2(\text{Cl})_2(\text{L1})_8(\text{OH}_2)_{12}]\text{Cl}_2\cdot 10\text{THF}$ (30): A similar procedure which gave **27** was followed for the preparation of **30**, using $\text{ErCl}_3\cdot 6\text{H}_2\text{O}$. Yield is 20%. Anal. Calc. (%) for $\text{C}_{138}\text{H}_{172}\text{Er}_6\text{Cd}_6\text{N}_8\text{Cl}_6\text{O}_{56}$ corresponding to replacement of four lattice THF by four H_2O leading to $[\text{Er}_6\text{Cd}_6(\text{CO}_3)_2(\text{OH})_4(\text{Cl})_4(\text{L1})_8(\text{H}_2\text{O})_{12}]\text{Cl}_2\cdot 6\text{THF}\cdot 4\text{H}_2\text{O}$ (found): C 35.04 (35.15), N 2.36 (2.30), H 3.66 (3.59). IR (KBr, cm^{-1}): 3445(w), 3031(b), 2965(w), 2935(w), 2830(w), 1665(s), 1612(m), 1585(s), 1551(s), 1493(s), 1483(s), 1260(m), 1253(w), 1175(m), 1110(w), 1079(m), 1034(m), 972(m), 860(w), 734(m), 637(w), 585(w).

8.8.2.31 Preparation of $[\text{Dy}_3\text{Cu}_2(\mu_3\text{-OH})_2(\text{L1})_5(\text{NO}_3)(\text{MeOH})_2(\text{H}_2\text{O})]\cdot 3\text{MeOH}$ (31): The same procedure was employed to prepare all complexes (**31-34**) and hence synthesis of only **31** is described here in detail. Mixture of $\text{Dy}(\text{NO}_3)_3\cdot 6\text{H}_2\text{O}$ (45 mg, 0.1 mmol), $\text{Cu}(\text{NO}_3)_2\cdot 2.5\text{H}_2\text{O}$ (24 mg, 0.1 mmol) and $\text{H}_2\text{L1}$ (48.6 mg, 0.2 mmol) in 20 mL of MeOH was stirred for 5-10 minutes in the presence of Et_3N (0.48 mmol, 48 mg). The hexagonal shape green-yellow crystal of **31** was obtained in 55% yield after one week from dark green solution from slow evaporation in air and also from diffusion of n-pentane to the solution. Anal. Calc. (%) for $\text{C}_{75}\text{H}_{79}\text{Cu}_2\text{Dy}_3\text{N}_6\text{O}_{26}$

(found): C, 42.91 (42.95); H, 3.796 (3.77); N, 4.006 (4.01). IR (KBr, cm^{-1}): 3400(w), 3057(b), 2963(w), 2935(w), 2834(w), 1610(m), 1585(s), 1551(s), 1493(s), 1481(s), 1453(w), 1383(s), 1302(s), 1260(m), 1253(w), 1170(m) 1105(w), 1079(m), 1032(m), 972(m), 860(w), 825(w), 733(m), 638(w), 587(w), 537(w), 503(w).

8.8.2.32 Preparation of $[\text{Gd}_3\text{Cu}_2(\mu_3\text{-OH})_2(\text{L1})_5(\text{NO}_3)(\text{MeOH})_2(\text{H}_2\text{O})]\cdot 3\text{MeOH}$ (32**):** A similar procedure which gave **31** was followed for the preparation of **32**, using $\text{GdCl}_3\cdot 6\text{H}_2\text{O}$. Yield is 50%. Anal. Calc. (%) for $\text{C}_{75}\text{H}_{79}\text{Cu}_2\text{Gd}_3\text{N}_6\text{O}_{26}$ (found): C, 43.32 (42.45); H, 3.82 (3.82); N, 4.04 (4.05). IR (KBr, cm^{-1}): 3400(w), 3057(b), 2963(w), 2935(w), 2834(w), 1610(m), 1585(s), 1551(s), 1493(s), 1481(s), 1453(w), 1383(s), 1302(s), 1260(m), 1253(w), 1170(m) 1105(w), 1079(m), 1032(m), 972(m), 860(w), 825(w), 733(m), 638(w), 587(w), 537(w), 503(w).

8.8.2.33 Preparation of $[\text{Tb}_3\text{Cu}_2(\mu_3\text{-OH})_2(\text{L1})_5(\text{NO}_3)(\text{MeOH})_2(\text{H}_2\text{O})]\cdot 3\text{MeOH}\cdot \text{H}_2\text{O}$ (33**):** A similar procedure which gave **31** was followed for the preparation of **33**, using $\text{TbCl}_3\cdot 6\text{H}_2\text{O}$. Yield is 55%. Anal. Calc. (%) for $\text{C}_{75}\text{H}_{81}\text{Cu}_2\text{Tb}_3\text{N}_6\text{O}_{27}$ (found): C, 42.84 (42.85); H, 3.88 (3.87); N, 3.99 (3.95). IR (KBr, cm^{-1}): 3400(w), 3345(w) 3057(b), 2963(w), 2935(w), 2834(w), 1610(m), 1585(s), 1551(s), 1493(s), 1481(s), 1453(w), 1383(s), 1302(s), 1260(m), 1253(w), 1170(m) 1105(w), 1079(m), 1032(m), 972(m), 860(w), 825(w), 733(m), 638(w), 587(w), 537(w), 505(w).

8.8.2.34 Preparation of $[\text{Ho}_3\text{Cu}_2(\mu_3\text{-OH})_2(\text{L1})_5(\text{NO}_3)(\text{MeOH})_2(\text{H}_2\text{O})]\cdot 3\text{MeOH}$ (34**):** A similar procedure which gave **31** was followed for the preparation of **34**, using $\text{HoCl}_3\cdot 6\text{H}_2\text{O}$. Yield is 45%. Anal. Calc. (%) for $\text{C}_{75}\text{H}_{79}\text{Cu}_2\text{Ho}_3\text{N}_6\text{O}_{26}$ (found): C, 42.84 (42.95); H, 3.87 (3.97); N, 3.99 (4.03). IR (KBr, cm^{-1}): 3400(w), 3057(b), 2963(w), 2935(w), 2834(w), 1610(m), 1585(s), 1551(s), 1493(s), 1481(s), 1453(w), 1383(s), 1302(s), 1260(m), 1253(w), 1170(m) 1105(w), 1079(m), 1032(m), 972(m), 860(w), 825(w), 733(m), 638(w), 587(w), 537(w), 503(w).

8.8.2.35 Preparation of $[\text{Dy}_2\text{Co}_2(\text{L1})_4(\text{NO}_3)_2(\text{THF})_2]\cdot 4\text{THF}$ (35**):** The same procedure was employed to prepare all complexes (**35-40**) and hence synthesis of only **35** is described here in detail. The mixture of $\text{Dy}(\text{NO}_3)_3\cdot 6\text{H}_2\text{O}$ (0.1 mmol, 45 mg), $\text{Co}(\text{NO}_3)_2\cdot 6\text{H}_2\text{O}$ (0.1 mmol, 29 mg) and $\text{H}_2\text{L1}$ (0.2 mmol, 48.6 mg) was stirred in 20 mL of methanol for 1 min in the presence of Et_3N (0.42 mmol, 42 mg). The red color solution was left undisturbed and after 30 min microcrystalline material was precipitated out which was dissolved in 15 mL THF. The slow evaporation from air produced red color block shaped crystals of **35** in 75% yield. Anal. Calc. (%) for $\text{C}_{60}\text{H}_{62}\text{Dy}_2\text{Co}_2\text{N}_6\text{O}_{24}$ corresponding to replacement of some THF by H_2O leading to

[Dy₂Co₂(L1)₄(NO₃)₂(THF)(H₂O)]·4H₂O (found): C 42.54 (42.46), N 4.96 (4.95), H 3.68 (3.70). IR (KBr, cm⁻¹): 3414(b), 3057(w), 2942(m), 2835(m), 1606(s), 1586(s), 1546(m), 1517(s), 1481(s), 1459(s), 1439(s), 1386(s), 1331(m), 1290(m), 1255(m), 1225(s), 1182(w), 1108(w), 1075(w), 1019(w), 966(m), 822(w), 737(s), 642(w), 588(w), 520(w).

8.8.2.36 Preparation of [Y₂Co₂(L1)₄(NO₃)₂(THF)₂].4THF (36): A similar procedure which gave **35** was followed for the preparation of **36**, using Y(NO₃)₃·6H₂O. Yield is 65%. Anal. Calc. (%) for C₆₀H₆₂Y₂Co₂N₆O₂₄ corresponding to replacement of some THF by H₂O leading to [Y₂Co₂(L1)₄(NO₃)₂(THF)(H₂O)]·4H₂O (found): C 46.58 (46.53), N 5.43 (5.45), H 4.04 (4.0). IR (KBr, cm⁻¹): 3414(b), 3057(w), 2942(m), 2835(m), 1606(s), 1586(s), 1546(m), 1517(s), 1481(s), 1459(s), 1439(s), 1386(s), 1331(m), 1290(m), 1255(m), 1225(s), 1182(w), 1108(w), 1075(w), 1019(w), 966(m), 822(w), 737(s), 642(w), 588(w), 520(w).

8.8.2.37 Preparation of [Gd₂Co₂(L1)₄(NO₃)₂(THF)₂].4THF (36): A similar procedure which gave **35** was followed for the preparation of **37**, using Gd(NO₃)₃·6H₂O. Yield is 55%. Anal. Calc. (%) for C₆₀H₆₂Gd₂Co₂N₆O₂₄ corresponding to replacement of some THF by H₂O leading to [Gd₂Co₂(L1)₄(NO₃)₂(THF)(H₂O)]·4H₂O (found): C 42.80 (42.76), N 4.99 (5.05), H 3.71 (3.77). IR (KBr, cm⁻¹): 3414(b), 3057(w), 2942(m), 2835(m), 1606(s), 1586(s), 1546(m), 1517(s), 1481(s), 1459(s), 1439(s), 1386(s), 1331(m), 1290(m), 1255(m), 1225(s), 1182(w), 1108(w), 1075(w), 1019(w), 966(m), 822(w), 737(s), 642(w), 588(w), 520(w).

8.8.2.38 Preparation of [Tb₂Co₂(L1)₄(NO₃)₂(THF)₂].4THF (38): A similar procedure which gave **35** was followed for the preparation of **38**, using Tb(NO₃)₃·6H₂O. Yield is 70%. Anal. Calc. (%) for C₆₀H₆₂Tb₂Co₂N₆O₂₄ corresponding to replacement of some THF by H₂O leading to [Tb₂Co₂(L1)₄(NO₃)₂(THF)(H₂O)]·4H₂O (found): C 42.72 (42.64), N 4.98 (4.93), H 3.70 (3.81). IR (KBr, cm⁻¹): 3414(b), 3057(w), 2942(m), 2835(m), 1606(s), 1586(s), 1546(m), 1517(s), 1481(s), 1459(s), 1439(s), 1386(s), 1331(m), 1290(m), 1255(m), 1225(s), 1182(w), 1108(w), 1075(w), 1019(w), 966(m), 822(w), 737(s), 642(w), 588(w), 520(w).

8.8.2.39 Preparation of [Ho₂Co₂(L1)₄(NO₃)₂(THF)₂].4THF (36): A similar procedure which gave **35** was followed for the preparation of **39**, using Ho(NO₃)₃·6H₂O. Yield is 73%. Anal. Calc. (%) for C₆₀H₆₂Ho₂Co₂N₆O₂₄ corresponding to replacement of some THF by H₂O leading to [Ho₂Co₂(L1)₄(NO₃)₂(THF)(H₂O)]·4H₂O (found): C 42.41 (42.49), N 4.94 (4.91), H 3.67 (3.70). IR (KBr, cm⁻¹): 3417(b), 3058(w), 2942(m), 2835(m), 1606(s), 1586(s), 1546(m), 1517(s),

1481(s), 1459(s), 1439(s), 1386(s), 1331(m), 1290(m), 1255(m), 1225(s), 1182(w), 1109(w), 1075(w), 1019(w), 966(m), 822(w), 737(s), 642(w), 589(w), 522(w).

8.8.2.40 Preparation of $[\text{Er}_2\text{Co}_2(\text{L1})_4(\text{NO}_3)_2(\text{THF})_2]\cdot 4\text{THF}$ (40**):** A similar procedure which gave **35** was followed for the preparation of **40**, using $\text{Er}(\text{NO}_3)_3\cdot 6\text{H}_2\text{O}$. Yield is 45%. Anal. Calc. (%) for $\text{C}_{60}\text{H}_{62}\text{Er}_2\text{Co}_2\text{N}_6\text{O}_{24}$ corresponding to replacement of some THF by H_2O leading to $[\text{Er}_2\text{Co}_2(\text{L1})_4(\text{NO}_3)_2(\text{THF})(\text{H}_2\text{O})]\cdot 4\text{H}_2\text{O}$ (found): C 42.30 (42.32), N 4.93 (4.98), H 3.66 (3.59). IR (KBr, cm^{-1}): 3415(b), 3057(w), 2942(m), 2835(m), 1606(s), 1586(s), 1546(m), 1517(s), 1481(s), 1459(s), 1439(s), 1386(s), 1331(m), 1290(m), 1255(m), 1225(s), 1183(w), 1108(w), 1075(w), 1019(w), 966(m), 822(w), 737(s), 642(w), 588(w), 521(w).

8.8.2.41 Preparation of $[\text{Dy}_4(\text{OH})_2(\text{L1})_4(\text{HL1})_2]\cdot 2\text{THF}$ (41**):** The same procedure was employed to prepare all complexes (**41-45**) and hence synthesis of only **41** is described here in detail. The mixture of $\text{DyCl}_3\cdot 6\text{H}_2\text{O}$ (0.1 mmol, 38 mg), $\text{CdCl}_2\cdot \text{H}_2\text{O}$ (0.11 mmol, 22 mg) and $\text{H}_2\text{L1}$ (0.2 mmol, 48.6 mg) was stirred in MeOH (20 mL) for 20 min in the presence of Et_3N (0.36 mmol, 36 mg) 20 mL of THF was added to the turbid yellow solution to get a clear orange-red clear solution. Yield is 65%. Anal. Calc. (%) for $\text{C}_{92}\text{H}_{86}\text{Dy}_4\text{N}_6\text{O}_{22}$ (found): C 48.51 (48.55); H 3.78 (3.86); N 3.65. (3.68). Selected IR data (KBr): $\nu(\text{cm}^{-1})$: 3431(w), 3052(w), 2968(w), 2834(w), 1611(s), 1584(s), 1542(w), 1496(s), 1481(s), 1460(s), 1451(s), 1338(s), 1385(m), 1331(s), 1285(s), 1259(s), 1228(s), 1178(s), 1151(w), 1103(w), 1080(w), 1031(w), 971(w), 911(w), 870(w), 821(w), 735(s), 710(m), 571(w), 497(w), 454(w).

8.8.2.42 Preparation of $[\text{Gd}_4(\text{OH})_2(\text{L1})_4(\text{HL1})_2]\cdot 2\text{THF}$ (42**)**

A similar procedure which gave **41** was followed for the preparation of **42**, using $\text{GdCl}_3\cdot 6\text{H}_2\text{O}$. Yield is 68%. Anal. Calc. (%) for $\text{C}_{92}\text{H}_{86}\text{Gd}_4\text{N}_6\text{O}_{22}$ (found): C 48.96 (48.86); H 3.84 (3.87); N 3.72. (3.70); Selected IR data (KBr): $\nu(\text{cm}^{-1})$: 3433(w), 3052(w), 2968(w), 2834(w), 1611(s), 1584(s), 1544(w), 1496(s), 1481(s), 1460(s), 1451(s), 1338(s), 1385(m), 1331(s), 1285(s), 1259(s), 1228(s), 1178(s), 1151(w), 1103(w), 1080(w), 1031(w), 971(w), 911(w), 870(w), 821(w), 735(s), 710(m), 571(w), 498(w), 454(w).

8.8.2.43 Preparation of $[\text{Tb}_4(\text{OH})_2(\text{L1})_4(\text{HL1})_2]\cdot 2\text{THF}$ (43**):** A similar procedure which gave **41** was followed for the preparation of **43**, using $\text{TbCl}_3\cdot 6\text{H}_2\text{O}$. Yield is 66%. Anal. Calc. (%) for $\text{C}_{92}\text{H}_{86}\text{Tb}_4\text{N}_6\text{O}_{22}$ (found): C 48.81 (48.75); H 3.84 (3.86); N 3.71. (3.68); Selected IR data (KBr): $\nu(\text{cm}^{-1})$: 3431(w), 3052(w), 2968(w), 2834(w), 1611(s), 1584(s), 1542(w), 1496(s), 1481(s),

1460(s), 1451(s), 1338(s), 1385(m), 1331(s), 1285(s), 1259(s), 1228(s), 1178(s), 1151(w), 1103(w), 1080(w), 1031(w), 971(w), 911(w), 870(w), 821(w), 735(s), 710(m), 571(w), 454(w).

8.8.2.43 Preparation of $[\text{Ho}_4(\text{OH})_2(\text{L1})_4(\text{HL1})_2]\cdot 2\text{THF}$ (44**):** A similar procedure which gave **41** was followed for the preparation of **44**, using $\text{HoCl}_3\cdot 6\text{H}_2\text{O}$. Yield 65%. Anal. Calc. (%) for $\text{C}_{92}\text{H}_{86}\text{Ho}_4\text{N}_6\text{O}_{22}$ (found): C 48.30 (48.35); H 3.78 (3.75); N 3.67. (3.70). Selected IR data (KBr, v/cm^{-1}): 3432(w), 3055(w), 2968(w), 2834(w), 1611(s), 1584(s), 1542(w), 1496(s), 1482(s), 1460(s), 1451(s), 1338(s), 1385(m), 1331(s), 1285(s), 1259(s), 1228(s), 1178(s), 1151(w), 1103(w), 1080(w), 1031(w), 971(w), 911(w), 870(w), 821(w), 735(s), 710(m), 571(w), 455(w).

8.8.2.43 Preparation of $[\text{Er}_4(\text{OH})_2(\text{L1})_4(\text{HL1})_2]\cdot 2\text{THF}$ (45**):** A similar procedure which gave **41** was followed for the preparation of **45**, using $\text{ErCl}_3\cdot 6\text{H}_2\text{O}$. Yield is 70%. Anal. Calc. (%) for $\text{C}_{92}\text{H}_{86}\text{Er}_4\text{N}_6\text{O}_{22}$ (found): C 48.11 (48.05); H 3.77 (3.75); N 3.66. (3.62); Selected IR data (KBr): $\text{v}(\text{cm}^{-1})$: 3432(w), 3054(w), 2969(w), 2834(w), 1611(s), 1585(s), 1542(w), 1496(s), 1482(s), 1460(s), 1452(s), 1338(s), 1385(m), 1331(s), 1285(s), 1259(s), 1228(s), 1178(s), 1151(w), 1103(w), 1080(w), 1031(w), 971(w), 911(w), 870(w), 821(w), 735(s), 710(m), 498(w), 453(w).

8.8.2.46 Preparation of $(\text{Et}_3\text{NH})_6[\text{Er}_4(\text{HL3})_2(\text{NO}_3)_{10}(\text{H}_2\text{O})_4](\text{NO}_3)_4$ (46**):** The same procedure was employed to prepare all complexes (**46-50**) and hence synthesis of only **46** is described here in detail. Mixture of $\text{Er}(\text{NO}_3)_3\cdot 6\text{H}_2\text{O}$ (90 mg, 0.2 mmol) and $\text{H}_3\text{L3}$ (27 mg, 0.1 mmol) in 15 mL of THF was stirred for 10-15 minutes in the presence of Et_3N (0.18 mmol, 18 mg). To the resulted yellow solution, ether was diffused and after three weeks light yellow color block shaped crystals of complex **46** were isolated in 40% yield. Anal. Calc. (%) for $\text{C}_{66}\text{H}_{128}\text{Er}_4\text{N}_{24}\text{O}_{54}$ (found): C 28.40 (28.55), H 4.62 (4.72), N 12.05 (12.01). IR (KBr, cm^{-1}): 3411(b), 3136(b), 2985(w), 2940(w), 1611(m), 1579(m), 1469(s), 1389(m), 1298(s), 1218(m), 1228(m), 911(w), 819(w), 739(w), 586(w), 550(w).

8.8.2.47 Preparation of $(\text{Et}_3\text{NH})_6[\text{Gd}_4(\text{HL3})_2(\text{NO}_3)_{10}(\text{H}_2\text{O})_4](\text{NO}_3)_4$ (47**):** A similar procedure which gave **46** was followed for the preparation of **47**, using $\text{Gd}(\text{NO}_3)_3\cdot 6\text{H}_2\text{O}$. Yield is 51%. Anal. Calc. (%) for $\text{C}_{66}\text{H}_{128}\text{Gd}_4\text{N}_{24}\text{O}_{54}$ (found): C 28.81 (28.75), H 4.62 (4.63), N 12.22 (12.15). IR (KBr, cm^{-1}): 3412(b), 3136(b), 2985(w), 2942(w), 1611(m), 1580(m), 1469(s), 1389(m), 1298(s), 1218(m), 1228(m), 911(w), 819(w), 739(w), 586(w), 551(w).

8.8.2.48 Preparation of $(\text{Et}_3\text{NH})_6[\text{Tb}_4(\text{HL3})_2(\text{NO}_3)_{10}(\text{H}_2\text{O})_4](\text{NO}_3)_4$ (48**):** A similar procedure which gave **46** was followed for the preparation of **48**, using $\text{Tb}(\text{NO}_3)_3\cdot 6\text{H}_2\text{O}$. Yield is 52%. Anal. Calc. (%) for $\text{C}_{66}\text{H}_{128}\text{Tb}_4\text{N}_{24}\text{O}_{54}$ (found): C 28.74 (28.70), H 4.67 (4.65), N 12.19 (12.05).

IR (KBr, cm^{-1}): 3410(b), 3136(b), 2985(w), 2940(w), 1610(m), 1578(m), 1470(s), 1389(m), 1298(s), 1218(m), 1228(m), 911(w), 819(w), 739(w), 586(w), 552(w).

8.8.2.49 Preparation of $(\text{Et}_3\text{NH})_6[\text{Dy}_4(\text{HL3})_2(\text{NO}_3)_{10}(\text{H}_2\text{O})_4](\text{NO}_3)_4$ (49**):** A similar procedure which gave **46** was followed for the preparation of **49**, using $\text{Dy}(\text{NO}_3)_3 \cdot 6\text{H}_2\text{O}$. Yield is 45%. Anal. Calc. (%) for $\text{C}_{66}\text{H}_{128}\text{Dy}_4\text{N}_{24}\text{O}_{54}$ (found): C 28.59 (28.69), H 4.65 (4.62), N 12.12 (12.16). IR (KBr, cm^{-1}): 3411(b), 3136(b), 2986(w), 2940(w), 1611(m), 1579(m), 1469(s), 1390(m), 1298(s), 1218(m), 1228(m), 911(w), 819(w), 739(w), 586(w), 550(w).

8.8.2.50 Preparation of $(\text{Et}_3\text{NH})_6[\text{Ho}_4(\text{HL3})_2(\text{NO}_3)_{10}(\text{H}_2\text{O})_4](\text{NO}_3)_4$ (50**):** A similar procedure which gave **46** was followed for the preparation of **50**, using $\text{Ho}(\text{NO}_3)_3 \cdot 6\text{H}_2\text{O}$. Yield is 47%. Anal. Calc. (%) for $\text{C}_{66}\text{H}_{128}\text{Ho}_4\text{N}_{24}\text{O}_{54}$ (found): C 28.49 (28.45), H 4.63 (4.76), N 12.08 (12.03). IR (KBr, cm^{-1}): 3411(b), 3139(b), 2985(w), 2940(w), 1612(m), 1579(m), 1469(s), 1389(m), 1298(s), 1218(m), 1228(m), 911(w), 820(w), 739(w), 585(w), 550(w).

8.8.2.51 Preparation of $[\text{DyCu}(\text{L2})(\text{OMe})(\text{NO}_3)_2(\text{H}_2\text{O})(\text{MeOH})] \cdot 2\text{MeOH}$ (51**):** The reaction of $\text{Dy}(\text{NO}_3)_3 \cdot 6\text{H}_2\text{O}$ (45 mg, 0.1 mmol), $\text{Cu}(\text{NO}_3)_2 \cdot 2.5\text{H}_2\text{O}$ (23.2 mg, 0.1 mmol) and $\text{H}_2\text{L2}$ (10.8 mg, 0.04 mmol) in 20 mL of MeOH in the presence of base triethylamine (Et_3N) (31.2 mg, 0.312 mmol) led to the dark green solution. The slow evaporation from air produced green color needle-shaped crystals of **51** in 30% yield. Anal. Calc. (%) for $\text{C}_{17}\text{H}_{25}\text{DyCuN}_4\text{O}_{14}$ corresponding to replacement of some MeOH by H_2O leading to $[\text{DyCu}(\text{L2})(\text{OMe})(\text{NO}_3)_2(\text{H}_2\text{O})(\text{MeOH})] \cdot 2\text{H}_2\text{O}$ (found): C 27.76 (27.75), N 7.61 (7.65), H 3.42 (3.45). IR (KBr, cm^{-1}): 3400(b), 3210(b), 3053(w), 2941(w), 2848(w), 2840(w), 1611(m), 1560(w), 1492(s), 1459(m), 1438(m), 1384(s), 1295(w), 1243(m), 1223(m), 1167(w), 1102(w), 1074(w), 966(w), 922(w), 861(w), 739(m), 709(m), 635(w), 585(w), 494(w).

8.8.2.52 Preparation of $[\text{DyCu}_2(\text{L2})_2(\text{OMe})_2(\text{NO}_3)(\text{H}_2\text{O})_2] \cdot \text{H}_2\text{O} \cdot 1.5\text{MeOH}$ (52**):** The reaction of $\text{Dy}(\text{NO}_3)_3 \cdot 6\text{H}_2\text{O}$ (45 mg, 0.1 mmol), $\text{Cu}(\text{NO}_3)_2 \cdot 2.5\text{H}_2\text{O}$ (23.2 mg, 0.1 mmol) and $\text{H}_2\text{L2}$ (10.8 mg, 0.04 mmol) in 20 mL of MeOH in the presence of base triethylamine (Et_3N) (24 mg, 0.24 mmol) led to the dark green solution. The slow evaporation from air produced green color block-shaped crystals of **52** in 30% yield. Anal. Calc. (%) for $\text{C}_{32}\text{H}_{38}\text{DyCu}_2\text{N}_5\text{O}_{15}$ corresponding to replacement of some MeOH by H_2O leading to $[\text{DyCu}_2(\text{L2})_2(\text{OMe})_2(\text{NO}_3)(\text{H}_2\text{O})_2] \cdot 2\text{H}_2\text{O}$ (found): C 37.60 (37.73), N 6.85 (6.88), H 3.74 (3.80). IR (KBr, cm^{-1}): 3401(b), 3226(b), 2980(w), 2941(w), 2913(w), 2807(w), 1613(m), 1558(w), 1494(s), 1462(s), 1438(m), 1338(s), 1384(s),

1365(s), 1294(s), 1243(s), 1224(s), 1169(w), 1102(m), 1071(s), 967(w), 921 (w), 860(w), 823(w), 794(w), 782(m), 737(m), 709(m), 649(w), 633(w), 583(w), 560(w), 476(w).

8.8.2.53 Preparation of [DyCu₂(L2)₂(N₃)₃(MeOH)(H₂O)]·3MeOH·1.5H₂O (53): Mixture of Dy(NO₃)₃·6H₂O (45 mg, 0.1 mmol), Cu(NO₃)₂·2.5H₂O (23.2 mg, 0.1 mmol), NaN₃ (24 mg, 0.38 mmol) and H₂L2 (27 mg, 0.1 mmol) in 20 mL of MeOH was stirred for 15 minutes in the presence of Et₃N (0.48 mmol, 24 mg). The black green color block shaped crystals of **53** were obtained in 30% yield after one week from dark green solution from slow evaporation in air. Anal. Calc. (%) for C₃₁H₄₀DyCu₂N₁₃O₁₃ corresponding to replacement of some MeOH by H₂O leading to [DyCu₂(L2)₂(N₃)₃(MeOH)(H₂O)]·3MeOH·2H₂O (found): C 34.08 (34.13), N 16.66 (16.68), H 3.69 (3.70). IR (cm⁻¹): 3390(b), 3063(w), 2941(w), 2095(s), 2054(s), 1608(s), 1560(s), 1496(s), 1459(s), 1440(s), 1384(s), 1373(s), 1278(m), 1240(m), 1220(s), 1168(w), 1102(w), 1078(m), 1025(w), 963(w), 949(w), 924(w), 857(m), 795(w), 748(w), 734(m), 708(m), 669(w), 647(w), 565(w), 520(w), 442(w), 412(w).

8.8.2.54 Preparation of [DyCu₃(L2)₃(OMe)₃]·1.5MeOH·0.215H₂O (54): The same procedure was employed to prepare all complexes (**54-58**) and hence synthesis of only **54** is described here in detail. A mixture of Dy(NO₃)₃·6H₂O (0.1 mmol, 45 mg) and Cu(NO₃)₂·2.5H₂O (0.1 mmol, 23mg) in 20 mL MeOH was reacted with H₂L2 (0.2 mmol, 54 mg) in the presence of Et₃N (0.48 mmol, 48mg) and stirred for 5-7 minutes to get a green solution. After three weeks transparent light green color hexagonal shaped crystals of **54** suitable for X-ray crystallography were isolated in 40 % yield. Anal. Calc. (%) for C_{49.50}H_{51.43}Cu₃DyN₆O_{13.72} (found): 45.63 (45.60), H 3.98 (3.95), N 6.45 (6.47). IR (KBr, cm⁻¹): 3053(b), 3077(w), 2935(w), 2834(w), 1612(m), 1556(s), 1493(s), 1459(s), 1438(w), 1358(s) 1295(m), 1243(w), 1218(m), 1170(m) 1102(w), 1078(m), 1040(m), 1078(m), 966(m), 915(w) 780(w), 735(m), 710(w), 631(w), 569(w), 504(w).

8.8.2.55 Preparation of [TbCu₃(L2)₃(OMe)₃]·MeOH (55): A similar procedure which gave **54** was followed for the preparation of **55**, using Tb(NO₃)₃·6H₂O. Anal. Calc. (%) for C₄₉H₄₉Cu₃N₆O₁₃Tb (found): C 45.99 (45.85), H 3.86 (3.85), N 6.56 (6.65). IR (KBr, cm⁻¹): 3058(b), 3077(w), 2935(w), 2834(w), 1612(m), 1556(s), 1493(s), 1459(s), 1438(w), 1381(s), 1356(s), 1293(m), 1242(w), 1218(m), 1170(m) 1102(w), 1040(m), 967(m), 915(w), 860(w), 780(w), 734(m), 711(w), 630(w), 579(w), 506(w).

8.8.2.56 Preparation of [GdCu₃(L2)₃(OMe)₃]·MeOH (56): A similar procedure which gave **54** was followed for the preparation of **56**, using Gd(NO₃)₃·6H₂O. Anal. Calc. (%) for

$C_{49}H_{49}Cu_3N_6O_{13}Gd$ (found): C 46.05 (46.15), H 3.86 (3.84), N 6.57 (6.65). IR (KBr, cm^{-1}): 3058(b), 3077(w), 2935(w), 2834(w), 1612(m), 1556(s), 1493(s), 1459(s), 1438(w), 1381(s), 1356(s), 1293(m), 1242(w), 1218(m), 1170(m) 1102(w), 1040(m), 967(m), 915(w), 860(w), 780(w), 734(m), 711(w), 630(w), 579(w), 506(w).

8.8.2.57 Preparation of $[HoCu_3(L_2)_3(OMe)_3] \cdot 1.5MeOH \cdot 0.215H_2O$ (57): A similar procedure which gave **54** was followed for the preparation of **57**, using $Ho(NO_3)_3 \cdot 6H_2O$. Anal. Calc. (%) for $C_{49.50}H_{51.43}Cu_3HoN_6O_{13.72}$ (found): 45.54 (45.62), H 3.97 (3.95), N 6.43 (6.42). IR (KBr, cm^{-1}): 3058(b), 3077(w), 2935(w), 2834(w), 1612(m), 1556(s), 1493(s), 1459(s), 1438(w), 1381(s), 1356(s), 1293(m), 1242(w), 1218(m), 1170(m) 1102(w), 1040(m), 967(m), 915(w), 860(w), 780(w), 734(m), 711(w), 630(w), 579(w), 506(w).

8.8.2.58 Preparation of $[ErCu_3(L_2)_3(OMe)_3] \cdot 1.5MeOH \cdot 0.215H_2O$ (58): A similar procedure which gave **54** was followed for the preparation of **58**, using $Er(NO_3)_3 \cdot 6H_2O$. Anal. Calc. (%) for $C_{49.50}H_{51.43}Cu_3ErN_6O_{13.72}$ (found): 45.46 (45.51), H 3.96 (3.98), N 6.43 (6.50). IR (KBr, cm^{-1}): 3058(b), 3077(w), 2935(w), 2834(w), 1612(m), 1556(s), 1493(s), 1459(s), 1438(w), 1381(s), 1356(s), 1293(m), 1242(w), 1218(m), 1170(m) 1102(w), 1040(m), 967(m), 915(w), 860(w), 780(w), 734(m), 711(w), 630(w), 579(w), 506(w).

8.8.2.59 Preparation of $[Dy_2Cu_6(OMe)_{2.76}(N_3)_{1.24}(L_2)_6(H_2O)(MeOH)(L_4)] \cdot 10MeOH \cdot 2H_2O$ (59): Mixture of $Dy(NO_3)_3 \cdot 6H_2O$ (45 mg, 0.1 mmol), $Cu(NO_3)_2 \cdot 2.5H_2O$ (58 mg, 0.25 mmol), $H_2L-1034$ (5 mg, 0.017 mmol), NaN_3 (21 mg, 0.32 mmol) and H_2L2 (54 mg, 0.2 mmol) in 20 mL of MeOH was stirred for 10 minutes in the presence of Et_3N (0.48 mmol, 48 mg) to get a dark green solution. The plate shape dark green crystals of **59** were obtained in 25% yield after one week by slow evaporation in air. Anal. Calc. (%) for $C_{119.76}N_{17.72}H_{144.28}O_{38.76}Dy_2Cu_6$ (found): C 45.54 (45.45), H 4.60 (4.72), N 7.86 (7.75). IR (KBr, cm^{-1}): 3414(s), 3053(w), 2935(w), 2834(w), 2096(s), 2061(m), 1617(s), 1601(s), 1560(w), 1492(s), 1480(s), 1458(s), 1338(s), 1384(s), 1358(s), 1243(s), 1218(s), 1169(w), 1100(w), 1077(w), 963(w), 915(w), 924, 856(w), 780(w), 735(m), 710(m), 631(w).

8.8.2.60 Preparation of $[Dy_9Cu_2(L_2)_4(HL_2)_4(OH)_8(CO_3)_3(NO_3)_3(H_2O)_4(EtOH)](NO_3)_2 \cdot 9EtOH \cdot 6H_2O$ (60): The same procedure was employed to prepare all complexes (**60-61**) and hence synthesis of only **60** is described here in detail. A mixture of $Dy(NO_3)_3 \cdot 6H_2O$ (45 mg, 0.1 mmol) and $Cu(NO_3)_2 \cdot 2.5H_2O$ (23 mg, 0.1 mmol,) in 20 mL EtOH was reacted with H_2L2 (54 mg, 0.2 mmol) in the presence of Et_3N (48 mg, 0.48 mmol) and stirred for 20 minutes to get a

green solution. After three weeks transparent light green color hexagonal shaped crystals of **60** suitable for X-ray crystallography were isolated in 40 % yield. Anal. Calc. (%) for $C_{143}H_{188}Cu_2Dy_9N_{21}O_{76}$ (found): C 34.30 (34.47), H 3.78 (3.81), N 5.87 (5.92). IR (KBr, cm^{-1}): IR (KBr, cm^{-1}): 3400(b), 3058(w), 2834(w), 1603(m), 1561(w), 1508(m), 1493(m), 1458(m), 1438(m), 1384(s), 1297(w), 1244(w), 1220(m), 1079(w), 968(w), 901(w), 855(w), 736(m), 710(m), 635(w).

8.8.2.61 Preparation of $[Er_9Cu_2(L2)_4(HL2)_4(OH)_8(CO_3)_3(NO_3)_3(H_2O)_4(EtOH)](NO_3)_2 \cdot 9EtOH \cdot 6H_2O$ (61**):** A similar procedure which gave **60** was followed for the preparation of **61**, using $Er(NO_3)_3 \cdot 6H_2O$. Yield is 42 %. Anal. Calc. (%) for $C_{143}H_{188}Cu_2Er_9N_{21}O_{76}$ (found): C 34.01 (34.27), H 3.75 (3.82), N 5.82 (5.76). IR (KBr, cm^{-1}): IR (KBr, cm^{-1}): 3402(b), 3058(w), 2834(w), 1605(m), 1561(w), 1508(m), 1493(m), 1458(m), 1439(m), 1384(s), 1297(w), 1244(w), 1220(m), 1079(w), 968(w), 901(w), 855(w), 736(m), 710(m), 636(w).

8.8.2.62 Preparation of $[Dy_2Cu(OH)(L2)_2(HL2)_2(H_2O)]Cl \cdot 5EtOH \cdot 2.5H_2O$ (62**):** A mixture of $DyCl_3 \cdot 6H_2O$ (45 mg, 0.1 mmol) and $Cu(NO_3)_2 \cdot 2.5H_2O$ (23 mg, 0.1 mmol,) in 20 mL EtOH was reacted with H_2L2 (54 mg, 0.2 mmol) in the presence of Et_3N (48 mg, 0.48 mmol) and stirred for 20 minutes to get a green solution. After three weeks transparent light green color block shaped crystals of **62** suitable for X-ray crystallography were isolated in 40 % yield. Anal. Calc. (%) for $C_{70}H_{88}ClCuDy_2N_8O_{21.50}$ (found): C 46.46 (46.57), H 4.90 (4.95), N 6.19 (6.25). IR (KBr, cm^{-1}): IR (KBr, cm^{-1}): 3438(b), 3055(w), 2928(w), 1612(s), 1561(s), 1510(m), 1493(m), 1458(m), 1445(m), 1383(s), 1297(w), 1245(w), 1220(m), 1079(w), 968(w), 860(w), 636(w).

Chapter 9: Crystallographic data

The crystal structure data for compounds 1-62 are presented here. More detailed information can be found in the cif files on the accompanying CD.

Table 9.1. Crystallographic tables

Compound	1	2	3	4
Formula	C ₆₂ H ₅₈ Dy ₂ N ₈ Ni ₂ O ₂₀	C ₆₁ H ₆₄ N ₆ Ni ₂ O ₂₃ Dy ₂	C ₆₁ H ₆₄ N ₆ Ni ₂ O ₂₃ Y ₂	C ₆₁ H ₆₄ N ₆ Ni ₂ O ₂₃ Gd ₂
Mr	1677.58			
Cryst size[mm]	0.39×0.34×0.16			
color	Green-yellow	Green	Green	Green
Cryst Syst	Monoclinic	Monoclinic	Monoclinic	Monoclinic
Space group	<i>P</i> 2 ₁ / <i>n</i>			
T[K]	150(2)	180(2)	180(2)	180(2)
<i>a</i> [Å]	13.2070(11)	11.9733 (12)	12.0901 (11)	12.0977 (12)
<i>b</i> [Å]	12.9862(8)	24.1473 (11)	24.2572 (12)	24.2660 (11)
<i>c</i> [Å]	18.1372(16)	11.1657 (9)	11.2376 (9)	11.2336 (8)
α [deg]	90.00	90.00	90.00	90.00
β [deg]	90.210(7)	108.506 (8)	108.012 (7)	108.116 (6)
γ [deg]	90.00	90.00	90.00	90.00
<i>V</i> [Å ³]	3110.7(4)	3061.31 (45)	3084.6 (3)	3149.6 (5)
<i>Z</i>	2			
ρ_{calcd} [g cm ⁻³]	1.791			
$\mu(\text{Mo K}\alpha)$ [mm ⁻¹]	3.054			
<i>F</i> (000)	1668			
reflns collected	26103			
unique reflns	7450			
<i>R</i> _{int}	0.0479			
reflns with <i>I</i> > 2 σ (<i>I</i>)	5563			
parameters/restraints	428/0			
GOF on <i>F</i> ²	0.978			
R1 [<i>I</i> > 2 σ (<i>I</i>)]	0.0516			
wR2 (all data)	0.1281			
Larg. differ peak/hole [e Å ⁻³]	1.364/-3.042			

Compound	5	6	7	8
Formula	C ₆₁ H ₆₄ N ₆ Ni ₂ O ₂₃ Tb ₂	C ₆₁ H ₆₄ N ₆ Ni ₂ O ₂₃ Ho ₂	C ₆₁ H ₆₄ N ₆ Ni ₂ O ₂₃ Er ₂	C ₂₀₂ H ₂₅₈ Dy ₆ N ₁₂ Ni ₆ O ₇₇
Mr	1684.44			5413.46
Cryst size[mm]	0.14×0.12×0.10			0.34×0.28×0.18
color	Green	Green	Green	Red-brown
Cryst Syst	Monoclinic	Monoclinic	Monoclinic	Monoclinic
Space group	<i>P</i> 2 ₁ / <i>c</i>			<i>C</i> 2/ <i>c</i>
T[K]	180(2)	180(2)	180(2)	150(2)
<i>a</i> [Å]	12.0955 (10)	12.1015 (12)	12.0905 (15)	46.8370 (14)
<i>b</i> [Å]	24.2560 (11)	24.2665 (15)	24.2660 (17)	17.1319 (5)
<i>c</i> [Å]	11.2336 (8)	11.2236 (8)	11.2236 (10)	36.2826 (11)
α [deg]	90.00	90.00	90.00	90.00
β [deg]	107.996 (6)	107.987 (6)	108.026 (9)	125.681 (2)
γ [deg]	90.00	90.00	90.00	90.00
<i>V</i> [Å ³]	3134.6 (4)	3147.4 (3)	3114.7 (6)	23648.1 (12)
<i>Z</i>	2			4
ρ_{calcd} [g cm ⁻³]	1.785			1.521
μ (Mo K α) [mm ⁻¹]	2.906			2.420
<i>F</i> (000)	1684			10936
reflns collected	18980			87003
unique reflns	6637			23285
<i>R</i> _{int}	0.054			0.029
reflns with <i>I</i> > 2 σ (<i>I</i>)	4361			20696
parameters/restraints	420/17			1276/18
GOF on <i>F</i> ²	1.02			1.06
<i>R</i> 1 [<i>I</i> > 2 σ (<i>I</i>)]	0.063			0.044
w <i>R</i> 2 (all data)	0.158			0.119
Larg differ peak/hole [e Å ⁻³]	3.22/−1.30			1.38/−2.83

Compound	9	10	11	12
Formula	C ₂₀₂ H ₂₆₀ Sm ₆ N ₁₂ Ni ₆ O ₇₈	C ₂₀₂ H ₂₆₀ Eu ₆ N ₁₂ Ni ₆ O ₇₈	C ₂₀₄ H ₂₆₈ Gd ₆ N ₁₂ Ni ₆ O ₈₀	C ₂₀₂ H ₂₅₈ Tb ₆ N ₁₂ Ni ₆ O ₇₇
Mr		5368.24	5464.06	
Cryst size[mm]		0.24×0.22×0.18	0.27×0.18×0.07	
color	Red-brown	Red-brown	Red-brown	Red-brown
Cryst Syst	Monoclinic	Monoclinic	Monoclinic	Monoclinic
Space group		<i>C</i> 2/ <i>c</i>	<i>C</i> 2/ <i>c</i>	
T[K]	180(2)	180(2)	180(2)	200(2)
<i>a</i> [Å]	46.5736 (12)	46.5726 (9)	46.584 (2)	46.8370 (14)
<i>b</i> [Å]	17.1898 (7)	17.1899 (5)	17.1877 (10)	17.1319 (5)
<i>c</i> [Å]	36.5234 (7)	36.5134 (7)	36.6334 (17)	36.2826 (11)
α [deg]	90.00	90.00	90.00	90.00
β [deg]	126.089 (1)	126.090 (1)	126.005 (3)	125.681 (2)

γ [deg]	90.00	90.00	90.00	90.00
V [Å ³]	23642.0 (9)	23622.0 (9)	23728 (2)	23648.1 (12)
Z		4	4	
ρ_{calcd} [g cm ⁻³]		1.509	1.530	
$\mu(\text{Mo K}\alpha)$ [mm ⁻¹]		2.118	2.201	
$F(000)$		10904	11072	
reflns collected		69734	74759	
unique reflns		25028	23340	
R_{int}		0.041	0.107	
reflns with $I > 2\sigma(I)$		19052	11268	
parameters/restraints		1230/19	1270/18	
GOF on F^2		1.02	0.97	
R1 [$I > 2\sigma(I)$]		0.039	0.047	
wR2 (all data)		0.107	0.081	
Larg differ peak/hole [e Å ⁻³]		2.50/-1.96	0.84/-1.07	

Compound	13	14	15	16
Formula	C ₁₂₅ H ₁₄₈ Dy ₄ N ₁₂ Ni ₈ O ₆₉	C ₁₂₅ H ₁₄₈ Y ₄ N ₁₂ Ni ₈ O ₆₉	C ₁₂₅ H ₁₄₈ Gd ₄ N ₁₂ Ni ₈ O ₆₉	C ₁₂₅ H ₁₄₈ N ₁₂ Ni ₈ O ₆₉ Tb ₄
Mr	4042.23			4027.91
Cryst size[mm]				0.31×0.24×0.20
color	Red-brown	Red-brown	Red-brown	Red-brown
Cryst Syst	Tetragonal	Tetragonal	Tetragonal	Tetragonal
Space group	$P-42_1c$			$P-42_1c$
T[K]	180(2)	180(2)	180(2)	180(2)
a [Å]	16.8147 (9)	16.8152 (12)	16.8146 (14)	16.7087 (4)
b [Å]	16.8147 (9)	16.8152 (15)	16.8146 (14)	16.7087 (4)
c [Å]	26.0296 (19)	26.0298 (20)	26.0298 (18)	26.0082 (8)
α [deg]	90.00	90.00	90.00	90.00
β [deg]	90.00	90.00	90.00	90.00
γ [deg]	90.00	90.00	90.00	90.00
V [Å ³]	7359.5 (8)	7362.5 (8)	7365.5 (8)	7261.0 (3)
Z	2			2
ρ_{calcd} [g cm ⁻³]	1.824			1.842
$\mu(\text{Mo K}\alpha)$ [mm ⁻¹]	3.103			3.035
$F(000)$	4044			4036
reflns collected	42649			30860
unique reflns	7826			7150
R_{int}	0.042			0.088
reflns with $I > 2\sigma(I)$	7240			6442
parameters/restraints	495/16			495/16
GOF on F^2	1.06			1.04
R1 [$I > 2\sigma(I)$]	0.048			0.052
wR2 (all data)	0.125			0.140

Larg differ peak/hole [$e \text{ \AA}^{-3}$]	0.66/−2.31			1.29/−0.79
--	------------	--	--	------------

Compound	17	18	19	20
Formula	$C_{125}H_{148}Ho_4 N_{12}Ni_8O_{69}$	$C_{125}H_{148}Er_4 N_{12}Ni_8O_{69}$	$C_{64}H_{78}Dy_2N_8Ni_4O_{34}$	$C_{128}H_{156}Dy_4 N_{12}Ni_8O_{68}$
Mr			2063.18	4070.33
Cryst size[mm]			0.39×0.23×0.20	
color	Red-brown	Red-brown	Green	Green
Cryst Syst	Tetragonal	Tetragonal	Monoclinic	Monoclinic
Space group			$P2_1/n$	$C2/m$
T[K]	180(2)	180(2)	180(2)	293
a [Å]	16.8127 (9)	16.8137 (8)	23.1589(10)	22.7585 (14)
b [Å]	16.8127 (6)	16.8147 (12)	14.1171(5)	28.2558 (17)
c [Å]	26.0275 (17)	26.0286 (19)	23.7776(10)	14.9151 (9)
α [deg]	90.00	90.00	90.00	90
β [deg]	90.00	90.00	108.869(3)	123.745 (5)
γ [deg]	90.00	90.00	90.00	90
V [Å ³]	7325.5 (8)	7334.5 (8)	7356.0(5)	7975.3 (8)
Z			4	2
ρ_{calcd} [g cm^{-3}]			1.863	1.695
$\mu(\text{Mo K}\alpha)$ [mm^{-1}]			3.106	2.863
$F(000)$			4136	4080
reflns collected			58042	27484
unique reflns			15604	8622
R_{int}			0.0506	0.042
reflns with $I > 2\sigma(I)$			11074	6671
parameters/restraints			1033/24	510/39
GOF on F^2			0.987	1.01
R1 [$I > 2\sigma(I)$]			0.0392	0.044
wR2 (all data)			0.0840	0.119
Larg differ peak/hole [$e \text{ \AA}^{-3}$]			1.322/-0.755	1.12/−1.03

Compound	21	22	23	24
Formula	$C_{75.50}H_{86}Cl N_5O_{25.50}Dy_2Zn_3$	$C_{75.50}H_{86}Cl N_5O_{25.50}Eu_2Zn_3$	$C_{75.50}H_{86}Cl N_5O_{25.50}Gd_2Zn_3$	$C_{75.50}H_{86}Cl N_5O_{25.50}Tb_2Zn_3$
Mr	2028.05			
Cryst size[mm]	0.28×0.22×0.13			
color	Yellow	Yellow	Yellow	Yellow
Cryst Syst	Monoclinic	Monoclinic	Monoclinic	Monoclinic
Space group	$P2_1/c$			
T[K]	150(2)	180(2)	180(2)	180(2)
a [Å]	16.9239(15)	16.9345(7)	16.9339(15)	16.9342(15)

b [Å]	25.395(2)	25.397(12)	25.375(12)	25.397(2)
c [Å]	20.8324(16)	20.8424(16)	20.8324(13)	20.8524(17)
α [deg]	90.00	90.00	90.00	90.00
β [deg]	109.339(6)	109.365(7)	109.343(5)	109.349(6)
γ [deg]	90.00	90.00	90.00	90.00
V [Å ³]	8448.4(13)	8547.6(15)	8518.5(10)	8438.4(16)
Z	4			
ρ_{calcd} [g cm ⁻³]	1.594			
$\mu(\text{Mo K}\alpha)$ [mm ⁻¹]	2.694			
$F(000)$	4068			
reflns collected	36775			
unique reflns	12098			
R_{int}	0.0749			
reflns with $I > 2\sigma(I)$	7844			
parameters/restraints	1009/9			
GOF on F^2	0.984			
$R1$ [$I > 2\sigma(I)$]	0.0602			
w $R2$ (all data)	0.1596			
Larg differ peak/hole [e Å ⁻³]	0.972/-1.809			

Compound	25	26	27	28
Formula	C _{75.50} H ₈₆ Cl N ₅ O _{25.50} Ho ₂ Zn ₃	C ₁₁₂ H ₁₇₀ Cl ₉ Dy ₇ N ₈ O ₆₇ Zn ₄	C ₁₅₄ H ₁₉₆ Cd ₆ Cl ₆ Dy ₆ N ₈ O ₅₆	C ₁₅₄ H ₁₉₆ Cd ₆ Cl ₆ Tb ₆ N ₈ O ₅₆
Mr		4418.59	4917.29	
Cryst size[mm]				
color	Yellow	Yellow	Yellow	Yellow
Cryst Syst	Monoclinic	Monoclinic	Monoclinic	Monoclinic
Space group		$C2/c$	$C2/m$	
T[K]	180(2)	100(2)	180(2)	180(2)
a [Å]	16.9229(5)	35.514 (4)	17.7884 (13)	17.7873 (17)
b [Å]	25.397(22)	16.183 (2)	33.2608 (19)	33.2612 (29)
c [Å]	20.8314(14)	28.373 (3)	16.4158 (10)	16.4148 (12)
α [deg]	90.00	90.00	90.00	90.00
β [deg]	109.319(16)	113.582	119.517 (5)	119.527 (15)
γ [deg]	90.00	90.00	90.00	90.00
V [Å ³]	8418.14(13)	14945 (3)	8451.9 (9)	8443.12 (14)
Z		4	2	
ρ_{calcd} [g cm ⁻³]		1.964	1.932	
$\mu(\text{Mo K}\alpha)$ [mm ⁻¹]		4.338	3.536	
$F(000)$		8676	4820	
reflns collected		22462	23993	
unique reflns		13193	8173	
R_{int}		0.090	0.072	

reflns with $I > 2\sigma(I)$		6357	5408	
parameters/restraints		801/12	402/3	
GOF on F^2		0.93	0.97	
R1 [$I > 2\sigma(I)$]		0.064	0.052	
wR2 (all data)		0.145	0.135	
Larg differ peak/hole [$e \text{ \AA}^{-3}$]		2.82/-1.55	1.33/-1.31	

Compound	29	30	31	32
Formula	$C_{154}H_{196}Cd_6Cl_6Ho_6N_8O_{56}$	$C_{154}H_{196}Cd_6Cl_6Er_6N_8O_{56}$	$C_{75}H_{79}Cu_2Dy_3N_6O_{26}$	$C_{75}H_{79}Cu_2Gd_3N_6O_{26}$
Mr			2095.02	
Cryst size[mm]			0.23×0.21×0.07	
color	Yellow	Yellow	Green-yellow	Green-yellow
Cryst Syst	Monoclinic	Monoclinic	Triclinic	Triclinic
Space group			$P-1$	
T[K]	180(2)	180(2)	100(2)	100(2)
a [Å]	17.7785 (12)	17.7865 (13)	12.8166(5)	12.8336(5)
b [Å]	33.2518 (19)	33.2618 (22)	14.0128(5)	14.0128(7)
c [Å]	16.4158 (12)	16.4158 (11)	21.8116(8)	21.8216(9)
α [deg]	90.00	90.00	92.059(1)	92.119(12)
β [deg]	119.527 (15)	119.537 (5)	94.409(1)	94.478(15)
γ [deg]	90.00	90.00	93.407(1)	93.407(1)
V [Å ³]	8391.8 (12)	8431.8 (9)	3895.6(3)	3935.7(5)
Z			2	2
ρ_{calcd} [g cm ⁻³]			1.786	
μ (Mo K α) [mm ⁻¹]			3.462	
$F(000)$			2070	
reflns collected			24938	
unique reflns			16679	
R_{int}			0.0141	
reflns with $I > 2\sigma(I)$			15464	
parameters/restraints			1038/9	
GOF on F^2			1.018	
R1 [$I > 2\sigma(I)$]			0.0240	
wR2 (all data)			0.0615	
Larg differ peak/hole [$e \text{ \AA}^{-3}$]			2.776/-1.118	

Compound	33	34	35	36
Formula	$C_{75}H_{81}Cu_2N_6O_{27}Tb_3$	$C_{75}H_{79}Cu_2Ho_3N_6O_{26}$	$C_{80}H_{92}Co_2Dy_2N_6O_{24}$	$C_{80}H_{92}Co_2N_6O_{24}Y_2$

Mr	2102.30		1964.46	1817.28
Cryst size[mm]			0.27×0.22×0.18	0.25×0.24×0.20
color	Green	Green	Red	Red
Cryst Syst	Triclinic	Triclinic	Triclinic	Triclinic
Space group	<i>P</i> -1		<i>P</i> -1	<i>P</i> -1
T[K]	180(2)	100(2)	150(2)	180(2)
<i>a</i> [Å]	12.8865 (6)	12.8122(9)	11.7308 (9)	11.7437 (12)
<i>b</i> [Å]	13.9703 (7)	14.0127(5)	13.2206 (11)	13.2227 (13)
<i>c</i> [Å]	21.9713 (9)	21.8017(8)	14.9021 (12)	14.9685 (14)
α [deg]	92.526 (3)	92.059(13)	109.024 (6)	109.568 (7)
β [deg]	94.680 (3)	94.409(16)	93.391 (6)	93.149 (8)
γ [deg]	93.081 (4)	93.437(17)	113.742 (6)	113.694 (7)
<i>V</i> [Å ³]	3931.9 (3)	3876.6(5)	1951.0 (3)	1956.5 (3)
<i>Z</i>	2		1	1
ρ_{calcd} [g cm ⁻³]	1.776		1.672	1.542
$\mu(\text{Mo K}\alpha)$ [mm ⁻¹]	3.279		2.393	1.968
<i>F</i> (000)	2084		992	938
reflns collected	26789		16703	13449
unique reflns	16609		9316	8261
<i>R</i> _{int}	0.039		0.026	0.021
reflns with <i>I</i> > 2 σ (<i>I</i>)	14607		8192	7037
parameters/restraints	1047/9		510/68	510/68
GOF on <i>F</i> ²	1.04		1.00	1.01
<i>R</i> 1 [<i>I</i> > 2 σ (<i>I</i>)]	0.043		0.041	0.038
w <i>R</i> 2 (all data)	0.114		0.106	0.101
Larg differ peak/hole [e Å ⁻³]	1.87/−2.09		0.86/−2.46	0.74/−0.55

Compound	37	38	39	40
Formula	C ₈₀ H ₉₂ Co ₂ Gd ₂ N ₆ O ₂₄	C ₈₀ H ₉₂ Co ₂ N ₆ O ₂₄ Tb ₂	C ₈₀ H ₉₂ Co ₂ Ho ₂ N ₆ O ₂₄	C ₈₀ H ₉₂ Co ₂ N ₆ O ₂₄ Er ₂
color	Red	Red	Red	Red
Cryst Syst	Triclinic	Triclinic	Triclinic	Triclinic
T[K]	150(2)	150(2)	150(2)	180(2)
<i>a</i> [Å]	11.7328 (9)	11.8539 (6)	11.8328 (3)	11.7416 (9)
<i>b</i> [Å]	13.2216 (12)	13.3457 (8)	13.3371 (6)	13.2282 (15)
<i>c</i> [Å]	14.9011 (11)	15.0886 (5)	15.0682 (9)	14.9271 (17)
α [deg]	109.074 (10)	109.030 (7)	108.894 (3)	109.547 (12)
β [deg]	93.395 (9)	93.570 (7)	93.483 (5)	92.983 (14)
γ [deg]	113.784 (6)	113.940 (6)	113.701 (8)	113.822 (11)
<i>V</i> [Å ³]	1991.0 (8)	2009.4 (6)	2009.5 (4)	1951.5 (6)

Compound	41	42	43	44	45
Formula	C ₉₂ H ₈₆ Dy ₄ N ₆ O ₂	C ₉₂ H ₈₆ Gd ₄ N ₆	C ₉₂ H ₈₆ Tb ₄ N ₆	C ₉₂ H ₈₆ Ho ₄ N	C ₉₂ H ₈₆ Er ₄ N ₆

	2	O ₂₂	O ₂₂	6O ₂₂	O ₂₂
Mr	2277.67				
Cryst size[mm]	0.12×0.10×0.08				
color	orange	orange	orange	orange	orange
Cryst Syst	Triclinic	Triclinic	Triclinic	Triclinic	Triclinic
Space group	<i>P</i> -1				
T[K]	180(2)	180(2)	180(2)	180(2)	180(2)
<i>a</i> [Å]	13.0093(11)	13.1475(8)	13.1113(8)	13.1120(10)	13.0986(8)
<i>b</i> [Å]	13.5557(11)	13.6900(10)	13.6840(12)	13.6936(13)	13.6746(10)
<i>c</i> [Å]	14.3725(13)	14.6015(11)	14.5697(12)	14.4541(11)	14.4370(11)
α [deg]	96.756(7)	96.666(6)	96.802(5)	96.845(4)	96.993(3)
β [deg]	110.049(7)	109.975(5)	109.985(4)	109.851(7)	109.809(3)
γ [deg]	114.407(6)	115.216(7)	114.867(4)	114.431(6)	114.271(5)
<i>V</i> [Å ³]	2066.2(3)	2126.2(2)	2120.9(2)	2117.9(3)	2112.7(4)
<i>Z</i>	1				
ρ_{calcd} [g cm ⁻³]	1.830				
μ (Mo K α) [mm ⁻¹]	3.795				
<i>F</i> (000)	1120				
reflns collected	15031				
unique reflns	8755				
<i>R</i> _{int}	0.0557				
reflns with <i>I</i> > 2 σ (<i>I</i>)	5575				
parameters/rest raints	577/5				
GOF on <i>F</i> ²	0.953				
R1 [<i>I</i> > 2 σ (<i>I</i>)]	0.0440				
wR2 (all data)	0.0823				
Larg differ peak/hole [e Å ⁻³]	0.886 /-1.205				

Compound	46	47	48	49	50
Formula	C ₆₆ H ₁₂₈ Er ₄ N ₂₄ O ₅₄	C ₆₆ H ₁₂₈ Gd ₄ N ₂₄ O ₅₄	C ₆₆ H ₁₂₈ Tb ₄ N ₂₄ O ₅₄	C ₆₆ H ₁₂₈ Dy ₄ N ₂₄ O ₅₄	C ₆₆ H ₁₂₈ Ho ₄ N ₂₄ O ₅₄
Mr	2790.96				
Cryst size[mm]	0.25×0.20×0.18				
color	Light yellow				
Cryst Syst	Triclinic	Triclinic	Triclinic	Triclinic	Triclinic
Space group	<i>P</i> -1				
T[K]	180(2)	180(2)	180(2)	180(2)	180(2)
<i>a</i> [Å]	12.8509(9)	12.8512(10)	12.8510(9)	12.8517(12)	12.8507(15)

b [Å]	13.0018(8)	13.0228(7)	13.0213(8)	13.0115(10)	13.0118(9)
c [Å]	16.1176(10)	16.1266(10)	16.1186(10)	16.1276(10)	16.1178(10)
α [deg]	93.847(5)	93.858(5)	93.867(5)	93.857(5)	93.859(5)
β [deg]	97.744(5)	97.745(12)	97.748(5)	97.749(6)	97.744(15)
γ [deg]	93.094(5)	93.124(7)	93.098(12)	93.088(6)	93.084(5)
V [Å ³]	2657.0(3)	2688.0(4)	2638.0(6)	2647.0(5)	2627.0(7)
Z	1				
ρ_{calcd} [g cm ⁻³]	1.744				
$\mu(\text{Mo K}\alpha)$ [mm ⁻¹]	3.232				
$F(000)$	1396				
reflns collected	18432				
unique reflns	11203				
R_{int}	0.0505				
reflns with $I > 2\sigma(I)$	8932				
parameters/restraints	675/46				
GOF on F^2	1.008				
$R1 [I > 2\sigma(I)]$	0.0479				
wR2 (all data)	0.1268				
Larg differ peak/hole [e Å ⁻³]	3.64/-1.64				

Compound	51	52	53	54
Formula	C ₁₉ H ₂₉ Cu DyN ₄ O ₁₄	C _{33.50} H ₄₂ Cu ₂ DyN ₅ O _{15.50}	C ₃₄ H ₄₅ Cu ₂ DyN ₁₃ O _{12.50}	C _{49.50} H _{51.43} Cu ₃ DyN ₆ O _{13.72}
Mr	763.50	1052.30	1125.41	1302.96
Cryst size[mm]		0.14 × 0.13 × 0.10	0.18 × 0.18 × 0.08	
color	Green	Green	Black-green	Green
Cryst Syst	Orthorhombic	Monoclinic	Triclinic	Triclinic
Space group	<i>Pbca</i>	<i>P2₁/n</i>	<i>P-1</i>	<i>P-1</i>
T[K]	293(2)	180(2)	180(2)	180(2)
a [Å]	10.8585 (8)	10.2499 (4)	13.5827 (8)	7.5743 (4)
b [Å]	19.4579 (15)	21.5702 (10)	13.8011 (9)	15.5298 (7)
c [Å]	25.2776 (19)	17.7446 (6)	15.2897 (10)	45.5572 (19)
α [deg]	90.00	90.00	103.033 (5)	86.135 (4)
β [deg]	90.00	97.761 (3)	112.976 (5)	89.988 (4)
γ [deg]	90.00	90.00	101.938 (5)	75.885 (4)
V [Å ³]	5340.7 (7)	3887.3 (3)	2427.9 (3)	5184.4 (4)
Z	8	4	2	4
ρ_{calcd} [g cm ⁻³]	1.899	1.798	1.539	1.669
$\mu(\text{Mo K}\alpha)$ [mm ⁻¹]	3.65	3.06	2.46	2.71
$F(000)$	3024	2104	1128	2613

reflns collected	36390	25456	16435	30703
unique reflns	5671	8219	10201	20005
R_{int}	0.070	0.034	0.019	0.039
reflns with $I > 2\sigma(I)$	5052	7661	9482	14951
parameters/restraints	365/4	529/8	564/17	1257/92
GOF on F^2	1.04	1.07	1.04	1.07
R1 [$I > 2\sigma(I)$]	0.052	0.036	0.035	0.074
wR2 (all data)	0.139	0.105	0.102	0.191
Larg differ peak/hole [$e \text{ \AA}^{-3}$]	2.83/-1.75	1.93/-1.03	1.46/-0.82	0.83/-2.24

Compound	55	56	57	58
Formula	C ₄₉ H ₄₉ Cu ₃ Tb N ₆ O ₁₃	C ₄₉ H ₄₉ Cu ₃ Gd N ₆ O ₁₃	C _{49.50} H _{51.43} Cu ₃ HoN ₆ O _{13.72}	C _{49.50} H _{51.43} Cu ₃ ErN ₆ O _{13.72}
Mr	1279.48			
Cryst size[mm]	0.38×0.12×0.10			
color	Green	Green	Black-green	Green
Cryst Syst	Monoclinic	Monoclinic	Triclinic	Triclinic
Space group	P2 ₁ /n			
T[K]	150(2)	180(2)	150(2)	100(2)
<i>a</i> [Å]	18.2690(12)	18.2685(10)	7.5552(5)	7.4927(9)
<i>b</i> [Å]	13.2129(7)	13.2132(17)	15.5281(12)	15.3983(19)
<i>c</i> [Å]	20.9321(16)	20.9422(12)	45.604(3)	45.223(5)
α [deg]	90.00	90.00	87.069(6)	86.832(2)
β [deg]	106.194(6)	106.195(5)	89.983(6)	89.888(2)
γ [deg]	90.00	90.00	75.944(6)	75.942(1)
<i>V</i> [Å ³]	4852.2(6)	4882.2(6)	5182.8(7)	5053.2(11)
<i>Z</i>	4			
ρ_{calcd} [g cm ⁻³]	1.751			
$\mu(\text{Mo K}\alpha)$ [mm ⁻¹]	2.809			
<i>F</i> (000)	2564			
reflns collected	27570			
unique reflns	9475			
R_{int}	0.0620			
reflns with $I > 2\sigma(I)$	7882			
parameters/restraints	669/4			
GOF on F^2	1.007			
R1 [$I > 2\sigma(I)$]	0.0573			
wR2 (all data)	0.1503			
Larg differ peak/hole [$e \text{ \AA}^{-3}$]	1.576/-2.803			

Compound	59	60	61	62
Formula	C _{119.76} H _{144.28} Cu ₆ Dy ₂ N _{17.72} O _{38.76}	C ₁₄₃ H ₁₈₈ Cu ₂ Dy ₉ N ₂₁ O ₇₆	C ₁₄₃ H ₁₈₈ Cu ₂ Er ₉ N ₂₁ O ₇₆	C ₇₀ H ₈₈ ClCu Dy ₂ N ₈ O _{21.50}
Mr	3158.41	5006.72		1809.47
Cryst size[mm]	0.18×0.09×0.03			0.23×0.21×0.12
color	Green	Green	Green	Green
Cryst Syst	Triclinic	Monoclinic	Monoclinic	Triclinic
Space group	<i>P</i> -1	<i>C</i> 2/ <i>c</i>		<i>P</i> -1
T[K]	100(2)	180(2)	180(2)	180(2)
<i>a</i> [Å]	13.8461 (18)	71.6587 (19)	71.5423 (44)	14.4155 (8)
<i>b</i> [Å]	14.5000 (19)	16.1332 (3)	16.0801 (10)	15.9560 (9)
<i>c</i> [Å]	18.406 (2)	34.8077 (9)	34.5991 (24)	18.0980 (11)
<i>α</i> [deg]	71.793 (2)	90.00	90.00	68.014 (4)
<i>β</i> [deg]	68.185 (2)	117.714 (2)	117.688 (4)	74.521 (5)
<i>γ</i> [deg]	82.770 (2)	90.00	90.00	87.975 (4)
<i>V</i> [Å ³]	3258.8 (7)	35624.2 (15)	35245.2 (25)	3710.3 (4)
<i>Z</i>	1	8		2
ρ_{calcd} [g cm ⁻³]	1.609	1.867		1.620
μ (Mo K α) [mm ⁻¹]	2.177	4.056		2.392
<i>F</i> (000)	1603	19624		1828
reflns collected	18522	141236		24053
unique reflns	13673	37784		14872
<i>R</i> _{int}	0.072	0.046		0.052
reflns with <i>I</i> > 2 σ (<i>I</i>)	10212	31130		12624
parameters/restraints	786/2	2247/300		877/49
GOF on <i>F</i> ²	0.198	1.13		1.01
R1 [<i>I</i> > 2 σ (<i>I</i>)]	0.080	0.056		0.068
wR2 (all data)	0.198	0.157		0.207
Larg differ peak/hole [e Å ⁻³]	2.50/ -1.55	2.62/ -1.69		5.96/ -2.32

Chapter 10

Bibliography

1. G. L. Verschuur, *Hidden attraction, The Mystery and History of Magnetism*. Oxford University Press, Oxford. **1993**.
2. A. H. Murrish, In *The physical principles of Magnetism*. Jhon Wiley and Sons, New York **1980**.
3. T. Lis, *Acta Cryts.* **1980**, *B36*, 2042.
4. A. Caneshi, D. Gatteschi, R. Sessoli, A. L. Barra, L. C. Brunel, M. Guillot, *J. Am. Chem. Soc.* **1991**, *113*, 5873.
5. R. Sessoli, H.-L. Tsai, A. R. Schake, S. Wang, J. B. Vincent, K. Folting, D. Gatteschi, G. Christou, D. N. Hendrickson, *J. Am. Chem. Soc.* **1993**, *115*, 1804.
6. (a) L. Thomas, F. Lioni, R. Ballou, D. Gatteschi, R. Sessoli, B. Barabara. *Nature* **1996**, *383*, 145. (b) J. R. Friedman, M. P. Sarachik, J. Tejada, R. Ziolo, *Phys. Rev. Lett.* **1996**, *76*, 3830.
7. E. K. Brechin, *Chem. Commun.* **2005**, 5141.
8. (a) D. Gatteschi, R. Sessoli, *Angew. Chem. Int. Ed.* **2003**, *42*, 268. (b) W. Wernsdorfer, R. Sessoli, *Science*, **1999**, *284*, 133.
9. M. N. Leuenberger, D. Loss, *Nature* **2001**, *410*, 789.
10. N. Ishikawa, T. Iino, Y. Kaizu, *J. Am. Chem. Soc.* **2002**, *124*, 11440.
11. (a) F. E. Mabbs, D. J. Machin, *Magnetism and Transition Metal Complexes*, Chapman and Hall, **1973**. (b) C. J. O'Connor, *Prog. Inorg. Chem.* **1982**, *29*, 203. (c) R. L. Carlin, *Magnetochemistry*, Springer-Verlag, **1986**. (d) O. Khan, *Molecular Magnetism*, VCH Publ. Inc. **1993**.
12. (a) D. MasPOCH, D. Ruiz-Molina, J. Veciana, *Chem. Soc. Rev.* **2007**, *36*, 770. (b) M. Kurmoo, *Chem. Soc. Rev.* **2009**, *38*, 1353.
13. C. G. Shull, W. A. Stranser and E. O. Wollan, *Phys. Rev.* **1951**, *83*, 333.
14. X.-N. Cheng, W.-X. Zhang, and X.-M. Chen, *J. Am. Chem. Soc.* **2007**, *129*, 15738.
15. X.-Y. Wang, L. Wang, Z.-M. Wang, G. Su, S. Gao, *Chem. Mater.* **2005**, *17*, 6369.
16. F. Palacio, *Introduction to Physical Techniques in Molecular Magnetism*, University of Zaragoza, Zaragoza, **1999**.

17. D. Gatteschi, R. Sessoli, J. Villain, *Molecular Nanomagnets*; Oxford University Press: New York, **2006** and references therein.
18. A.-L. Barra, A. Caneschi, A. Cornia, D. Gatteschi, L. Gorini, L.-P. Heiniger, R. Sessoli, L. Sorace, *J. Am. Chem. Soc.* **2007**, *129*, 10754.
19. G. Aromí, E. K. Brechin, *Struct. Bonding*, **2006**, *122*, 1 and references therein.
20. M. Murrie, H. Stoeckli-Evans, H. U. Güdel, *Angew. Chem. Int. Ed.* **2001**, *40*, 1957.
21. M. Murrie, *Chem. Soc. Rev.* **2010**, *39*, 1986 and references herein.
22. (a) A. K. Boudalis, Y. Sanakis, J. M. Clemente-Juan, B. Donnadieu, V. Nastopoulos, A. Mari, Y. Coppel, J.-P. Tuchagues, S. P. Perlepes, *Chem. Eur. J.* **2008**, *14*, 2514. (b) D. E. Freedman, W. H. Harman, T. D. Harris, G. J. Long, C. J. Chang, J. R. Long, *J. Am. Chem. Soc.* **2010**, *132*, 1224.
23. (a) C. Sangregorio, T. Ohm, C. Paulsen, R. Sessoli, D. Gatteschi, *Phys. Rev. Lett.* **1997**, *78*, 4645. (b) A. M. Ako, V. Mereacre, Y. Lan, W. Wernsdorfer, R. Clérac, C. E. Anson, A. K. Powell, *Inorg. Chem.* **2010**, *49*, 1.
24. A. M. Ako, V. Mereacre, I. J. Hewitt, R. Clérac, L. Lecren, C. E. Anson, A. K. Powell, *J. Mater. Chem.* **2006**, *16*, 2579.
25. S. Piligkos, G. Rajaraman, M. Soler, N. Kirchner, J. V. Slageren, R. Bircher, S. Parsons, H.-U. Güdel, J. Kortus, W. Wernsdorfer, G. Christou, E. K. Brechin, *J. Am. Chem. Soc.* **2005**, *127*, 5572.
26. S. L. Castro, Z. Sun, C. M. Grant, J. C. Bollinger, D. N. Hendrichson, G. Christou, *J. Am. Chem. Soc.* **1998**, *120*, 2365.
27. Y. Zhang, U. M. Mallik, N. Rath, G. T. Yee, R. Clérac, S. M. Holmes, *Chem. Commun.* **2010**, *46*, 4953.
28. C. J. Milios, A. Vinslava, W. Wernsdorfer, S. Moggach, S. Parsons, S. P. Perlepes, G. Christou, E. K. Brechin, *J. Am. Chem. Soc.* **2007**, *129*, 2754.
29. A. Cornia, D. Gatteschi and R. Sessoli, *Coord. Chem. Rev.* **2001**, *219-221*, 573.
30. M. U. Anwar, Y. Lan, L. M. C. Beltran, R. Clérac, S. Pfirrmann, C. E. Anson, A. K. Powell, *Inorg. Chem.* **2009**, *48*, 5177.
31. H. J. Eppley, H. L. Tsai, N. Devries, K. Folting, G. Christou, D. N. Hendrickson, *J. Am. Chem. Soc.* **1995**, *117*, 301.

32. T. Kuroda-Sowa, M. Lam, A. L. Rheingold, C. Frommen, W. M. Reiff, M. Nakano, J. Yoo, A. L. Maniero, L. C. Brunel, G. Christou, D. N. Hendrickson, *Inorg. Chem.* **2001**, *40*, 6469.
33. R. Boča, *Coord. Chem. Rev.* **2004**, *248*, 757.
34. N. Ishikawa, T. Iino, Y. Kaizu, *J. Phys. Chem.* **2002**, *106*, 9543.
35. (a) N. Ishikawa, M. Sugita, T. Ishikawa, S. Koshihara, Y. Kaizu, *J. Am. Chem. Soc.* **2003**, *125*, 8694. (b) N. Ishikawa, M. Sugita, T. Ishikawa, S. Koshihara, Y. Kaizu, *J. Phys. Chem. B.* **2004**, *108*, 11265.
36. (a) Y. Gao, G.-F. Xu, L. Zhao, J. Tang, Z. Liu, *Inorg. Chem.* **2009**, *48*, 11495. (b) Y.-Z. Zheng, Y. Lan, C. E. Anson, A. K. Powell, *Inorg. Chem.* **2008**, *47*, 10813. (c) P.-H. Lin, T. J. Burchell, L. Ungur, L. F. Chibotaru, W. Wernsdorfer, M. Murugesu, *Angew. Chem. Int. Ed.* **2009**, *48*, 9489. (d) G. Abbas, Y. Lan, G. E. Kostakis, W. Wernsdorfer, C. E. Anson, A. K. Powell, *Inorg. Chem.* **2010**, *49*, 8067 and references herein.
37. (a) S.-S. Bao, L.-F. Ma, Y. Wang, L. Fang, C.-J. Zhu, Y.-Z. Li, L.-M. Zheng, *Chem. Eur. J.* **2007**, *13*, 2333. (b) P.-H. Lin, T. J. Burchell, R. Clérac, M. Murugesu, *Angew. Chem., Int. Ed.* **2008**, *47*, 8848. (c) G.-F. Xu, Q.-L. Wang, P. Gamez, Y. Ma, R. Clérac, J. Tang, S.-P. Yan, P. Cheng, D.-Z. Liao, *Chem. Commun.* **2010**, *46*, 1506.
38. (a) J. Tang, I. Hewitt, T. N. Madhu, G. Chastanet, W. Wernsdorfer, C. E. Anson, C. Benelli, R. Sessoli, A. K. Powell, *Angew. Chem. Int. Ed.* **2006**, *45*, 1729. (b) J. Luzon, K. Bernot, I. J. Hewitt, C. E. Anson, A. K. Powell, R. Sessoli, *Phys. Rev. Lett.* **2008**, *100*, 247205. (c) L. F. Chibotaru, L. Ungur, A. Soncini, *Angew. Chem. Int. Ed.* **2008**, *47*, 4126. (d) I. Hewitt, Y. Lan, C. E. Anson, J. Luzon, R. Sessoli, A. K. Powell, *Chem. Commun.* **2009**, 6765.
39. (a) H. Ke, G.-F. Xu, Y.-N. Guo, P. Gamez, C. M. Beavers, S. J. Teat, J. Tang, *Chem. Commun.* **2010**, *46*, 6057. (b) M. T. Gamer, Y. Lan, P. W. Roesky, A. K. Powell, R. Clérac, *Inorg. Chem.* **2008**, *47*, 6581.
40. B. Hussain, D. Savard, T. J. Burchell, W. Wernsdorfer, M. Murugesu, *Chem. Commun.* **2009**, 1100.
41. I. Hewitt, J. Tang, T. N. Madhu, C. E. Anson, Y. Lan, J. Luzon, M. Etienne, R. Sessoli, A. K. Powell, *Angew. Chem., Int. Ed.* **2010**, *49*, 6352.

42. T. Kajiwara, M. Nakano, Y. Kaneko, S. Takaishi, T. Ito, M. Yamashita, A. Igashira-Kamiyama, H. Nojiri, Y. Ono, Y. Kojima, *J. Am. Chem. Soc.* **2005**, *127*, 10150.
43. C. Benelli, D. Gatteschi, *Chem. Rev.* **2002**, *102*, 2369 and references herein.
44. (a) S. Osa, T. Kido, N. Matsumoto, N. Re, A. Pochaba, J. Mrozinski, *J. Am. Chem. Soc.* **2004**, *126*, 420. (b) F. Mori, T. Nyui, T. Ishida, T. Nogami, K.-Y. Choi, H. Nojiri, *J. Am. Chem. Soc.* **2006**, *128*, 1440. (c) J.-P. Costes, W. Wernsdorfer, *Inorg. Chem.* **2006**, *45*, 5. (d) J.-P. Costes, F. Dahan, M. Auchel, F. Dahan, V. Peyrou, S. Shova, W. Wernsdorfer, *Inorg. Chem.* **2006**, *45*, 1924. (e) T. Hamamatsu, T. Kido, K. Yabe, M. Towatari, S. Osa, N. Matsumoto, N. Re, A. Pochaba, J. Mrozinski, J.-L. Gallani, A. Barla, P. Imperia, C. Paulsen, J.-P. Kappler, *Inorg. Chem.* **2007**, *46*, 4458. (f) T. Hamamatsu, K. Yabe, M. Towatari, N. Matsumoto, N. Re, A. Pochaba, J. Mrozinski, *Bull. Chem. Soc. Jpn.* **2007**, *80*, 523. (g) T. Kajiwara, M. Nakano, S. Takaishi, M. Yamashita, *Inorg. Chem.* **2008**, *47*, 8604. (h) T. Kajiwara, K. Takahashi, T. Hiraizumi, S. Takaishi, M. Yamashita, *CrystEngComm.* **2009**, *11*, 2110. (i) G. Novitchi, W. Wernsdorfer, L. F. Chibotaru, J.-P. Costes, C. E. Anson, A. K. Powell, *Angew. Chem. Int. Ed.* **2009**, *48*, 1614. (j) C. Aronica, G. Pilet, G. Chastanet, W. Wernsdorfer, J.-F. Jacquot, D. Luneau, *Angew. Chem. Int. Ed.* **2006**, *45*, 4659.
45. (a) J.-P. Costes, F. Dahan, A. Dupuis, J.-P. Laurent, *Chem. Eur. J.* **1998**, *4*, 1616. (b) Z. Xu, P. W. Read, D. E. Hibbs, M. B. Hursthouse, K. M. A. Malik, B. O. Patrick, S. J. Rettig, M. Seid, D. A. Summers, M. Pink, R. C. Thompson, C. Orvig, *Inorg. Chem.* **2000**, *39*, 508. (c) J.-J. Zhang, S.-M. Hu, L.-M. Zheng, X.-T. Wu, Z.-Y. Fu, J.-C. Dai, W.-X. Du, H.-H. Zhang, R.-Q. Sun, *Chem. Eur. J.* **2002**, *8*, 5742. (d) S. R. Bayly, Z. Xu, B. O. Patrick, S. J. Rettig, M. Pink, R. C. Thompson, C. Orvig, *Inorg. Chem.* **2003**, *42*, 1576. (e) F. Mori, T. Ishida, T. Nogami, *Polyhedron*, **2005**, *24*, 2588. (f) A. M. Madalan, K. Bernot, F. Pointillart, M. Andruh, A. Caneschi, *Eur. J. Inorg. Chem.* **2007**, 5533. (g) T. Shiga, N. Ito, A. Hidaka, H. Ōhkawa, S. Kitagawa, M. Ohba, *Inorg. Chem.* **2007**, *46*, 3492. (h) X.-J. Kong, Y.-P. Ren, L.-S. Long, Z. Zheng, G. Nichol, R.-B. Huang, L.-S. Zheng, *Inorg. Chem.* **2008**, *47*, 2728. (i) T. Yamaguchi, Y. Sunatsuki, H. Ishida, M. Kojima, H. Akashi, N. Re, N. Matsumoto, A. Pochaba, J. Mroziński, *Inorg. Chem.* **2008**, *47*, 5736. (j) J.-P. Costes, T. Yamaguchi, M. Kojima, L. Vendier, *Inorg. Chem.* **2009**, *48*, 5555. (k) S. Igarashi, S.-i. Kawaguchi, Y. Yukawa, F. Tuna, R. E. P. Winpenny, *Dalton*

- Trans.*, **2009**, 3140. (l) C. Papatriantafyllopoulou, T. C. Stamatatos, C. G. Efthymiou, L. Cunha-Silva, F. A. A. Paz, S. P. Perlepes, G. Christou, *Inorg. Chem.* **2010**, *49*, 9743.
46. (a) E. Pointillart, K. Bernot, R. Sessoli, D. Gatteschi, *Chem. Eur. J.* **2007**, *13*, 1602. (b) V. Chandrasekhar, B. M. Pandian, R. Boomishankar, A. Steiner, J. J. Vittal, A. Hourri, R. Clérac, *Inorg. Chem.* **2008**, *47*, 4918. (c) J.-P. Sutter, S. Dhers, R. Rajamani, S. Ramasesha, J.-P. Costes, C. Duhayon, L. Vendier, *Inorg. Chem.* **2009**, *48*, 5820. (d) C. G. Efthymiou, T. C. Stamatatos, C. Papatriantafyllopoulou, A. J. Tasiopoulos, W. Wernsdorfer, S. P. Perlepes, G. Christou, *Inorg. Chem.* **2009**, *48*, 9737. (e) T. Yamaguchi, J.-P. Costes, Y. Kishima, M. Kojima, Y. Sunatsuki, N. Bréfuel, J.-P. Tuchagues, L. Vendier, W. Wernsdorfer, *Inorg. Chem.* **2010**, *49*, 9125. (f) T. D. Pasatoiu, M. Etienne, A. M. Madalan, M. Andruh, R. Sessoli, *Dalton Trans.*, **2010**, *39*, 4802.
47. (a) V. Chandrasekhar, B. M. Pandian, R. Azhakar, J. J. Vittal, R. Clérac, *Inorg. Chem.* **2007**, *46*, 5140.
48. (a) F. Chen, W. Lu, Y. Zhu, B. Wu, X. Zheng, *J. Coord. Chem.* **2009**, *62*, 808. (b) X.-Q. Zhao, Y. Lan, B. Zhao, P. Cheng, C. E. Anson, A. K. Powell, *Dalton Trans.* **2010**, *39*, 4911.
49. (a) G. Abbas, Y. Lan, V. Mereacre, W. Wernsdorfer, R. Clérac, G. Buth, M. T. Sougrati, F. Grandjean, G. J. Long, C. E. Anson, A. K. Powell, *Inorg. Chem.* **2009**, *48*, 9345. (b) M. N. Akhtar, V. Mereacre, G. Novitchi, J.-P. Tuchagues, C. E. Anson, A. K. Powell, *Chem. Eur. J.* **2009**, *15*, 7278.
50. (a) A. Mishra, W. Wernsdorfer, K. Abboud, G. Christou, *J. Am. Chem. Soc.* **2004**, *126*, 15648. (b) A. Mishra, W. Wernsdorfer, S. Parson, G. Christou, E. Brechin, *Chem. Commun.* **2005**, 2086. (c) C. Zaleski, E. Depperman, J. Kampf, M. Kirk, V. Pecoraro, *Angew. Chem. Int. Ed.* **2004**, *43*, 3912. (d) V. Mereacre, A. M. Ako, R. Clérac, W. Wernsdorfer, G. Filoti, J. Bartolomé, C. E. Anson, A. K. Powell, *J. Am. Chem. Soc.* **2007**, *129*, 9248. (e) V. Mereacre, A. M. Ako, R. Clérac, W. Wernsdorfer, I. J. Hewitt, C. E. Anson, A. K. Powell, *Chem. Eur. J.* **2008**, *14*, 3577. (f) C. Papatriantafyllopoulou, W. Wernsdorfer, K. A. Abboud, G. Christou, *Inorg. Chem.* **2011**, *50*, 421.
51. (a) C. E. Burrow, T. J. Burchell, P.-H. Lin, F. Habib, W. Wernsdorfer, R. Clérac, M. Murugesu, *Inorg. Chem.* **2009**, *48*, 8051. (b) X.-Q. Lü, W.-X. Feng, Y.-N. Hui, T. Wei, J.-R. Song, S.-S. Zhao, W.-Y. Wong, W.-K. Wong, R. A. Jones, *Eur. J. Inorg. Chem.*

- 2010**, 2714. (c) M. Morimoto, H. Miyasaka, M. Yamasita, M. Irie, *J. Am. Chem. Soc.* **2009**, *131*, 9823.
52. (a) Y.-Q. Sun, J. Zhang, G.-Y. Yang, *Chem. Commun.* **2006**, 4700. (b) Y.-X. Chi, S.-Y. Niu, Z.-L. Wang, J. Jin, *Eur. J. Inorg. Chem.* **2008**, 2336. (c) N. Pooransingh, E. Pomerantseva, M. Ebel, S. Jantzen, D. Rehder, T. Polenova, *Inorg. Chem.* **2003**, *42*, 1256. (d) O. Pouralimardan, A.-C. Chamayou, C. Janiak, H. Hosseini-Monfared, *Inorg. Chim. Acta.* **2007**, *360*, 1599. (e) J. Chakraborty, S. Thakurta, G. Pilet, D. Luneau, S. Mitra, *Polyhedron* **2009**, *28*, 819. (f) F. Mohan, N. S. Gupta, M. P. Gupta, A. Kumar, M. Kumar, *Inorg. Chim. Acta.* **1988**, *152*, 25.
53. (a) N. Kitajima, S. Hikichi, M. Tanaka, Y. Moro-oka, *J. Am. Chem. Soc.* **1993**, *115*, 5496. (b) D. Aguilà, L. A. Barrios, F. Luis, Repollés, O. Roubeau, S. J. Teat, G. Aromí, *Inorg. Chem.* **2010**, *49*, 6784.
54. (a) H. I. Karunadasa, C. J. Chang, J. R. Long, *Nature* **2010**, *464*, 1329. (b) D. M. D'Alessandro, B. Smit, J. R. Long, *Angew. Chem. Int. Ed.* **2010**, *49*, 6058. (c) L. J. Murray, M. Dincă, J. R. Long, *Chem. Soc. Rev.* **2009**, *38*, 1294. (d) G. J.-C. Bünzli, C. Piguet, *Chem. Soc. Rev.* **2005**, *34*, 1048.
55. (a) R. T. Wegh, H. Donker, K. D. Oskam, A. Meijerink, *Science* **1999**, *283*, 663 and references herein. (b) F. Auzel, *Chem. Rev.* **2004**, *104*, 139.
56. X. Gu, D. Xue, *Inorg. Chem.* **2007**, *46*, 3212.
57. K. P. O'Donnell, B. Hourahine, *Eur. Phys. J. Appl. Phys.* **2006**, *36*, 91 and references herein.
58. J. Zhang, P. D. Badger, S. J. Geib, S. Petoud, *Angew. Chem. Int. Ed.* **2005**, *44*, 2508.
59. (a) M. Ferbinteanu, H. Miyasaka, W. Wernsdorfer, K. Nakata, K. Sugiura, M. Yamashita, C. Coulon, R. Clérac, *J. Am. Chem. Soc.* **2005**, *127*, 3090. (b) L. Lecren, W. Wernsdorfer, Y. Li, O. Roubeau, H. Miyasaka, R. Clérac, *J. Am. Chem. Soc.* **2005**, *127*, 11311.
60. O. Waldmann, *Inorg. Chem.* **2007**, *46*, 10035.
61. (a) P. He, M. L. Tong, X.-M. Chen, *Inorg. Chem.* **2005**, *44*, 8285. (b) V. Baskar, K. Gopal, M. Helliwell, F. Tuna, W. Wernsdorfer, R. E. P. Winpenny, *Dalton Trans.* **2010**, *39*, 4747.

Chapter 11

Appendix A: List of compounds

- 1 $[\text{Dy}_2\text{Ni}_2(\text{L}1)_4(\text{NO}_3)_2(\text{DMF})_2]$ (**1**)
- 2 $[\text{Dy}_2\text{Ni}_2(\text{L}1)_4(\text{NO}_3)_2(\text{MeOH})_2] \cdot 3\text{MeOH}$ (**2**)
- 3 $[\text{Y}_2\text{Ni}_2(\text{L}1)_4(\text{NO}_3)_2(\text{MeOH})_2] \cdot 3\text{MeOH}$ (**3**)
- 4 $[\text{Gd}_2\text{Ni}_2(\text{L}1)_4(\text{NO}_3)_2(\text{MeOH})_2] \cdot 3\text{MeOH}$ (**4**)
- 5 $[\text{Tb}_2\text{Ni}_2(\text{L}1)_4(\text{NO}_3)_2(\text{MeOH})_2] \cdot 3\text{MeOH}$ (**5**)
- 6 $[\text{Ho}_2\text{Ni}_2(\text{L}1)_4(\text{NO}_3)_2(\text{MeOH})_2] \cdot 3\text{MeOH}$ (**6**)
- 7 $[\text{Er}_2\text{Ni}_2(\text{L}1)_4(\text{NO}_3)_2(\text{MeOH})_2] \cdot 3\text{MeOH}$ (**7**)
- 8 $[\text{Dy}_2\text{Ni}_2(\text{CO}_3)(\text{L}1)_4(\text{MeOH})_6]_2[\text{Dy}_2\text{Ni}_2(\text{CO}_3)(\text{L}1)_4(\text{MeOH})_5(\text{H}_2\text{O})] \cdot 14\text{MeOH}$ (**8**)
- 9 $[\text{Sm}_2\text{Ni}_2(\text{CO}_3)(\text{L}1)_4(\text{MeOH})_6]_2[\text{Sm}_2\text{Ni}_2(\text{CO}_3)(\text{L}1)_4(\text{MeOH})_4(\text{H}_2\text{O})_2] \cdot 15\text{MeOH}$ (**9**)
- 10 $[\text{Eu}_2\text{Ni}_2(\text{CO}_3)(\text{L}1)_4(\text{MeOH})_6]_2[\text{Eu}_2\text{Ni}_2(\text{CO}_3)(\text{L}1)_4(\text{MeOH})_4(\text{H}_2\text{O})_2] \cdot 15\text{MeOH}$ (**10**)
- 11 $[\text{Gd}_2\text{Ni}_2(\text{CO}_3)(\text{L}1)_4(\text{MeOH})_6]_2[\text{Gd}_2\text{Ni}_2(\text{CO}_3)(\text{L}1)_4(\text{MeOH})_4(\text{H}_2\text{O})_2] \cdot 17\text{MeOH}$ (**11**)
- 12 $[\text{Tb}_2\text{Ni}_2(\text{CO}_3)(\text{L}1)_4(\text{MeOH})_6]_2[\text{Tb}_2\text{Ni}_2(\text{CO}_3)(\text{L}1)_4(\text{MeOH})_5(\text{H}_2\text{O})] \cdot 14\text{MeOH}$ (**12**)
- 13 $[\text{Dy}_4\text{Ni}_8(\text{CO}_3)_4(\text{L}1)_8(\text{NO}_3)_2(\text{H}_2\text{O})_8(\text{MeOH})_4](\text{NO}_3)_2 \cdot 5\text{MeOH} \cdot 4\text{H}_2\text{O}$ (**13**)
- 14 $[\text{Y}_4\text{Ni}_8(\text{CO}_3)_4(\text{L}1)_8(\text{NO}_3)_2(\text{H}_2\text{O})_8(\text{MeOH})_4](\text{NO}_3)_2 \cdot 5\text{MeOH} \cdot 4\text{H}_2\text{O}$ (**14**)
- 15 $[\text{Gd}_4\text{Ni}_8(\text{CO}_3)_4(\text{L}1)_8(\text{NO}_3)_2(\text{H}_2\text{O})_8(\text{MeOH})_4](\text{NO}_3)_2 \cdot 5\text{MeOH} \cdot 4\text{H}_2\text{O}$ (**15**)
- 16 $[\text{Tb}_4\text{Ni}_8(\text{CO}_3)_4(\text{L}1)_8(\text{NO}_3)_2(\text{H}_2\text{O})_8(\text{MeOH})_4](\text{NO}_3)_2 \cdot 5\text{MeOH} \cdot 4\text{H}_2\text{O}$ (**16**)
- 17 $[\text{Ho}_4\text{Ni}_8(\text{CO}_3)_4(\text{L}1)_8(\text{NO}_3)_2(\text{H}_2\text{O})_8(\text{MeOH})_4](\text{NO}_3)_2 \cdot 5\text{MeOH} \cdot 4\text{H}_2\text{O}$ (**17**)
- 18 $[\text{Er}_4\text{Ni}_8(\text{CO}_3)_4(\text{L}1)_8(\text{NO}_3)_2(\text{H}_2\text{O})_8(\text{MeOH})_4](\text{NO}_3)_2 \cdot 5\text{MeOH} \cdot 4\text{H}_2\text{O}$ (**18**)
- 19 $[\text{Dy}_2\text{Ni}_4(\text{OH})_2(\text{L}1)_4(\text{MeOH})_4(\text{NO}_3)_4] \cdot 4\text{MeOH}$ (**19**)
- 20 $[\text{Dy}_4\text{Ni}_8(\text{OH})_4(\text{L}1)_8(\text{MeOH})_4(\text{H}_2\text{O})_4(\text{C}_2\text{O}_4)_2](\text{NO}_3)_4 \cdot 4\text{H}_2\text{O} \cdot 8\text{MeOH}$ (**20**)
- 21 $[\text{Dy}_2\text{Zn}_3(\text{OH})(\text{L}1)_5(\text{MeOH})_{2.5}(\text{OH}_2)_{1.5}]\text{Cl} \cdot 3\text{MeOH} \cdot 2.5\text{H}_2\text{O}$ (**21**)
- 22 $[\text{Eu}_2\text{Zn}_3(\text{OH})(\text{L}1)_5(\text{MeOH})_{2.5}(\text{OH}_2)_{1.5}]\text{Cl} \cdot 3\text{MeOH} \cdot 2.5\text{H}_2\text{O}$ (**22**)
- 23 $[\text{Gd}_2\text{Zn}_3(\text{OH})(\text{L}1)_5(\text{MeOH})_{2.5}(\text{OH}_2)_{1.5}]\text{Cl} \cdot 3\text{MeOH} \cdot 2.5\text{H}_2\text{O}$ (**23**)
- 24 $[\text{Tb}_2\text{Zn}_3(\text{OH})(\text{L}1)_5(\text{MeOH})_{2.5}(\text{OH}_2)_{1.5}]\text{Cl} \cdot 3\text{MeOH} \cdot 2.5\text{H}_2\text{O}$ (**24**)
- 25 $[\text{Ho}_2\text{Zn}_3(\text{OH})(\text{L}1)_5(\text{MeOH})_{2.5}(\text{OH}_2)_{1.5}]\text{Cl} \cdot 3\text{MeOH} \cdot 2.5\text{H}_2\text{O}$ (**25**)
- 26 $[\text{Dy}_7\text{Zn}_4(\text{OH})_4(\text{L}1)_8(\text{Cl})_6(\text{H}_2\text{O})_4]\text{Cl}_3 \cdot 35\text{H}_2\text{O}$ (**26**)
- 27 $[\text{Dy}_6\text{Cd}_6(\text{CO}_3)_2(\text{OH})_4(\mu\text{-Cl})_2(\text{Cl})_2(\text{L}1)_8(\text{OH}_2)_{12}]\text{Cl}_2 \cdot 10\text{THF}$ (**27**)
- 28 $[\text{Tb}_6\text{Cd}_6(\text{CO}_3)_2(\text{OH})_4(\mu\text{-Cl})_2(\text{Cl})_2(\text{L}1)_8(\text{OH}_2)_{12}]\text{Cl}_2 \cdot 10\text{THF}$ (**28**)

- 29 $[\text{Ho}_6\text{Cd}_6(\text{CO}_3)_2(\text{OH})_4(\mu\text{-Cl})_2(\text{Cl})_2(\text{L}1)_8(\text{OH}_2)_{12}]\text{Cl}_2 \cdot 10\text{THF}$ (29)
- 30 $[\text{Er}_6\text{Cd}_6(\text{CO}_3)_2(\text{OH})_4(\mu\text{-Cl})_2(\text{Cl})_2(\text{L}1)_8(\text{OH}_2)_{12}]\text{Cl}_2 \cdot 10\text{THF}$ (30)
- 31 $[\text{Dy}_3\text{Cu}_2(\mu_3\text{-OH})_2(\text{L}1)_5(\text{NO}_3)(\text{MeOH})_2(\text{H}_2\text{O})] \cdot 3\text{MeOH}$ (31)
- 32 $[\text{Gd}_3\text{Cu}_2(\mu_3\text{-OH})_2(\text{L}1)_5(\text{NO}_3)(\text{MeOH})_2(\text{H}_2\text{O})] \cdot 3\text{MeOH}$ (32)
- 33 $[\text{Tb}_3\text{Cu}_2(\mu_3\text{-OH})_2(\text{L}1)_5(\text{NO}_3)(\text{MeOH})_2(\text{H}_2\text{O})] \cdot 3\text{MeOH} \cdot \text{H}_2\text{O}$ (33)
- 34 $[\text{Ho}_3\text{Cu}_2(\mu_3\text{-OH})_2(\text{L}1)_5(\text{NO}_3)(\text{MeOH})_2(\text{H}_2\text{O})] \cdot 3\text{MeOH}$ (34)
- 35 $[\text{Dy}_2\text{Co}_2(\text{L}1)_4(\text{NO}_3)_2(\text{THF})_2] \cdot 4\text{THF}$ (35)
- 36 $[\text{Y}_2\text{Co}_2(\text{L}1)_4(\text{NO}_3)_2(\text{THF})_2] \cdot 4\text{THF}$ (36)
- 37 $[\text{Gd}_2\text{Co}_2(\text{L}1)_4(\text{NO}_3)_2(\text{THF})_2] \cdot 4\text{THF}$ (37)
- 38 $[\text{Tb}_2\text{Co}_2(\text{L}1)_4(\text{NO}_3)_2(\text{THF})_2] \cdot 4\text{THF}$ (38)
- 39 $[\text{Ho}_2\text{Co}_2(\text{L}1)_4(\text{NO}_3)_2(\text{THF})_2] \cdot 4\text{THF}$ (39)
- 40 $[\text{Er}_2\text{Co}_2(\text{L}1)_4(\text{NO}_3)_2(\text{THF})_2] \cdot 4\text{THF}$ (40)
- 41 $[\text{Dy}_4(\text{OH})_2(\text{L}1)_4(\text{HL}1)_2] \cdot 2\text{THF}$ (41)
- 42 $[\text{Gd}_4(\text{OH})_2(\text{L}1)_4(\text{HL}1)_2] \cdot 2\text{THF}$ (42)
- 43 $[\text{Tb}_4(\text{OH})_2(\text{L}1)_4(\text{HL}1)_2] \cdot 2\text{THF}$ (43)
- 44 $[\text{Ho}_4(\text{OH})_2(\text{L}1)_4(\text{HL}1)_2] \cdot 2\text{THF}$ (44)
- 45 $[\text{Er}_4(\text{OH})_2(\text{L}1)_4(\text{HL}1)_2] \cdot 2\text{THF}$ (45)
- 46 $(\text{Et}_3\text{NH})_6[\text{Er}_4(\text{HL}3)_2(\text{NO}_3)_{10}(\text{H}_2\text{O})_4](\text{NO}_3)_4$ (46)
- 47 $(\text{Et}_3\text{NH})_6[\text{Gd}_4(\text{HL}3)_2(\text{NO}_3)_{10}(\text{H}_2\text{O})_4](\text{NO}_3)_4$ (47)
- 48 $(\text{Et}_3\text{NH})_6[\text{Tb}_4(\text{HL}3)_2(\text{NO}_3)_{10}(\text{H}_2\text{O})_4](\text{NO}_3)_4$ (48)
- 49 $(\text{Et}_3\text{NH})_6[\text{Dy}_4(\text{HL}3)_2(\text{NO}_3)_{10}(\text{H}_2\text{O})_4](\text{NO}_3)_4$ (49)
- 50 $(\text{Et}_3\text{NH})_6[\text{Ho}_4(\text{HL}3)_2(\text{NO}_3)_{10}(\text{H}_2\text{O})_4](\text{NO}_3)_4$ (50)
- 51 $\text{DyCu}(\text{L}2)(\text{OMe})(\text{NO}_3)_2(\text{H}_2\text{O})(\text{MeOH})] \cdot 2\text{MeOH}$ (51)
- 52 $[\text{DyCu}_2(\text{L}2)_2(\text{OMe})_2(\text{NO}_3)(\text{H}_2\text{O})_2] \cdot \text{H}_2\text{O} \cdot 1.5\text{MeOH}$ (52)
- 53 $[\text{DyCu}_2(\text{L}2)_2(\text{N}_3)_3(\text{MeOH})(\text{H}_2\text{O})] \cdot 3\text{MeOH} \cdot 1.5\text{H}_2\text{O}$ (53)
- 54 $[\text{DyCu}_3(\text{L}2)_3(\text{OMe})_3] \cdot 1.5\text{MeOH} \cdot 0.215\text{H}_2\text{O}$ (54)
- 55 $[\text{TbCu}_3(\text{L}2)_3(\text{OMe})_3] \cdot \text{MeOH}$ (55)
- 56 $[\text{GdCu}_3(\text{L}2)_3(\text{OMe})_3] \cdot \text{MeOH}$ (56)
- 57 $[\text{HoCu}_3(\text{L}2)_3(\text{OMe})_3] \cdot 1.5\text{MeOH} \cdot 0.215\text{H}_2\text{O}$ (57)
- 58 $[\text{ErCu}_3(\text{L}2)_3(\text{OMe})_3] \cdot 1.5\text{MeOH} \cdot 0.215\text{H}_2\text{O}$ (58)
- 59 $[\text{Dy}_2\text{Cu}_6(\text{OMe})_{2.76}(\text{N}_3)_{1.24}(\text{L}2)_6(\text{H}_2\text{O})(\text{MeOH})(\text{L}4)] \cdot 10\text{MeOH} \cdot 2\text{H}_2\text{O}$ (59)

- 60** [Dy₉Cu₂(L2)₄(HL2)₄(OH)₈(CO₃)₃(NO₃)₃(H₂O)₄(EtOH)](NO₃)₂·9EtOH·6H₂O (**60**)
- 61** [Er₉Cu₂(L2)₄(HL2)₄(OH)₈(CO₃)₃(NO₃)₃(H₂O)₄(EtOH)](NO₃)₂·9EtOH·6H₂O (**61**)
- 62** [Dy₂Cu(OH)(L2)₂(HL2)₂(H₂O)]Cl·5EtOH·2.5H₂O (**62**)

Appendix B: List of organic ligands

- H₂L1** (E)-2-(2-hydroxy-3-methoxy-benzylideneamino)phenol
- H₂L2** (E)-N'-(2-hydroxy-3-methoxybenzylidene)-benzohydrazide
- H₃L3** (E)-N'-(2-hydroxy-3-methoxybenzylidene)-(2-hydroxy)-benzohydrazide
- H₂L4** bis-(E)-N,N'-(2-hydroxy-3-methoxy)-benzylhydrazone

Appendix C: List of abbreviations

Ln	lanthanide
EtOH	ethanol
Me	methyl
Py	pyridine
Ph	phenyl
MeOH	methanol
MeCN	acetonitrile
DMF	dimethylformamide
DMSO	dimethylsulfoxide
mg	milligram
mL	millilitre
mmol	millimole
IR	infrared
NMR	nuclear magnetic resonance
EPR	electron paramagnetic resonance
SQUID	super-conducting quantum interference device
ac	alternating current
dc	direct current
D	zero-field splitting parameter
K	kelvin

Oe	oersted
H	field
Hz	hertz
M	magnetisation
T	temperature
T	tesla
T _b	blocking temperature
T _c	critical temperature
h	hour
χ	molar magnetic susceptibility
χ'	in-phase magnetic susceptibility
χ''	out-of-phase magnetic susceptibility
μ_B	bohr magneton
U _{eff}	effective energy barrier
cm ³	cubic centimetres
b	broad
d	doublet
t	triplet
s	singlet (NMR), strong (IR)
THF	tetrahydrofurane
m	multiplet (NMR), medium (IR)
NIR	near infra red
w	weak
MOFs	metal organic frameworks
SMM	single molecule magnet
UV	ultra-violate

Acknowledgements

It is a great pleasure for me to express my sincere thanks and heartfelt gratitude to my supervisor, Prof. Dr. A. K. Powell for her excellent guidance, constant encouragement, continuous support, letting me work with my own ideas and giving me different opportunities to learn and handle different instruments and deal with people from different countries throughout the course of this work. I am grateful to her for giving me the liberty of thought and work. I would like to take this opportunity to express my sincere gratitude to Dr. C. E. Anson and Dr. G. E. Kostakis for collecting and solving and explaining the kind of problems and how to deal with the crystallographic data presented in this thesis. I would also like to thank them for giving me valuable suggestions throughout my research work. Many thanks to Dr. R. Clérac for his enthusiasm in the beginning of my Ph.D, Dr. Oliver Waldman for enriching my understanding and Dr. W. Wernsdorfer for magnetic single crystal hysteresis measurements. Thanks to Dr. Ghenadie Novitchi for teaching comments towards the better understanding. I would like to thank Dr. Yanhua Lan for performing the SQUID measurements of all the compounds and for their magnetic studies. She taught me how to operate SQUID machine. She also helped me to overcome some of the doubts in order to have a clear idea about some magnetic phenomenon in the field of molecular magnetism. I thank to Dr. Lianne Beltran for friendly behavior during my stay in Germany. I specially thank to Dr. George E Kostakis for collecting crystal data and solving the crystal structures and giving useful tips while writing my manuscripts and also teaching me the topos program. George is always with me like a friend, philosopher and guide. His inspiration and faith showed me the right paths. I also specially thank George, Valeriu, Chirs and Annie for thoroughly checking my thesis and to Dirk for translation of the conclusion from English to German. I am thankful to Getraud Amschlinger and Patricia Jaeger for all their help in both official as well as unofficial works. Thanks to Rolf Lehmann for solving any technical problems with the instruments and for being there whenever I needed him. I am very much thankful to H. Henke for teaching how to operate PPMS for heat capacity measurements. At South Campus of KIT, I thank Dr. Matern and Frau H. Berberich for measuring NMR spectra. Thanks to Frau S. Lude for providing elemental analysis. I also thank Frau G. Leichle, Frau S. Böcker and all other technical staffs for their help in chemical stores, maintenances and jolly behavior. The micro-analysis data helped a lot to know whether it has lost some solvent molecules or not and some cases it helped to guess whether I got some new complexes. I would

like to thank all the group members for helping and giving me friendly suggestions. Thanks to Dirk and Sanjit for giving me little software's and for his help and company in Karlsruhe. Sanjit and Dirk helped me a lot regarding the problem with my laptop/computers. Thanks to Frederik for teaching me the Stoe diffractometer handling and Zeeshan for all the hilarious moments and helping me in the laboratory. Thanks to Amin, Amer, Sven, Markus, Dirk, Jürgen, Lena, Irina, Mostafa, Denis, Madhu, Julia and Sudarshana for their help in respective moments. I thank my friends, Biswajit, his wife, Abhishek, Asamanjoy, Murugesh and Hari for their great company during the stay in Karlsruhe. I thank my M. S guide Dr. P. S. Mukherjee for introducing me in this interdisciplinary field. I am always hugely guided by invisible helping mind and knowledge given in my class XI-XII standard by my teacher IES Engg. Swapan Mondal. He gave me the best direction in my life. Finally, I would like to thank my fiancée Sudipta Roy for her inspiration, continuous support and encouragement at any time required. The faith and confidence of my teachers, my parents, sisters, brothers and relatives on me helped me to reach wherever I am today.

Curriculum vite

Name: Kartik Chandra Mondal
 Date of birth: 28 October 1983
 Place of birth: Khukurdaha (West Bengal), India
 Marital status: Single
 Nationality: Indian

Education

June 1999 Secondary education from Khukurdaha I.C.M.M High School under WBBSE Board, Khukurdaha, West Midnapur, W. B, India.
 July 2001 Higher Secondary education from Khukurdaha I.C.M.M High School, under WBCHSE Board, Khukurdaha, West Midnapur, W. B, India.
 July 2004 Bachelor in Chemistry (B.Sc) from Chemistry Department, Ramakrishna Mission, Narendrapur under University of Calcutta, W.B, India
 August 2007 Master in Chemistry (M.S) from Department of Chemistry, Institute of Science (I.I.Sc), Bangalore, India
 April 2011 Ph.D from Karlsruher Institut für Technologie (KIT) under Prof. Dr. Annie K Powell

Fellowships and Awards: Int.Ph.D Research Fellowship, Indian Institute of Science, Bangalore, India.
 Awarded 1st prize for best poster in MTIC-XII, IIT Madras on 6th of December 2007

Research Experience:

June-July - 2005 Summer project under Prof. Dr. S. Bhattacharya in the *Dept. of Organic Chemistry*. I.I.Sc, Bangalore, India
 December - 2005 Winter project under Prof. Dr. T. N. Guru Rao, SSCU, I.I.Sc, Bangalore, India.
 June - 2006 Course project under Prof. Dr. M. S. Hegde, SSCU, I.I.Sc, Bangalore, India.

January 2006 Master project under Dr. Partha S. Mukherjee, IPC, I.I.Sc, Bangalore,
to April - 2008 India.

List of Publications

1. **Kartik C. Mondal**, Mike G. B. Drew, and Partha S. Mukherjee,
Synthesis of a Mn₆ Cluster and Its Self-Assembly of an Azido-Bridged Polymer.
Inorg. Chem. **2007**, 46(14), 5625-5629. (Article) DOI: 10.1021/ic0702670
2. **Kartik C. Mondal**, Y. Song and Partha. S. Mukherjee, *Self assembly of a Mn₉ nanoscopic mixed-valent Cluster: Synthesis, crystal Structure and Magnetic Property, a SMM.* *Inorg. Chem.*; **2007**, 46(23), 9736-9742. (Article); DOI: 10.1021/ic701018x
3. **Kartik C. Mondal**, Oindrila Sengupta, M. Nethaji and P. S. Mukherjee,
Assembling metals (Co^{II} and Mn^{II}) with pyridylcarboxylates in the presence of azide: synthesis, structural aspects and magnetic behavior of three coordination polymers. *Dalton.Trans.* **2008**, 767-775. (Article) DOI: 10.1039/b715460g
4. **Kartik C. Mondal** and Partha S. Mukherjee, *Three New Cu–Azido Polymers and Their Systematic Interconversion: Role of the Amount of the Blocking Amine on the Structural Diversity and Magnetic Behavior.* *Inorg. Chem.*, **2008**, 47 (10), pp 4215–4225. DOI: 10.1021/ic702232d
5. **Kartik C. Mondal** and Partha S. Mukherjee, *Mn(II) azido chain using a new amide ligand: synthesis, crystal structure and variable temperature magnetic behavior.* *Synthesis and reactivity of Inorganic, Metal-Organic, and Nano-metal Chemistry*, **2007**, 37(9), 735-739. (Invited article, has appeared in September issue)._DOI: 10.1080/15533170701675147
6. **Kartik C. Mondal**, Oindrila Sengupta and Partha. S. Mukherjee.
Synthesis and characterization of a rare hemiacetalate bridged incomplete Cu^{4II} dicubane cluster. *Inorg. Chem. Commun.*, **2009**, 12(7), 682-685. DOI: 10.1016/j.inoche.2009.05.027
7. **Kartik C. Mondal**, O. Sengupta, P. Dutta, M. Seehra, S. K. Nayak and Partha S. Mukherjee, *Three-dimensional 3d–4f heterometallic polymers containing both azide and carboxylate as co-ligands.* *Inorg. Chim. Acta.*, **2009**, 362, 1913-1917.

doi:10.1016/j.ica.2008.09.018

8. George E. Kostakis, **Kartik C. Mondal**, Ghulam Abbas, Yanhua Lan, Ghenadie Novitchi, Gernot Buth, Christopher E. Anson and Annie K. Powell, *[Cu(N3)(p-CPA)]_n: a two dimensional network exhibiting spin reorientation*. *CrystEngComm*, **2009**, *11*, 2084. DOI: 10.1039/b905707b.
9. G.E. Kostakis, **Kartik C. Mondal**, C.E. Anson and A.K. Powell, *Influence of the Metal Radius on the Dimensionality of Hydrogen-Bonded Metal Supramolecular Frameworks in the Metal / p-BDTH2 (1,4-Benzeneditetrazol-5-yl) Reaction System*. *Polyhedron*, **2009**, DOI: 10.1016/j.poly.2009.05.057.
10. **Kartik C. Mondal**, George E. Kostakis, Yanhua Lan, Christopher E. Anson and Annie K. Powell, *Spin Canting and metamagnetic behaviour of a new species from hydrothermal Co(II) 3-Trans-Pyridylacrylate system*. *Inorg. Chem.* **2009**, *48*, 9205-9213. (Article). DOI: 10.1021/ic900886y
11. Zeeshan Majeed, **Kartik C. Mondal**, George E. Kostakis, Yanhua Lan, Christopher E. Anson and Annie K. Powell, *[LnNa(PhCO₂)₄] (Ln = Ho, Dy): the first examples of chiral srs 3D networks constructed using the monotopic benzoate ligand*. *Chem. Commun.* **2010**, *46*, 2551-2553. (Article). DOI: 10.1039/b923998g
12. Zeeshan Majeed, **Kartik C. Mondal**, George E. Kostakis, Yanhua Lan, Christopher E. Anson and Annie K. Powell, *Structure and magnetic properties of a decanuclear Mn^{II}₂Mn^{III}₂Dy₆ aggregate*. *Dalton. Trans.* **2010**, 4740-4743. (Article). DOI: 10.1039/c000082e
13. **Kartik C. Mondal**, Bappa Gole, S. R. Batten and Partha S. Mukherjee. *Synthesis and characterization of a rare hemiacetalate bridged incomplete Cu^{II}₄ cluster and two 1D chain of defect cubane Na₂Ni₂: Synthesis, Crystal Structure, magnetic property, EPR and theoretical study*. (submitted)

Participation in Conferences and meetings

- MTIC-XII, IIT Madras on 6th of December 2007, Chennai, India, December, 2007.
- 11th International Conference on Molecular Magnetism (ICMM), Florence, Italy, September, 2008.
- 2nd Karlsruhe – Strasbourg Chemical Link Karlsruhe, Germany, December, 2008.